Dissertations, Master's Theses and Master's Reports - Open

2009

Electron transport in E x B devices

Emily C. Fossum
Michigan Technological University

ELECTRON TRANSPORT IN $\mathbf{E} \times \mathbf{B}$ DEVICES

By

EMILY C. FOSSUM

A DISSERTATION

Submitted in partial fulfillment of the requirements

for the degree of

DOCTOR OF PHILOSOPHY

(Mechanical Engineering–Engineering Mechanics)

MICHIGAN TECHNOLOGICAL UNIVERSITY

2009

This dissertation, "Electron Transport in $\mathbf{E} \times \mathbf{B}$ Devices", is hereby approved in partial fulfillment of the requirements for the degree of DOCTOR OF PHILOSOPHY in the field of Mechanical Engineering–Engineering Mechanics.

DEPARTMENT:
Mechanical Engineering–Engineering Mechanics

Signatures:

Dissertation Advisor   _____
Dr. Lyon B. King

Department Chair   _____
Dr. William Predebon

Date   _____

To my parents. You have encouraged me to reach for the stars and have never stopped believing in me, even during times when I may not have believed in myself.

Abstract

You know, it would be sufficient to really understand the electron.
Albert Einstein

A Hall thruster, an $\mathbf{E} \times \mathbf{B}$ device used for in-space propulsion, utilizes an axial electric field to electrostatically accelerate plasma propellant from the spacecraft. The axial electric field is created by positively biasing the anode so that the positively-charged ions may be accelerated (repelled) from the thruster, which produces thrust. However, plasma electrons are much smaller than ions and may be accelerated much more quickly toward the anode; if electrons were not impeded, a "short circuit" due to the electron flow would eliminate the thrust mechanism. Therefore, a magnetic field serves to "magnetize" plasma electrons internal to the thruster and confines them in gyro-orbits within the discharge channel. Without outside factors electrons would be confined indefinitely; however, electron-neutral collisions provide a mechanism to free electrons from their orbits allowing electrons to cross the magnetic field toward the anode, where this process is described by classical transport theory. To make matters worse, cross-field electron transport has been observed to be 100-1000 times that predicted by classical collisional theory, providing an efficiency loss mechanism and an obstacle for modeling and simulations in Hall thrusters.

The main difficulty in studying electron transport in Hall thrusters is the coupling that exists between the plasma and the fields, where the plasma creates and yet is influenced by the electric field. A device has been constructed at MTU's Isp Lab, the Hall Electron Mobility Gage, which was designed specifically to study electron transport in $\mathbf{E} \times \mathbf{B}$ devices, where the coupling between the plasma and electric field was virtually eliminated. In this device the two most cited contributors to electron transport in Hall thrusters, fluctuation-induced transport, and wall effects, were absent. Removing the dielectric walls and plasma fluctuations, while maintaining the field environment in vacuum, has allowed the study of electron dynamics in Hall thruster fields where the electrons behave as test particles in prescribed fields, greatly simplifying the environment. Therefore, it was possible to observe any effects on transport not linked to the cited mechanisms, and it was possible to observe trends of the enhanced mobility with control parameters of electric and magnetic fields and neutral density– parameters that are not independently variable in a Hall thruster.

The result of the investigation was the observation of electron transport that was $\sim$ 20-100 times the classical prediction. The cross-field electron transport in the Mobility Gage was generally lower than that found in a Hall thruster so these findings do not negate the possibility of fluctuations and/or wall collisions contributing to transport in a Hall thruster. However, this research led to the observation of enhanced cross-field transport that had not been previously isolated in Hall thruster fields, which is not reliant on momentum-transfer collisions, wall collisions or fluctuations.

Acknowledgments

This dissertation is not a product of my own hands, but so much more a product of all those who have been there to lead me, guide me, carry me, correct me, and stand by me, with respect to everything in my life, technical or not.

First and foremost, I would like to thank my advisor Brad King. Brad, you have invested so much in me over the years and I thank you for taking that chance and believing in me. Thank you for allowing me to go my own direction at times and roping me in when I needed to be pointed in a new direction. Thank you for providing support, honesty, guidance, encouragement and friendship. I will certainly miss our whiteboard brainstorming sessions, among many other things. I honestly cannot thank you enough for all that you have done for me. I would also like to extend my gratitude to the National Science Foundation (Grant CBET-0348048) for the funding that made this project possible.

An enormous thanks goes out to my committee members for their countless hours of guidance and feedback. Dr. Donna Michalek, thank you for your support throughout my *decade* at MTU, through my undergrad and into my graduate work, you have guided me and been an example to me. Dr. Brian Fick, you have been a valuable addition to the faculty at MTU. Your enthusiasm and humor make science fun. Thank you for all of the help in and out of class. Dr. Melissa Meyer, thank you taking the time and effort to travel back to MTU. Thanks also for your encouragement and feedback in many aspects of my research and career. Dr. Yevgeny Raitses, thank you so much for agreeing to serve on my committee. You feedback is invaluable and your research has been instrumental in my own. To the entire committee, you have all been so generous with your time, resources, and advice. I truly don't deserve all of the help you have given me, but I am eternally grateful for it. Thank you!

To the Isp-ers that have gone before me: Alex, Dean and Jason. Thanks for all of the help over the years and setting the bar for the Isp Lab. Thanks to you, the Isp Lab went from a basement closet to taking over an entire floor of the MEEM. You have put us on the map at MTU and throughout the research community. Dean a special thanks to you for breaking the mold, which was responsible for countless Isp Lab and even university-wide policies; I am not sure if it is fame or notoriety, but either way we are well known. To those that remain: Makela, Jerry, Carrie, and Rob, good luck in your journey. It is a long but valuable one. Keep raising the bar. Thanks to everyone from the Isp Lab for the entertainment, the whiteboard sessions, establishing and sustaining my coffee addiction, sharing facilities, and sharing your ideas. To our master machinists, Marty and Jesse, my research would not have been possible without your countless hours of help. The design and fabrication process was truly a collaborative effort.

Thanks also to the office staff (Joan, Nancy, Connie, Renee, Marlene and JoAnne),

for all of your help and sometimes futile attempts to keep me organized. This department (and I especially) would be lost without you. Rob Rowe, thanks so much for all of your help (and musical entertainment) in the machine shop. Thanks to the Graduate School Office, especially Deb and Nancy, for keeping me on track in this whole process. And a special thanks to our department head, Bill Predebon, for dedicating countless hours to this department.

Thank you to those at NASA-Glenn (or formerly at NASA-Glenn), George Williams, Hani Kamhawi, John Foster, Rich Hofer, Louis Piñero, Don Jaworske and Mike Patterson. Thanks for your help so early in my graduate school career. You all were instrumental in getting me started in the world of EP. Thanks also, to countless others within the research community, all of those at (and formerly at) Michigan (PEPL), Stanford (SPDL), Princeton and PPPL, NASA-JPL, and Edwards AFB, you have helped enormously through discussions and through your own research. A special thanks to Keidar, Hofer, Boyd, Kaganovich, Spektor, Raitses, Thomas, Meezan, and Cappelli, my work relies heavily on the work you have done and are doing. Thank you for all of the progress you have made in this field.

Dr. Mario Fajardo, thanks so much for all of your patience in waiting for this document to get finished. I tremendously enjoyed working with you on our proposal and look forward to working with you in the next chapter of my career.

I would also like to thank those that helped with the software and graphics for putting this document together. Gowtham, I can't thank you enough for putting this template together saving me many hours of formatting and frustration with LaTeX 2_ε (a program that I have grown to love). Also, thanks for good discussions at the KBC and the inspiring energy you have in all you do. Your enthusiasm is contagious. I'd also like to thank Neal Hersig for his online course in Blender[1] whose instruction was instrumental in the creation of the graphics throughout this document.

My beloved family, Mom, Dad, Karin, Ben, and Allie, thanks to all of you for pretending to be interested in the "electron flea circus" and even more, thanks for all of the support you have given me over the years. Dad, a special thanks for the countless hours pouring over math problems at the kitchen counter. That prepared me better than I ever could have imagined for a career in science. Mom, thanks to your influence I have followed in your footsteps in becoming a perpetual student. I will always be a student in life, whether within formal education or not. Karin, thanks for providing the endless competition, love, and support only an older sister could provide. Ben, thanks so much for joining our family– you are everything I could ever ask for in a brother. A special thanks to my newborn niece, Allie, thanks for waiting until after I turned in my dissertation draft to be born so I could be there to welcome you into the world. Also, thanks for reminding me to make time for family during a period of my life when I probably would not have. And to my loving grandfather, the late William F. Nettekoven, thanks for being an amazing role model, in engineering

and in character... I wish you were here to see me graduate.

To my best friend, Matt. Thanks so much for all you have done for me over the years. From building decks, fashion advice (is there a wrinkle there?), nerdy engineering conversations, and weekend getaways to insightful discussions and personal development, you have been there to support me, guide me and be the best partner in crime anyone could ever ask for.

Carrie, I have so much to thank you for. Lattes, Friday MUB muffins, advice, personal and research related, rides, dragging me to the gym, recipes, second breakfast, endless laughs, introducing me to Comsol and Blender, and giving me a push every so often when I needed it most. No thanks to anyone out in California for stealing Carrie from Houghton, except possibly Mike Nakles, indirectly, for coercing Carrie and thus, me, to work out.

There are so many others I would like to thank for so many things. Deb, Alicia, Charlie, Shawn, Jen, Karen, Erin, Jess, Monica, Sam, Sarah, Brian, Britta, Saira, Irvania, Marla, Cheyenne, and Copper, thanks for the times you called, dragged me out of the lab, welcomed me home, sent me a note, or in some other way cheered me up. Each of you has helped me and influenced me in your own way, and I appreciate your friendship more than I could ever tell you. Thanks to the folks at Panara for being there as my favorite backup plan. And a special thanks to Saira, thank you more than ever for reintroducing me to the love of God. I think you were an angel sent by Him.

I would also like to thank the late Dr. Richard P. Feynman (1918-1988), his daughter Michelle Feynman and his son Carl Feynman, for their work on *Perfectly Reasonable Deviations from the Beaten Track: The Letters of Richard P. Feynman*[2]. This book was truly inspiring at a time when I needed to be reminded of the enthusiasm I (most of the time) have for science and to pick me up with humor and assurance during the times when my enthusiasm was overcome by frustration. Please, if you are a student or teacher in any scientific or educational field (and maybe even a non-scientific field, but why then, are you reading this dissertation?), I recommend that you get your hands on this book. My favorite advice:

> *"Study hard what interests you the most in the most undisciplined, irreverent and original manner possible."*

Above all, I would like to thank the Lord God. Thank You for guidance, correction, answered and unanswered prayers, and reminding me over and over that this, among many other things, I cannot do alone. I truly am nothing and could do nothing without You. I would especially like to thank You for the perfection You have created in Nature and for allowing all of us to uncover Your wonder, piece by piece, through scientific research.

Romans 1:20

For since the creation of the world God's invisible qualities— his eternal power and divine nature— have been clearly seen, being understood from what has been made, so that men are without excuse.

Contents

List of Figures

List of Tables

Nomenclature

$\mathbf{B}$, B	Magnetic field vector, magnitude
B_m, B_0	Maximum and mid-plane magnetic field strength in a magnetic bottle configuration, see equation (2.8), page 19
B_r, B_z	Radial, axial components of the magnetic field
$\hat{\mathbf{b}}$	Unit vector in the direction of the magnetic field
D	Diffusion constant (free)
$D_\perp$	Cross-magnetic-field diffusion constant
$\Delta \mathbf{x}$	Displacement of particle after time, t, see equation (2.35), page 35
Δz_{a-c}	Axial distance between anode and cathode in the Hall Electron Mobility Gage
δ	Average step size, i.e. average distance traveled between collisions, see equation (2.35), page 35
$\mathbf{E}$, E	Electric field vector. magnitude
$E_\perp$	Electric field transverse to magnetic field
E_z	Axial electric field
e	Elementary charge, 1.602×10^{-19} C
ϵ_0	Permittivity of free space (vacuum), 8.854×10^{-12} C^2/(N-m)
$\bar{\epsilon}_i$	Average energy change per collision, see equation (7.8), page 201
$F_{\mathbf{E}\cdot\hat{\mathbf{b}}}$	Force on electrons due to an electric field parallel to the magnetic field, see equation (4.3), page 94
F, f	Distribution function normalized to n, normalized to 1
Γ_{ew}	Electron flux to the channel walls, see equation (3.1), page 63

h	Planck's constant, 6.626068×10^{-34} m^{2}kg/s
I_a	Anode current, page 142
I_c	Cathode current, page 142
I_d	Total discharge current (typically used in reference to a Hall thruster)
I_e	Electron current
$I_e m$	Emission current, page 142
I_h	Filament heater current, page 143
I_i	Ion current
I_p	Probe current, page 142
I_{sp}	Specific impulse
i	Imaginary unit, $\sqrt{-1}$
J	Current density
J_a	Current density at the anode of the Hall Electron Mobility Gage
J_c	Current density at the cathode of the Hall Electron Mobility Gage
J_{ez}	Axial electron flux
J_p	Probe current density, see equation (6.5), page 158
k	Boltzmann constant, 1.3807×10^{-23} J/K
$k, \mathbf{k}$	Wavenumber, wave vector
L_{plasma}	Characteristic length scale of the plasma body
λ_D	Debye length
λ_m	Mean free path
ℓ_{f-a}	Path length of electron trajectory from filament (loading point) to anode
m_e	Mass of electron, 9.109×10^{-31} kg
M_n	Mass of neutrals
m	Mass of particle, kg

m_j	Mass of species j
$\mu_\perp$	Cross-magnetic-field mobility constant
μ	Mobility constant (free)
μ_{Bohm}	Bohm mobiltiy coefficient, see equation (2.65), page 49
μ_{ez}	Axial mobility in the Hall Electron Mobility Gage, see equation (7.1), page 177
μ_{mag}	Magnetic moment, see equation (2.5), page 17
n_0	Unperturbed particle density, neutral density or density of target particles
n_e	Electron density
$\tilde{n}_e$	Oscillating electron density, see equation (2.67), page 49
n_i, n_{ij}	Ion density, Density of ions with charge j, where $j = 1, 2, ...$
n_j	Density of species j
ν_{AN}	Anomalous collision frequency
ν_{bounce}	Bounce frequency, page 136
$\nu_{coll.}$, ν_m	Collision frequency for collisions of type $coll.$, momentum-transfer collision frequency
ν_{ew}	Electron-wall collision frequency, see equation (3.3), page 63
ν_i	Ionization collision frequency, see equation (7.10), page 202
ν_{mag}	Magnetron frequency, page 136
ω_c, ω_{ce}	Cyclotron (Larmor) frequency, electron cyclotron frequency
Ω_H	Hall parameter, see equation (2.43), page 38
ω_P	Electron plasma frequency
p	Pressure
$\Phi_{eff.}$	Effective potential well of the Hall Electron Mobility Gage, see equation (4.2), page 93
ϕ, Φ	Electrostatic potential

ϕ_0	Unperturbed electrostatic potential
ϕ_{local}	Local unperturbed potential
ϕ_s	Sheath potential, see equation (3.2), page 63
$\tilde{\phi}$	Oscillating electrostatic potential, see equation (2.66), page 49
φ	Work function for electron emission from a surface, see equation (4.4), page 96
q	Particle charge
R	Ideal gas constant, 8.314 J/(mol-K), see equation (5.4), page 114
R_m	Magnetic mirror ratio, B_0/B_m, see equation (2.8), page 19
r_L	Larmor radius, see equation (2.2), page 14
ρ	Charge density
$\sigma_{coll.}$	Collision cross-section for collision type *coll.*
$\tau_{en}, \nu_{en}, \sigma_{en}$	Electron-neutral collision time, frequency, cross-section
T	Temperature, K
T_e	Electron temperature
$\tau_{coll.}, \tau_m$	Mean time between collisions of type *coll.*, mean time between momentum-transfer collisions
$\tau_{ee}, \nu_{ee}, \sigma_{ee}$	Electron-electron collision time, frequency, cross-section
$\tau_{ei}, \nu_{ei}, \sigma_{ei}$	Electron-ion collision time, frequency, cross-section
τ_p	Particle confinement time in the Hall Electron Mobility Gage, see equation (5.25), page 131
τ_{res}	Residence time of particles within the Hall Electron Mobility Gage, see equation (7.15), page 207
θ_m	Magnetic mirror loss cone angle
u_{ez}	Bulk axial electron velocity
u_{iz}	Bulk axial ion velocity
$u_{\perp,net}$	Net cross-field velocity

V_{ac}	Anode-to-cathode voltage in the Hall Electron Mobility Gage
V_d	Discharge voltage (Hall thruster)
V_f	Filament bias voltage, page 143
V_p	Probe voltage, page 142
$\mathbf{v}$, v	Velocity vector, magnitude
$\bar{v}$	Average particle velocity
v_c	Critical velocity to overcome the potential well, see equation (5.9), page 122
$\mathbf{v}_D$	Fluid drift velocity, see equation (2.13), page 23
$\mathbf{v}_{\mathbf{E}\times\mathbf{B}}$	Drift velocity due to the $\mathbf{E}\times\mathbf{B}$ drift, see equation (2.3), page 16
$\mathbf{v}_f$	Particle drift due to the presence of a force orthogonal to the magnetic field, see equation (2.3), page 17
v_f	Flow velocity, page 158
$\mathbf{v}_{\nabla B}$	Particle drift due to a gradient in the magnetic field (Grad-B drift), see equation (2.4), page 17
$v_\perp$	Particle velocity perpendicular to the magnetic field
v_{th}	Thermal velocity, page 158
$\left(\frac{\partial f}{\partial t}\right)_c$	Boltzmann collision term
$e\phi_w$	Depth of electrostatic potential well, eV
$\mathbf{E}\times\mathbf{B}$	In reference to the charged particle drift arising perpendicular to both $\mathbf{E}$ and $\mathbf{B}$ due to the crossed fields
$\ln\Lambda$	Coulomb logarithm, see equation (2.58), page 44

Chapter 1

Introduction

1.1 Hall Thruster Overview

Hall thrusters are highly efficient in-space propulsion devices used mainly for satellite station-keeping and orbit transfer maneuvers. The early development of the Hall thruster began in the U.S. and Russia independently in the early 1960s. In the late 1960s the U.S. diverted their research efforts to other devices with higher attainable specific impulse, most specifically the gridded-ion thruster[10]. The Russian Hall thruster effort continued, and in 1972 the first operational Hall thruster, the SPT-60, was launched aboard the Meteor spacecraft[11]. Over the next 30 years more than 140 Russian Hall thrusters were launched as primary propulsion aboard spacecraft. Throughout the Russian effort efficiency analyses and performance measures were used to optimize Hall thruster performance[11, 12].

Due to the success of the Russian Hall thruster program and the release of the Russian technical documents outlining the development efforts of Hall thrusters following the fall of the USSR, the U.S. launched plans to pursue Hall thruster research and integrate Hall thruster technology into existing systems in the 1990s. Hall thrusters are particularly well suited for satellite station-keeping and orbit transfer

maneuvers, which has been the main use of the technology[13]. The first Hall thruster on a U.S. spacecraft was the Russian-designed and -built D-55 TAL, launched in 1998 for the National Reconnaissance Office (NRO) Space Technology Experiment Satellite (STEX)[14], a mission designed specifically for testing and validation of advanced propulsion concepts. The European Space Agency (ESA) used a Hall thruster as primary propulsion for the lunar orbiting mission, SMART-1 (Small Mission for Advances Research in Technology)[15]. The first commercial use of a Hall thruster was in 2004 by Space Systems Loral for the MBSAT satellite using SPT-100s[16] manufactured by the Russian company, Fakel. It was not until December of 2006 that a U.S. designed Hall thruster was put in operation; the BHT-200 Hall thruster was launched for the Air Force TacSat-2, which was designed and built by Busek Co., and successful in-space operation was confirmed in March of 2007[17]. Hall thrusters have grown in acceptance in the U.S. in recent years and plans are in place for the use of the Aerojet-designed BPT-4000 by Lockheed Martin Space Systems for the Air Force Advanced-EHF defense communications satellite[18]. Mission analysis has also been presented for using the BPT-4000 for deep space missions[19] which was the original vision of electric propulsion technology as outlined in the early 1900s[20].

There are two competing Hall thruster configurations, the anode-layer (TAL) and the stationary plasma thruster (SPT). The differences between the two will not be discussed at length but are mentioned to point out that variations in Hall thruster configuration exist and this dissertation is concerned with the SPT-type Hall thruster. (A detailed description of each can be found in Ref. [11].) The description of Hall thruster physics from this point forward is in reference to the SPT-type Hall thruster. The physics of a Hall thruster will be covered in more detail in Chapter 3 and only a brief overview is presented here. Fig. 1.1 shows a picture of a flight-scale Hall thruster in operation and a cross-section illustrating the main features of a Hall thruster. Hall thrusters are operated by employing an axial electric field, E_z, through the application of a high positive voltage on the anode, which repels positive ions from the spacecraft.

This acceleration of ions provides the thrust needed to accelerate the spacecraft[11]. A cathode external to the main thruster body supplies electrons to the discharge
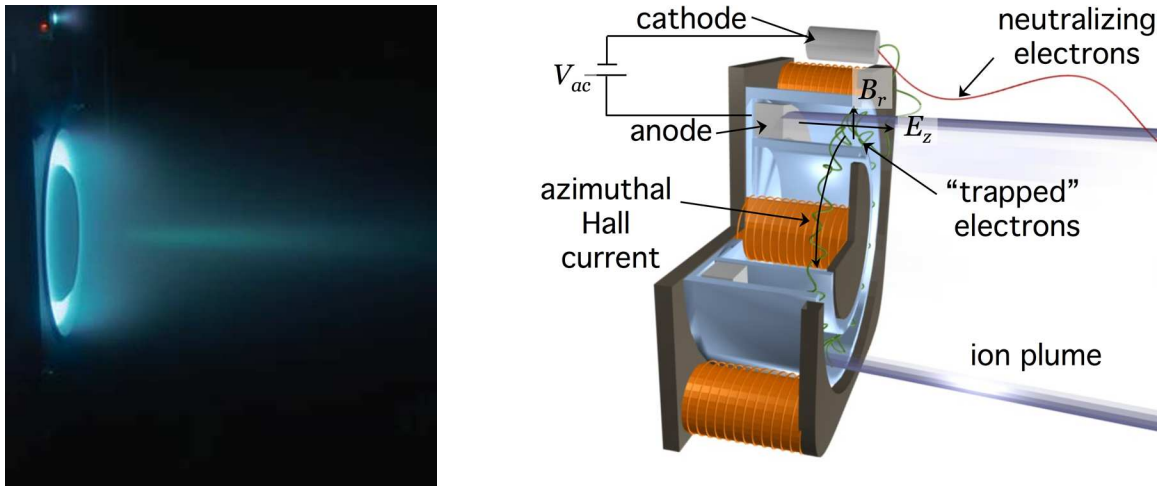
Figure 1.1: Hall Thruster in Operation (left) and schematic of a Hall thruster cross section (right).

stream of ions so that the spacecraft remains neutral. In addition, the cathode also supplies electrons to the discharge channel for the purpose of ionizing propellant neutrals through electron-impact ionization. Since electrons are highly mobile due to their small mass, any applied electric field would cause the electrons to stream to the anode and the massive ions would experience negligible acceleration. Therefore, by applying a radial magnetic field, B_r, the axial velocity of the electrons is turned to a gyration perpendicular to the applied magnetic field and their motion to the anode is significantly inhibited. Because of this, the ions, whose gyro-radius is much larger than the thruster dimensions due to their large mass, can be accelerated by the electric field, where their deflection due to the magnetic field is negligible, while electron motion is impeded. (For a detailed discussion of charged particle motion the reader is referred to Section 2.1.1 as only a qualitative description is presented here.) Electrons are able to migrate to the anode across the radial magnetic field lines by cross-field mobility; this creates a current indicated on Fig. 1.2 as "recycle current." (The details of cross-field mobility are presented in greater detail in Sections
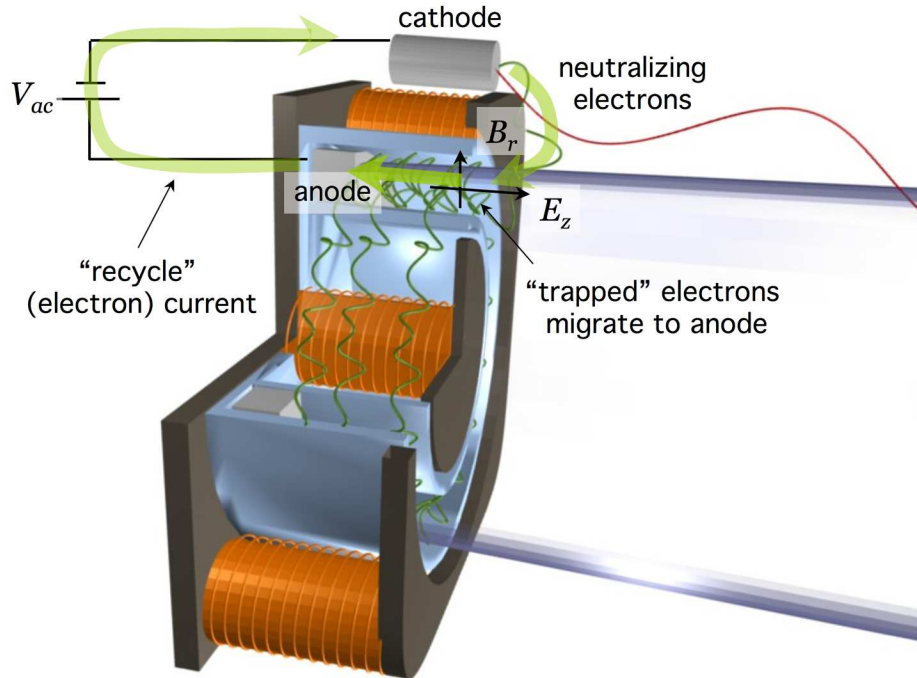
Figure 1.2: Cross-field electron mobility in the Hall thruster discharge channel leads to "recycle" current.

2.2 and 2.3.) Axial electron mobility perpendicular to the magnetic field has been found to be 100-1000 times larger than classically predicted[21], which limits Hall thruster efficiency because of the excess current to the anode. At high discharge voltages electron mobility to the anode has been found to degrade the efficiency of the thruster[22] and to limit the exit velocity to below $\sim$30,000 m/s ($I_{sp} \sim$3,000 s) if the thruster is to be operated at optimal efficiency.

1.2 Electron Mobility in Hall Thrusters

Cross-field electron mobility, $\mu_\perp$, is defined as the constant of proportionality between the bulk cross-field velocity of electrons, $u_\perp$, and the electric field transverse to the

magnetic field, $E_\perp$. This relation is given by

$$u_{\perp,net} \; = \; \mu_\perp E_\perp \qquad\qquad (1.1)$$

Classical theory accounts for electrons' ability to cross magnetic field lines by momentum-transfer collisions, which free the electrons from their gyro-orbits allowing them to migrate perpendicular to the field toward the anode. It is well known that electron mobility in Hall thrusters is much higher than can be accounted for by momentum-transfer collisions alone and is 100-1000 times the classical collisional model[21]. Therefore, an unknown mechanism exists, separate from momentum-transfer collisions, that is responsible for the experimentally observed mobility, generally called "anomalous" or "collisionless" mobility. Several theories exist to account for the "anomalous" mobility observed in Hall thrusters (covered in detail in Sections 2.3, 3.3.2, and 3.3.3) but the physical description of the enhanced mobility from first principles remains unknown. The theories of Hall thruster anomalous mobility can be generally categorized into two main groups: wall effects (3.3.2) and fluctuation-induced mobility(3.3.3).

Transport due to wall effects comes from the idea that an electron suffering a collision with a channel wall should have the same effect as an electron-neutral collision, which would contribute to the mobility. Since electrons are thermally mobile along radial magnetic field lines, they may suffer these collisions at the inner and outer channel walls. However in operation, a negative sheath builds up at the channel walls repelling the bulk of electrons from the walls and only electrons with energy sufficient to overcome this sheath may reach the walls. Therefore, quantifying the wall collisions is not entirely straightforward[23], but estimates show that near-wall conductivity does not adequately account for the entirety of the enhanced mobility observed[24].

Fluctuation-induced transport states that oscillations can contribute to the cross-

field electron mobility. The plasma environment of a Hall thruster is known to be non-quiescent, where field and density oscillations in the discharge chamber have been observed and characterized over a large range of frequencies[25] spanning from 1 kHz to 5 MHz, with investigations ongoing to characterize higher frequency oscillations up to 10 MHz and higher[26]. The main idea behind fluctuation-induced mobility in a Hall thruster is that a fluctuating electric potential creates axial $\mathbf{E} \times \mathbf{B}$ drifts resulting in a net transport toward the anode, due to the second-order effect in the correlation of potential and density fluctuations. Fluctuation-induced mobility is complicated to diagnose or isolate because the processes are coupled, where the fields control and are controlled by the electron motion. This is further complicated by geometrical effects and sheath effects, which act to enhance or dampen various waves and modes in the plasma, so that the resulting mobility is highly dependent on the specific geometry of the thruster[27].

Having a greater understanding of the electron mobility in a Hall thruster would be useful in several respects. The obvious aspiration would be to eliminate the excess mobility. If Hall thruster electron mobility could be suppressed to the classical value, Hall thrusters within the typical operating regime could achieve much higher efficiencies, as the backstreaming electron current usually accounts for 20-30 percent of the total discharge current (i.e. $I_e/I_d \sim 0.2-0.3$)[28, 12]. Based on the analysis by Kim[12], if the electron contribution to the discharge current is reduced by a factor of $1/10$ ($I_e/I_d \sim 0.02 - 0.03$), a Hall thruster at 50 percent total efficiency could stand to gain ~ 30 percent in efficiency. This is a gross approximation, however, because the assumption was made that all other efficiency parameters remain constant, and it is suspected that in reality there would be drastic changes in the ionization and acceleration processes. Even so, the point remains that the electron current is an efficiency loss mechanism in a Hall thruster and suppressing it could correspond to efficiency gains. Furthermore, at high discharge voltages the excess electron mobility is thought to be responsible for the limitation of I_{sp}[22], so suppressing the electron

mobility could also extend the operating regime of a Hall thruster.

Suppressing the electron mobility could create a more ideal thruster, in terms of efficiency or extending the range of operating parameters, but practically speaking, the suppression of electron mobility to the classical value is not feasible in the near term due to the widespread lack of understanding in turbulent plasma transport. A more realizable benefit to understanding Hall thruster electron mobility is the advantage provided to modeling and scaling of Hall thrusters. Modeling efforts of the Hall thruster discharge have led to highly accurate predictions of Hall thruster properties including performance parameters such as thrust, specific impulse and efficiency, discharge parameters such as the plasma potential structure, ionization and acceleration regions, and time varying behavior such as ionization oscillations, transit time oscillations and the time variation of the ion energy distribution function[29, 30, 31, 32, 33, 34]. However, these codes are limited because the predictions are highly dependent on the treatment of electron mobility, which varies between models but is almost always treated empirically based on experimental data. Some attempts have been made to generalize electron transport by region in the Hall thruster[32, 34] so that the models can be applied to new geometries and operating regimes (for example, using the Bohm diffusion and mobility coefficients outside the channel and transitioning to wall-collision dominated transport inside the channel). However, the results of these models can not be considered entirely reliable, since the electron mobility is thought to be highly dependent on plasma geometry and sheath structure and the physics underlying these dependencies are not present in such models. A complete understanding of the physics involved in anomalous mobility, from first principles, could substantially improve modeling efforts, so that Hall thruster models can be used for design and optimization without the use of corresponding experimental data.

In studying electron mobility in Hall thrusters it is very difficult to separate the effects of individual parameters because as one parameter changes, the entire plasma

7

environment responds. For example, in changing the magnetic field strength or shape in a Hall thruster, the plasma responds such that one has also changed the electric field strength and shape, the electron density, and the electron temperature, which act to change the plasma properties such as the Debye length and plasma frequency, resulting in changed oscillatory behavior. The ionization and acceleration regions are also changed by the above parameters, and thus neutral density and momentum transfer collision frequency have changed as well. Therefore, the direct effect of the magnetic field on mobility can never be investigated as a standalone parameter in a Hall thruster. One must rely on models or empirical formulas to predict the properties as a result of the change in one parameter (or resulting properties can be experimentally measured), so that mobility can be only investigated in response to all of the properties that have changed. Historically, models have not been able to accurately predict the properties of the Hall thruster discharge without using fit parameters that are based on experimental data specific to the thruster being modeled. In determining the origin of anomalous mobility it would be useful to be able to investigate the trends of the mobility in response to each parameter independently. If the response of anomalous mobility to a change in each parameter is known, much insight can be gained concerning the physical mechanism responsible for the anomalous mobility.

1.3 Problem Statement, Aim, and Scope

The exact physics of electron mobility in Hall thrusters remains largely unknown in the electric propulsion research community. Electron mobility, especially fluctuation-induced and/or "anomalous" mobility, is a multi-dimensional problem where there is a significant gap between theory and experiment. The coupled nature of the self-fields and transport make it a very difficult non-linear problem to solve explicitly. The aim of this work is to reproduce the Hall thruster "anomalous" electron mobility in a highly controlled, uncoupled environment, where parameters such as the electric

field structure, electron density, and field fluctuations can be measured and controlled externally. The goal in this investigation is not to determine the origin and growth of instabilities or other contributors to anomalous mobility but to provide an environment where these contributors can be observed and/or controlled in a straightforward manner. In this environment, electron mobility trends can be observed in response to each controllable parameter independently so that the physical mechanisms responsible for anomalous mobility can be investigated from first principles.

Toward this goal, an apparatus was constructed, the Hall Electron Mobility Gage, as a diagnostic tool to investigate anomalous mobility in an "uncoupled" environment. The most important difference between this device and a Hall thruster was the absence of waves and oscillations due to an extremely low-density plasma where collective effects are negligible. Also, the dielectric walls typically found in a Hall thruster discharge channel were removed, which greatly simplified the electric field. The Hall Electron Mobility Gage provided the unique ability to observe mobility in response to a single parameter while holding all other variables essentially constant. This made it possible to examine the trends of the mobility in response to fundamental parameters such as magnetic field and electric field strengths and neutral density, which in a Hall thruster would not be feasible. Anomalous mobility was observed in the simplified environment of this device indicating that a mechanism exists, separate from plasma fluctuations and wall effects, that is responsible for enhanced mobility. The magnitude of mobility observed in the Hall Electron Mobility Gage was lower than that which is typically observed in Hall thrusters, so these results do not negate the possibility of wall-effects and/or fluctuations contributing to mobility. However, the investigation presented herein has identified that another mobility mechanism exists even in the absence of wall collisions or fluctuations. The goal of this project was to confirm that the observed mobility could not be accounted for by traditional classical mechanisms (momentum-transfer collisions), observe trends of the anomalous mobility, make suggestions for the source of the elevated mobility and correlate these

to mobility mechanisms that could also be present in a Hall thruster.

1.4 Contribution of this Research (Overview)

The achievement of this work has been the observation of enhanced, non-classical mobility in field conditions similar to a Hall thruster where wall effects and plasma fluctuations, the two most cited contributors to anomalous mobility, were absent. Since collective effects and wall effects were not pertinent, investigating the mobility in this environment achieved three purposes. First, it was possible to isolate any effects not linked to fluctuation-induced mobility (much like the insight achieved by Dubin and O'Neil in like-particle transport[35, 36]; see Section 3.4) based on geometry or static field conditions. For example, it was possible to observe the effects of non-orthogonal $\mathbf{E}$ and $\mathbf{B}$-fields at the edges of the channel annulus, where in a Hall thruster discharge these field conditions at the channel periphery are so internally coupled to the plasma environment that investigating this effect alone would be impossible. Second, the anomalous mobility was examined in direct response to external parameters, which allowed for the assessment of mobility trends with E, B and background pressure (neutral density). Finally, external fluctuations that arise out of noise in electrical circuitry were measured and controlled and effects of these fluctuations were documented. These observations suggested yet another transport mechanism that had not previously been isolated or observed that enhances mobility in the geometry specific to a Hall thruster.

1.5 Organization

The organization of this document is presented so that the reader is aware of the specific goal and purpose of each part of this dissertation. Chapter 2 begins with an

extensive background of charged particle motion in electric and magnetic fields and particle transport, both classical and "anomalous." These concepts are applied to the fields and geometry of a Hall thruster to describe the s transport in the Hall thruster. Chapter 3 presents the history of Hall thruster research, specifically in electron transport, and presents the current initiatives in electron mobility research. A critical review is presented to outline the present state of the field, point to gaps in scientific knowledge, and to present the general strategies being implemented in electron transport research. The aim and scope of this investigation are presented in more detail to show the contribution of this dissertation to the field as a whole. Chapters 4 and 5 present the details of the Hall Electron Mobility Gage, that was designed to meet the needs outlined in Section 1.3, namely the recreation of "anomalous" mobility in a highly-controlled environment free from the coupling effects that complicate mobility research. Chapter 4 includes the physical design and construction including physical structure and field design, and justification for the design decisions are provided. Chapter 5 presents an extensive analytical characterization of the plasma environment of the Hall Electron Mobility Gage for comparison with the Hall thruster discharge plasma. This characterization is done to determine the extent of applicability for the results of the Hall Electron Mobility Gage mobility studies. An analysis of the characteristic electron dynamics within the Hall Electron Mobility Gage is also presented in Chapter 5. Chapter 6 presents the experimental setup for the Hall Electron Mobility Gage including diagnostic techniques and test methods. Chapter 6 also presents the tests and results for the verification of the design and diagnostic techniques, to demonstrate the validity of the experimental methods. The results of mobility experiments are presented in Chapter 7 showing mobility versus the control parameters of electric field, magnetic field and pressure. Several additional mobility investigations are presented in Chapter 7, which provide insight into the mechanisms which may cause enhanced mobility and additional analysis is presented that provides support for the existence of a collisionless mechanism for electron transport. Through

11

various means, the material presented in Chapter 7 provides evidence of non-classical mobility in the Hall Electron Mobility Gage and also identifies certain mechanisms that have been eliminated as possible contributors to mobility. Chapter 8 provides concluding remarks and suggestions for future work. The appendices include supplemental material including a statistical error analysis, effectiveness of calibration and tuning procedures and further investigation of the diagnostic techniques.

Chapter 2

Charged Particle Transport

The purpose of this chapter is to gather the relevant concepts in charged particle transport, which are used and referenced throughout the remainder of this dissertation. Section 2.1 provides the background for single-particle motion in electric and magnetic fields and expands to include the collective description of a plasma which describes plasma behavior in a macroscopic sense. Section 2.2 covers classical collisional transport, which describes the effect of particle collisions on net transport. This section lays the groundwork for transport from first principles, which are used in subsequent sections when describing anomalous transport using the same principles. Secton 2.3 addresses collisionless or "anomalous" transport with a focus on Bohm diffusion and mobility, which was the first derived and most commonly referenced description of anomalous transport. These concepts are summarized here and the reader is referred to an extensive bibliography of plasma physics texts and technical journals for more rigorous derivations and important benchmarks in plasma transport theory.

2.1 Fundamental Plasma Concepts

2.1.1 Single Particle Motion

Single particle dynamics create the foundation of plasma physics and are necessary to describe the plasma behavior in the Hall Electron Mobility Gage. The particle dynamics in electric and magnetic fields are presented in this section including relevant particle drifts and the magnetic mirror. The particle drifts are used to describe the bulk motion of the plasma due to the electric and magnetic field structure. The magnetic mirror is an important concept for the electron dynamics in the discharge channel of a Hall thruster[37] and in the radial confinement in the Hall Electron Mobility Gage, which will be revisited in Section 5.3.1.

The fundamental nature of plasmas is captured in the Lorentz equation. The Lorentz equation is given by

$$m\frac{d\mathbf{v}}{dt} \ = \ q(\mathbf{E} + \mathbf{v} \times \mathbf{B}) \tag{2.1}$$

which defines the trajectory of a charged particle in response to electric and magnetic fields. It is well known that a charged particle in a magnetic field gyrates in a circular orbit perpendicular to the magnetic field. This characteristic motion is derived from the Lorentz equation[38] and is defined by the frequency and radius of gyration:

$$\omega_{ce} \ \equiv \ \frac{qB}{m} \qquad\qquad r_L \ \equiv \ \frac{mv_\perp}{qB} \tag{2.2}$$

which is generally referred to as the gyro- or Larmor frequency and radius. This gyration occurs in a plane that is is perpendicular to the magnetic field; particle velocities parallel to the magnetic field are unaffected by the field and particles move along field lines with their thermal velocities, $v_\parallel$.

If fields are constant or the field conditions vary slowly in space and/or time compared to the gyro-orbit of the particle, the guiding center drift equations[39, 40] describe the velocity of the "guiding center" of the gyrating particle due to the field conditions. The guiding center description[39] averages the motion over a gyro orbit so that the equations of motion are greatly simplified, which has been proven to be a useful tool for capturing the relevant dynamics of the net particle motion[40]. There are several drifts that arise due to forces and field gradients and each is described in the following section.

In the presence of an electric field perpendicular to the magnetic field the center of the gyrating charged particle (i.e. the guiding center) experiences a drift over many gyrations that is perpendicular to both $\mathbf{E}$ and $\mathbf{B}$. This drift occurs because the particle gains energy through half the gyration while the particle loses energy through the successive half of the gyration due to the electric field. In the direction of the electric field the net motion is zero because the velocity gain exactly equals the velocity loss over a gyration; however, there is a velocity imbalance transverse to the electric field as shown in Fig. 2.1 where during the half of the orbit the particle is moving faster (to the right) and the other half of the orbit the particle is moving slower (to the left), resulting in a non-zero net transverse velocity. As an example, the electric field is defined to be in the z-direction, perpendicular to a magnetic field defined in the x-direction (Fig. 2.1). In this case the net particle drift is in the y-direction. This drift motion is derived from the Lorentz equation[38] where the net drift velocity over many gyrations is given to be

$$\mathbf{v_{E \times B}} = \frac{E_z}{B_x}\hat{\mathbf{j}}$$

In the general case where the E and B fields are not exactly orthogonal the drift velocity becomes:

$$\mathbf{v_{E \times B}} = \frac{\mathbf{E} \times \mathbf{B}}{B^2} \tag{2.3}$$
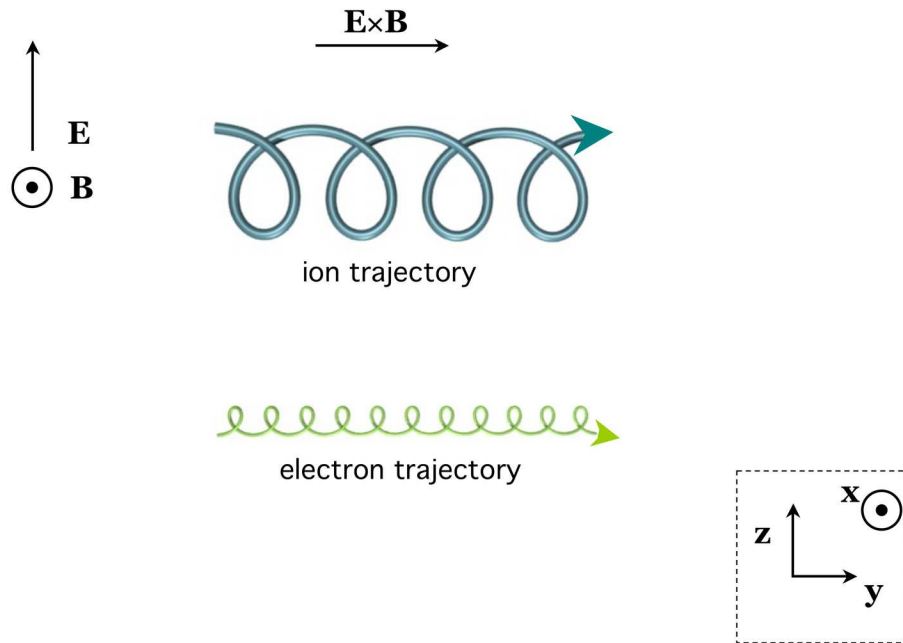
Figure 2.1: $\mathbf{E} \times \mathbf{B}$ drift for an ion trajectory and electron trajectory (not to scale).

The $\mathbf{E} \times \mathbf{B}$ drift has no dependence on the particle charge, q, meaning particles of both positive and negative charges drift in the same direction, provided they are both "magnetized" (see Section 2.2.2). The dependence on q is absent because the particles gyrate in opposite directions but also gain and lose energy in opposite directions; thus, for ions the upper half of the orbit (in Fig. 2.1) the particle is moving faster (to the right) and for electrons the lower half of the orbit the particle is moving faster (also to the right). A similar drift appears for electrons and ions in the presence of any force orthogonal to the magnetic field; however, if that force is not dependent on the charge, q, (such as gravity) the resulting drift for electrons and ions will be in opposite directions. In this case the particle drift is given by:

$$\mathbf{v}_f = \frac{1}{q} \frac{\mathbf{F} \times \mathbf{B}}{B^2}$$

If a magnetic field gradient exists perpendicular to $\hat{\mathbf{b}}$, where $\hat{\mathbf{b}} = \mathbf{B}/B$ is a unit vector in the direction of the magnetic field, a drift arises out of the non-constant gyro-orbit due to the spatial variation in B. This is called the ∇B (grad-B) drift where the magnetic field is stronger during half the orbit leading to a smaller Larmor radius and the field is weaker during the successive half of the orbit leading to a larger Larmor radius resulting in a net transverse velocity perpendicular to the magnetic field and the gradient. This drift is given by

$$\mathbf{v}_{\nabla B} = \frac{1}{2} v_\perp r_L \frac{\mathbf{B} \times \nabla B}{B^2} \tag{2.4}$$

Because the field varies spatially, the size of the Larmor radius is important, as this governs the net change in position over a Larmor gyration that gives rise to the drift velocity. Thus, the drift is not independent of species.

If there is a gradient of B in the direction of $\hat{\mathbf{b}}$ a "magnetic mirror force" exists that causes particles to move away from the stronger magnetic field to the weaker field. This magnetic mirror force exists due to the adiabatic invariant, the magnetic moment given by

$$\mu_{mag} \equiv \frac{mv_\perp^2}{2B} \tag{2.5}$$

The magnetic moment must be constant, so as a particle moves by thermal motion into a region of stronger B-field, $v_\perp$ must also increase. If $v_\perp$ increases, in order for the total energy of the particle to be conserved, $v_\parallel$ must decrease. At some point, if the field gets strong enough, $v_\parallel$ eventually goes to zero, causing the particle to be reflected back into a region of lower B. This force acts in the direction of the magnetic field and is given by

$$F_\parallel = -\mu \nabla (\mathbf{B} \cdot \hat{\mathbf{b}})$$

where $\hat{\mathbf{b}}$ is the unit vector in the direction of the magnetic field. Magnetic mirrors utilize this concept as a mechanism for confinement of charged particles where a

"magnetic bottle" is created through an axial magnetic field that has "pinched" ends, as shown in Fig. 2.2. The magnetic mirror force is directly proportional to the perpendicular energy of the charged particle (Eqn. (2.5)). Thus, the magnetic mirror has the ability to confine charged particles with very high energies provided that some suitable fraction of this energy is in the perpendicular direction. However, in the case where there is no perpendicular energy (i.e. $v_\perp = 0$) there is no confining force on the electron and an electron is lost, regardless of the total energy of the particle. It follows that trapping in a magnetic mirror is dependent on the pitch angle of the velocity vector with respect to the magnetic field rather than the total magnitude of the total energy of the particle. Particles having $v_\perp/v_\parallel$ greater than some critical value will be trapped, while others will have sufficient parallel energy to overcome the ∇B and escape the mirror. This ratio of velocities defines what is referred to as the loss cone. If the velocity vector of a particle is represented in velocity space there exists a region representing a range of velocity vectors, the mirror loss cone, where the particle is no longer confined by the magnetic mirror (Fig. 2.3). If the velocity vector lies within this region the particle is no longer confined by the magnetic mirror; however, outside of this region, in confined velocity space the particle is confined regardless of the magnitude of its velocity. The mirror loss cone is found using the combination of the adiabatic invariant, μ_{mag}, with conservation of energy, where

$$\mu_{0,mag} = \frac{mv_{0\perp}^2}{2B_0} = \frac{mv_\perp'^2}{2B'} \tag{2.6}$$

and

$$\frac{mv_0^2}{2} = \frac{mv_\perp'^2}{2} \tag{2.7}$$

In Eq. 2.7 (conservation of energy equation) v_0 is the velocity of the particle at the mid-plane of the mirror (minimum magnetic field) and v' is the velocity of the particle at its turning point. At the turning point $v_\parallel = 0$ so all of its kinetic energy is captured by $v_\perp$, and the energy balance becomes $v_\perp'^2 = v_0^2$. The resulting loss cone

18
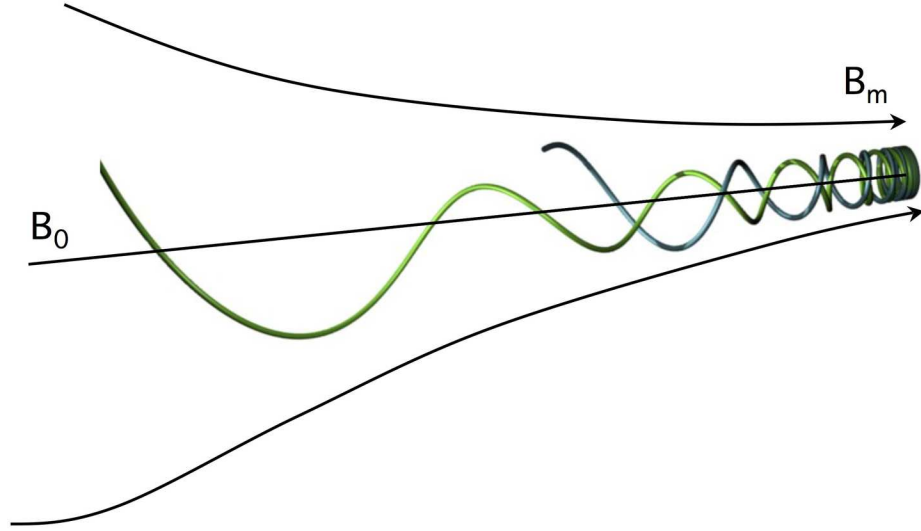
Figure 2.2: Charged particle trajectory in a magnetic mirror.

is described by

$$\frac{v_0^2}{v_{0\perp}^2} \;=\; \sin^2\theta_m \;=\; \frac{B_0}{B_m} \;=\; \frac{1}{R_m} \tag{2.8}$$

where θ_m is the minimum pitch angle a charged particle can have and still be trapped, B_m is the maximum magnetic field and R_m is defined as the mirror ratio.

Other drifts arise due to magnetic field curvature (curvature drift) and spatially-varying and/or time-varying electric fields (non-uniform-E and polarization drift, respectively). A derivation of these can be found in Chapter 2 of Ref. [38], among other introductory plasma physics texts[41, 42]. In the field conditions of interest (i.e. Hall thrusters and the Hall Electron Mobility Gage) the ∇B drift and other drifts are much smaller than the $\mathbf{E} \times \mathbf{B}$ drift[43] and will be, for the most part, neglected in this dissertation. As previously stated, the above drift equations rely on the assumption that fields vary slowly compared to the Larmor gyration so that the net effect averaged over a particle gyration can be determined and the particle motion is represented
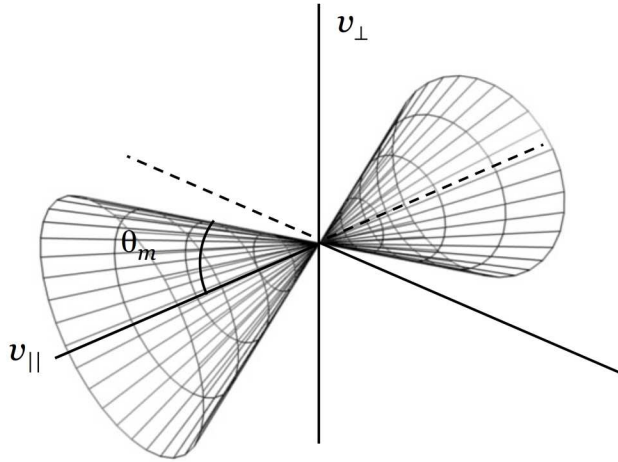
Figure 2.3: Magnetic mirror loss cone in velocity space.

by these equations describing the motion of the guiding center. If this condition is not met, the guiding center model no longer holds and the particle trajectory must be determined directly by the Lorentz equation.

2.1.2 Collective Description

Single particle dynamics have been considered, thus far, in externally applied fields, but the compelling dynamics of a plasma are realized when considering the interaction of many particles. Since each particle creates its own field and interacts with all other particles, the many-body collection of particles quickly becomes complicated when tracing each individual particle and its interaction with all other particles through self-consistent magnetic and electric fields. Luckily, certain behaviors have been characterized through collective descriptions (fluid or kinetic) so that individual

particle trajectories may be replaced by a macroscopic description that captures the relevant plasma dynamics. This section explains the parameters that are used to describe plasma behavior in a macroscopic sense and also defines the limits of such a collective description. Rather than a rigorous derivation of the parameters, more emphasis is placed on the physical significance and qualitative description of each, and the reader is directed to plasma physics texts and technical papers for a more exhaustive mathematical description.

Plasmas naturally tend to quasi-neutrality, where the density of positive and negative charges are roughly equal due to the strength of the Coulomb forces between particles combined with good conductivity resulting in rapid equalization of any charge disturbance. In a plasma, a charge perturbation (the presence of a charge concentration, for example) causes other particles in the plasma to arrange themselves in order to offset the perturbation as they are attracted or repelled from the charge concentration due to the Coulomb interaction. However, because the particles have thermal energy they may overcome the Coulomb potential to form a "cloud" around the charge perturbation with size and density according to the energy distribution of the particles. The Debye length is given as a measure to quantify this type of plasma behavior conceptually representing the balance of thermal energy (opposes shielding) to potential energy (fosters shielding). Quantitatively, the Debye length arises out of the solution to the Poisson equation where the density is given as a Maxwellian distribution in the presence of a potential. The Debye length is specifically defined as the point that the potential is shielded to $1/e$ of the perturbation potential due to the charge concentration. Mathematically this is given as

$$\phi = \phi_0 \exp\left(-\frac{|x|}{\lambda_D}\right) \tag{2.9}$$

where the full Debye length in a quasi-neutral plasma is given by

$$\lambda_D \;=\; \sqrt{\frac{\epsilon_0 k/q^2}{n_e/T_e + \sum_{ij} j^2 n_{ij}/T_i}} \;=\; \sqrt{\frac{\epsilon_0 k T_e}{n_e q^2}} \qquad (2.10)$$

Various derivations of this quantity can be found in Refs. [38, 41, 42]. The approximation on the right hand side is made that the electron temperature is much higher than the ion temperature $(T_e \gg T_i)$, so that the ions can be neglected. (Equivalently, this approximation represents the fact that ions respond much more slowly to electric fields and are assumed to be infinitely massive compared to electrons, so electrons move through a grid of ions.) Because of the tendency of charges to equalize the fields, the approximation can be made that in a plasma several Debye lengths in size, the ion density is approximately equal to the electron density (i.e. $n_e \sim n_i \sim n$), which by definition is the quasi-neutral assumption. Alternatively, for lengths shorter than the Debye length, charge imbalances which violate quasi-neutrality are possible due to the thermal energy opposing the Coulomb forces. This separation of collective and thermal phenomena at the physical scale of the Debye length will be explored in more rigorous detail in Section 2.1.3 with respect to the collective description of plasma oscillations.

The fluid description of a plasma replaces the individual particles with fluid elements that are described by macroscopic properties such as density and temperature. The fluid description is used as a tool to describe plasma behavior in the macroscopic sense and the two most important equations, the fluid equation of motion and the continuity equation, are briefly presented here as they will be utilized in both the description of oscillations and in transport theory. The fluid equation of motion is given by

$$m_j n_j \left[\frac{d\mathbf{v}_j}{dt} + (\mathbf{v}_j \cdot \nabla)\mathbf{v}_j \right] \;=\; q_j n_j (\mathbf{E} + \mathbf{v}_j \times \mathbf{B}) - \nabla p_j - mn\nu\mathbf{v}_j \qquad (2.11)$$

where ∇p is the pressure term and $mn\nu\mathbf{v}_j$ is the collision term, and j corresponds to the species, ions or electrons, where a separate equation is used for each (two-fluid description). The fluid equation of motion represents that of the Lorentz force equation, but two terms are added on the right hand side to account for effects arising out of the collection of particles, the pressure term arising out of density gradients and the collision term arising out of momentum exchanges with neutral gas. Also, the convective derivative $(d\mathbf{v}_j/dt + \mathbf{v}_j \cdot \nabla\mathbf{v}_j)$ arises out of the transformation from a particle reference frame (moves with particles) to the fluid element reference frame (fixed in space). The velocity is assumed to be a Maxwellian distribution, where this assumption is implicit in the pressure term; however, the fluid equation is often relatively insensitive to the actual velocity distribution as only the average velocity is important (which is described by the temperature in the pressure term)[38].

The continuity equation states that the number of particles in a volume element are conserved and is given by

$$\frac{\partial n_j}{\partial t} + \nabla \cdot (n_j \mathbf{v}_j) = 0 \tag{2.12}$$

In the fluid description, the pressure term arising out of density gradients leads to a *drift* that only is present within fluid description, even though the particles themselves do not drift. This drift arises because the density gradient causes more particles to be moving downward than upward due to the direction of gyration. This is given by

$$\mathbf{v}_D = -\frac{\nabla p \times \mathbf{B}}{qnB^2} \tag{2.13}$$

Another variation in the fluid description is the elimination of the ∇B drift. Since the magnetic component of the Lorenz force cannot add energy to the particles, the presence of the magnetic field cannot change the momentum. A fluid with a Maxwellian distribution of particle velocities will still be Maxwellian in the presence of a magnetic field and the flux of particles through the fluid elements will be constant.

The curvature and the $\mathbf{E} \times \mathbf{B}$ drifts are unchanged in the fluid description.

The full set of fluid equations include Eqs. (2.11) and (2.12), Maxwell's equations in vacuum, the equation of state relating pressure and density, and the Poisson equation*. Together these equations give a self-consistent description of the plasma dynamics and fields. (A derivation of the fluid equation can be found in Chapter 7 of Ref. [38] and a description of the full set of fluid equations can be found in Chapter 3 of Ref. [38].) The fluid description requires several assumptions to "close" the equations, such as an assumption of temperature and velocity/energy distribution, collisions, and viscosity (neglected in Chen's fluid description[38]). The fluid description becomes inadequate in certain cases where the dynamics of the particles depends strongly on the particle energy and/or velocity such as in magnetic mirror geometries[44, 45], or in the growth and propagation of various plasma instabilities[46, 47].

The kinetic description contains one less assumption than the fluid description, as the kinetic description includes the velocity distribution, instead of assuming a Maxwellian distribution (or some other distribution with average velocity, $\bar{v}_e$), as is done in the fluid description. The discussion of distributions will be revisited in Section 5.3.2, and several descriptions of velocity and energy distributions can be found in Ref. [48]. The fundamental equation of motion (Boltzmann equation) for the kinetic description of a plasma is given by

$$\frac{\partial f}{\partial t} + \mathbf{v} \cdot \nabla f + \frac{q}{m} \left(\mathbf{E} + \mathbf{v} \times \mathbf{B} \right) \cdot \frac{\partial f}{\partial \mathbf{v}} = \left(\frac{\partial f}{\partial t} \right)_c \qquad (2.14)$$

where $(\partial f / \partial t)_c$ represents the change in the distribution function due to collisions. If collisions are neglected, this reduces to the Vlasov equation, where the right-hand-side of Eq. (2.14) is taken to be zero. The effects of collisions on the distribution function depend on the interacting species and nature of collisions, which has been

---

*The "plasma approximation" is often used in place of the Poisson equation where $n_i = n_e$ is used as a mathematical shortcut. A good discussion of this point is presented in Section 3.6 of Ref. [38].

the subject of numerous experimental, numerical, and theoretical investigations[49]. If the collision term cannot be neglected, the collision term is often represented by one of two models: the BGK model[50] or the Fokker-Planck model([51] and p. 31 of Ref. [52]). In general, the BGK model assumes that each collision results in a trajectory that (immediately) populates a Maxwellian distribution. The Fokker-Planck model represents small momentum changes leading to the population of the Maxwellian (or other "final" distribution) that corresponds to a "random walk" in velocity space. In plasma physics the BGK model is generally used to describe the changes in the velocity distribution function when there is a large momentum transfer in collisions such as in electron-neutral collisions, whereas the Fokker-Planck model is often used where there are small momentum changes, such as in Coulomb collisions, which produce small-angle deflections. Collisions are addressed more fully in Section 2.2.3. The BGK model is presented in more detail in Section 5.3.2, in the derivation of radial confinement time and radial losses due to electron-neutral collisions within the Hall Electron Mobility Gage. A great description and rigorous derivation of the kinetic and two-fluid descriptions, including all assumptions and commentary/guidelines for the use of several approximations, may be found in Chapter 5 of Ref. [53].

2.1.3 Plasma Oscillations

Plasma oscillations have been hypothesized to be responsible for cross-field electron transport in a Hall thruster[54, 25, 55], as well as several other plasma devices[56]. Fluctuation-induced transport is discussed in more detail in Section 3.3.3, where this section provides an introduction to plasma oscillations with regard to their origin and ability to be sustained. A fundamental condition of plasma oscillations is presented demonstrating that oscillations may be sustained on length scales large compared to the Debye length but are damped out by the thermal motion of particles on length scales shorter than the Debye length. This fact is imperative in the neglect of plasma

oscillations in the Hall Electron Mobility Gage which will be discussed in Section 5.2.

It is well known that plasmas may support macroscopic collective behavior such as plasma oscillations and transmission of waves. In this section a description of plasma oscillations is derived from the electron fluid equation, adapted from Chen[38], neglecting thermal motion, in order to establish the basics of collective oscillations including a derivation of the well-known plasma frequency. Then a more generalized description, adapted from Pines and Bohm[57], is presented, based on the microscopic, single-particle description, that takes into account thermal motion as well as the collective effects. As described conceptually in Section 2.1.2, the Coulomb forces act to enhance collective behavior, whereas the random thermal motion opposes this behavior. Here it is shown that the Debye length provides the division between collective and thermal effects, where on length scales large compared to the Debye length, Coulomb forces predominate the motion, and on length scales small compared to the Debye length, the plasma behavior is governed by the random thermal motion and disturbances tend to die out instead of being sustained as oscillations.

Plasma oscillations arise out of disturbances in the plasma density. If electrons are displaced from their equilibrium positions (ions are assumed to be an infinitely massive, uniform background grid) the increased local electron density drives electrons back to the area deficient in electrons. However, because of the electron inertia, they overshoot their original position and continue to oscillate about this equilibrium position, as ions, due to their large mass, do not have time to respond; the frequency of this oscillation (electron plasma frequency) is constant and depends only on the electron density. Here, the expression for plasma frequency is found in a simplified case where thermal motion and collisions are neglected and only electrostatic oscillations are present (neglecting the magnetic field). To describe the plasma motion the fluid equations of motion and continuity are used. The Poisson equation may be used in the case of plasma oscillations as the time varying fields arise due to the violation of quasi-neutrality and are fast enough that ions do not have time to neutralize the

charge separation. The electron fluid equations of motion and continuity and Poisson equation under these approximations reduce to

$$mn_e \left[\frac{\partial \mathbf{v}_e}{\partial t} + (\mathbf{v}_e \cdot \nabla) \mathbf{v} \right] = q n_e \mathbf{E} \tag{2.15}$$

$$\frac{\partial n_e}{\partial t} + \nabla \cdot (n_e \mathbf{v}_e) = 0 \tag{2.16}$$

$$\epsilon_0 \nabla \cdot \mathbf{E} = -q(n_i - n_e) \tag{2.17}$$

Here the fluid equation of motion (Eq. (2.11)) is modified to reflect the assumptions of collisionless ($\nu_{coll} = 0$), electrostatic ($B = 0$) and cold ($kT = 0$), so the pressure, collision, and $\mathbf{v} \times \mathbf{B}$ force terms vanish. The quantities E, n_e and v are all assumed to have constant equilibrium quantities with superimposed sinusoidal, time-varying perturbations of constant frequency (e.g. $n_e = n_0 + n_1 \exp(i(kx - \omega t))$ and likewise for E and v). Amplitudes of n_1, E_1 and v_1 are taken to be complex to capture any differences in phase between the oscillating quantities. It is also assumed that the equilibrium condition is a neutral plasma at rest, so there is no equilibrium electric field, no spatial gradient in the equilibrium density, and zero equilibrium velocity. The ion density is assumed to be constant and equal to the equilibrium electron density, which then both vanish in the Poisson equation. The final assumption is that the velocity is small enough that only linear terms are retained and higher order terms are neglected (i.e. $\mathbf{v} \cdot \nabla v = 0$, $n_1 v_1 = 0$). With all of these assumptions the three equations (Eqs. (2.15)-(2.17)) above are reduced to[†]

$$m \left[\frac{\partial \mathbf{v}_1}{\partial t} \right] = q \mathbf{E}$$

$$\frac{\partial n_1}{\partial t} + \nabla \cdot (n_0 \mathbf{v}_1) = 0$$

$$\epsilon_0 \nabla \cdot \mathbf{E} = -q n_1$$

[†]For simplification in notation the time varying components are represented by an abbreviated notation, where $n_1 = n_1 \exp(i(kx - \omega t))$, etc.

Taking the time and spatial derivatives gives the three equations in expanded form:

$$-im\omega v_1 e^{i(kx-\omega t)} = qE_1 e^{i(kx-\omega t)}$$

$$-i\omega n_1 e^{i(kx-\omega t)} + n_0 ik v_1 e^{i(kx-\omega t)} = 0$$

$$-ik\epsilon_0 E_1 e^{i(kx-\omega t)} = -qn_1 e^{i(kx-\omega t)}$$

Using these three equations and three unknown time-varying quantities (n_1, v_1 and E_1) an expression can be given in terms of the velocity

$$-im\omega v_1 e^{i(kx-\omega t)} = -i\frac{n_0 q^2}{\epsilon_0 \omega} v_1 e^{i(kx-\omega t)}$$

The non-trivial solution gives

$$\omega_P = \left(\frac{n_0 q^2}{\epsilon_0 m}\right)^{1/2} \tag{2.18}$$

which is the plasma frequency.

The derivation above makes a gross simplification in neglecting thermal motion and thus the plasma behavior is described by perfectly organized oscillations that occur at the plasma frequency. Pines and Bohm present a microscopic-kinetic solution that does not neglect the thermal motion and also does not make any assumption a priori on the oscillatory behavior of the time varying quantities (e.g. no assumption of sinusoidal or constant frequency oscillations, as in Chen's description). In principle the derivation by Pines and Bohm is similar to Chen's description in that the time varying plasma behavior is described by fluctuations in plasma density. Since density can be described as a function of position, the first and second time derivatives of plasma density, which are presented by Pines and Bohm, contain velocity and acceleration terms. The acceleration term is described by the equation of motion due to the Coulomb forces and thus encompasses only the inter-particle interactions,

yet the velocity term additionally contains the random thermal motion, which would be present even in absence of Coulomb interaction between particles. Pines and Bohm describe all parameters in terms of their Fourier components, which allow for fluctuations of all frequencies and wavelengths, some of which are collective (such as the collective oscillation at the plasma frequency) and some of which arise out of the random motion of the particles that have no frequency or phase relations. Therefore, the microscopic-kinetic description by Pines and Bohm contains both the collective effects contributing to organized oscillations as well as the thermal effects that act to oppose the collective effects. The details of this derivation are described as follows.

Pines and Bohm start with the interaction of point particles to describe the equation of motion for a particle in response to all other particles (deriving from the potential energy of interaction between the ith and jth electrons).

$$\frac{d\mathbf{v}_i}{dt} = -\left(\frac{4\pi q^2 i}{m}\right) \sum_{ij} \frac{\mathbf{k}}{k^2} e^{i\mathbf{k}(x_i - x_j)} \tag{2.19}$$

This is then extended to the collective description by giving the equation of motion of a single particle as it interacts with a density of particles rather than a sum of discreet particles. The density in terms of Fourier components is given as

$$\rho_k = \sum_i e^{i\mathbf{k}\cdot\mathbf{x}_i} \tag{2.20}$$

so the equation of motion then becomes

$$\frac{d\mathbf{v}_i}{dt} = -\left(\frac{4\pi q^2 i}{m}\right) \sum_k \frac{\mathbf{k}}{k^2} \rho_k e^{i\mathbf{k}\cdot\mathbf{x}_i}. \tag{2.21}$$

The first and second time derivatives of density are then given as

$$\frac{d\rho_k}{dt} = -i \sum_i (\mathbf{k} \cdot \mathbf{v}) \, e^{i\mathbf{k}\cdot\mathbf{x}_i}. \tag{2.22}$$

29

Substituting the equation of motion into the second derivative results in

$$\frac{d^2 \rho_k}{dt^2} = -\sum_i (\mathbf{k} \cdot \mathbf{v}_i)^2 e^{i\mathbf{k} \cdot \mathbf{x}_i} - \sum_{k'ij \ k' \neq 0} \left(\frac{4\pi q^2}{m k'^2} \right) \mathbf{k} \cdot \mathbf{k}' e^{i(\mathbf{k}' - \mathbf{k}) \cdot \mathbf{x}_j}. \tag{2.23}$$

The second summation in the equation above can be simplified by separating it into two parts $\mathbf{k} = \mathbf{k}'$ and $\mathbf{k} \neq \mathbf{k}'$. For $\mathbf{k} = \mathbf{k}'$ the first exponential in the second term vanishes, removing the dependence on $\mathbf{x}_i$ so the sum over i is just the number of particles, n_0. For $\mathbf{k} \neq \mathbf{k}'$ Pines and Bohm show that the phases expressed in $\exp(i(k' - k) \cdot \mathbf{x}_i)$, which depend on random particle position, cause these terms to average out to zero. Equation (2.23) then becomes

$$\frac{d^2 \rho_k}{dt^2} = -\sum_i (\mathbf{k} \cdot \mathbf{v}_i)^2 e^{-i\mathbf{k} \cdot \mathbf{x}_i} - \left(\frac{4\pi n_0 q^2}{m} \right) \sum_i e^{-i\mathbf{k}' \cdot \mathbf{x}_i} \tag{2.24}$$

The first term in Eq. (2.24) includes the contribution to the plasma density fluctuations due to random thermal velocities, whereas the second term comes from only the particle interactions through Coulomb forces. It can be seen here that for sufficiently long wavelengths or for sufficiently small thermal velocities ($\mathbf{kv} \rightarrow 0$), Eq. (2.24) reduces to the second order differential equation:

$$\frac{d^2 \rho_k}{dt^2} + \left(\frac{4\pi n_0 q^2}{m} \right) \rho_k = 0 \tag{2.25}$$

The solution to the differential equation is an oscillation at the plasma frequency

$$\omega_P = \left(\frac{4\pi n_0 q^2}{m} \right)^{1/2} \tag{2.26}$$

Therefore, Eq. (2.24) gives the same result as the simplified description above when thermal velocity is neglected, where the particle densities exhibit perfectly organized oscillations at the plasma frequency. If $\mathbf{kv}$ is large however, and can not be neglected, the density oscillations are governed by the first term of Eq. (2.24). Here

the frequency of oscillation is given by $\omega = \mathbf{k}\mathbf{v}$ which varies for all particles. Therefore, if even at a given point in time the phases of such oscillations were correlated they would quickly become disorganized by the random frequencies arising out of the thermal velocity. Equation (2.24) then represents the balance of collective behavior given by the Coulomb interaction and the randomizing behavior given by the thermal motion that acts to oppose the organized behavior. A comparison between these two terms gives rise to the relative contribution of each of these effects. Mathematically this is represented by the inequality

$$\left(\frac{4\pi n_0 q^2}{m} \right)^{1/2} \gg \left\langle (\mathbf{k} \cdot \mathbf{v})^2 \right\rangle \tag{2.27}$$

where satisfying the inequality of Eq. (2.27) represents the case where collective effects may be sustained by the plasma. Rearranged, assuming an isotropic Maxwellian distribution with temperature T, this gives

$$k \ll \left(\frac{12\pi n_0 q^2}{m \left\langle \mathbf{v}_i^2 \right\rangle} \right)^{1/2} = \lambda_D^{-1} \tag{2.28}$$

Interestingly, this gives a separation of phenomenon at the Debye length. For scales much longer than the Debye length ($k \ll \lambda_D^{-1}$) collective effects dominate the particle motion and organized oscillations can be sustained. However, for scales much smaller than the Debye length, the random thermal motion opposes the collective behavior, which tends to randomize disturbances so that collective oscillations cannot be supported.

2.1.4 Non-neutral Plasmas

The formation of a plasma through creating electron-ion pairs, combined with good conductivity, ensures that the plasma be quasi-neutral in most cases. The total charge of the plasma body is zero, as equal densities of positive and negative charges

31

are available for neutrality and rapid electron motion acts to equalize any charge separation. However, if only like-charged particles are introduced into the system from an external source or a charge species is removed from the system, and the plasma is confined by electric and/or magnetic fields, the plasma may violate quasi-neutrality. (Without confinement the self-field of a non-neutral plasma would cause all of the particles to repel each other eliminating the plasma.) An analogous derivation of Debye length and plasma frequency can be made for non-neutral plasmas where the charge perturbation is a perturbation against the "background" self-field (instead of zero-field as in quasi-neutral plasmas). Outside of the Debye sphere the background self-field of the non-neutral plasma is unaffected by the charge perturbation. This is similar to the quasi-neutral case where the field is regarded as zero outside the Debye sphere surrounding a charge perturbation. This derivation can be found in Davidson[58] and results in the exact same formulation as Eq. (2.10). For purposes of clarification, a one-component plasma refers to a plasma strictly containing only one species whereas the designation of a non-neutral plasma only indicates that there is a violation of charge neutrality in the bulk plasma but may contain both positive and negative species. While most of the equations describing quasi-neutral plasma behavior are unchanged with regard to non-neutral plasmas, one assumption generally made in the fluid description, is obviously not valid. This is the plasma approximation where the Poisson equation is generally replaced by $n_i = n_e$. In a non-neutral plasma strong self-fields exist due to the collection of charges, where the Poisson equation must be solved explicitly.

2.2   Classical Diffusion and Mobility

Neglecting particle interactions, charged particles follow the trajectories described by the Lorentz equation (Eq. (2.1)) in the presence of magnetic and electric fields. However, momentum changes arise from collisions with other particles, which must

be accounted for when describing the bulk motion of the plasma. Diffusion and mobility in plasmas describe the effects of collisions on the transport phenomena of charged particles, where this is defined as the classical description for charged particle transport. The distinction between diffusion and mobility lies in the mechanism driving transport, where diffusion is defined by a net flux due to a density gradient, and mobility is defined by a net flux due to an electric field or equivalently electric potential gradient. This dissertation is concerned with mobility rather than diffusion, because electric potential gradients are much more significant than density gradients in the plasmas motivating this research (namely, Hall thrusters). Therefore, the focus in subsequent sections will be on mobility; however, the derivations for both mobility and diffusion will be made here as both come from the fluid equation of motion.

2.2.1   Free Diffusion and Mobility

Free diffusion and mobility are concerned with transport phenomena in the case of zero magnetic field. The following sections present the fundamentals of diffusion and mobility in this context, where the same principles will then be applied to the case where a magnetic field is present. These principles are even used loosely to describe certain types of anomalous mobility, as will be presented in Section 2.3. The building blocks of diffusion and mobility lie in the definitions that follow in presenting the most simplified illustration.

The mean free path of a particle traveling through a medium of "target" particles is given by

$$\lambda_m \;=\; \frac{1}{n_0 \sigma_{coll.}} \tag{2.29}$$

where n_0 is the density of "target" particles and sigma is the collision cross-section, which is essentially a probability of collision, expressed in terms of area (m^2), for given input parameters of incident energy and target species. (A derivation of the mean free path can be found in Chen, Ref. [38].) For the purposes of this analysis, the

collision cross-section, $\sigma_{coll.}$, (discussed in more detail in Section 2.2.3) is assumed to be constant. If particles are traveling with a certain velocity, the mean time between collisions is given by the distance traveled (λ_m) divided by the average particle speed:

$$\tau_{coll.} = \frac{\lambda_m}{\bar{v}} \tag{2.30}$$

This corresponds to a collision frequency of

$$\nu_{coll.} = n_0 \sigma_{coll.} \bar{v} \tag{2.31}$$

The diffusion and mobility coefficients come from the fluid equation of motion (Eq. (2.11)), where, in order to simplify, it is assumed[38] that the collision frequency is large enough that dv/dt is neglected and the left hand side of the fluid equation can be taken to be zero. Then solving for the velocity gives

$$\mathbf{v} = \frac{q}{m\nu}\mathbf{E} - \frac{kT}{m\nu}\frac{\nabla n}{n} \tag{2.32}$$

Equation (2.32) shows how the velocity of the fluid is related to the electric potential and density gradients. The diffusion and mobility coefficients are then defined by the constants of proportionality in the relation of velocity to the electric field and density gradient:

$$\mu \equiv \frac{q}{m\nu} \tag{2.33}$$

$$D \equiv \frac{kT}{m\nu} \tag{2.34}$$

The diffusion coefficient is in units of m^2/s and mobility coefficient is in units of m^2/(V-s). The units of variance in distance (m^2) per time for both mobility and diffusion are notable, and will be discussed below.

Diffusion mathematically represents the linear growth in time of the position vari-

ance of a group of particles, with the constant of proportionality between variance and time being defined by the diffusion constant, $\sigma^2 = Dt^\ddagger$. This relation is made obvious by the units of the diffusion constant, m^2/s. Diffusion can be investigated by considering a mathematically equivalent description using a discrete random-walk process. In a random-walk process, particles are assumed to have straight-line trajectories between collisions, where the particle moves a distance given by the mean free path and the direction of the trajectory after the collision is given to be random, with collisions taking place on a time scale determined by the collision frequency. Einstein's 1905 paper on Brownian motion[60] showed the mathematical equivalence between the discrete random walk and continuous diffusion, providing the link between microscopic motion (random walk) and macroscopic observables (diffusion), which actually gave credence to the existence of atoms as discrete particles rather than a continuous medium. Through this examination of the microscopic motion, it becomes much easier to examine the diffusion and mobility processes from first principles, especially when the fluid equation may not capture the dynamics of the mechanism driving transport, as in anomalous mobility.

The diffusion constant can be represented in the following form based on the random-walk process[59]

$$D = \frac{\left\langle (\Delta\mathbf{x}\,(t))^2 \right\rangle - \left\langle \Delta\mathbf{x}\,(t) \right\rangle^2}{n_{dim}t} \;=\; \frac{\delta^2}{\tau} \tag{2.35}$$

where $\Delta\mathbf{x}$ is the displacement of a particle after time t, δ is the average distance a particle travels between collisions in the random walk (in terms of free diffusion, this is equivalent to the mean free path given by Eq.(2.29)), τ is the mean time between collisions (which is the inverse of the collision frequency $\tau = 1/\nu$), and n_{dim} is the number of spatial dimensions.

---

‡In some texts, such as Ref. [59], the diffusion constant is defined as $\sigma^2 = 2Dt$ to make Fick's equations more "tidy". A discussion of this is found in Chapter 2 of Ref. [59]. Here the factor of 2 is dropped in order to maintain consistency with the diffusion and mobility constants defined in Eq. (2.33) and Eq. (2.34).

To show equivalence of the random walk with the fluid description of diffusion and mobility (Eqs. 2.33 and 2.34), the diffusion and mobility coefficients are determined for the case of a Maxwellian distribution (assumed in the fluid description) using the random walk description, as shown below. The square of the mean step size can be found from the expected value of the speed squared, $\langle v^2 \rangle$,

$$\delta^2 = \langle (v\tau)^2 \rangle = \langle v^2 \rangle \tau^2 \tag{2.36}$$

and the average square speed is given by the Maxwellian distribution where

$$\langle v^2 \rangle = 4\pi \left(\frac{\beta}{\pi} \right)^{3/2} \int_0^\infty v^2 e^{-\beta v^2} dv = \frac{kT}{m} \tag{2.37}$$

Therefore the diffusion constant is given by

$$D = \langle v^2 \rangle \tau = \frac{kT}{m}\tau = \frac{kT}{m\nu} \tag{2.38}$$

The mobility coefficient arises from a persistent directional bias to normal thermal diffusion due to the presence of an external force. In terms of the random walk, a particle is scattered isotropically in a collision so the average initial velocity and displacement after a collision due to the random thermal motion is zero. However, in the presence of a force, the particle is accelerated for an amount of time, τ, between collisions, displacing the particle by

$$\Delta \mathbf{x} = \frac{\mathbf{a}\tau^2}{2} = \frac{\mathbf{F}\tau^2}{2m} \tag{2.39}$$

always in the direction of the force. Therefore, the average drift velocity is given by

$$\mathbf{v}_d = \frac{\mathbf{F}\tau}{m} \tag{2.40}$$

This drift velocity, obtained by simple methods, is the same drift velocity that would be achieved by deriving the average velocity of a distribution of particles undergoing a random walk with a bias (i.e. $\langle \Delta x \rangle^2 \neq 0$) using Eq. (2.35). The reader is referred to Ref. [59] for the complete derivation and more extensive discussion. This drift velocity may be used to relate mobility and diffusion which results in the Einstein relation (sometimes referred to as the Einstein-Smoluchowski relation). To derive the Einstein relation from Eq. (2.40), the numerator and denominator are multiplied by D, and substituting $D = kT/m\nu$ in the denominator results in the relation

$$\mathbf{v}_d = \frac{\mathbf{F}D}{kT} \tag{2.41}$$

To apply this to mobility of charged particles in an electric field where $\mathbf{v}_d = \mu\mathbf{E}$ and $\mathbf{F} = q\mathbf{E}$ the relation becomes

$$\mu = \frac{qD}{kT} \tag{2.42}$$

which is the same functional relation between Eq. (2.33) and Eq. (2.34). The main purpose of presenting the concept of the random walk is to show that the diffusion and mobility coefficients can be defined explicitly under any conditions where the average step length and time between steps (collisions) is known. The random-walk description can be used to define the diffusion and mobility coefficients in the case of magnetized and fluctuation-induced transport, as will be shown in Sections 2.2.2 and 2.3, respectively.

2.2.2 Magnetized Diffusion and Mobility

The application of a magnetic field reduces the transport in the direction perpendicular to the applied field as the $\mathbf{v} \times \mathbf{B}$ force prohibits particles from streaming freely in this direction and holds particles in Larmor gyrations. A particle is said to be magne-

tized if there are many Larmor gyrations between momentum-transfer collisions and unmagnetized if the particle undergoes several collisions in a single gyration. This is quantified by the Hall parameter where

$$\Omega_H \;=\; \frac{\omega_{ce}}{\nu_m} \;=\; \omega_{ce}\tau_m \tag{2.43}$$

The magnitude of the Hall parameter is an indication of the degree of magnetization where the plasma is said to be magnetized if $\Omega_H \gg 1$ and unmagnetized if $\Omega_H \ll 1$. Analytically, the diffusion and mobility in the presence of a strong magnetic field is derived from the fluid equation of motion in a way analogous to the derivation for free diffusion. The derivation presented here is adapted from that of Chen[38]. (Similar derivations are found in Brown[61] among other introductory plasma physics texts.) Starting with the fluid equation of motion again (Eq. (2.11)), defining the magnetic field in the **z**-direction, and taking the left side of Eq(2.11) to be zero, the velocity in the x- and y-directions[§] is given by

$$v_x \;=\; \frac{qE_x}{m\nu_m} - \frac{kT}{m\nu_m}\frac{\partial n}{\partial x} + \frac{qB_z}{m\nu_m}v_y \tag{2.44}$$

$$v_y \;=\; \frac{qE_y}{m\nu_m} - \frac{kT}{m\nu_m}\frac{\partial n}{\partial y} + \frac{qB_z}{m\nu_m}v_x \tag{2.45}$$

Solving the simultaneous equations and substituting the free diffusion and mobility coefficients from Eq. (2.33) and Eq. (2.34), respectively, results in the velocity equations for the x- and y-components:

$$v_x\left(1 + \omega_{ce}^2\tau_m^2\right) \;=\; \mu E_x - \frac{D}{n}\frac{\partial n}{\partial x} - \omega_{ce}^2\tau_m^2\frac{E_y}{B_z} + \omega_{ce}^2\tau_m^2\frac{kT}{qB_z}\frac{1}{n}\frac{\partial n}{\partial y} \tag{2.46}$$

$$v_y\left(1 + \omega_{ce}^2\tau_m^2\right) \;=\; \mu E_y - \frac{D}{n}\frac{\partial n}{\partial y} - \omega_{ce}^2\tau_m^2\frac{E_x}{B_z} + \omega_{ce}^2\tau_m^2\frac{kT}{qB_z}\frac{1}{n}\frac{\partial n}{\partial x} \tag{2.47}$$

[§]The motion in the z-direction is unaffected by the magnetic field and transport along the magnetic field is described by free diffusion and mobility.

Here the last two terms on the right-hand side arise out of the $\mathbf{E} \times \mathbf{B}$ and diamagnetic drifts, respectively. The first two terms are the free diffusion and mobility terms, however the equation for velocity is modified by the term $(1 + \omega_{ce}^2 \tau_m^2)$, where $\omega_{ce} \tau_m$ is the Hall parameter defined by Eq. (2.43). The new diffusion and mobility coefficients for motion perpendicular to the magnetic field are then given by

$$D_\perp = \frac{D}{1 + \omega_{ce}^2 \tau_m^2} \qquad (2.48)$$

$$\mu_\perp = \frac{\mu}{1 + \omega_{ce}^2 \tau_m^2} \qquad (2.49)$$

The result in the case of low Hall parameter approaches that of free diffusion and mobility, and as the Hall parameter increases the perpendicular motion is increasingly impeded by the magnetic field. Using these definitions for perpendicular diffusion and mobility, the equation for the bulk cross-field velocity can be simplified to read

$$\mathbf{u}_\perp = \mu_\perp \mathbf{E} - D_\perp \frac{\nabla n}{n} + \frac{\mathbf{v}_{\mathbf{E} \times \mathbf{B}} + \mathbf{v}_D}{1 + \omega_{ce}^2 \tau_m^2} \qquad (2.50)$$

In the case of large Hall parameter the diffusion and mobility coefficients reduce to

$$D_\perp = \frac{kT\nu_m}{m\omega_{ce}^2} \qquad (2.51)$$

$$\mu_\perp = \frac{\nu_m}{\omega_{ce}B} \qquad (2.52)$$

In the case of high Hall parameter the cross-field diffusion and mobility can be derived using the concept of a random walk, similar to the derivation presented in Section 2.2.1 for free diffusion and mobility[¶]. Here the step size is taken to be the Larmor radius, as particles gyrate around magnetic field lines and simply cannot free themselves unless their trajectories are altered by a momentum-transfer collision. Thus the maximum distance traveled between collisions is the Larmor radius, r_L. Referring back to Eq.

[¶]The author is unaware of a similar derivation of random-walk transport in the case of magnetized diffusion and mobility.

(2.35) the diffusion constant is given as $D = \delta^2/\tau$. The square step size is given to be $\delta^2 = (r_L)^2$, where the Larmor radius is a function of the thermal velocity. The square step size is then given by

$$\delta^2 = \left(\frac{m}{qB}\right)^2 \langle v^2 \rangle = \frac{\langle v^2 \rangle}{(\omega_{ce})^2} \tag{2.53}$$

By substitution, using Eq. (2.37) for $\langle v^2 \rangle$ the diffusion coefficient is represented by

$$D_\perp = \frac{kT}{m\omega_{ce}^2}\nu_m \tag{2.54}$$

which is the same result as Eq. (2.51). The mobility can be derived from this using the Einstein relation, but also can be derived by inspection of the drift velocity. By the latter approach, the drift velocity given by Eq. (2.40) does not apply, as the acceleration in the direction of the force no longer takes place for the time, τ, between collisions but only until the particle is turned by the magnetic field. The drift velocity must be obtained then by the displacement of the particle due to the force only until it is turned by the magnetic field. This displacement is defined by the Larmor radius where Eq. (2.39) is replaced by

$$\Delta\mathbf{x} = \frac{m \langle \mathbf{v_E} \rangle}{qB} = \frac{1}{\omega_{ce}}\left(\frac{E}{B}\right) \tag{2.55}$$

where $\langle \mathbf{v_E} \rangle$ is the average velocity in the direction of the electric field given by E/B, assuming perfectly orthogonal E and $B^{\|}$. The particle can only be displaced $\Delta\mathbf{x}$ per collision so the drift velocity represents how fast these "steps" are being taken, shown by the relation

$$\mathbf{v}_d = \Delta\mathbf{x}\nu_m = \frac{\nu_m}{\omega_{ce}B}\mathbf{E} \tag{2.56}$$

Thus the mobility becomes

$$\mu_\perp = \frac{\nu_m}{\omega_{ce}B} \tag{2.57}$$

$^{\|}$The velocity in Eq. (2.55) does not include thermal motion since $\langle \mathbf{v}_{thermal} \rangle = 0$.

which again is the same result as Eq. (2.52). Comparing Eq. (2.54) and Eq. (2.57), it is seen that the Einstein relation still holds for magnetized diffusion and mobility.

2.2.3 Classical Collision Species

In Sections 2.2.1 and 2.2.2, for the determination of collision frequency, the cross-section for collision was taken to be constant and the meaning behind the cross-section was not discussed in detail. Here the different types of collisions are explored and the meaning and value of the cross-section for each type of collision is presented in greater detail. The possible binary collisions for an electron are electron-neutral, electron-electron and electron-ion collisions. Each of these has a different cross-section based on the interaction between the species, which are discussed in detail below.

The electron-neutral collision process results in an electron scattering diffusively (where the direction or the resulting velocity vector has no preferential direction) after a collision with a neutral. The electron-neutral collision cross-section, σ_{en}, depends on the neutral species and the relative velocity of the colliding particles. In this description the neutrals are assumed to be stationary, as $\bar{v}_e \gg \bar{v}_n$; if this is not the case then the electron velocity in Eq. (2.31) is replaced by relative velocity between the two species. Figure 2.4 shows the electron-neutral cross-section for argon as a function of electron energy[3]. (Argon is presented here because it is the neutral gas species used in the majority of the experiments discussed in the remainder of this dissertation.) The momentum-transfer collision cross-section is found from empirical data and shown as a solid line. Inelastic collisions are also found empirically, where the first excitation and the first ionization cross-sections are shown in Fig. 2.4 as a thin line and dashed line, respectively.

In a momentum-transfer collision the amount of energy that is transferred from an electron to a neutral is proportional to the mass ratio m_e/M_n which for argon is $\sim 1 \times 10^{-5}$. Therefore, momentum-transfer collisions are responsible for changing the
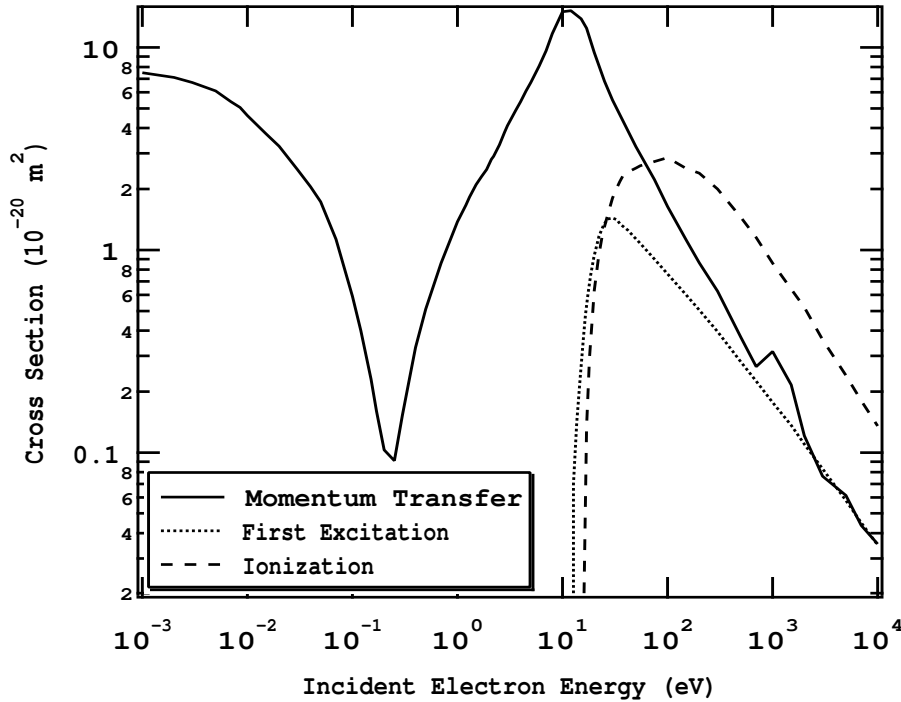
Figure 2.4: Momentum-transfer, first excitation, and ionization collision cross-sections for electron collisions with argon atoms.(Data obtained from Ref. [3]

momentum of electrons colliding with neutrals (i.e. directional scattering) but many momentum-transfer collisions are needed to cause any significant energy change to the electron species. Therefore, the time for a significant energy change while undergoing electron-neutral collisions is much longer than the time for significant direction change (this point will become important in Sections 5.2.3 and 5.3.2). In an inelastic collision however, the change in energy of an electron is appreciable and loses energy on the order of the threshold energy for the inelastic collision. For argon the threshold energy for the first excitation energy is 11.5 eV and for ionization is 15.8 eV.

A Coulomb collision refers to the interaction between two charged particles, rather than a charged particle (electron) and a neutral. Here electron-electron collisions and electron-ion collisions are both presented. When discussing electron-neutral collisions a single interaction (collision) results in a significant amount of momentum change

42

by a large-angle scattering event. A single Coulomb collision may also result in a large-angle scattering event if the particles come sufficiently close to each other (this distance is represented by b_0 in Fig. 2.5) in the interaction, giving rise to a collision cross-section given by $\sigma = \pi b_0^2$. However, in contrast to collisions with neutrals, where there is no interaction between the particles until their spacing is on the order of the size of the particle, charged particles can interact with each other over a distance up to the Debye length (where $\lambda_D \gg b_0$), where the long-range interactions result in only a small deflection (Debye length is presented in Section 2.1.2, Eq. (2.10)). It has been found that these small deflections significantly increase the effective cross-section for Coulomb collisions so that $\sigma > \pi b_0^2$, where the cumulative effect of these small deflections becomes significant relative to the much less frequent large-angle Coulomb collisions, which was first recognized by Spitzer[62]. Various derivations of the cross-section for Coulomb collisions can be found in Spitzer, Helander[63], Goldston and Rutherford[41], among others. The general form of the collision frequency (Eq. (2.31)) still holds but the variables take on a slightly different meaning. Rather than being defined by a single collision, the collision frequency for Coulomb collisions represents the sum of many collisions where the collision time, $\tau_{ee} = 1/\nu_{ee}$, is defined as the time after which the sum of all small angle deflections equals one large-angle deflection, often called the 90-degree scattering time.

The form of Eq. (2.31) is still used but the cross-section depends on more than the target species and incident energy, rather it is an intrinsic property of the plasma itself because of the dependence on the Debye length. The cross-section is derived from equations of motion rather than being experimentally determined. The estimated cross-section is inversely dependent on the relative velocity of the interacting species. The cross-section falls off rapidly with increasing velocity as the particles spend less time in the interaction and would be deflected only a small amount. The cross-section increases with the Debye length as this represents the space over which particles can interact. The dependence of the cross-section on the Debye length is described by the
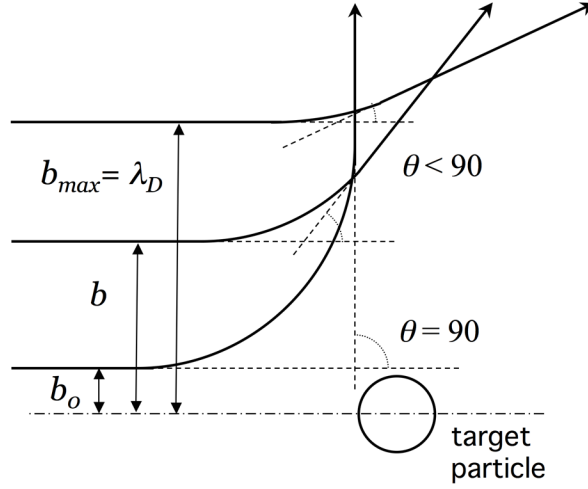
Figure 2.5: Impact parameter for Coulomb collisions.

Coulomb logarithm, which is given by $\ln \Lambda$, where

$$\ln \Lambda \equiv \ln \left(\frac{b_{max}}{b_{min}} \right) = \ln \left(\frac{\lambda_D 2\pi\epsilon_0 m_e \bar{v}_e^2}{e^2} \right) \qquad (2.58)$$

As the Debye length increases, the space in which particles may influence each other increases. However, also as the Debye length increases, the average deflection in each interaction decreases because the average distance of interaction is consequently larger. The physical meaning of the Coulomb logarithm comes from the balance between the increase in interaction space as the Debye length increases (maximum distance of interaction, λ_D) and the reduction of the deflection angle for the average interaction as the Coulomb force decreases with distance. Because the force between particles falls off rather slowly with distance, the Coulomb logarithm (and thus cross-section) increases with increasing Debye length and thus the collision cross-section increases with Debye length, but the increase is rather slow (logarithmic dependence)

and the Coulomb logarithm varies only slightly across a large range of plasmas where most laboratory plasmas have a Coulomb logarithm in the range of 10-20. In general, the effect of the Coulomb interaction captured by the Coulomb logarithm serves to increase the collision cross-section by an order of magnitude, which is often significant in fully-ionized plasmas. The collision cross-section is represented as

$$\sigma_{ee} \approx \frac{e^4 \ln \Lambda}{4\pi \epsilon_0^2 m_e^2 \bar{v}_e^4} \tag{2.59}$$

and the equation for electron-electron collision frequency is given by

$$\nu_{ee} \approx \frac{\sqrt{2}}{12\pi^{3/2}} \frac{n_e e^4 \ln \lambda}{\epsilon_0^2 m_e^{1/2} T_e^{3/2}} \tag{2.60}$$

Like-particle collisions do not contribute to total mass transport as their effects exactly cancel (p. 177 of Ref. [38]). Only under certain conditions** do like-particle collisions contribute to any appreciable net particle flux. However, collisions between unlike particles (electron-ion) do contribute to net particle flux. The electron-ion collision frequency is similar to the electron-electron collision frequency (Eq. (2.60)) but modified to reflect the ion density and the average charge of an ion (to account for multiple ionization) so that

$$\nu_{ei} \approx \frac{\nu_{ee} n_i Z^2}{n_e} \tag{2.61}$$

The small-angle deflection Coulomb collisions have been found to be an extremely important transport mechanism, especially in fully-ionized plasmas where the neutral density is low. Coulomb collisions can only be neglected in cases where a combination of parameters exist, such as a high electron temperature combined with a high neutral density as is found in Hall thrusters (see Section 5.2.3), that cause electron-neutral collisions to be the dominant transport mechanism. The reader is directed to Chapter

---

**For example, $\mathbf{E} \times \mathbf{B}$ drift collisions derived by O'Neil *et al*[35, 64].

5, Section 5.2.3 for a complete analysis of the relevant particle collisions in Hall thrusters and in the Hall Electron Mobility Gage.

2.3   Fluctuation-induced Transport

Often in magnetized plasmas the charged particle transport has been experimentally observed to be much higher than could be accounted for by classical collisions. The enhanced transport, often called "anomalous" transport, has been observed in a large number of configurations, including arc plasma discharges[65], magnetically confined fusion plasmas[66, 67, 68], magnetron discharges[24, 69, 70], and Hall thruster plasmas[21, 71, 24], among others, and is usually several orders of magnitude higher than classical transport. The most prominent theory for the enhanced transport is fluctuation-induced transport, which encompasses a number of coupled processes.

It is well known that plasmas have the ability to sustain oscillations and waves arising from various instabilities and excitation mechanisms[72, 73] over a distance of many Debye lengths. Because of this ability, particles in the plasma experience waves as time varying electric and/or magnetic fields, which change their characteristic motion according to the Lorentz force. However, since the particles themselves are responsible for the existence of the oscillating fields, when their characteristic motion is changed, the wave itself is also changed, which provides the fundamental coupling of fluctuation-induced transport. The origin of plasma oscillations is beyond the scope of this dissertation. The reader is directed to the theoretical and experimental descriptions of the growth and propagation of plasma waves in the following references [72, 73, 74, 75]. The remainder of this section will focus on the physical mechanism by which such fluctuations cause transport.

The term Bohm diffusion is often used to describe all fluctuation-induced transport, as Bohm was the first to derive the theory of this type of transport [76] [65].

Bohm makes an attempt to quantify the diffusion transport in terms of a random walk of the $\mathbf{E} \times \mathbf{B}$ drift of electrons. This concept was expanded on through a derivation by Yoshikawa and Rose in attempts to theoretically quantify the net transport due to random density fluctuations. As described previously, an electric field perpendicular to a magnetic field creates a drift perpendicular to both $\mathbf{E}$ and $\mathbf{B}$ (over several gyrations). Therefore an oscillating electric field (where the frequency of oscillation is much lower than the cyclotron frequency, $\omega' \ll \omega_{ce}$) in the presence of a magnetic field would create an oscillating drift term, perpendicular to both, with an amplitude and frequency corresponding to the strength and frequency of the electric field perturbation. By this mechanism the $\mathbf{E} \times \mathbf{B}$ drift resulting from the oscillating field displaces the particle many Larmor radii across the magnetic field (in Bohm's example [65] the drift length was 100 times the Larmor radius). If the $\mathbf{E} \times \mathbf{B}$ disturbances act as a randomizing process then the motion becomes a random-walk process with the step length on the order of the average drift amplitude. By the theory of Bohm, the oscillating drift creates a random walk where the diffusion coefficient can be described by the usual form of Eq. (2.35). This description for Bohm diffusion is adapted from Bohm[65] and Helander [63]. The step size corresponds to the $\mathbf{E} \times \mathbf{B}$ deflection resulting from the field oscillation. Therefore, the step length is related to the fluctuation by

$$\delta \;=\; \langle \tau v_{\mathbf{E} \times \mathbf{B}} \rangle \;=\; \tau \frac{\nabla \phi}{B} \sim \tau \frac{\phi}{\delta} \frac{1}{B} \tag{2.62}$$

where $\nabla \phi$ is the electric field amplitude of the fluctuation (not the static electric field, if one is present). Then the square step size is given by

$$\delta^2 \;\sim\; \tau \frac{\phi}{B} \tag{2.63}$$

Driven by an instability, the plasma oscillations increase exponentially with time; however, the diffusion process acts to damp the waves. Therefore there is a balance that is achieved where the oscillations reach a steady state with the mean amplitude

estimated by ϕ_{sat}, which is the saturation amplitude of the wave. Bohm presented the estimated value of $e\phi_{sat}/kT = 16$ [65] which was semi-empirically determined. The relation of the saturation amplitude, ϕ_{sat}, to the temperature of the plasma, kT, has theoretical justification as the maximum potential that can occur in a plasma is dependent on kT due to Debye shielding. The factor 16 was empirically determined and agrees with experiments within a factor of two or three (p. 193 of Ref. [38]). This value is highly dependent on the nature of the waves, however, and relies on the assumption that the waves originate and are sustained within the plasma. The resulting diffusion coefficient is given by

$$D \approx \frac{\phi_{sat}}{B} \approx \frac{kT}{16qB} \qquad (2.64)$$

The oscillations themselves are postulated to arise self-consistently out of plasma instabilities caused by collective effects, but by the theory of Bohm, the effect on charged particles is based on the equations for single particles in the presence of external fields. Therefore, the origin of the electric field fluctuations is of little consequence to the motion of the particles beyond what the collective effects present as "external" fields. The only difference between that which is caused by self-sustaining oscillations (plasma modes) and externally applied oscillations is the existence of a "saturation" amplitude, which would not exist as a self-consistent quantity if oscillations were imposed externally (e.g., by an oscillating potential applied to electrodes). On this argument, Bohm mobility could be observed in any case where an oscillating electric field is present, transverse to the magnetic field, regardless of the growth and propagation of instabilities within the plasma. However, if collective plasma effects are not present, the random-walk step size will vary depending on the nature of the external field fluctuations and will not be governed by the inherent properties of waves in plasmas. By using the Einstein relation (Eq.(2.42)) Bohm diffusion is generally

translated to Bohm mobility[77] where

$$\mu_{Bohm} = \frac{1}{16B} \tag{2.65}$$

In another description of fluctuation-induced mobility, which arises out of very specific circumstances, it is shown that a net transport can occur due to electrostatic waves transverse to the static electric field. This explanation is adapted from Thomas[55] and shows a second order effect due to the combined effect of potential and density fluctuations. Assume oscillating density and potential waves are established transverse to the static electric field (previously established as E_z) and the magnetic field (B_x) (in the $\mathbf{E} \times \mathbf{B}$ Hall current direction) given by

$$\phi(t) = \phi_0 + \tilde{\phi} = \phi_0 + \phi \cos(k_y y - \omega' t) \tag{2.66}$$

$$n_e(t) = n_{e,0} + \tilde{n}_e = n_{e,0} + n_e \cos(k_y y - \omega' t - \gamma) \tag{2.67}$$

where γ is the difference in phase between the density and potential fluctuations (shown in Fig. 2.6). The resulting oscillating $\mathbf{E} \times \mathbf{B}$ drift in the z-direction is given by

$$v_z(t) = \frac{1}{B_x} \frac{\partial}{\partial y}(\phi(t)) = -k_y \frac{\phi}{B_x} \sin(k_y y - \omega' t) \tag{2.68}$$

Thus the current density in the z-direction is given by

$$J_{ez}(t) = q(n_{e,0} + n_e \cos(k_y y - \omega' t - \gamma))\left(-k_y \frac{\phi}{B} \sin(k_y y - \omega' t)\right) \tag{2.69}$$

Averaged over a period gives

$$\langle J_{ez}(t) \rangle = -q k_y n_e \frac{\phi}{B} \sin(\gamma) \tag{2.70}$$

Explained conceptually, this result indicates that if there is a higher electron density
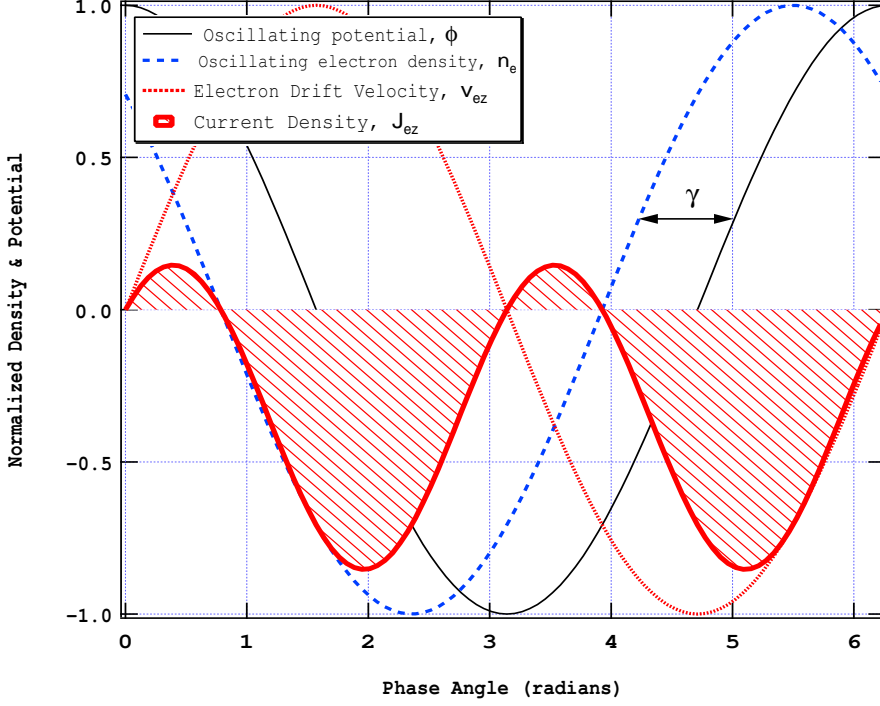
Figure 2.6: Depiction of Eqs. (2.67), (2.68), (2.69) and (2.70) where a second-order effect produces a net J_{ez} (cross-hatched) averaged over a period.

in regions where the $\mathbf{E} \times \mathbf{B}$ drift is in the direction of qE_z and a lower electron density in regions where the $\mathbf{E} \times \mathbf{B}$ drift is directed opposite qE_z, there will be a net transport (averaged over one period) in the direction of qE_z (in a Hall thruster this would be toward the anode for electrons), that is dependent upon the phase difference between the oscillating quantities of density, $\tilde{n}_e$, and electrostatic potential, $\tilde{\phi}$ (or equivalently oscillating electric field, $\tilde{E}$). This type of transport is outlined in Janes and Lowder[21] where it is recognized that the average transverse electric field, $E_\theta = E_{trans.}$, goes to zero but the average of $n_e E_{trans.}$ does not, giving rise to net electron transport due to the fluctuating $\mathbf{E} \times \mathbf{B}$ drift in the direction of qE_z. However, by this description, the net electron transport could just as easily occur in the direction opposite qE_z, as no physical principle is cited for the details of the phase correlation. In other words, if the phase shift, γ, is in the range $0 \leqslant \gamma \leqslant \pi$, the net transport is in the qE_z direction, but if the phase shift is in the range $\pi \leqslant \gamma \leqslant 2\pi$, the net transport is opposite

the qE_z direction and no physical reason is provided that guarantees the phase shift be in the former range. Furthermore, this is a simplified description that does not entirely describe the plasma behavior in most conditions, which are characterized by random conditions that still result in net transport. Nonetheless, this provides a visual representation of how the fluctuating $\mathbf{E} \times \mathbf{B}$ drifts can lead to net transport due to a second-order effect.

Yoshikawa and Rose[78] presented a rigorous non-linear derivation that predicts a collisionless net transport in the direction of E_z and in the direction of $-\nabla n/n$ (mobility and diffusion, respectively) arising out of random fluctuations in density (isotropic turbulence). The purpose of Yoshikawa and Rose's work was to theoretically derive the Bohm coefficient, $1/16$. They describe the mechanism driving transport by realizing that a density fluctuation in the $\mathbf{E} \times \mathbf{B}$ (Hall) direction would correspond to a fluctuating electric field also in the Hall direction. The fluctuating electric field creates a fluctuating axial $\mathbf{E} \times \mathbf{B}$ drift (depicted in Fig. 2.6), where Yoshikawa and Rose also recognize that net transport must be due to a second-order effect since the "first-order fluctuating $\mathbf{E} \times \mathbf{B}$ drifts average to zero"[78]. However, the second-order effect in Yoshikawa and Rose's work arises out of random fluctuations (defined by a statistical variance) rather than the coherent fluctuations depicted in Fig. 2.6.

The derivation can be found in Ref. [78] and only the final result and qualitative description is presented here. Equation [31] combined with Eq. [10] in Ref. [78] gives the result for the net transport in the direction of the static electric field (E_z) and/or density gradient ($\nabla n/n$) due to turbulent fluctuations which have been assumed to be uniform in all directions. Equation (2.71) is adapted to reflect the orientation of B in the x-direction and E in the z-direction as has been presented throughout this chapter, and the axial electron motion is expressed in terms of z-velocity rather than flux for comparison to the transport equations derived in Section 2.2.

$$v_z = \frac{\pi}{4}S\left(\frac{E_z}{B} + \frac{kT_e}{qB}\frac{\nabla_z n}{n}\right) - a\left(\frac{E_z}{B} + \frac{kT_e}{qB}\frac{\nabla_z n}{n}\right) \qquad (2.71)$$

The resulting description of transport presents two competing effects with the coefficients S and a, where S is given by

$$S = \frac{\langle (n - n_0)^2 \rangle}{n_0^2} \tag{2.72}$$

and represents the mean-square deviation of the density fluctuation and a represents the inverse Hall parameter $(1/(\omega_{ce}\tau_m))$ so that the second term in Eq. (2.71) is the equation for classical transport. If $S \gg a$, either because of strong density fluctuations or even moderate fluctuations in a highly magnetized plasma with infrequent collisions, the resulting transport tends to Bohm transport where the diffusion and mobility coefficients would be given by

$$D_{Bohm} = \frac{\pi k T_e}{4qB} \frac{\langle (n - n_0)^2 \rangle}{n_0^2} \tag{2.73}$$

$$\mu_{Bohm} = \frac{\pi}{4B} \frac{\langle (n - n_0)^2 \rangle}{n_0^2} \tag{2.74}$$

This result suggests that in highly magnetized plasmas fluctuation-induced mobility prevails when the collision frequency is low and magnetic field is high and/or when the plasma is hot and confined, where classical transport prevails in a quiescent plasma environment or an environment with a low magnetic field and/or high collision frequency (low Hall parameter, Ω_H).

2.4 Summary

This chapter has laid the foundation for charged particle transport, where Chapter 3 uses these concepts to explain the electron transport in the specific environment of a Hall thruster, and Chapter 5 references these concepts in the analytical characterization of the plasma within the Hall Electron Mobility Gage. Single-particle motion

was presented to explain the characteristic motion of charged particles in prescribed magnetic and electric fields, which will be used in describing electron dynamics in the Hall thruster channel and comparing them to the electron dynamics within the Hall Electron Mobility Gage. In the field conditions of a Hall thruster and the Hall Electron Mobility Gage the dominant bulk motion is the $\mathbf{E} \times \mathbf{B}$ drift due to the crossed electric and magnetic fields, where other drift terms can be generally neglected. Collective descriptions, both fluid and kinetic, were also briefly presented. The concept of magnetic mirrors was presented to describe the process of confinement of particles through a magnetic field gradient. The confinement provided by magnetic mirrors was shown to be dependent on the direction of the velocity vector, where in magnetic mirror confinement devices, an isotropic Maxwellian velocity distribution, which is assumed in the fluid description, must be replaced by a non-Maxwellian distribution that can only be captured using the kinetic description. The kinetic description will be used in 5.3.2 to analyze the effect of collisions on the radial confinement of electrons in the Hall Electron Mobility Gage, which is achieved through electrostatic and magnetic mirror confinement mechanisms.

It has been shown that a separation of plasma phenomena exists at the Debye length where on length scales small compared to the Debye length, single particle effects dominate and on length scales large compared to the Debye length, collective effects dominate. This may be translated to state that waves and plasma oscillations cannot be sustained and will be damped on length scales smaller than the Debye length. This point is extremely important in describing the electron dynamics within the Hall Electron Mobility Gage, discussed in detail in Chapter 5. It has also been noted that non-neutral plasmas exhibit similar phenomena as neutral plasmas with equivalent expressions for Debye length and plasma frequency, where the similarity is also important so that these concepts (especially Deybe length) may be translated directly to the non-neutral plasma environment of the Hall Electron Mobility Gage.

Classical diffusion and mobility were presented in order to outline the mech-

anisms for collisional transport. While the diffusion and mobility equations were initially derived from the fluid equations of motion, the same equations result from a random-walk description which describes diffusion and mobility from a microscopic standpoint. The random-walk description was shown to be equivalent to the fluid description for transport when a Maxwellian distribution of velocities was assumed. However, the random-walk description of transport processes may also be used in a much more general sense, such as the description of Bohm transport, where the step length and the characteristic time between steps (randomizing events) is known. Classical transport is rarely observed in practice, with regard to magnetized plasmas, where some type of anomalous mechanism is usually present. The general theory of fluctuation-induced transport was presented, which is primarily cited for anomalous cross-field transport, in order to describe the physical mechanism by which fluctuations may cause anomalous cross-magnetic-field transport.

Chapter 3

Hall Thrusters & Related Research

3.1   Introduction

This chapter provides a review of research in electron transport in Hall thrusters and also includes an overview of other configurations where pertinent discoveries have been made in magnetized plasma transport. Section 3.2 outlines the general physics of a Hall thruster, which was covered briefly in Section 1.1. Section 3.3 applies the general transport theory presented in Sections 2.1 - 2.3 to the specifics of a Hall thruster, presenting both classical and anomalous mobility mechanisms focusing on the research efforts and the current state of the field. Section 3.4 addresses other relevant configurations where charged particle transport is of concern, with special attention to the contributions due to fusion research, which has been responsible for many of the advances in the understanding of charged particle transport. The final section, Section 3.5, presents a critical evaluation of the state of research, revealing areas that remain unresolved or require greater attention and outlines the contribution of the research presented herein.

3.2 Physics of Hall Thrusters

Hall thrusters are in-space propulsion devices that are particularly well suited for orbit transfer maneuvers and satellite station-keeping[13]. Hall thrusters are generally considered electrostatic propulsion devices as the acceleration mechanism is achieved through the application of a DC electric field*. There are two competing Hall thruster configurations[11], the anode-layer (TAL) and the stationary plasma thruster (SPT), where this is mentioned only to specify that the discussion presented herein is concerned with the SPT-type Hall thruster. The magnetic field in the Hall thruster is indirectly involved in the acceleration mechanism. The radial magnetic field is employed to impede electron motion, which acts as a "resistor" allowing a large potential difference to exist over the discharge channel. In this way, the magnetic field governs the electrostatic potential structure in the discharge channel and thus is directly involved in creating the electric field that accelerates propellant ions, which provides the thrust in Hall thrusters.

A brief overview of the physics of a Hall thruster was presented in Chapter 1 , whereas a more detailed description is given here. A cross section of a Hall thruster was shown in Figure 1.1 with the relevant features identified, namely the anode which also acts as a propellant feed, the external cathode, the simplified circuitry and resulting fields (magnetic and electric) and the discharge plume. Neutral propellant is introduced at the anode region of the discharge channel. The axial electric field is created by the applied voltage between the anode inside the discharge channel and the external plasma or free space, which is at or near the cathode potential. This electric field accelerates electrons supplied from the cathode toward the anode. Electrons gain energy from the electric field sufficient to ionize propellant neutrals by electron-impact ionization. Ions created in the discharge channel are subsequently

---

*as opposed to electrodynamic to describe pulsed devices or electromagnetic where the magnetic field is directly utilized in the acceleration mechanism

accelerated away from the anode through the axial electric field and ejected from the thruster to produce the thrust necessary to accelerate the spacecraft. For the ions expelled from the thruster, the cathode supplies an equivalent number of electrons to the exhaust plume to maintain spacecraft neutralization.

The radial magnetic field in the discharge channel provides an integral role in the operation of a Hall thruster. Electrons are highly mobile due to their small mass. If there were no magnetic field, any applied electric field would cause the electrons to stream to the anode and the massive ions would experience very little acceleration relative to the electrons. Therefore, a radial magnetic field, created through magnetic windings on the inner and outer magnetic poles, is applied so that the electron axial velocity is turned into a gyration perpendicular to the magnetic field and their motion to the anode is significantly inhibited. Superimposed on the small-scale gyrations, the electrons assume an azimuthal drift due to the crossed axial-electric and radial-magnetic fields and are essentially "confined" axially in the gyro-orbits and azimuthal $\mathbf{E} \times \mathbf{B}$ orbits. The field is specifically tuned so that the electron gyro-orbit is smaller than apparatus dimensions, yet ions, due to their large mass $(10^4 - 10^5$ times the mass of electrons) have a gyro-orbit that is much larger than apparatus dimensions. The deflection of ions due to the magnetic field is negligible so they are accelerated primarily in the axial direction through the cloud of "confined" electrons on nearly straight paths from the thruster. Since electrons are thermally mobile and freely stream along magnetic field lines but their motion is impeded across field lines, the magnetic field lines have been postulated to form electric equipotential surfaces[11]. Axial electron motion is impeded the most at the point where the magnetic field is the strongest, whereby creating the largest gradient in electric potential. This region is designated as the "acceleration region" of the Hall thruster.

As described in Chapter 2, electrons are able to cross magnetic field lines by collisions, which free them from the confined orbits, giving rise to cross-field mobility. Through cross-field mobility, electrons migrate to the anode creating a current

indicated in Figure 1.2 as "recycle current." These collisions are desired, as this is the process by which propellant neutrals are ionized (through electron-impact ionization). However, it has been shown that the electron mobility observed in Hall thrusters greatly exceeds that which can be accounted for by collisions alone [21, 71]. Any recycle current in excess of that which is needed to ionize the propellant becomes an efficiency loss, as power is required to maintain the current but contributes nothing to the operation of the Hall thruster in terms of propellant ionization or thrust. Therefore, understanding the mechanism of cross-field mobility is important for thruster efficiency. Furthermore, computational models, which are used to predict performance parameters and failure mechanisms of Hall thrusters, depend highly on the treatment of cross-field mobility which historically has been determined empirically [29, 30, 31, 32, 33, 34], so understanding the mechanism for electron transport from first principles is necessary for more accurate modeling without the use of experimental data. The mechanisms for electron transport in Hall thrusters are identified and described in the following sections, including classical mobility and what is termed "anomalous" mobility. Anomalous cross-field mobility for Hall thrusters is postulated to arise due to two main contributors: the interaction at the dielectric walls (wall effects) and fluctuation-induced mobility (previously described in the general case in Section 2.3).

3.3   Mobility Research in Hall Thrusters

Hall thruster research began simultaneously, but independently, in the United States and Russia in the early 1960s[21, 79, 80]. Hall thrusters were in some ways favorable over gridded ion thrusters, mainly due to the presence of electrons in the ion acceleration channel which eliminates the space charge limitation that exists in gridded

ion thrusters[12][†]. Furthermore, the use of a magnetic field rather than acceleration grids removes a known failure mechanism in gridded ion thrusters through the erosion of the grids. However, the characteristic level of I_{sp} in gridded ion thrusters (5,000-10,000 s) was not realized at reasonable efficiencies in Hall thrusters due to degrading efficiency at high discharge voltages. Hall thrusters were limited to an I_{sp} of ~1,000-2,000 s if they were to operate at optimal efficiency[22, 9]. [‡]

Janes and Lowder were the first in the U.S. to document the "anomalous" cross-field electron mobility in the Hall thruster geometry in 1966. They found the current due to backstreaming electrons to be two to three orders of magnitude higher than predicted by classical theory. In their investigation they observed low frequency azimuthal fluctuations in density, suggesting a polarization field in the azimuthal direction (E_θ), where the anomalous mobility could be accounted for by a secondary drift term in the axial direction. It should be noted that this is not the first observation of "anomalous" mobility or diffusion, only the first documentation in the Hall thruster geometry. Anomalous diffusion was the subject of many experimental investigations and theoretical descriptions prior to Janes and Lowder's work [81, 76, 39, 62] that date back to the late 1940s to which Janes and Lowder compare their findings. In the late 1960s, the U.S. reduced efforts on Hall thrusters due to lack of progress and focused efforts on other electric propulsion devices, specifically the gridded ion thruster, that showed more promise at the time for the criteria being sought[11].

Hall thruster research continued in Russia, with much of the research effort led by Morozov and Esipchuk[11]. Much of the focus of Esipchuk was on the instabilities in Hall thruster plasmas that govern the growth and propagation of plasma density fluctuations thought to be responsible for anomalous mobility. The typical present day Hall thruster, coming out of these Russian efforts, has a much different configuration

---

[†]The presence of only ions between the acceleration grids of a gridded ion thruster limits the discharge current density.

[‡]Hall thrusters may be operational at higher specific impulse (5,000-10,000 s) but at significantly degraded efficiencies.

and operating parameters than that initially studied by Janes and Lowder (lower overall magnetic field, "pinched" magnetic field at inner/outer radii of discharge channel rather than strictly radial, narrower pole pieces, lower discharge voltage, and narrower channel) where these changes are a result of a number of empirical studies done for performance optimization[12, 82]. Even though performance was optimized, the anomalous mobility continued to be a significant efficiency limitation.

Hall thruster research efforts in the U.S. and Europe grew rapidly in the 1990s due mainly to the success of the Russian efforts in Hall thruster development and the release of Russian technical documents after the fall of the USSR. A number of research efforts are ongoing in the U.S. and internationally to explore the anomalous mobility in Hall thrusters[83, 33, 8, 34, 84]. The two most cited contributors to anomalous mobility are collisions with dielectric walls (usually termed wall effects) and plasma fluctuations (fluctuation-induced mobility). It has been found with near certainty that both of these factors play a role in the Hall thruster electron mobility, but the exact contribution of each and the reciprocal effects that exist between the two remains unknown. These will each be discussed in the following sections along with the current state of the research field.

3.3.1   Classical Electron Mobility

Classical theory accounts for the electron transport due to momentum-transfer collisions, which free the electrons from their gyro-orbits, allowing them to migrate across B-field lines toward the anode in Hall thrusters. Electron density gradients will have a much smaller effect on net electron flux in Hall thrusters than the applied electric field so the classical cross-field diffusion term is neglected and usually only mobility considered. Electrons experience momentum transfer collisions through collisions with ions or neutrals. Neutral density in a typical Hall thruster varies from $\sim 10^{18} - 10^{21}$ m^{-3}

($\sim 10^{12} - 10^{15}$ cm^{-3})[§] in the discharge channel where the minimum neutral density is found at the acceleration region. For xenon propellant and a typical value of $T_e = 20$ eV, a typical neutral density in the acceleration region ($\sim 10^{19}$ m^{-3}) corresponds to an electron neutral collision frequency of $\nu_{en} = 5 \times 10^6$ s^{-1}. Since quasi-neutrality is assumed everywhere in a Hall thruster the ion density is assumed to be approximately equal to the electron density which is typically $\sim 10^{18}$ m^{-3}[9]. Equation (2.61) is used to determine the electron-ion collision frequency which is found to be $\nu_{ei} \sim 10^5$ s^{-1} for an electron temperature of ~ 20 eV. The cyclotron frequency, given a typical magnetic field of 120 G (0.012 T) is $\omega_{ce} = 2 \times 10^9$ s^{-1}. This gives a Hall parameter (ω_{ce}/ν_m)[¶] of about 400 meaning the electrons are highly magnetized in this region. If the cross-field mobility behaved classically, using Eq. (2.52), this would correspond to a mobility coefficient of 0.01-0.1 m^2/(V-s) (using the values for neutral density, collision frequency and magnetic field described above).

Strictly classical mobility has never been observed in the acceleration region of a Hall thruster where the neutral density is low and the magnetic and electric fields are high (regions of high Hall parameter). Classical collisional mobility in a Hall thruster has only been observed upstream of the acceleration region, where the neutral densities are high and magnetic field is significantly weaker which gives rise to a much lower Hall parameter ($\Omega_H \sim 1 - 10$)[71], where electrons are very weakly magnetized. In the acceleration region of a Hall thruster, where electrons are magnetized, the mobility coefficient has been experimentally found to be on the order of ~ 10 m^2/(V-s) which is 2-3 orders of magnitude higher than the classical value[71]. In these cases the contribution of classical collisional mobility is overwhelmed by the "anomalous" mobility. The relative contribution of classical mobility and anomalous mobility has been found to be very sensitive to the electron Hall parameter in other magnetized

---

[§]These values are typical of many laboratory Hall thrusters operating in the 1.5 kW range, such as the SPT-100 and BPT-2000[9].

[¶]ν_m represents the collision frequency for all momentum transfer collisions, both Coulomb (electron-ion) and electron-neutral.

plasmas as well [54, 85], where a high Hall parameter renders the plasma susceptible to the growth of instabilities that drive anomalous transport. Thus, classical theory is insufficient to describe electron transport in the acceleration region of a Hall thruster and other descriptions of electron transport must be established. The two most prevalent descriptions of anomalous electron transport in Hall thrusters are given in Section 3.3.2 and 3.3.3.

3.3.2 Wall Effects

In a Hall thruster, dielectric walls of the discharge channel insulate the plasma from the magnetic circuit and allow an electric field to exist along the axial length of the discharge channel. The contribution of the walls to the electron mobility is suggested to have two potential effects: first, the simpler of the two is that the collisions of electrons with walls have an effect similar to electrons colliding with neutrals; second, the interaction at the wall could create, enhance, or dampen plasma instabilities. The former is discussed here where walls will be treated as another collision species with an effect analogous to classical electron-neutral collisions; the latter is essentially grouped into Section 3.3.3 in the discussion of fluctuation-induced mobility with only brief mention in this section. Since electrons are thermally mobile along radial magnetic field lines, and since the channel width ($\sim$ 2 to 3 cm) is much smaller than the mean free path for electron collisions with neutrals ($\sim$ 1 m) an electron has several opportunities to collide with the channel walls before colliding with a neutral. However, in steady-state operation a negative sheath builds up on the dielectric walls so that only electrons with sufficient energy (parallel to the magnetic field) to overcome the sheath can collide with the dielectric walls. Electrons with insufficient energy are reflected by the sheath and are directed back to the center of the channel annulus. If the electron distribution function is taken to be Maxwellian then the flux to the walls

is given according to Gombosi's equation for flux to a surface [48]:

$$\Gamma_{ew} = \frac{1}{4}\bar{v}_e n_e \exp\left(\frac{-e\phi_s}{kT_e}\right) \tag{3.1}$$

where the sheath potential, ϕ_s, is determined from the electron and ion flux to the wall:

$$\phi_s = \frac{kT_e}{e}\ln\left(\sqrt{\frac{m_i}{2\pi m_e}}\right) \tag{3.2}$$

The electron-wall collision frequency is given by[55]

$$\nu_{ew} = \frac{1}{2}\frac{\bar{v}_e}{\ell}\exp\left(\frac{-e\phi_s}{kT_e}\right) \tag{3.3}$$

where ℓ is the channel width. For typical parameters of a Hall thruster this corresponds to an electron-wall collision frequency of $\sim 10^5$ s^{-1}, which is comparable with the classical collision frequency with neutrals. Eqs. (3.1)-(3.3) assume an isotropic Maxwellian distribution. However, the assumption of this distribution could only be valid if the mean free path is much shorter than the channel width.[||] The assumption of an isotropic Maxwellian distribution in the discharge channel of a Hall thruster has been shown to be incorrect[23], as the infrequent collisions fail to maintain the thermalized electron distribution. In a kinetic treatment of Ref. [23] it was found that the electron distribution function is highly anisotropic and strongly depleted at high energies in the direction parallel to the magnetic field due to losses at the walls. The bulk of electrons that remain in the plasma have a long mean free path and do not repopulate the Maxwellian tail, causing Eqs. (3.1)-(3.3) to overestimate the flux to the walls. By this argument, the flux of electrons to the walls is determined by the rate of repopulation of the Maxwellian tail of the velocity distribution parallel to the magnetic field. The Maxwellian tail of the parallel electron velocity distribution is repopulated by the scattering of high-energy electrons from a direction perpendicular

---

[||]Many electron collisions are required for momentum and energy transfer to continually maintain the Maxwellian distribution in spite of the anisotropic losses for velocities normal to the walls.

to the magnetic field to a direction parallel to the magnetic field (into the "loss cone" which was presented in Section 2.1.1 and will be revisited in Section 5.4), which is caused by electron-neutral collisions. This creates an electron flux to the walls that is considerably lower than that presented by equations Eqs. (3.1)-(3.3) and depends on the electron-neutral collision frequency in the same way as classical mobility. This may imply that the wall effects do not significantly contribute to the electron mobility; however, it has been shown that changes in the wall material and channel width significantly affect the discharge properties of a Hall thruster[23, 86, 87] showing that the influence of the dielectric walls cannot be ignored. The actual role of the dielectric walls in Hall thruster operation continues to be a subject of debate, where it is not clear if the changes in the dielectric walls directly contribute in part to electron mobility through near-wall conductivity as outlined by Eqs. (3.1)-(3.3) or provide a secondary effect on electron mobility by enhancing or dampening fluctuation-induced mobility in some way.

The effects of secondary electron emission (SEE) from the dielectric walls has been investigated for contribution to the axial electron flux. The SEE is hypothesized to contribute to mobility in two ways[23]: 1.) the SEE can form a stream of electrons that could possibly contribute to fluctuations by the two-stream instability, 2.) in the reflection of the SEE beam between the dielectric walls (secondary electrons gain sufficient energy to overcome the sheath on the opposing channel wall) the electrons may contribute to the axial current because of the axial motion due to the gyration and the difference in phase angle of the gyration at the reflection. The first effect can only be treated in a self-consistent solution describing fluctuation-induced mobility (discussed in the following section). The second effect is a single-particle effect that may be investigated analytically/computationally such as is done in Kaganovich *et al.*[23] and may also be investigated experimentally separate from the operation of a Hall thruster (see Section 3.5).

3.3.3 Fluctuation-Induced Mobility

The theory of fluctuation-induced mobility states that oscillations can contribute to the cross-field electron mobility. The plasma environment of a Hall thruster is known to be non-quiescent, where field and density oscillations in the discharge of a Hall thruster have been observed over a large range of frequencies spanning from 1 kHz to 5 MHz [25], with investigations ongoing to characterize higher frequency oscillations up to 10 MHz and higher[26]. For fluctuation-induced mobility to explain axial transport in a Hall thruster there must be azimuthal fluctuations in density and potential, which result in a fluctuating $\mathbf{E} \times \mathbf{B}$ drift in the axial direction. The Bohm mobility coefficient is often used to describe the fluctuation-induced mobility in Hall thrusters where the mobility is given by

$$\mu_{Bohm} = \frac{1}{16B} \tag{3.4}$$

As discussed in Section 2.3, Bohm mobility describes the transport due to fluctuations of the $\mathbf{E} \times \mathbf{B}$ drifts due to plasma turbulence. The dependence on $1/B$ comes from the drift velocity (E/B), and the coefficient of $1/16$ was empirically determined by Bohm (details are provided in Section 2.3). The coefficient of $1/16$ is dependent on the specific plasma environment and thus does not adequately capture the variation of the fluctuation-induced mobility in Hall thrusters along the axial length of the discharge channel where the plasma environment (namely Hall parameter and growth of instabilities, which give rise to enhanced transport) may change dramatically. The Bohm coefficient does provide surprising agreement and is on the same order of magnitude as experimental results[71]. However, the theory of fluctuation-induced mobility, when described using the constant coefficient $1/16$, fails to capture variations in plasma fluctuation behavior over the axial length of the discharge channel (which correspond to variations in the empirical constant).

Fluctuation-induced mobility may be more adequately described by taking into

account the nature of the plasma fluctuations in the determination of the anomalous mobility coefficient, rather than assuming a Bohm-type plasma. As described in Section 2.3, the first order $\mathbf{E} \times \mathbf{B}$ drifts average to zero; however, the net second-order effect due to the correlation of density fluctuations and electric field fluctuations gives rise to a non-zero axial electron flux that can be calculated analytically by Eq. (2.71). Phase correlated density and potential fluctuations have been experimentally observed in a Hall thruster for low frequency waves (5-10 kHz)[21]. Based on this analysis, Janes and Lowder found an experimental coefficient of 1/11 (average over the length of the discharge channel) for the specific environment of the Hall thruster under investigation in their experiments. In hopes of observing similar phenomena, high frequency fluctuations have been experimentally investigated [55, 26, 88, 89] where accurate data was desired in the 60-600 kHz range; however, instrumentation has been limiting at high frequencies[26] and experiments are ongoing.

Rather than requiring specific phase and frequency information, the description by Yoshikawa and Rose [78] was given in terms of the statistical variation of fluctuations, where the resulting fluctuation-induced mobility coefficient is a function of the mean-square deviation of the density fluctuations, which can be measured directly. (A critical assumption is made by Yoshikawa and Rose by presuming isotropic turbulence and treating fluctuation amplitude as a scalar quantity.) Meezan[71] obtained time resolved electrostatic probe measurements to gain an estimate of the fluctuation amplitude to experimentally determine the mobility coefficient described by Yoshikawa and Rose's analysis. Meezan compared this mobility coefficient with the mobility coefficient found using direct measurements of axial electron flux and density and found strong agreement between the two. These results provided credence to fluctuation-induced mobility in Hall thruster geometries; however, the coefficient for fluctuation-induced mobility using Yoshikawa and Rose relies on experimental data. A method to determine the nature of the plasma fluctuations based on known conditions (both plasma and geometrical properties) is necessary so that the electron

mobility can be determined explicitly without experimental data. This need led to the utilization of quasi-linear theory for the Hall thruster environment in order to predict the growth and evolution of fluctuations, which is described in the following paragraph.

Attempts have been made to characterize plasma fluctuations as a function of thruster and/or plasma parameters so that the cross-field electron mobility can be predicted without use of experimental data and empirical correlations. This may seem like a hopeless task as a magnetized plasma has been found to be susceptible to a variety of instabilities which contribute to the growth and propagation of waves. However, what has been observed in practice is that plasma waves exhibit a non-linear feedback mechanism where various waves are excited but the total amplitude saturates so that the fluctuations are sustained, yet do not grow (this is often called "non-linear stabilization"[56]). A quasi-linear kinetic approach for describing this process was developed through a collection of work by Krall *et al.*[90, 91, 92] among others[93, 94, 95, 96], largely for fusion research, which was used to predict the growth and evolution of instabilities resulting in fluctuation-induced electron transport. In general the quasi-linear approach defines plasma parameters in terms of time-averaged quantities plus a fluctuating term and takes into account second-order effects that arise out of the combination of two first order terms, where the second order-effects cause net transport.** The quasi-linear approach was first used for electric propulsion devices in a theoretical derivation by Choueiri[54] for magnetoplasmadynamic (MPD) thrusters, which was validated experimentally through the independent results from Black *et al.*[85].

Thomas[55] provided the first application of the quasi-linear transport theory to Hall thrusters, whose work was expanded on by Spektor[83]. The quasi-linear method of quantifying fluctuation-induced transport involves predicting the expected

---

**A good top-level description of this theory and methods can be found in Cook[56] and Stringer[97]. More elaborate derivations of the quasi-linear model can be found in Bernstein and Engelmann (1966)[98]; Davidson (1972)[96]; and Cook (1974)[99].

behavior of fluctuations (wavenumber, frequency and phase relations) based on time averaged plasma and field quantities through solving the dispersion relation, which describes the susceptibility to certain plasma fluctuations. Based on this "susceptibility" to plasma fluctuations an anomalous electron collision frequency, ν_{AN}, is calculated through the quasi-linear transport model. The quasi-linear method holds promise for much more accurate computational models, as the process lends itself well to iterative procedures. The anomalous collision frequency can be calculated from profiles of plasma properties (density, velocity, temperature) and fields (electric and magnetic), the computed ν_{AN} is used to predict plasma and field profiles, which can be used to determine a new ν_{AN}, etc. Toward this goal Thomas[55] developed a simple local dispersion relation derived from the fluid equations over the discharge channel of a Hall thruster, where Spektor[83] extended this to a generalized fluid dispersion relation, taking into account several terms neglected by Thomas. At the time of publication of this dissertation these studies have not produced results agreeing with experiments due to simplifications and uncertainty in pertinent parameters; however, the method shows great promise for describing anomalous transport from first principles rather than from empirical results as has been done historically for Hall thruster electron transport.

3.4   Other Plasma Transport Studies

Anomalous diffusion has been observed in magnetic confinement fusion devices, where the fusion community has been primarily responsible for the majority of advances in plasma transport theory. In fusion plasmas, densities of $10^{20} - 10^{22}$ m^{-3} must be confined for 1-10 s and heated to thermonuclear temperatures, where anomalous cross-field transport has been the limiting factor in achieving "break-even" operation for energy generation[68]. It was found that the diffusion of the plasma could not be explained by classical electron-neutral collisions and could not be explained by large-

angle scattering between charged particles. Since the plasma was nearly fully ionized, the enhanced transport spawned the theory of long-range small-deflection Coulomb collisions derived by Spitzer[62] (presented in Section 2.2.3). The enhanced transport also gave rise to the derivation of neoclassical transport where particles exhibit a characteristic orbit (often called the "banana orbit") much larger than the Larmor radius, where the banana orbit becomes the modified step size of the random walk[66]. Even with the inclusion of Coulomb collisions and neoclassical transport, however, it was found that various instabilities caused significant increases in cross-field transport, termed L-mode diffusion (low-confinement mode). It was discovered by Wagner *et al.*[67] that much of the turbulence could be suppressed by strong plasma shear that would lower the diffusion, termed H-mode diffusion (high-confinement mode), by the distortion and breaking up of turbulent eddies. This concept of plasma shear has been applied to models in Hall thrusters where a similar suppression of fluctuation-induced transport has been suspected[100]. The fusion research community is credited with much of the development of the theory of plasma turbulence, especially in the development of quasi-linear theory (described above in Section 3.3.3), and is on the forefront of new research in turbulent plasma transport.

Anomalous electron transport has been found in other configurations resembling the geometry of a Hall thruster; in the general case this geometry would be considered a Hall Effect Accelerator (HEA) or a closed $\mathbf{E} \times \mathbf{B}$ device. Hall Effect Accelerators were explored as a candidate for neutral beam injection for fusion plasmas in the 1970s[101] and were rejected due to the low fraction of ion current to discharge current (i.e. excessive electron mobility). More recently, geometry similar to a Hall thruster is found in planar magnetron discharges for material sputtering, where anomalous mobility has been observed in these devices, as well[102]. Currently, the goal in the planar magnetron discharge research community is much the same as the goal in the Hall thruster research community, where a physical description of the anomalous mobility in the general case would be useful for computer modeling efforts in order to

predict discharge parameters[102, 103, 69]. In the operation of a pulsed magnetron it was found that the anomalous electron conductivity exceeded the Bohm value, where the pulse length was 10-100 μs with a repetition rate of 50 Hz.[69] (Because of the pulse length, processes that occur at frequencies lower than 10-100 kHz will not be fully developed.) It was suspected that in this case, fluctuations were able to achieve higher saturation amplitudes than in DC operation causing the mobility to exceed the Bohm value which is based on saturation in steady state operation.

In studying plasma diffusion, insight into fundamental plasma physics processes has been gained through the investigation of non-neutral plasmas. Non-neutral plasmas exhibit similar phenomena as quasi-neutral plasmas such as Debye shielding, oscillations and stability[91, 58] (as previously explained in Section 2.1.4). Near-classical mobility has been observed in Penning traps [58, 104], which provide a simple environment where disturbances have been applied in a controlled manner to excite plasma modes, investigate instabilities and drive transport. Classical and fluctuation-induced transport through investigations of waves and oscillations [105, 106], growth of instabilities[107, 108], neo-classical transport[109, 110] and like-particle collisional transport [35, 111] have been investigated through the use of non-neutral plasmas. Furthermore, a reduction in plasma density has been used to reduce collective effects in order to study single particle dynamics in Penning trap fields[112].

It is obvious that the matter of anomalous transport is not unique to Hall thrusters, rather this dilemma extends across several disciplines whose applications are concerned with magnetic confinement of plasmas. Therefore, the solution to anomalous transport will likely come out of a collaborative effort benefiting from advances across several disciplines. For example, quasi-linear theory to describe plasma turbulence was first developed in the fusion community but has been used in several other disciplines to describe similar plasma behavior. Furthermore, charged particle traps have been used to confirm fundamental plasma physics processes that have been theoretically proposed and to replicate processes observed in fusion plasmas. The ap-

proach in the research presented in this dissertation, likewise, utilizes the non-neutral, low-density plasma approach for discovery of Hall thruster processes.

3.5   Critical Review & Contributions

The main goal of current Hall thruster research is to extend and enhance the performance of Hall thrusters over a wider range of operating parameters. This goal carries with it a number of requirements. Much of Hall thruster physics is empirically understood, but to scale the operating parameters outside of the current regime, an understanding of the fundamental physics of Hall thrusters is necessary, namely the growth of instabilities and fluctuations, the physics at the dielectric walls, and their contribution to electron mobility. Second, there is a desire to understand and control fluctuations in hopes of suppressing electron mobility to increase the efficiency of Hall thrusters within their typical operating parameters. Third, which is coupled into the previous requirements, there is a desire to accurately model the physics of a Hall thruster for future designs, scaling and optimization, and lifetime analysis. Current computer models contain a number of "fit" parameters to describe electron mobility that may not apply in all situations. In some cases electron mobility is given a constant collision frequency in the discharge channel[31, 32] or the discharge channel is divided into "regions" where each region is given a particular electron mobility "mode" (such as classical, Bohm, wall dominated, etc.)[34]. Attempts have been made to incorporate physical principles into empirical models such as the shear-based model developed by Scharfe *et al.*[100, 113] where $\mathbf{E} \times \mathbf{B}$ shear (where the E and B fields change significantly along the axial length of the discharge channel) is hypothesized to suppress turbulent transport. These models have provided better agreement with experiment than using a less detailed model such as Bohm and have also successfully replicated discharge oscillations characteristic of Hall thrusters, but the empirical fit parameters have still been found to be sensitive to the specific Hall

thruster and operating parameters modeled and are not applicable across-the-board.

The exact mechanism involved in fluctuation-induced mobility is not clearly defined and empirical formulations are generally used in practice. The following series of unknowns involved with fluctuation-induced mobility complicate an exact derivation from first principles: 1.) the origin of the fluctuations and saturation mechanisms, 2.) the steady-state solution describing the nature of the fluctuations (in terms of fluctuation amplitudes/phases of various quantities) 3.) the transport as a function of fluctuation characteristics. The origin of instabilities and growth of the fluctuations is highly dependent on the geometry and plasma boundary conditions, which make it case specific (unknown #1). Further complicating fluctuation-induced transport, the coupling between the self-sustained fluctuations and transport is not at all straightforward (unknown #2). Disregarding the complicated feedback in sustained fluctuations and transport, theories describing exactly how these fluctuations result in transport are varied (unknown #3). However, the third unknown is the most developed in terms of theory where several descriptions exist[78, 76, 56] and discrepancies between differing theories are small. Cook[56] maintains (and the author agrees) that the *real* problem with fluctuation-induced transport is the self-consistent solution describing the origin, growth and saturation of the fluctuations (unknowns #1 and #2). Toward a solution to the *real* problem, Thomas[55] and Spektor[83] have taken steps to apply quasi-linear theory (developed previously for other applications) to form a description of fluctuation-induced transport relevant to Hall thrusters. These derivations show promise for a solution to describe the anomalous transport in Hall thrusters; however, it is suspected that relevant physics is absent from the current derivations as experimental results have not been replicated thus far. It is also suspected that the problem of anomalous mobility in Hall thrusters is truly non-linear, where spatial and temporal interactions exist between waves that would not be adequately captured by the quasi-linear approach.

The influence of the dielectric wall-plasma interaction is also not adequately de-

scribed by current theories. The dielectric wall material and discharge channel width have been shown to significantly affect Hall thruster discharge properties[86], where the changes are attributed to altered electron mobility, but the exact physics to describe the influence of the dielectric walls is lacking. The difficulty with describing the effects of the dielectric walls is the coupling that exists between the sheath structure at the dielectric walls and the growth/origin of instabilities, fluctuations where the effect of the dielectric walls needs to be incorporated within the self-consistent solution for fluctuation-induced mobility (i.e. incorporated into the solution of unknown #1 and #2 described in the previous paragraph). This coupling exists for two main reasons: 1.) wall effects have been hypothesized to be the source of instabilities such as the two stream instability caused by secondary electron emission (SEE) from the channel walls[23] or the sheath instability[27] and 2.) the effective collision frequency due to collisions with walls depends on the large-angle scattering frequency within the plasma, where the turbulence is responsible for an amount of directional scattering. Some have used an empirical coefficient for the turbulent collision frequency in models to account for the scattering due to turbulence so that an accurate electron flux to the walls could be calculated[23], but no "closed form" solution has been employed (where the turbulent collision frequency could be modified by the wall collision frequency). To the author's knowledge, the effect of the dielectric walls has not been included in models predicting the growth of instabilities (for example the inclusion of the SEE effects) and taken into account in turbulent mobility. In terms of experimental research, separating the wall effects from fluctuation-induced mobility is not possible in an operating Hall thruster. However, the effects of the SEE reflection from the dielectric walls (explained in Section 3.3.2 and in Kaganovich *et al.*[23] may be separated experimentally by an investigation such as the research presented herein.

Much of the focus of Hall thruster research has been on measuring and predicting oscillations coupled with understanding the single-particle dynamics within the electric and magnetic fields of a Hall thruster. Ongoing modeling efforts in Hall thruster

electron mobility have produced substantial results in the past decade mainly due to an increase in computational power. However, it is thought that the research community may benefit from isolating certain factors so as to understand a single contributor alone, without the coupling that exists between hypothesized mechanisms for mobility. Isolating effects can never solve the non-linear effects that exist in a Hall thruster; however, an attempt to simplify the plasma environment may be able to provide understanding of a single aspect exhaustively. For example, attempts have been made to understand effects analogous to neoclassical mobility[55] in a Hall thruster and to understand the contribution from SEE reflection from the dielectric walls, both from a theoretical standpoint, but these effects can not be experimentally verified in the Hall thruster environment. Experimental verification of these concepts is impossible in the complex environment of a Hall thruster as the fundamental physics of the dominating mobility mechanisms is not well understood, so they cannot be separated. However, a method is proposed in this work that would enable the study of these fundamental concepts without these complicating/coupling factors so that effects acting on a single particle level may be investigated.

The achievement of this work has been the observation of enhanced, non-classical mobility in the Hall Electron Mobility Gage. The electron mobility apparatus was constructed at Michigan Tech's Ion Space Propulsion (I_{sp}) Lab in order to study electron dynamics in the defining electric and magnetic fields of a Hall-effect thruster with the goal of understanding the mechanism(s) responsible for the observed anomalous cross-field mobility. Measurements using the Hall Electron Mobility Gage have demonstrated the ability to observe cross-field electron mobility, where the experimental mobility has been found to be between the Bohm and classical predictions. These results are confounding as the two most cited contributors to anomalous mobility in Hall thrusters, dielectric wall effects and plasma fluctuations, were absent in this device. The most significant deviation between a Hall thruster plasma and the plasma in the Hall Electron Mobility Gage is that collective plasma effects such as

74

waves and instabilities within the plasma theoretically cannot exist (as will be explained in Chapter 5, Section 5.2.1), such that any enhanced mobility will be due to external parameters that are not internally coupled to the plasma environment. Dielectric walls typically found in a Hall thruster also have been removed in this device, where the plasma was confined using only electric and magnetic fields and collisions with the physical geometry of the apparatus were found to be negligible (see Section 5.3). Since wall effects were absent and collective effects could not persist in this plasma, investigating the mobility achieved three purposes. First, with this device it was possible to investigate any effects not linked to fluctuation-induced mobility (much like the insight achieved by O'Neil *et al.* in like-particle transport[35, 36] or like Eggleston *et al.* in resonant particle transport[112, 114]) that are based on geometry or static field conditions. In a Hall thruster discharge, the field conditions are so internally coupled to the plasma environment (the sheath structure is likely governed, at least in part, by the plasma oscillations and resulting cross-field transport) that investigating this effect alone would be impossible. Second, the anomalous mobility was examined in direct response to the external parameters without changing the plasma environment so that mobility versus E, B and neutral density could be investigated for scaling trends. Finally, it was possible to control and measure external fluctuations that could contribute to the plasma mobility such as externally applying field perturbations or measuring and/or controlling fluctuations that arise out of noise in electrical circuitry.

These observations suggested yet another transport mechanism that had not previously been isolated or observed that enhances mobility in the geometry specific to a Hall thruster. Therefore, a new mechanism for transport is proposed based on the effects of the bounce motion– that is the thermal motion along radial magnetic field lines as electrons oscillate between the inner and outer channel walls. At the "sheath" edge in a Hall thruster, which is analogous to the inner and outer radii of the confining volume in the Hall Electron Mobility Gage, the electric field changes drastically over

a relatively small distance, and thus is non-constant over a cyclotron orbit; because of this, standard drift equations that rely on the assumption of slowly varying electric and magnetic fields relative to the cyclotron orbit no longer apply. While the reason for the anomalous mobility is not known for certain, the available data shows that the mobility is correlated with the electron bounce frequency within the radial potential well. One hypothesized model to describe this mobility suggests that the electrons are able to step a distance on the order of the Larmor radius with each reflection from the confining field boundary. This type of behavior could be caused by cyclotron orbit distortion, in which the electric and/or magnetic fields change within a time period short compared with the gyro-time. In such fields, which are present near the reflection points in the apparatus, the guiding-center model is not valid and it is possible that particles entering this region with random gyro-phase exhibit a type of specular reflection, similar to what would occur in a momentum transfer collision, with a net motion of the guiding center in the direction of the applied electric field. This type of approach, that is, the use of a low-density, uncoupled plasma to study fundamental plasma processes, which has been utilized in Penning trap research for insight into fusion plasma processes, has never been conducted in the Hall thruster configuration.

Chapter 4

Design & Fabrication of Device

4.1 Purpose & Overview of Design

Some of the challenges in studying anomalous cross-field mobility in Hall thrusters (and in any device for that matter) were presented in Chapters 2 and 3. Historically, the difficulty in plasma transport studies has been the coupling that exists between the self-field of the plasma (including fluctuations) and the transport of the plasma. This chapter presents the design of a new device, the Hall Electron Mobility Gage, (shown in Fig. 4.1) which was designed as a diagnostic tool for investigating electron mobility in Hall thruster fields. The purpose of the design of the Hall Electron Mobility Gage was to replicate as many features of the Hall thruster environment as possible, while simplifying the plasma environment. The plasma environment could be simplified by 1.) minimizing the coupling that exists between the plasma and the electric/magnetic field structure, 2.) removing plasma oscillations, and 3.) removing the complex interaction at the plasma-dielectric wall interface. In a Hall thruster the plasma self-field, which is greatly influenced by the magnetic field, defines the shape and strength of the electric field[11, 7, 115] (as described in Section 3.2) so that the magnetic and electric fields cannot be varied independently. Removing this coupling would require a

Figure 4.1: Photograph of the Hall Electron Mobility Gage (cathode electrode and center front plate have been removed and are shown in the photo laying in front of the apparatus). Orientation shown at the bottom right of the figure. (Photo courtesy of Ref. [4])

low-density plasma so that the self-field could be regarded as negligible. Consequently, the field conditions would be considered rigid and defined by the vacuum solution and the electric field could conceivably be controlled independently of the magnetic field. The plasma self-field also has been shown to define the nature of waves and oscillations in a Hall thruster[55, 83] (as described in Section 3.3.3). A long Debye length relative to plasma dimensions results in a plasma that is defined by thermal motion of particles and cannot sustain collective oscillations on these length scales (described in Section 2.1.3). Therefore, the goal in the design of the Mobility Gage was to create a plasma with a long characteristic Debye length. This approach was also

used by Eggleston *et al.* in modified Malmberg-Penning trap experiments to reduce the collective effects that were postulated to enhance transport[108, 112]. Thus, in reducing the density and increasing the Debye length, simplification #1 and #2 may be achieved. The dielectric walls in a Hall thruster exist to insulate the discharge channel from the magnetic circuit so that an axial electric field may be sustained over the discharge channel. The dielectric walls also provide a physical barrier for radial plasma confinement. However, the physics of the plasma-dielectric wall interface and effects on cross-field mobility remain largely unknown[86, 23]. In order to remove this complication (#3), the dielectric walls were not employed in the Hall Electron Mobility Gage.

It was assumed *a priori* that the desired plasma environment (low density, long Debye length) could be created*. The design of the electric and magnetic fields relied on this assumption, and the goal then became to recreate the defining Hall thruster electric and magnetic fields in vacuum. The two challenges in creating these fields in vacuum were first, to align the electric equipotentials and magnetic field lines and second, to provide radial confinement without dielectric walls. (Both of these conditions are achieved in a Hall thruster through the self-consistent plasma fields.) In the design process the magnetic field was designed first to replicate the magnetic field of a Hall thruster. The electric field was then created through contoured electrodes that exactly match the magnetic field lines, so that equipotentials (which form parallel to the electrodes) align with magnetic field lines. Radial confinement in the absence of dielectric walls was achieved at the confinement volume periphery through the departure of the vacuum electrostatic equipotential lines and magnetic field lines at the inner and outer radii, which creates a confining electrostatic potential well. Sections 4.2 and 4.3 present the design of the magnetic and electric field, respectively. Section 4.4 presents a qualitative introduction to the radial confinement mechanism in the absence of dielectric walls (which is presented analytically in Chapter 5). Section

---

*Of course, the removal of the dielectric walls would provide no engineering difficulty, and this ability was also assumed.

4.5 presents the mechanism for trap loading. Some comments about the design are presented in Section 4.6, including a set of criteria that will be addressed in the subsequent chapters to assess how well the design has met its purpose. The resulting plasma environment and characteristic electron dynamics in the fields presented herein will be explored in Section 5. The device is experimentally characterized in Chapter 6 to assess the validity of the assumptions that are made *a priori*, which are discussed in this chapter. Machine drawings of the physical structure of the Hall Electron Mobility Gage may be found in Appendix A. Several of the design aspects presented in this chapter have been previously reported elsewhere[116, 117, 118, 119, 120].

4.2   Magnetic Field

The magnetic field topology was designed to replicate that of a Hall thruster. The Hall thruster magnetic circuit is based on a C-core design that has been rotated about a center axis so that the vacuum gap creates an annular channel with a radial magnetic field between the inner and outer pole pieces. Similarly, the coaxial design of the Hall Electron Mobility Gage employs N_c turns of windings around the inner and outer core pieces where a current, I_c, supplied to these windings creates a magnetic flux through the core material. Laboratory Hall thrusters commonly have the single azimuthal outer coil geometry as is utilized in the Hall Electron Mobility Gage (Fig. 4.2). However, flight scale Hall thrusters (shown in Fig. 1.1) often have four or more cylindrical outer magnetic coils uniformly spaced around the periphery spanning the front and back plates that similarly induce magnetic flux but provide mass savings over the strictly azimuthal geometry. The azimuthally symmetric geometry was chosen in this case to ensure azimuthal uniformity and to improve reliability of axisymmetric field models.

The magnetic field topology has been shown to have great importance in thruster
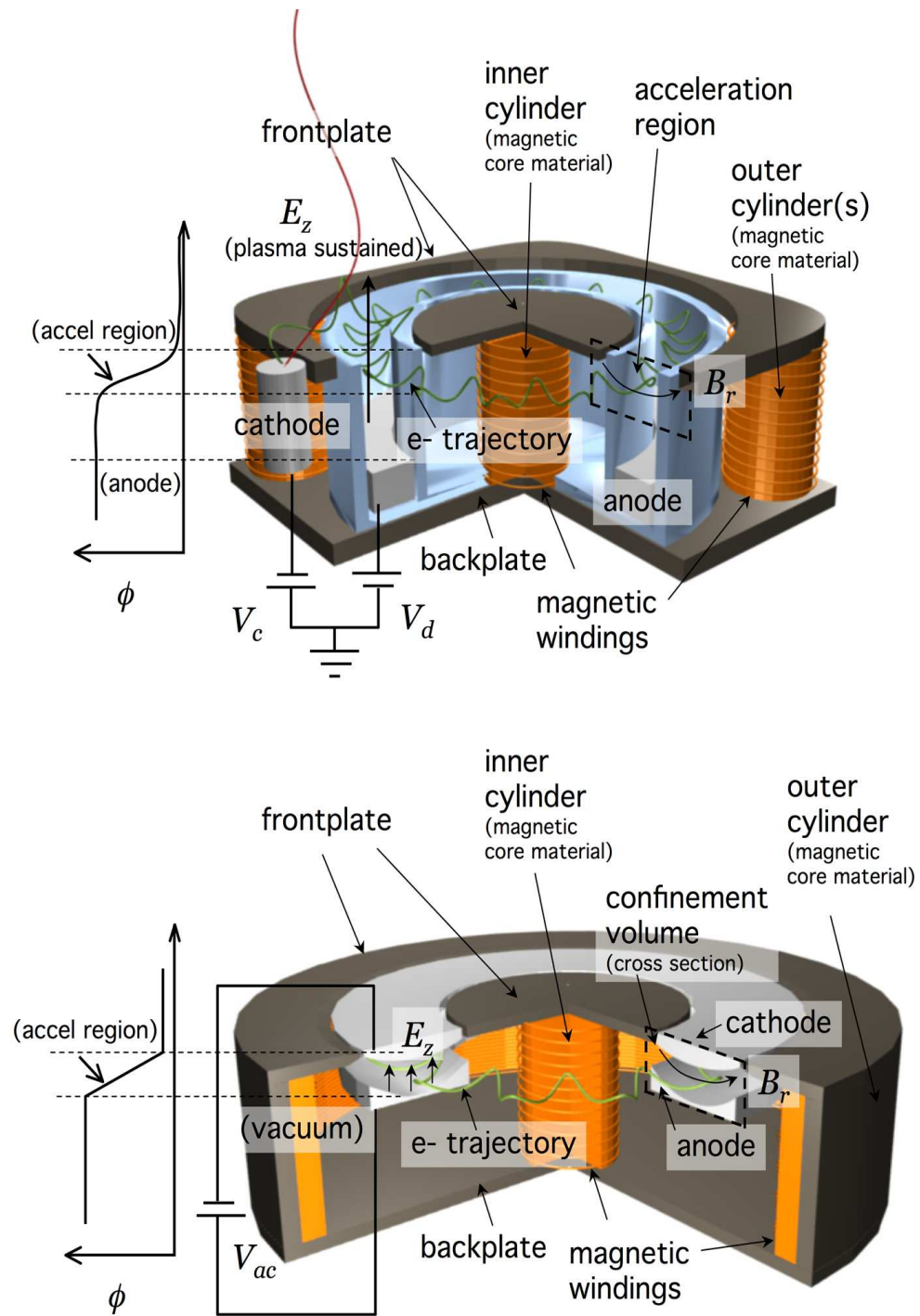
Figure 4.2: Schematic of the defining features of a Hall thruster (top) and the Hall Electron Mobility Gage including electric field creation and resulting potential (qualitative).

efficiency and operation†. The main features of a modern Hall thruster magnetic field are the symmetry in the magnetic field lines about the channel centerline and the concavity of the field lines (rather than strictly radial, as was exhibited in the early Hall thruster designs[21]), which both create a point of minimum magnetic field at channel centerline. This creates a magnetic mirror, as charged particles tend toward areas of lower magnetic field, that confines the plasma at the center of the channel and away from the dielectric walls (described more thoroughly in Section 2.1.1). It was also found that for the stability of the plasma (ion) flow in the Hall thruster the magnetic field should increase axially with distance from the anode[11]. These features were captured in the design of the Hall Electron Mobility Gage. Figure 4.3 shows the shape of the core material and resulting magnetic field map where magnetic field lines are superimposed on the magnetic field magnitude contour plot. Figure 4.4 shows the magnitude of the radial and axial magnetic field profile with axial distance at the point of minimum magnetic field and at the inner and outer radii (location of axial profile is shown in Fig. 4.3). Figure 4.4 shows the same axial profile of the magnetic field for a NASA-173Mv1 Hall thruster[5]. In the Hall Electron Mobility Gage the outer magnetic pole is beveled and the inner pole is thicker and un-beveled (detailed dimensions are found in Appendix A, Figs. A.6 and A.7). Since the field diverges radially there is naturally an enhanced magnetic mirror at the inner pole, so the beveled outer pole enhances the field convergence, and consequently enhances the magnetic mirror. The magnetic mirror has been found to play a role in Hall thruster electron confinement[37, 82] and likewise serves to enhance the electrostatic potential well confinement in the Hall Electron Mobility Gage (discussed qualitatively in Section 4.5 and analytically in Section 5.3).

The area of interest for this research corresponds to the "acceleration" region of a Hall thruster (noted in Fig. 4.2). The definition of the "acceleration" region varies

---

†Ref. [5] provides a study of Hall thruster operating parameters due to changes in magnetic field. A good overview of the design criteria of the magnetic field in Hall thrusters, with respect to efficiency of electron confinement, is outlined in Ref. [82].
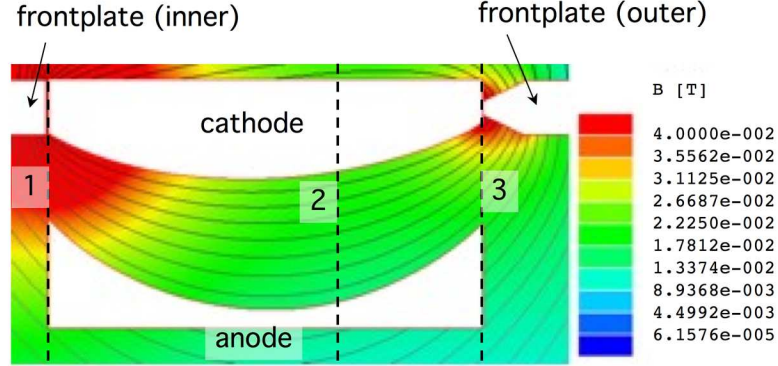
Figure 4.3: Magnetic field map for the cross section of the Hall Electron Mobility Gage confinement volume; Locations r_1, r_2, and r_3 correspond to the location of the axial profiles shown in Fig. 4.4 and in Fig. 4.9.

but is often correlated with the axial region that captures the point of maximum radial magnetic field and extends axially in both directions where the radial magnetic field falls to 60-80 percent of maximum[34]. Unfortunately, because of the requirements for confinement (explained in Section 4.5) it is not possible to examine the region exactly centered about the maximum magnetic field in the Hall Electron Mobility Gage; rather the confinement volume (bounded by the cathode electrode in Fig. 4.3) starts at the magnetic field line extending just inside the pole pieces. This corresponds to the point where the magnetic field is about 90 percent of maximum. The region examined in the Hall Electron Mobility Gage extends from the point of 90 percent of B_{max} to the point where the field falls off to 60 percent of the maximum magnetic field.

The magnetic poles were constructed of 1018 low-carbon steel, mainly due to the relatively high magnetic permeability and commercial availability (iron purity 98.8%). Other materials, such as magnetic iron (iron purity 99.95%) have a higher magnetic
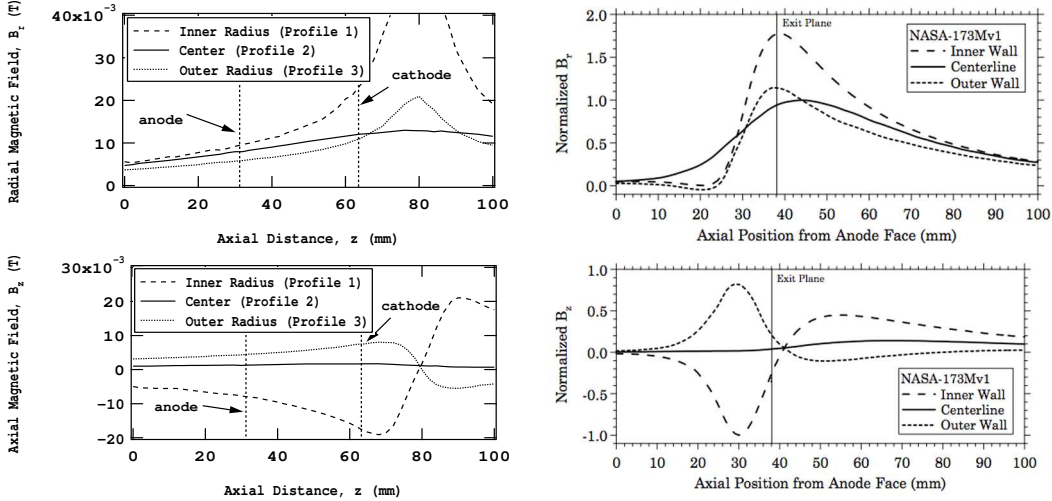
Figure 4.4: Axial profiles of the radial magnetic field (top) and axial magnetic field (bottom) for the Mobility Gage (left) and the NASA-173Mv1[5] (right) taken at locations r_1(dashed), r_2 (solid), and r_3 (dotted) corresponding to the radial locations indicated in Fig. 4.3.

permeability but would have been cost prohibitive, and such materials were deemed unnecessary at the early stages of development in this project. The B-H curve for 1018 low carbon steel is shown in Fig. 4.5.

As was presented in Section 3.2 the criteria for the magnetic field strength in a Hall thruster is such that electrons are highly magnetized but ions are weakly affected by the magnetic field. A magnetic field strength of 100 G clearly meets this criteria in the Hall Electron Mobility Gage with a 1.7-mm electron Larmor radius (assuming $T_e = 20$ eV), which is much smaller than apparatus dimensions, and a 0.62-m ion Larmor radius (for argon ions, assuming an ion velocity of 1.5×10^4 m/s calculated in Section 5.2.3), which is much larger than apparatus dimensions. The inner and outer magnetic coils have 620 and 310 turns, respectively. A coil current of 2.0 A (so that the inner and outer coils are at 1240 Amp-turns and 620 Amp-turns, respectively) results in a field strength of 100 G at the channel centerline. The magnetic core material saturates when the magnetic field inside the material exceeds 1 T (10,000 G). The inner core material saturates to this point at $\sim$ 2000 Amp-turns on the
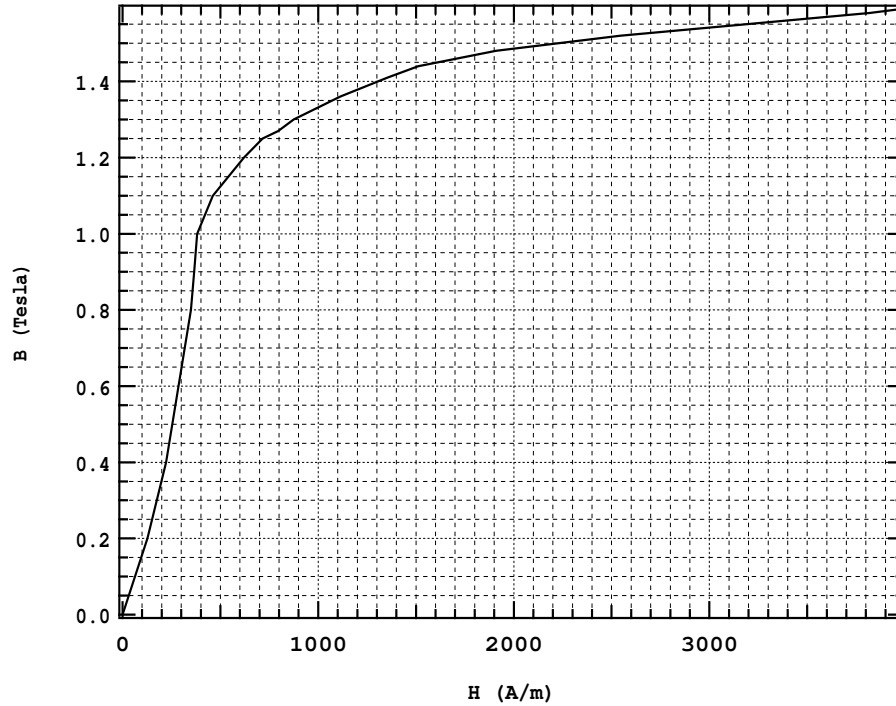
Figure 4.5: B-H curve for 1018 Low Carbon Steel. (Data for this figure obtained from Ref. [6])

inner coil; however, the outer pole does not reach saturation at ~ 1000 Amp-turns (corresponding to the same value of current). This results in a distortion of the field shape instead of just an (intended) change in the field magnitude if the inner and outer Amp-turns are increased proportionally past the current where the inner core material saturates. Therefore, when the inner pole saturates (where large increases in applied field correspond to small increases in magnetization) the current on the inner windings must be increased at a greater rate than that on the outer windings in order to preserve the field shape while increasing its magnitude. Using the B-H curve shown in Fig. 4.5, it was possible to simulate the effect of magnetic saturation using the magnetic field solver, Maxwell SV[121]. Figure 4.6 shows the saturation of the inner core material. The resulting "ideal" inner and outer magnetic coil Amp-turns are plotted in Fig. 4.7, which eliminate any field distortion. (This tuning procedure was also published in part in Ref. [118]. Experimental verification of the "optimal"
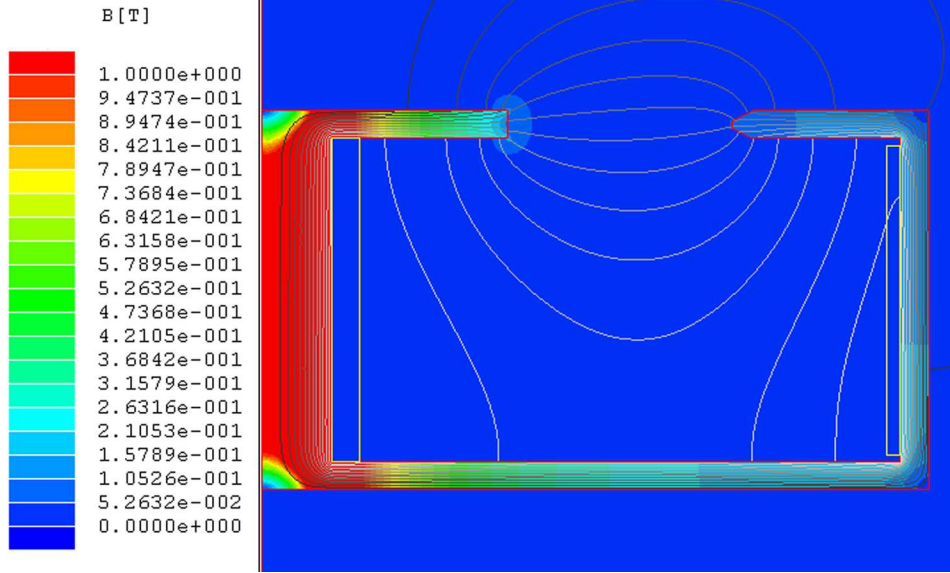
Figure 4.6: Magnetic field model for the Hall Electron Mobility Gage showing magnetic saturation of the inner core material with 2000 Amp-turns on the inner coil and 1000 Amp-turns out the outer coil.

inner and outer coil currents is presented in Section 6.2.1.)

The design of the device was created to be as large as possible while remaining within practical limitations (e.g. availability of materials and in-house fabrication). The design resulted in apparatus dimensions being about four times larger than a typical 1.5 kW Hall thruster[‡]. The objective of the geometrical size was to enable trap operation over a greater range of magnetic fields (lower) without the electron Larmor radius approaching apparatus dimensions. The inequality shown in Eq. (4.1) represents the condition that the Larmor radius (Eq. (2.2)) be much smaller than the electrode spacing (Δz_{a-c}), so that the electrode spacing axially extends several gyro-orbits.

$$\Delta z_{a-c} \gg \frac{m_e u_\perp}{q B_r} \tag{4.1}$$

Since one goal of this work was to explore mobility trends over a range of magnetic fields, and material constraints prevented magnetic fields above about 200 G, a Hall

---

[‡]SPT-100, BPT-2000 or other similar type Hall thrusters[9]
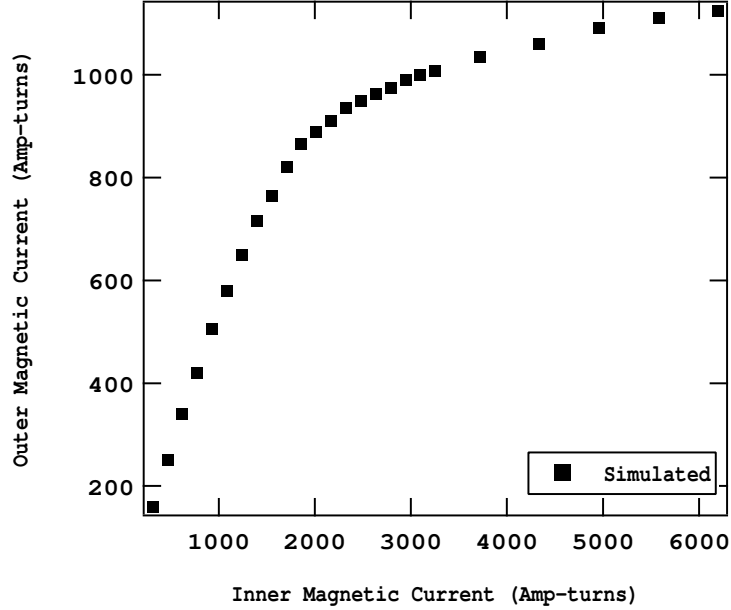
Figure 4.7: Ideal outer coil current versus inner coil current for simulated magnetic field data.

thruster-sized device was not feasible, as the range of magnetic fields would be severely limited while maintaining the inequality of Eq. (4.1). Therefore, to extend the range of magnetic fields, the size of the Hall Electron Mobility Gage was increased to the limits of in-house fabrication. In this configuration, a magnetic field of ~ 50 G would result in a Larmor radius (3 mm for $T_e = 20$ eV) that is an order of magnitude smaller than the electrode spacing (30 mm), allowing the inequality of Eq. (4.1) to be maintained over the range of 50 G$< B < 200$ G, which provides the limits of the magnetic field within the Mobility Gage.

4.3   Electric Field

In the Hall thruster environment the electric field is highly dependent on the plasma response to the magnetic field. A cartoon schematic representing the electric field creation and potential structure in a Hall thruster is shown in Fig. 4.2. The elec-

tric potential structure and resulting field for a Hall thruster are shown in Fig. 4.8. Electrons are highly mobile along magnetic field lines so any applied potential will be immediately equalized by rapid electron motion along the magnetic field lines; therefore, magnetic field lines are often approximated as electric equipotential lines[11]. Electrons are significantly impeded axially in their motion across magnetic field lines so that large electric potential gradients may be supported perpendicular to the magnetic field. Minimizing the coupling between the electric and magnetic fields in the Hall Electron Mobility Gage requires the plasma density to be many orders of magnitude lower than that which is found in a Hall thruster, so that there would be negligible plasma contribution to the applied electric field (see Section 5.2.1). Assuming this criterion could be met, the electric field was regarded as (nearly) equivalent to the vacuum solution which, in effect, would separate the electric and magnetic fields into two separate independent variables. The challenge then lay in creating the potential structure and resulting electric field, analogous to the complex Hall thruster plasma field, in vacuum. The vacuum electric field was required to meet the following goals: 1.) to create lines of electric equipotential coincident with magnetic field lines and 2.) to emulate the negative sheath structure that exists at the dielectric walls of a thruster to provide radial confinement.

It was found that both of these criteria could be achieved through the utilization of contoured electrodes. The curved electrodes would create curved equipotential lines that would coincide with the magnetic field contours. The sheath was replicated through the departure of electric equipotential lines and magnetic field lines at the periphery of the confinement volume, which would create a confining electric field parallel to magnetic field lines much like that of the Hall thruster sheath. The sheath and confining structure is discussed in more detail in Section 4.4 and the focus of this section is on the creation of the electric field for the bulk of the confinement volume. As described in Section 4.2, the magnetic field was modeled to replicate the acceleration region of a Hall thruster. A magnetic/electric field solver, Maxwell
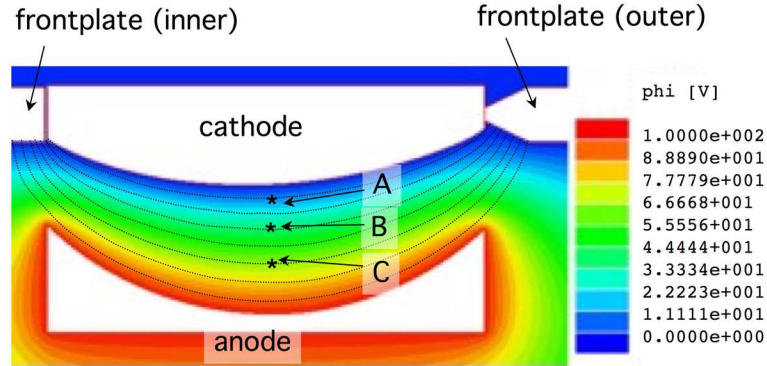
Figure 4.8: Electric equipotentials shown as color contours with superimposed magnetic field lines (black) for the cross section of the Hall Electron Mobility Gage confinement volume; points (z_1), (z_2) and (z_3) correspond to the locations of the potential well profiles shown in Fig. 4.10.

SV[121], was used to map the field lines, and physical electrodes were designed such that the electrode surfaces were coincident with local magnetic field lines. Figure 4.8 shows the contoured electrodes and the magnetic field lines superimposed on the electric equipotential lines. With the contoured electrode structure, the electric equipotential lines (surfaces) would extend parallel to the electrodes such that the magnetic field lines and equipotential lines coincide. In this configuration electrons would be thermally mobile along field lines with their guiding center paths parallel to the electrode contours. The x-y pairs for the electrode contours are presented in Table 4.3.

The coordinates for the contours were transferred into a solid modeling program (IDEAS) so that 3-D solid models of the electrodes could be created computationally. Using the IDEAS solid model, a CNC tool path was generated within IDEAS in order to machine each electrode contour, which were physically milled using a Haas®4-axis CNC mill. The physical electrodes were then smoothed and polished on a manual

Table 4.1: (x,y) pairs for anode and cathode electrode contours; origin is defined at the center (axial and radial) of the inner magnetic pole

x (mm)	Anode, y (mm)	Cathode, y (mm)
111.5	53.38	73.38
115.5	49.53	71.27
119.5	46.32	69.41
123.5	43.55	67.89
127.5	41.19	66.61
131.5	39.16	65.55
135.5	37.39	64.68
139.5	35.92	63.98
143.5	34.71	63.44
147.5	33.78	63.07
151.5	33.09	62.84
155.5	32.63	62.74
159.5	32.38	62.78
163.5	32.29	62.95
167.5	32.53	63.27
171.5	33.04	63.73
175.5	33.80	64.33
179.5	34.83	65.06
183.5	36.13	65.92
187.5	37.69	66.93
191.1	39.38	68.07
195.5	41.76	69.36
199.5	44.20	70.84
203.5	47.11	72.57
207.5	50.45	74.76
209.5	52.34	76.01

lathe. (A photograph of the finished electrodes can be seen in Fig. 4.1) The resulting anode and cathode electrode surfaces precisely match the magnetic field contours created by the magnetic poles as shown in Fig. 4.8.

The choice of the axial location within the magnetic field structure for the parallel plates was described in Section 4.2. The anode electrode was placed at the point where the magnetic field had dropped to 60 percent of the maximum magnetic field. The

cathode electrode was placed at the point where the magnetic field was at 90 percent of maximum, which was necessary for the confinement scheme, as described in Section 4.4. In this configuration the electrode spacing would be ∼ 30 mm. In order to create an electric field of $2 - 40$ V/mm typically found in Hall thrusters (2-10 V/mm was cited in Ref. [71], ∼ 5 V/mm in Ref. [23], 20 V/mm in Ref. [5], and up to 40 V/mm in Ref. [7]), a potential difference of 50-1200 V would need to be applied between the anode and cathode electrodes. However, power supply availability limited the anode-to-cathode voltage to 600 V and preliminary experiments showed significant arcing at fields above 300 V. Therefore, for most of the experiments presented herein, the anode-to-cathode voltage was kept in the range 50 V $< V_{ac} <$ 300 V. The axial profile of potential and axial electric field are shown in Fig. 4.9 for $V_{ac} = 100$ V where the profiles were obtained at radial locations corresponding to locations (r_1), (r_2), and (r_3) indicated on Fig. 4.3. Axial profiles of potential and electric field for the SPT-P5 Laboratory Hall thruster[7] at various radial locations are also shown for comparison. The term "local" potential, used frequently throughout this document, refers to the unperturbed vacuum potential found from the electrostatic field solver. For example if the emission filament (described in Section 4.5) is said to be biased to "local" potential, its bias is set to match the potential of the vacuum solution at the location of the filament. It follows then that "local" potential at a particular location changes proportionally with the applied anode-to-cathode potential.

4.4   Radial Confinement

In the discharge channel of a Hall thruster a negative sheath exists at the dielectric walls that serves to repel the bulk of electrons from the walls and confine them to the channel annulus. This sheath is emulated in the Hall Electron Mobility Gage through the departure of electric equipotential and magnetic field lines at the confinement volume periphery. The departure is shown in Fig. 4.8 and the rationale for the sheath

91
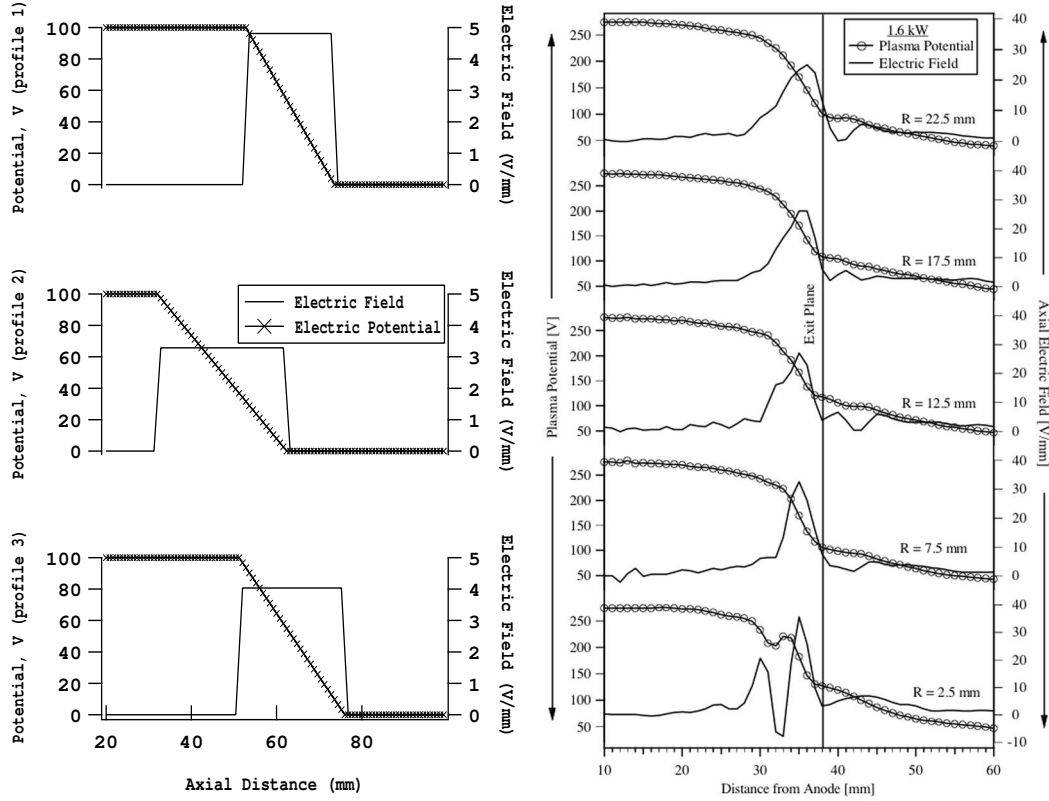
Figure 4.9: Axial profile of electric potential (×'s) and electric field (solid) for the Hall Electron Mobility Gage (left) for the axial profile at radial location r_1 (top), r_2 (middle), and r_3 (bottom) indicated in Fig. 4.3 and the axial profile of electric potential (○'s) and electric field (solid) for an SPT-P5 Hall Thruster (right)[7].

analysis is described qualitatively in the following argument. Since electrons are constrained to follow B-field lines (between collisions), they have a point of minimum potential energy at the center of the confining volume where the B-field is coincident with the electric equipotentials. As an electron travels from this region towards either edge of the confinement volume, the electric potential decreases as the magnetic field lines depart from the electric equipotentials. This repels electrons from the confinement volume periphery to the center of the confinement volume as an electric field exists along the magnetic field line ($\mathbf{E} \cdot \hat{\mathbf{b}} \neq 0$) that acts to decelerate the parallel velocity, $v_{\parallel}$. The magnetic field lines passing through the confinement volume terminate on the iron pole pieces, which are held at cathode potential, thus the total

92

potential difference from trap center to trap edge along a B-field line (where the magnetic field lines intersect the pole) represents the depth of the confining potential well.

Consider, for instance, an electron constrained to the B-field line that is coincident with the 60 V equipotential at trap center (point (z_3) in Fig. 4.8). In order to impact the iron pole at the trap periphery, the electron must climb a 60-V potential hill because the electron is constrained to the magnetic field line. Therefore, an electron on the magnetic field line at 60 V in the center of the confining volume would be in a 60-eV electrostatic potential well. Because an electron at this location can have no more total kinetic energy than 60 eV, based on the loading mechanism described in Section 4.5, it is clear that this potential well would reflect the bulk of electrons to the center of the confinement volume and only the electrons in the high energy tail of the Maxwellian distribution could overcome the confining potential. This is also described in more detail in Section 5.2 in an analysis of radial confinement time. This confinement is analogous to the confinement due to the negative sheath on the dielectric walls of a Hall thruster, where only the high-energy electrons are able to overcome this potential and are lost to the walls. (For all the tests reported in this work the cathode and magnetic pole pieces are electrically connected as is represented in Fig. 4.8. However, the two can be electrically isolated if differing electric field conditions are desired in future experiments.)

Quantitatively the potential well provided by the parallel electric field can be described by integrating the forces acting parallel to B along the length of a magnetic field line from the inner magnetic core material to the outer magnetic core material. The force due to the electric field was found to be much more significant than any other force acting on the electron parallel to the magnetic field (centrifugal force due to the $\mathbf{E} \times \mathbf{B}$ drift and magnetic mirror force explained in Section 2.1.1) and thus the centrifugal and magnetic mirror forces were neglected in this analysis. This analysis of potential well was published in part in Ref. [118]. The along-field potential was
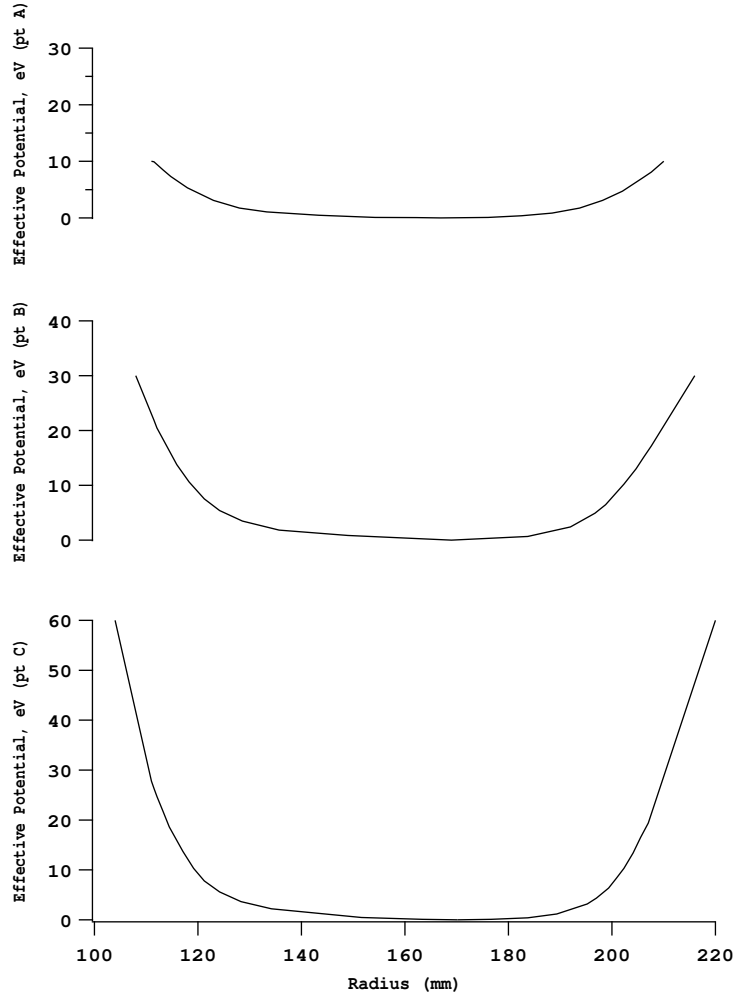
Figure 4.10: "Along-field" potential well for magnetic field lines intersecting locations z_1 (top), z_2 (middle) and z_3 (bottom) in Fig. 4.8.

determined by the equation

$$\Phi_{eff}(r) \; = \; \int F_{\mathbf{E} \cdot \hat{\mathbf{b}}} dr \qquad (4.2)$$

where Φ_{eff} is the effective potential well and $F_{\mathbf{E} \cdot \hat{\mathbf{b}}}$ is given by

$$F_{\mathbf{E} \cdot \hat{\mathbf{b}}} \; = \; q(\mathbf{E} \cdot \hat{\mathbf{b}}) \qquad (4.3)$$

Figure 4.10 shows the "along-field" potential well for the magnetic field lines inter-

secting locations (z_1), (z_2), and (z_3) in Fig. 4.8. It is shown in Fig. 4.10 that the well depth of (z_1), (z_2), and (z_3) equals the potential difference between the vacuum potential at each location, V_{local}(10 V, 30 V, 60 V, respectively), and the potential of the cathode. It can also be seen by Figure 4.10 that the effective potential of the well is relatively "flat" over the bulk of the confinement volume indicating that electrons experience mostly thermal motion ($\mathbf{E} \cdot \hat{\mathbf{b}} \sim 0$) and are only strongly reflected at the edges of the confinement volume where $\mathbf{E} \cdot \hat{\mathbf{b}} \neq 0$. This example is for $V_{ac} = 100$ V; however, this holds true for all electric fields at all locations.

4.5   Electron Loading

The goal of the trap loading mechanism was to emit low energy electrons at a point within the potential well so that the majority of emitted electrons could be confined within the trapping volume (as opposed to injecting electrons from outside the potential well, which could then gain enough energy falling into the potential to escape through the opposite side of the well). This was achieved by placing a thermionically emitting filament entirely within the confining volume at a finite distance from the cathode (as opposed to coincident with the cathode where there would be no potential well) and positioning it on channel centerline, so that electrons were injected at the minimum of the potential well.

The filament that was used consisted of a single square loop of 5 mil (0.005 in.; 0.127 mm) thoriated tungsten wire where the wire ends were compression fitted into a twin-bore alumina tube to make electrical contact with copper leads. The end of the alumina tubing was coated with an electrically insulating ceramic adhesive (Resbond 919 High Resistance Ceramic Adhesive and Potting Compound) covering the filament insertion points and leaving a small horizontal length of the filament exposed (~ 3.5 mm). The resistance across the exposed wire is ~ 0.1 Ω corresponding to a voltage
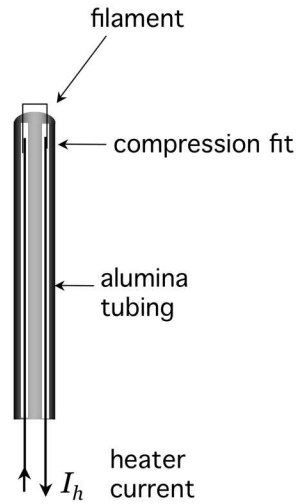
Figure 4.11: Schematic of the electron loading filament.

drop of ~ 250 mV for a typical heater current of 2.5 A. The effect of this voltage drop is negligible in the operation of the Hall Electron Mobility Gage as will be discussed in Section 6.3.5 in a characterization of the electron loading mechanism. The alumina tube was inserted through an aperture in the cathode electrode and secured in place using a setscrew where the emission filament was located ~ 3 mm from the cathode surface for most experiments. A schematic of the filament is shown in Fig. 4.11.

Thoriated tungsten is often used for electron emission purposes due to its relatively low work function of 2.6 eV (i.e. the energy required to liberate an electron from the surface of the metal). The relation of emission current, temperature and work function, is given by the Richardson-Dushman equation:

$$J \;=\; AT^2 \exp\left(-\frac{\varphi}{kT}\right) \tag{4.4}$$

where J is the emission current density, T is the absolute temperature (K), φ is the

work function, k is Boltzmann's constant, and A is Richardson's constant given by:

$$A = \frac{4\pi m_e k^2 e}{h^3} = 1.20173 \times 10^6 \text{ Am}^{-2}\text{K}^{-2} \qquad (4.5)$$

Here, m_e is the electron mass, e is the elementary charge and h is Planck's constant. The Richardson-Dushman equation is given for the emission in the zero-field case. However, if an external electric field is present (as would be the case in the Hall Electron Mobility Gage), the field enhances the emission and the thermionic emission equation is modified to be

$$J = AT^2 \exp\left(-\frac{(\varphi - \Delta\varphi)}{kT}\right) \qquad (4.6)$$

where $\Delta\varphi$ serves to reduce the work function and is given by

$$\Delta\varphi = \sqrt{\frac{e^3 E}{4\pi\epsilon_0}} \qquad (4.7)$$

where ϵ_0 is the vacuum permittivity and E is the applied external electric field.

An isolated DC heater circuit was employed to heat the filament so that electrons would be thermally emitted from the tungsten surface. Within the Hall Electron Mobility Gage the filament is in the presence of an axial electric field. To determine the accelerating electric field, in order to compute $\Delta\varphi$, a numerical solution was obtained using Maxwell SV[121] for the filament held at "local" potential§ as well as at 15V above local potential (electron attracting), and 15 V below local potential (electron repelling), which are both presented in Fig. 4.12. It is seen that even when the filament is above the "local" unperturbed potential there still exists an electric field serving to accelerate the electrons from the filament toward the anode, although this field is made weaker as bias potential is increased. The accelerating electric field

§The "local" unperturbed vacuum potential could be determined from the Maxwell SV[121] numerical solution in absence of the filament.
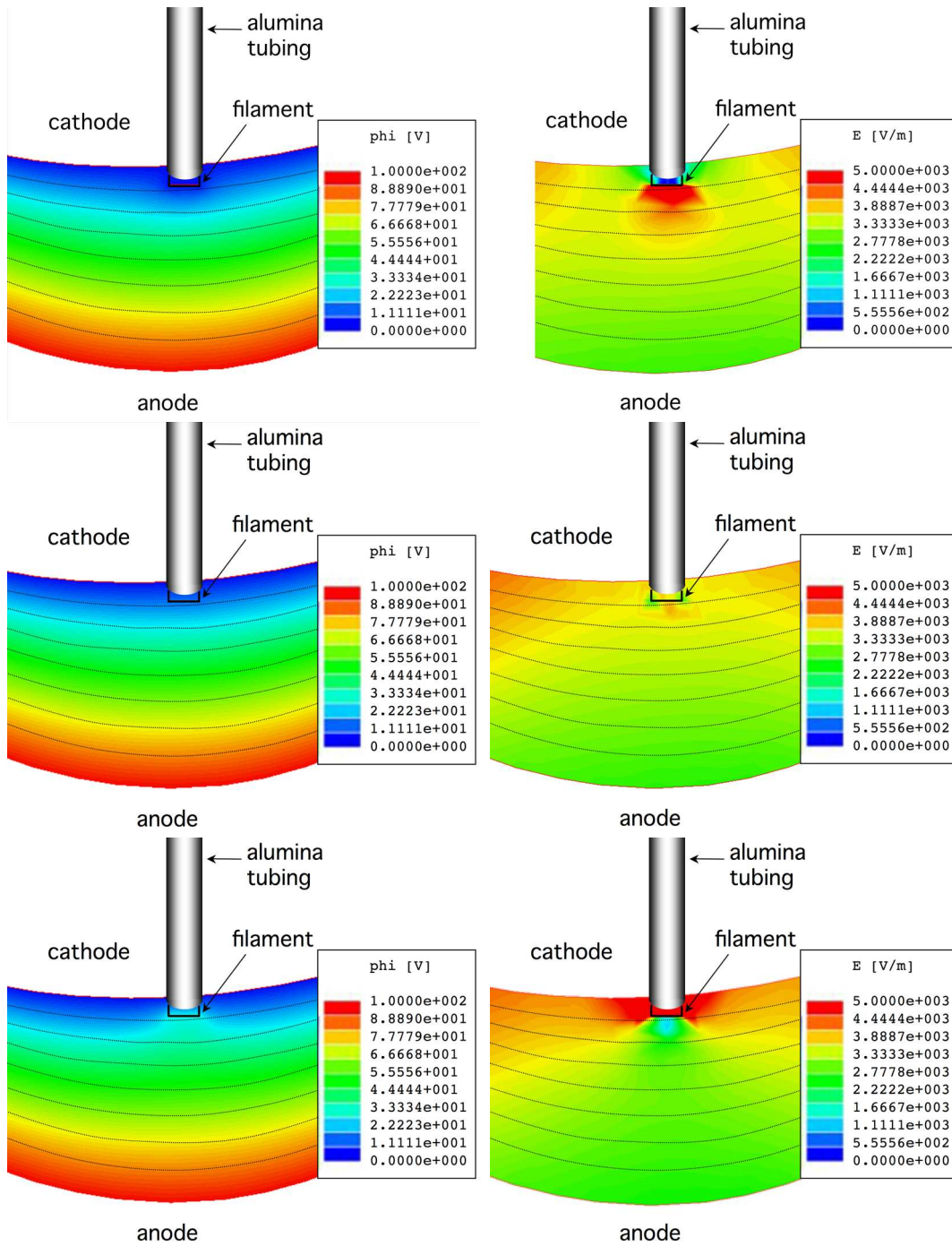
Figure 4.12: The potential structure in the presence of the filament (left) and the resulting electric field (right) for the filament biased to cathode potential (top), "local" potential (center) and 15 V above "local" potential (bottom), for an anode-to-cathode voltage of 100 V.

directly below the filament (serving to assist electron emission) is 3.9×10^3 V/m and 1.3×10^3 V/m, for the filament biased to "local" potential and 15 V above local potential, respectively. The field is 5.6×10^3 V/m for the filament biased 15 V below local potential. For these fields the field-assisted emission is small, where $\Delta \varphi \sim 0.001$ eV and provides very little modification to the work function. Since the emission is highly dependent on the temperature (shown in Eq. (4.7)) and barely modified by the electric field it was assumed *a priori* that a heater current could be used to control the electron emission current and thus density within the confinement volume (see Section 6.3.2 for a characterization of emission current and resulting electron density within the confinement volume).

The I-V characteristics of the emission filament differs from an emitting filament in a dense plasma (such as an emissive probe typically used to measure plasma potential[122]). The shielding provided in a dense plasma would reflect low energy electrons back to the filament if the filament were biased above local potential so that electron emission could be negated at biases (with respect to local potential) on the order of the emitted electron temperature. Electron emission in the Hall Electron Mobility Gage would not be eliminated under the same conditions due to the long Debye length and absence of shielding. If the filament were biased to "local" potential, the perturbation due to the presence of the filament would be minimized.

The emitted electrons were assumed to have < 1 eV of energy at the surface of the filament upon emission, where this assumption was based on the experimental emission data of Hutson[123]. If electrons could be emitted in a potential well deeper than this, they would be confined. Equation (4.2) was used to determine the potential well at the location of the filament (for the case of $V_{ac} = 100$ V), which is shown in Fig. 4.13. At the lowest field strength of $V_{ac} = 50$ V (and thus the smallest potential well), at a distance 3 mm from the cathode, the potential well is > 5 eV so that confinement would be achieved. Electrons gain energy quickly as they are accelerated by the electric field from the filament. However, the gain in energy corresponds to
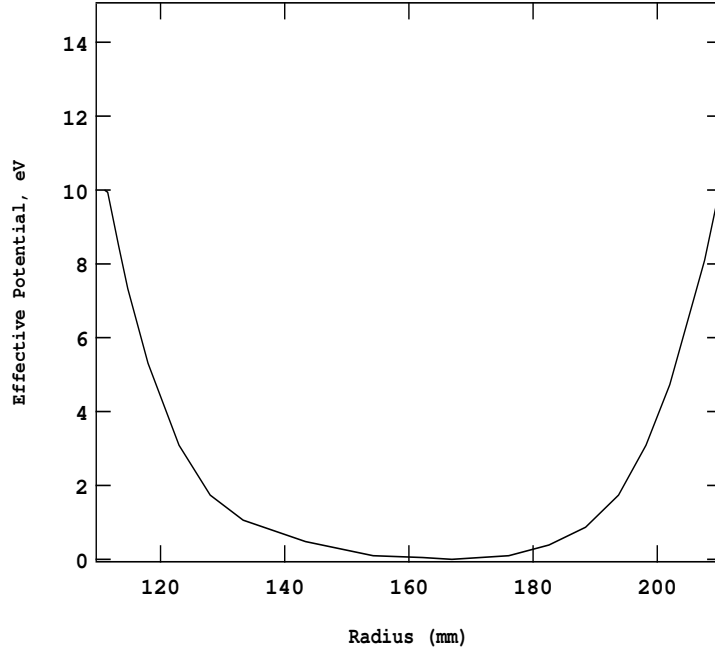
Figure 4.13: The potential well at the location of the filament for an anode-to-cathode voltage of 100 V.

an axial displacement where the depth of the potential well increases at the same rate of energy gain. Therefore, in terms of the example presented in Section 4.4, electrons that have reached point z_3 (local potential of 60 V) have fallen through a potential of $V(z_3) - V(\text{filament}) = 60 \text{ V} - 10 \text{ V} = 50$ V. Electrons then have energy $\epsilon(z_3) - \epsilon(\text{filament}) + \epsilon(\text{initial}) < 51$ eV and yet are confined by a 60 eV potential well. Confinement considerations will be explored more thoroughly in Section 5.2.

4.6 Design Comments

This chapter contains the design of the physical apparatus that will be analytically and experimentally characterized in the following chapters. The ultimate goal was to create a device where it would be possible to vary the electric field, magnetic field and neutral density independently in order to observe the trends of transport in a

Hall-thruster-like environment. The following assumptions were made *a priori* that require validation both through analytical and experimental means. First, the most notable assumption was that the plasma density within the confinement volume could be sufficiently low so that the electric field could be considered rigid and prescribed by the vacuum field of the physical electrodes. If this criterion is met, the electric field may be explicitly controlled independent of other parameters as described in Section 4.3. This assumption will be presented analytically in Chapter 5 and experimentally verified in Chapter 6. Second, it was assumed that the bulk of electrons could be confined electrostatically so that the confinement would be analogous to the confinement provided by the negative sheath at the surface of the dielectric walls in a Hall thruster. This assumption will be examined analytically in an analysis of confinement and losses in Chapter 5, which allows for removal of the complicated, dynamic structure of the negative sheath and replaces it with an explicitly known field environment. Upon meeting these criteria the controlled parameters, especially of electric and magnetic field, would be uncoupled and may be varied independently for electron mobility investigations.

Chapter 5

Analytical Characterization

5.1   Introduction

The purpose of this chapter is to present the relevant plasma properties and dynamics of electrons in the Hall Electron Mobility Gage and compare them to those of Hall thrusters. The plasma created in the Mobility Gage is intended to be different from a Hall thruster plasma in ways that would simplify the experimental observations of transport by isolating variable parameters that affect mobility. A similar attempt to simplify the plasma environment was made by by Eggleston[112] in Penning trap research. In reducing the plasma density by two orders of magnitude and using an externally applied field to simulate the mutually repelling self-field of the non-neutral plasma, Eggleston was able to eliminate the collective plasma effects in order to study fundamental particle motion in the Penning trap. In Eggleston's work, the plasma density was reduced for the same reasons presented herein: to simplify the plasma environment and remove complicating non-linear collective plasma effects such as self-sustaining waves and oscillations. The plasma environment of Eggleston's work was significantly different than that of the Penning trap to which Eggleston compares his findings, and both are vastly different from fusion plasmas, but relevant

discoveries have been made in fundamental plasma transport that correlate between the simplified and more complex plasma environments despite the differing plasma properties[109, 124, 110, 125]. In the same way, the goal in this research is to gain insight into fundamental transport processes in Hall thruster fields by investigating a low-density, non-neutral plasma and identifying fundamental transport processes that may be applicable to the Hall thruster plasma environment. This chapter presents the plasma properties of the Hall Electron Mobility Gage, contrasts them with a Hall thruster, and yet identifies processes which are similar fundamentally.

By Chen's definition (Section 1.4-1.6 of Ref. [38]), the collection of charged particles in this device is loosely defined as a "plasma." The first criterion given by Chen is that the plasma must be many Debye lengths in size. In this device, for the range of electron densities and temperatures considered, the Debye length is much longer than any other characteristic dimension (described in Section 5.2.2), violating this criterion. The requirement of many Debye lengths allows a plasma to be described by its collective aspects (presented in Section 2.1.3), where on length scales small compared to the Debye length, particles must be described by individual particle trajectories. The violation of this criterion then signifies the removal of the collective plasma behavior responsible for sustaining waves and oscillations. Chen's second criterion is that a large number of particles are contained within a sphere of radius Debye length (i.e. a Debye sphere). The number of particles contained in a Debye sphere is $\sim 1 \times 10^9 - 1 \times 10^{11}$ meeting this criterion. The final criterion is that the plasma frequency be much greater than the electron-neutral collision frequency. The plasma frequency is orders of magnitude higher than the electron-neutral collision frequency in the Hall Electron Mobility Gage. This criterion may also be interpreted to mean that the mean collision time (and mean free path) is long for electron-neutral collisions and that particle motion is defined by the response to electric and magnetic fields rather than by "nearest-neighbor" interactions as in a neutral gas. This criterion is met in the plasma of the Hall Electron Mobility Gage, where the mean free path

between electron-neutral collisions is much longer than inter-particle spacing and any other characteristic dimension of the device. Chen does not include relative ion and electron densities in the definition of plasma but often quasi-neutrality is assumed when considering Debye shielding and plasma frequency, among other characteristics. The specific intention in the Hall Electron Mobility Gage investigations was to create a low-density plasma, by externally supplying electrons (rather than through a gas discharge) where the electron density may, at times, be significantly greater than the ion density. Davidson[58] shows that confined non-neutral plasmas exhibit the same collective phenomena where properties such as Debye length (which is an important quantity for the Hall Electron Mobility Gage, see Section 5.2.1) and plasma frequency are equivalently defined so that plasma characteristics may be applied regardless of quasi-neutrality. In light of these criteria, the term "plasma" is used rather broadly with respect to the Hall Electron Mobility Gage to describe the collection of charged particles contained within the trapping volume.

The remainder of this chapter is organized into three sections, the first being the nature of the plasma in this device, the second being the dynamics of the confined plasma, and the third being the relevance to Hall thrusters. The most significant property of the plasma in this device is a long Debye length, which has several consequences that will be described in Section 5.2 (briefly described in the preceding paragraph). Other properties of the plasma in this device are presented in Section 5.2, such as self-fields and relevant collision processes, which have consequences for theoretical comparisons, diagnostics, and radial confinement. Section 5.3 investigates the characteristic electron motion within the device including relevant time and length scales and radial trapping characteristics. Also in this section, an analysis of confinement time is presented, based on collisions that would enable electrons to exit the trap radially; it is important to determine the radial confinement time to ensure that the dominant electron flux is axial in the Hall Electron Mobility Gage, especially considering the absence of dielectric walls which provide a physical barrier to radial

Table 5.1: Comparison of plasma parameters and collision frequencies in the Hall Electron Mobility Gage and a Hall Thruster (SPT-100, BPT-2000 or similar[9])

Parameter	Mobility Gage	Hall Thruster
Density		
Electron	$10^9 - 10^{11}$ m^{-3}	$\sim 10^{18}$ m^{-3}
Neutral	$10^{16} - 10^{18}$ m^{-3}	$10^{18} - 10^{21}$ m^{-3}
Ion	$< 10^{11}$ m^{-3}	$\sim 10^{18}$ m^{-3}
Electron Temperature	$10 - 40$ eV	$10 - 30$ eV
Debye Length	$0.100 - 1.5$ m	$10^{-5} - 10^{-4}$ m
Collision Frequency		
Electron-Neutral	$10^3 - 10^5$ s^{-1}	$10^5 - 10^8$ s^{-1}
Electron-Ion	$10^{-2} - 10^{-1}$ s^{-1}	$10^5 - 10^6$ s^{-1}
Electron-Wall	negligible	$10^5 - 10^8$ s^{-1}
Turbulent	negligible (?)	10^6 s^{-1}
Fields		
Electric	$1 \times 10^3 - 1 \times 10^4$ V/m	$2 \times 10^3 - 4 \times 10^4$ V/m
Magnetic	$0.005 - 0.018$ T	~ 0.016 T
$\mathbf{E} \times \mathbf{B}$ Drift Velocity	$1 \times 10^5 - 1 \times 10^6$ m/s	$\sim 2.5 \times 10^6$ m/s
Channel Dimensions		
Inner Radius	110 mm	35 mm
Outer Radius	210 mm	50 mm
Channel Width	100 mm	15 mm
Dynamical Frequency		
Cyclotron (Larmor)	$\sim 2 \times 10^9$ s^{-1} (3×10^8 Hz)	$\sim 2 \times 10^9$ s^{-1} (3×10^8 Hz)
Bounce	1×10^7 Hz	1×10^8 Hz
Magnetron	$1 \times 10^5 - 1 \times 10^6$ Hz	8×10^6 Hz
Thrust	0 mN	~ 80 mN

flux in typical Hall thrusters. The plasma parameters and collision frequencies of the Hall Electron Mobility Gage are presented in Table 5.1 and for comparison, the same parameters are presented for the plasma in the discharge channel of a Hall thruster[9]. Finally, the electron motion within the Hall Electron Mobility Gage is compared with the electron motion in Hall thrusters, showing similar dynamics, despite the substantially dissimilar plasma properties.

5.2 Plasma Parameters

5.2.1 Debye Length

The scaling of the Debye length with other characteristic length scales is of utmost importance when considering self-fields and collective effects such as waves and oscillations within the Hall Electron Mobility Gage. In the non-neutral plasma of the Hall Electron Mobility Gage for the conditions of 10 eV$< T_e <$40 eV (Section 6.3.3); $1 \times 10^9 \text{m}^{-3} < n_e < 1 \times 10^{11} \text{m}^{-3}$ (Section 6.3.2) the Debye length (given by Eq. (2.10)) is in the range of 0.100 m$< \lambda_D <$1.50 m. In all cases the Debye length is on the order of or larger than the characteristic dimensions of the electron trap, as the channel width is 0.100 m and spacing between the electrodes is 0.03 m. Only when electrons first enter the trapping volume at energies $\sim$ 1 eV is the Debye length less than the channel width. In this case electrons gain energy quickly as the field is typically 2-10 V/mm and the Debye length would quickly become larger than trap dimensions outside the immediate vicinity of the trap-loading filament.

There are several consequences to having a long Debye length with respect to plasma dimensions. The most obvious consequence is that external electric fields may penetrate the plasma, as there is no Debye shielding. This fact may suggest that long-range Coulomb forces are important (discussed in Section 5.2.3) as the Coulomb interaction between individual particles is unshielded. However, the dependence of the Coulomb collision cross-section on Debye length (as presented in Section 2.1.2) is logarithmic. The weak, logarithmic dependence and the fact that neutral density is much greater than charged particle density renders Coulomb collisions insignificant, as presented quantitatively in Section 5.2.2. The absence of shielding indicates that the applied external electric field is not significantly shielded by the plasma and thus may be considered rigid and is given by the vacuum solution. This indicates that the plasma contribution to the electric field is negligible, which allows the electric

field to be externally controlled independent of other parameters, most importantly independent of the magnetic field.

A second consequence of the long Debye length concerns collective effects in the plasma. Plasmas exhibit collective behavior such as oscillations and the propagation of waves through the plasma. Because of the properties of the plasma in the Hall Electron Mobility Gage, these plasma behaviors cannot be sustained based on the description presented in Section 2.1.3. It is shown in Section 2.1.3 that the thermal motion of individual particles acts to oppose waves and collective effects where the separation of phenomena (thermal versus collective) exists at the Debye length[57]. On length scales short relative to the Debye length, as in the Hall Electron Mobility Gage, thermal effects dominate the motion and act to damp out any collective oscillations. This is realized by the inequality of Eq. (2.28), in that waves with wavelength shorter than the Debye length will not be sustained by the plasma. Thus, particle motion is governed primarily by thermal motion of particles in externally applied fields. This fact has important implications concerning plasma waves and collective plasma effects that may be sustained within the Hall Electron Mobility Gage. Fundamentally, a long Debye length does not permit sustained plasma waves to exist within the Mobility Gage, an attribute that is imperative in simplifying the plasma environment. Thus, the low-density, high-temperature plasma and resulting long Debye length achieves two purposes in simplifying the Hall thruster plasma environment: 1.) in allowing the electric field to be controlled independently of the magnetic field and 2.) in negating the possibility of fluctuation-induced transport.

5.2.2   Plasma Self-fields

The relative density of electrons and ions is important in determining the space-charge fields experienced by the plasma. Plasmas generally tend to quasi-neutrality where

the ion density is often assumed to be equal to the electron density*. However, if a charged species is introduced into the system from an external source or a species is removed from the system, and the plasma is confined by electric and/or magnetic fields, the plasma may violate quasi-neutrality. The absence of shielding ions results in a self-field (i.e. electrons always repel each other).

In the Hall Electron Mobility Gage external electrons are supplied to the trapping volume, and if no ionizing collisions take place, the plasma will be considered a one-component plasma. If electrons are able to obtain sufficient energy (greater than the ionization potential) from the applied electric field they may suffer ionizing collisions with background neutrals. The ionization potential of argon is 15.7 eV[3], which is the background gas (neutral density 10^{16} to 10^{18} m^{-3}) used in the experiments presented herein (shown in Fig. 2.4). The total energy available from the electric field is 50-300 eV, which greatly exceeds the ionization potential. Because the energy for ionization is available, the ion density may vary greatly, depending on the conditions of pressure, which governs the mean free path, λ_m, for electron-neutral collisions, and magnetic field, which governs the filament-to-anode path length, ℓ_{f-a}, of electrons in the trapping volume. The ion density also may vary depending on the electric field as greater energy is available to primary electrons and also to electrons born in ionizing collisions.

The probability for ionization will be highly dependent on the parameters of pressure, electric and magnetic field. At low pressures and no magnetic field the probability of an electron suffering a collision in the electrode spacing of the confinement volume is extremely small. This may be realized by comparing the mean free path for electron-neutral collisions, λ_m, with the filament-to-anode path length, ℓ_{f-a}. The mean free path for electron-neutral collisions for the lowest pressures investigated, $\lambda_m = 1/(n_0\sigma)$, is greater than 300 m, which is nearly five orders of magnitude larger

---

*Section 3.6 of Ref. [38] provides a good explanation of the applicability of the plasma approximation.

than the anode-cathode electrode spacing. If electrons are unmagnetized they travel on straight-line trajectories from the filament to the anode (a distance of $\ell_{f-a} = 0.03$ m), so there is negligible chance of ionization. In these conditions the relative ion density is expected to be insignificant and the plasma is considered non-neutral (most likely a one-component plasma)[†].

Increasing the magnetic field to the point where electrons are magnetized increases ℓ_{f-a} in the Hall Electron Mobility Gage, where the application of a magnetic field causes electrons to gyrate perpendicular to the magnetic field and drift azimuthally due to the $\mathbf{E} \times \mathbf{B}$ drift. The axial velocity is significantly impeded so that the filament-to-anode path length could approach the mean free path for electron-neutral collisions. The increased path length results in a much higher probability for ionizing collisions. In the limit of strictly classical mobility, the filament-to-anode path length, ℓ_{f-a}, of magnetized electrons in the Hall Electron Mobility Gage must be greater than or equal to the mean free path for electron-neutral collisions, since theoretically electrons are trapped by the magnetic field and will travel within the confinement volume indefinitely until a collision occurs. Even in the case of non-classical mobility it is well known across several disciplines that magnetized electrons in the closed drift have much longer paths than unmagnetized electrons, which would increase probability of ionization[126, 127, 23]. The path length for electrons in the case of anomalous mobility depends highly on the mechanism driving mobility but most anomalous mobility coefficients are found to be at least inversely proportional to B (i.e. an increase in B reduces mobility, which results in a longer confinement time and thus a longer filament-to-anode path length, ℓ_{f-a}).

Increasing the pressure significantly increases the probability for ionizing collisions by reducing the mean free path, λ_m, for electron-neutral collisions. The highest pressures investigated result in a λ_m of 1 m, which is still much larger than the

---

[†]This is loosely described as a plasma as there is no confinement and the plasma body consists only of an electron beam.

anode to cathode electrode spacing, but given an applied magnetic field, this is on the order of the length of an $\mathbf{E} \times \mathbf{B}$ "magnetron" orbit around the channel annulus or on the order of 10 radial "bounces" from the inner radius to outer radius of the annulus along a magnetic field line. (Particle dynamics are discussed in greater detail in Section 5.3.)

Depending on the parameters of pressure, electric field, and magnetic field, the plasma in the Hall Electron Mobility Gage may violate quasi-neutrality, where a space-charge field would exist due to the absence of shielding ions. In the lowest pressures investigated, ionization is expected to be negligible, where the electron self-field would be the greatest. The magnitude of the induced negative space charge is found from a solution to the Poisson equation,

$$\nabla^2 \Phi = \frac{\rho}{\epsilon_0} = \frac{q_e n_e + q_i n_i}{\epsilon_0} \tag{5.1}$$

where Φ is the electric potential and ϵ_0 is the vacuum permittivity. The Poisson equation is generally not used to determine plasma potential in quasi-neutral plasmas (Section 3.6 in Ref. [38]) because of the tendency for plasmas to maintain neutrality except on short time scales. However, the Poisson equation is applicable to non-neutral plasmas[58] because of the strong violation of neutrality due to the collection of like charges.

In the case of low neutral pressure, ion density is assumed to be zero and the Poisson equation becomes

$$\nabla^2 \Phi = \frac{\rho}{\epsilon_0} = \frac{q_e n_e \left(r\right)}{\epsilon_0} \tag{5.2}$$

This analysis presents an upper bound to the space-charge field because the ion density in this argument is assumed to be zero. As described above, ionization is expected to occur under certain conditions, where the presence of ions would act

to reduce the space-charge repulsion. Since the experiments in the Hall Electron Mobility Gage are sensitive primarily to the radial space-charge field (the axial space-charge field is a negligible contribution to the applied electric field), the geometry is approximated as a cylindrical annulus infinite in the z-dimension with inner radius r_{in} and outer radius r_{out}. Thus, the potential becomes a function of radius only due to symmetry in θ and z. If the electron density is assumed to be constant over the volume of the annulus (i.e. $n_e(r) = $ const. $r_{in} < r < r_{out}$) then, integrating Eq. (5.1) twice in cylindrical coordinates (and dividing by n_e), the space-charge potential becomes

$$\frac{\Phi}{n_e} = \frac{q}{4\epsilon_0} \left[r_{out}^2 - r^2 + \left(r_{out}^2 - r_{in}^2 \frac{\ln\left(r_{out}/r\right)}{\ln\left(r_{in}/r_{out}\right)} \right) \right] \tag{5.3}$$

For the physical scale of the apparatus used in the present investigation the maximum potential mid-radius of the annulus is $\Phi/n_e \sim 2 \times 10^{-11}$ V-m^3. This ratio is used to define the maximum theoretical electron density and the maximum "operating" density as follows.

Since electrons are radially confined in an electrostatic potential well (see Section 5.3.1) the maximum theoretical density limit is a function of the potential well depth. The maximum theoretical density is the electron density that would create a potential that would exactly cancel the electrostatic potential well. This maximum density is shown in Figure 5.1 as a dashed line. Above this maximum density the self-field of a one-component electron plasma would overwhelm the confining potential and would be entirely anti-confining. The magnitude of the space-charge field may be made negligible compared to applied fields by adjusting the electron density within the confinement volume. Here it is proposed that if the space-charge potential is on the order of one percent of the confining potential, the space-charge potential may be considered negligible. A solid line is shown in Figure 5.1 indicating a density corresponding to a radial self-field that is one percent of the potential well depth. The potential well is in the range of $10 - 300$ V (described in Section 4.4 and in more detail in Section 5.3.1) over the majority of the confining volume, which varies

112
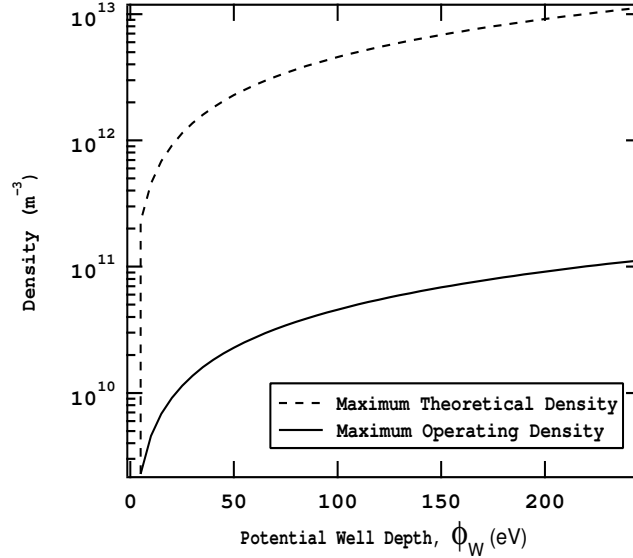
Figure 5.1: Electron density limit for confinement in the Hall Electron Mobility Gage.

with both axial location and applied electric field. Thus, if the electron density were limited by this criterion to $n_e \sim 10^{10} - 10^{11}$ m^{-3} (typical for non-neutral particle traps [112, 124, 128]), then the maximum space-charge potential would be less than one percent of the potential well depth, which would not significantly alter the electron trajectories from those determined by the vacuum electric field alone.[‡]

In the quasi-neutral plasma of a Hall thruster, because the electrons are magnetized and ions are not, the $\mathbf{E} \times \mathbf{B}$ drift causes a Hall current to exist[129]. Likewise, a Hall current exists in the Electron Mobility Gage because of the $\mathbf{E} \times \mathbf{B}$ drift of electrons that creates a magnetic field that opposes the applied magnetic field. This Hall current exists regardless of the ion density, as the ions are unmagnetized and are accelerated axially and do not contribute to the Hall current. Assuming uniform density throughout the trapping volume, which is limited to $10^{10} - 10^{11}$ m^{-3} as described

---

[‡]During the course of experiments electron density was monitored using a planar Langmuir probe (described in Section 6.3.2), and the emission characteristics of the tungsten injection filament (described in Section 4.4 and 6.3.2) were controlled to limit the electron density. Proof of the ability to control electron density is presented in Chapter 6.

above, the magnetic field induced by the Hall current is on the order of 1×10^{-11} Tesla, which is negligible compared to the 0.01-Tesla applied magnetic field. Thus, the magnetic and electric fields are considered rigid and are given by the vacuum solution.

5.2.3 Collisions

In the Hall Electron Mobility Gage electrons may collide with neutrals, ions, or other electrons. It was found that electron-neutral collisions are primarily responsible for the momentum scattering of electrons, and electron-electron and electron-ion collisions provide insignificant contributions to directional scattering. It was found, however, due to their similar mass, electron-electron collisions contribute in part to the energy exchange of electrons within the Hall Electron Mobility Gage. Each of these are presented in greater detail below and assessed for their contribution to classical cross-field electron mobility and energy transfer. This section is not intended to be an exhaustive kinetic description of collisions within the Hall Electron Mobility Gage, but only presents order of magnitude estimates in order to gauge the relative importance of collision species for momentum and energy transfer.

Electron-neutral Collisions. Equation (2.31) was used to determine the collision frequency for electron-neutral collisions. The density of neutrals may be controlled by the flow rate of the background gas (described in Section 6.2.2). The neutral density may be found from the ideal gas law:

$$n_0 = \frac{p}{RT} \tag{5.4}$$

Using Eq. (5.4), background pressures of $10^{-6} - 10^{-4}$ Torr correspond to neutral densities in the range of 10^{16} to 10^{18} m^{-3} (using $T = 298$ K). The cross-section

for momentum-transfer electron-neutral collisions was found from the Siglo database (argon cross sections are shown in Fig. 2.4), and for the approximate electron temperature within the confinement volume (~ 20 eV) the cross section was estimated to be $\sim 9 \times 10^{-20}$ m^2. Based on a Maxwellian distribution the average electron velocity ($\bar{v} = \sqrt{8kT/\pi m}$) is 3×10^6 m/s, given an electron temperature of 20 eV. Equation (2.31) then results in a momentum-transfer electron-neutral collision frequency in the range of $\nu_{en} = 10^3$ to 10^5 s^{-1} for the conditions investigated. (The electron-neutral collision frequency of Hall thrusters is on the order of $\nu_{en} = 10^5$ to 10^8 s^{-1}.) Electron-neutral collisions lead to significant momentum transfer of electrons (i.e. significant directional changes) but result in very little energy transfer per collision because of the large disparity in mass. The energy transferred in elastic collisions is proportional to $mM/(m+M)^2$ [62] where m and M are the masses of colliding particles. If $m \ll M$ (as with electrons and argon atoms) the energy transfer is proportional to the mass ratio between electrons and neutrals, which for argon is on the order of $m_e/M_{Ar} = 10^{-5}$. The *rate* of energy transfer depends on the energy transferred per collision ($\delta\epsilon$) times the collision frequency, ν_{ee}, which is $(\delta\epsilon)\,\nu_{ee} = 10^{-2}E_0$ to $10^0 E_0$ J/s, where E_0 is the initial kinetic energy of electrons.

Electron-ion Collisions. The electron-ion collision frequency was found using Eq. (2.61). An estimate of the maximum ion density is needed to quantify the electron-ion collision frequency and may be obtained by the following method. Because electrons are supplied externally and electron-ion pairs may be created within the confinement volume, the total electron current ($I_e = qAn_e u_{ez}$) must be greater than or equal to the ion current ($I_i = qAn_i u_{iz}$), where $qAn_e u_{ez} \geqslant qAn_i u_{iz}$. With this in mind, the relative ion density to electron density may be estimated by comparing the axial velocity of each species, where

$$n_i \leqslant (u_{ez}/u_{iz})\,n_e \tag{5.5}$$

The axial velocity of ions accelerated through a potential (neglecting ion-neutral collisions), ϕ, is given by

$$u_{iz} = \sqrt{\frac{2e\phi}{m_i}} \tag{5.6}$$

Assuming uniform ion production over the region of the Hall Electron Mobility Gage confinement volume, the average axial velocity of ions may be estimated as being accelerated through half the total anode-to-cathode voltage where

$$u_{iz} = \sqrt{\frac{eV_{ac}}{m_i}} \tag{5.7}$$

For an anode-to-cathode voltage of $V_{ac} = 100$ V, this corresponds to an axial velocity of 1.5×10^4 m/s. Classical and Bohm mobility may provide a lower and upper bound of electron velocity, respectively, to bracket the axial electron velocity. The axial velocity of electrons due to classical mobility, using Eq. (2.52) and Eq. (1.1), an electric field of 3×10^3 V/m and magnetic field of 0.01 T, was found to be in the range of 0.2 to 20 m/s (for the range of momentum-transfer collision frequency described above). The axial velocity of electrons due to Bohm mobility, using Eq. (2.65) and Eq. (1.1), was found to be 2×10^4 m/s. By using the Bohm mobility for axial electron velocity, the inequality in Eq. (5.6) becomes $n_i \leqslant (1.3) n_e$ and thus ion density was found to be at most on the same order as the electron density. As described in Section 5.2.2, the electron density should be limited to $\sim 10^{10}$ to 10^{11} m^{-3}. Therefore, a maximum ion density of 10^{10} to 10^{11} m^{-3} was assumed. For a Debye length of 0.33 m, (calculated using an approximate electron density of 10^{10} m^{-3} and electron temperature of 20 eV), the resulting Coulomb logarithm is ~ 22 (Eq. (2.56))[§]. The electron-ion collision frequency was then calculated using Eq. (2.61) (and Eq. (2.60)), assuming singly charged ions, and was found to be in the range of 10^{-2} to 10^{-1} s^{-1}. Figure 5.2 shows the Coulomb collision frequency for electron-electron and electron-ion collisions (which are equal for $n_e \sim n_i$ and singly charged

---

[§]Because of the logarithmic dependence the Coulomb logarithm varies very little over all parameters within the Hall Electron Mobility Gage where $21 \lesssim \ln \Lambda \lesssim 23$.
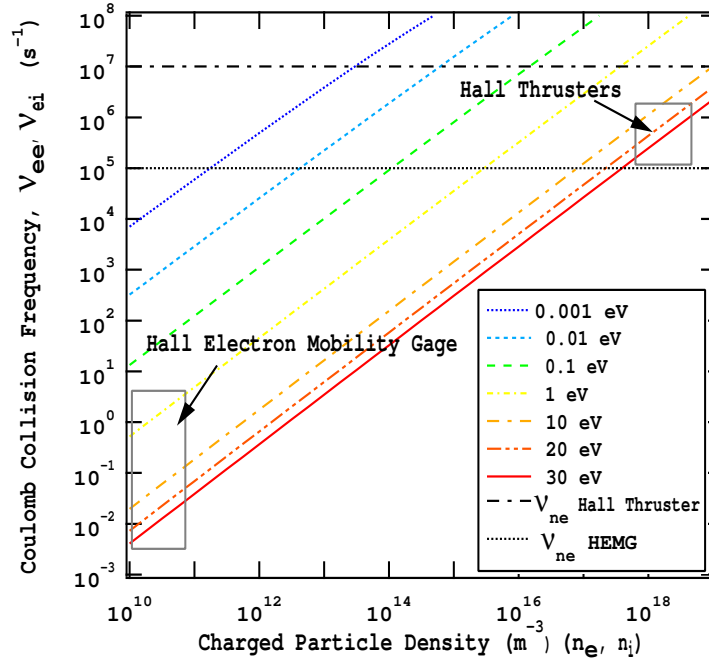
Figure 5.2: Coulomb collision frequency as a function of electron or ion density (assuming single ionization) for electron-electron and electron-ion collisions. Colors indicate incident electron energy.

ions) for a range of electron temperatures[¶]. The collision frequency for electron-ion collisions was found to be much less than that of electron-neutral collisions and has been thus neglected in any calculation of classical momentum-transfer collision frequency. Electron-ion collisions also were found to be negligible in energy transfer compared with electron-neutral collisions, as the low collision frequency combined with the small energy transfer per collision resulted in an energy transfer rate on the order of $10^{-7}E_0$ to $10^{-6}E_0$ J/s.

Electron-electron Collisions. As described in Section 2.2.3, electron-electron collisions do not contribute to electron transport because the momentum effects of the like-particle collision exactly cancel (also described in Ref. [38], p. 177). However, an appreciable energy exchange occurs in each electron-electron collision due to the

---

[¶]$\ln \Lambda$ was estimated to be ~ 20 since for Hall Thrusters $\ln \Lambda \sim 17$ and for the Hall Electron Mobility Gage $\ln \Lambda \sim 22$. Certainly this estimate does not affect the order of magnitude of the collision frequency for either and provides a good estimate for comparison.

equivalent mass of colliding species. The energy exchange in electron-electron colli-
sions is proportional to $mM/(m + M)^2$, where $m = M = m_e$, so the energy transfer
per collision is on the order of $(1/4)E_0$. For an electron density of 10^{10} to 10^{11} m^{-3},
electron temperature of 20 eV, and a Coulomb logarithm of 22, the electron-electron
collision frequency was determined to be in the range of 10^{-2} to 10^{-1} s^{-1}. The rate
of energy exchange is then on the order of $10^{-3}E_0$ to $10^{-2}E_0$ s^{-1}. For the lowest
neutral densities and highest electron densities the energy exchange due to electron-
electron collisions is on the same order as that of electron-neutral collisions, but under
most conditions electron-electron collisions may be considered negligible in terms of
energy-transfer.

Because the effects of the Coulomb interaction fall off so quickly with both in-
creasing temperature (average particle velocity) and decreasing density, electron-ion
Coulomb collisions provide negligible momentum transfer for this sparsely populated,
high-temperature plasma. Because like-particle collisions do not contribute to a net
momentum transfer, electron-electron collisions are also insignificant for momentum
scattering. Thus, the dominant momentum transfer mechanism is through electron-
neutral collisions. Energy transfer within the Hall Electron Mobility Plasma takes
place on a much longer time scale than momentum transfer, where electron-neutral
and electron-electron collisions may both contribute to electron energy exchange but
result in an energy transfer rate, which is much lower than the momentum transfer
collision frequency. The importance of these differing time scales is emphasized in
Section 5.3.2.

5.3   Electron Dynamics

The magnetic field within the Hall Electron Mobility Gage impedes axial electron
motion; however, electrons freely move parallel to the magnetic field lines. Without
some type of radial confinement, analogous to the dielectric walls found at the inner

and outer channel of a Hall thruster, electrons would be lost radially. In order to evaluate cross-field electron mobility, the radial losses must be small so that the dominant electron flux is axial, through cross-field electron mobility, rather than radial along field lines. The radial confinement is achieved by a confining electrostatic potential at the trap inner and outer radii, due to the departure of electrostatic equipotential lines from magnetic field lines (at the edges of the confinement volume). This confinement is enhanced by a magnetic mirror due to increasing B_r near the iron pole faces. A schematic of a particle trajectory within this confinement scheme is shown in Fig. 5.3. The following sections outline the radial confinement mechanism(s), quantify a radial confinement time in order to compare radial loss rate with the axial transport rate, and describe the resulting electron motion within the Hall Electron Mobility Gage. The analysis in Sections 5.3.1 and 5.3.2 was published in part in Ref. [119].
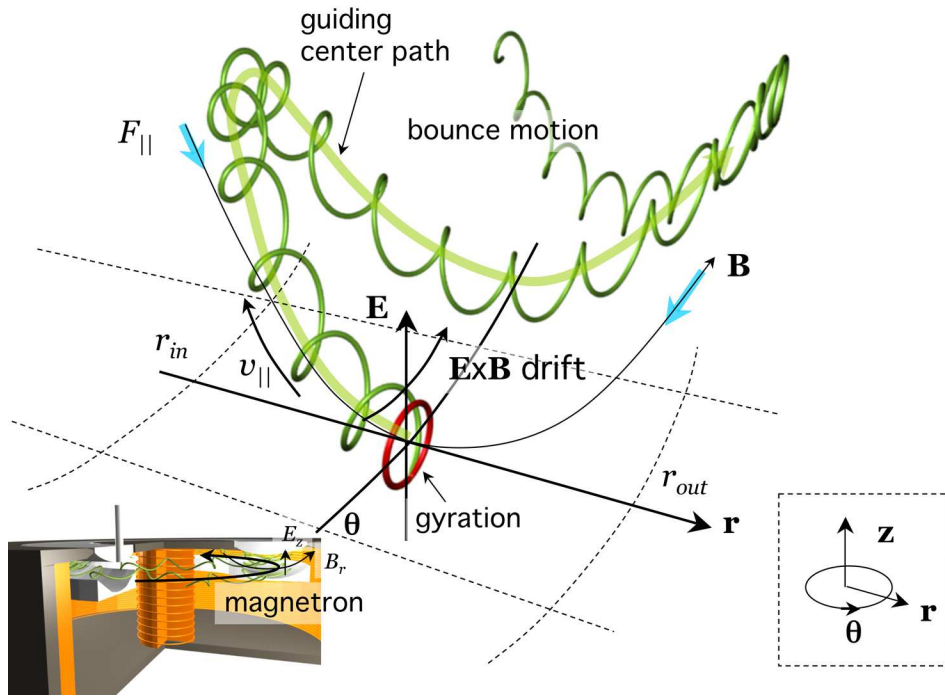
Figure 5.3: Schematic representation of an electron trajectory within the potential well of the Hall Electron Mobility Gage (top) and an axial view of the guiding center trajectory within the channel annulus (bottom). Orientation is shown in the bottom right of each. Trajectories are not shown to scale.

5.3.1 Radial Confinement Characteristics

Since electrons are thermally mobile along magnetic field lines, the forces acting on electrons in the direction of the magnetic field are important in determining radial confinement. The total net force (confining and anti-confining) needs to be confining to create a potential well where the magnitude of the potential is greater than thermal energy of electrons. The thermal velocity and space charge repulsion would act to oppose confinement and the electric field force and magnetic mirror force would act to enhance confinement of particles. The space charge was addressed in Section 5.2.2 and may be considered negligible if the electron density is limited. Thus, this section investigates the confining forces electrostatic and magnetic mirror, (described qualitatively in Section 4.3) to determine their effectiveness of confinement compared with the electron thermal velocity, which acts to oppose confinement.

In the Hall Electron Mobility Gage, electrons are radially confined based on both the direction and magnitude of their velocity vectors. The velocity vectors that would result in confinement and losses may be mapped in velocity "space" to show regions that are confined or lost. The confinement "space" in the Hall Electron Mobility Gage may best be understood by inspection of the magnetic mirror confinement, which is strictly direction dependent, and then expanded to include the electrostatic potential well confinement, which is both direction and energy dependent.‖

Within a simple magnetic mirror there exists a region in velocity space, the loss cone, where if velocity trajectories lie within this region, the particle is no longer confined by the magnetic mirror. (This concept was described in detail in Section 2.1.2 and the simple loss cone shown in Fig. 2.3) The loss cone is defined by the angle of the velocity vector, θ_m, which is the minimum pitch angle an electron may have and still be confined by the magnetic mirror. The loss cone angle is a function

---

‖The radial confinement scheme of the Hall Electron Mobility Gage resembles that of a magnetic mirror trap with electrostatic "end-stoppers" [130].

of the mirror ratio, R_m, which is defined as the ratio of maximum magnetic field to minimum magnetic field. In the configuration of the Hall Electron Mobility Gage, the mirror ratio was found to be ~ 2 and the resulting loss cone was found to be $\theta_m \sim 45°$.

Trapping by magnetic mirrors is not a new concept, and in fact has been used with much success in trapping positrons and other high temperature particles and plasmas [45, 131, 130]. However, confinement times in magnetic mirrors are limited, as particle velocities are directionally scattered by collisions. Particles whose trajectories may be initially trapped will eventually undergo a collision process where the resulting velocity trajectories are scattered in velocity space such that they eventually fall within the loss cone. Numerous investigations have been undertaken to quantify this process[45, 131, 130], and it is generally accepted that a simple magnetic mirror configuration can not feasibly trap particles for much more than a 90° collision time. (A 90° collision may be either a large angle scattering event, such as an electron-neutral collision, or the cumulative effect of many small angle deflections totaling 90°, as in Coulomb collisions, both outlined in Section 2.2.3.) In the Hall Electron Mobility Gage, scattering into the region of velocity space within the magnetic mirror loss cone occurs within a few collisions, which does not provide an effective radial trap, as tens of collisions are required for an electron to move through the trap axially by classical mobility. However, many magnetic mirror geometries also incorporate electrostatic confinement to enhance the confining magnetic mirror[130], where this concept is also exhibited in the Hall Electron Mobility Gage.

An electrostatic potential well is created by an electrostatic force acting parallel to the magnetic field due to the departure of electric equipotential lines and magnetic field lines at the confinement volume periphery. This is explained in Section 4.3. The magnitude of the potential well, given by ϕ_w, is equal to the potential difference between the local potential at the center of the confinement volume annulus and the cathode. To demonstrate the incorporation of an electrostatic potential well in

addition to the magnetic mirror confinement, the analysis of a velocity space loss cone is extended to include the fact that radial losses from the confinement volume depend on velocity *magnitude* as well as direction. The new velocity space "loss region" is determined similarly to the original loss cone presented in Section 2.1.2 except the conservation of energy equation (Eq. (2.7)) is replaced by[130]

$$\frac{mv_0^2}{2} = \frac{mv_\perp'^2}{2} + e\phi_w \qquad (5.8)$$

The additional term $e\phi_w$ is the depth of the electrostatic potential well (expressed in terms of energy) given by the potential difference, ϕ_w, between the local potential at the center of the trap on a given magnetic field line and the cathode potential (as described in Section 4.3). The parallel component of velocity necessary to overcome this confining potential and exit the trap (via collision with the iron pole) is given as the critical velocity,

$$v_c = \sqrt{2e\phi_w/m}. \qquad (5.9)$$

Combining equations (2.6) and (5.8) and solving for $v_0^2/v_{0\perp}^2$ gives

$$\sin^2\theta_c = \left\{ \begin{array}{ll} \left(1 - v_c^2/v_e^2\right)/R_m & v_e \geqslant v_c \\ 0 & v_e < v_c \end{array} \right\} \qquad (5.10)$$

where v_e is the magnitude of the electron velocity. This results in a loss region that is represented as a hyperboloid, which is velocity magnitude and direction dependent, shown in Fig. 5.4. The velocity space loss region is important in determining the radial confinement time of electrons within the Hall Electron Mobility Gage.

5.3.2   Radial Confinement Time

Electrons that are radially confined within the Hall Electron Mobility Gage could eventually be scattered into the velocity-space loss region (Fig. 5.4) by collisions

123
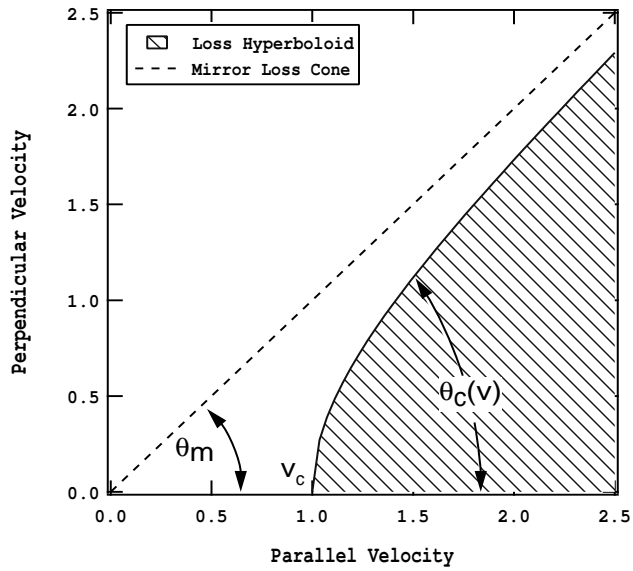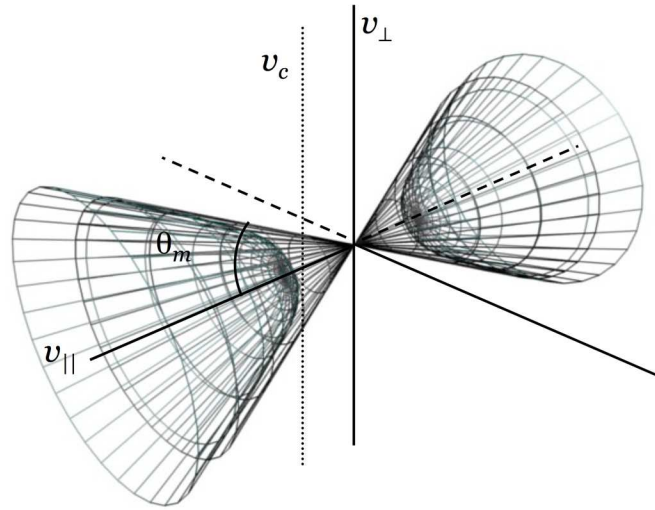
Figure 5.4: Magnetic mirror loss cone and magnetic/electrostatic loss hyperboloid shown in three dimensions (above) and two dimensions normalized for $v_c = 1$(below).

124

giving rise to a finite radial confinement time. Numerous analyses of collisional losses in magnetic mirrors are available concerning fully-ionized plasmas where small angle deflections due to Coulomb interactions have a much greater effect than large angle scattering (electron-neutral) collisions[45, 130]; this is because most plasmas confined using magnetic mirrors are fully ionized and the neutral density is negligible. These analyses investigate collisional losses as a diffusion process in velocity space, as small angle collisions produce a "random walk"-type process of velocity trajectories[130, 45], most often using the Fokker-Planck[52, 51] model to describe the effect of collisions on the changes in the velocity distribution. However, in a partially ionized plasma, like that within the Mobility Gage, the dominant scattering mechanism is large-angle scattering by electron-neutral collisions. A "random-walk" diffusion in velocity space is not applicable, as the final direction of the velocity vector is unrelated to the initial direction of the velocity vector, in electron-neutral collisions. (The reader is directed to Section 2.1.2 on the kinetic treatment of the Boltzmann collision term and Section 5.2.3 on relevant collision dynamics). Therefore, an analysis of confinement time where large-angle scattering events are the dominant loss mechanism is necessary in this case.

In the analysis presented here the electron flux into the loss region (i.e. radial losses) is investigated in order to determine a radial confinement time. A summary of the derivation is presented as follows. First, the BGK (Bhatnagar-Gross-Krook) model[50] was used to obtain an equation for the velocity distribution as a function of time due to large-angle scattering collisions. The BGK model accounts for randomized events that act to deplete one distribution and repopulate another. Within this equation are the initial (non-Maxwellian) and final (Maxwellian) velocity distributions. The initial velocity distribution was derived given confinement properties of the Hall Electron Mobility Gage and was substituted into the BGK model along with the final Maxwellian distribution. This resulted in an equation for the time evolution of the velocity distribution from time $t = 0$ to ∞ due to collisions (the Boltzmann

collision term). Recognizing that the Hall Electron Mobility Gage would be operated in steady state and the loss region would always be empty (total relaxation to a Maxwellian distribution would never be achieved; the "empty loss cone" assumption is described in more detail in the following paragraph), the loss of electrons from the confinement volume was obtained by investigation of the change in the distribution at time $t = 0$, which represents the time when the loss region would be empty. The confinement time was then determined as the density divided by the volumetric flux of electrons exiting the confinement volume, and the radial confinement time was compared to the axial confinement time (time it takes for an electron to traverse the confinement volume axially from cathode to anode). It was found through this analysis that radial losses would be very small so that the primary electron flux would be axial. The details of this derivation are presented below.

For simplification, within this derivation an electron whose trajectory has been scattered into the loss region has been considered permanently "lost" from the confinement volume (recombined at the magnetic poles) and effects such as secondary electron emission from the magnetic poles were neglected. Because particle transit times (radially) across the physical confining volume were found to be short compared with collision times, a particle that had been scattered into the loss cone was assumed to be lost before it could scatter again and re-enter the confining volume. Therefore, the velocity space loss region was assumed to be empty in steady state operation of the Hall Electron Mobility Gage. A similar description of a strongly depleted loss region was presented by Kaganovich *et al.*[23]. The type of distribution resulting from an empty loss region is non-Maxwellian as there are voids in velocity space in both direction and magnitude. Scattering collisions have the effect of replenishing these voids in velocity space, as collisions drive a distribution to a Maxwellian state. Since particles in the loss region have been assumed to immediately exit the trap (they have zero lifetime in the loss region) the flux of particles exiting the trap was found from investigation of the flux of particles into the loss region. This flux of electrons

126

was determined by an analysis of the relaxation of the initial non-Maxwellian distribution function within the confinement volume (in velocity space), to a Maxwellian distribution as collisions populate the loss region.

In Section 5.2.3 it was noted that the time for significant momentum transfer (directional scattering) was found to be much shorter than the time for significant energy transfer to occur. For the purposes of simplification, the energy relaxation[**] is taken to occur on the same time scale as directional scattering. This approximation provides an upper bound to the flux of electrons from the confining volume, as the filling of the high-energy Maxwellian tail (which is responsible for losses) will occur more slowly than this approximation assumes.

The Boltzmann collision term in the BGK approximation (sometimes referred to as the Krook collision operator) is given by:

$$\frac{\delta F(t, \mathbf{r}, \mathbf{v})}{\delta t} = -\frac{F(t, \mathbf{r}, \mathbf{v})}{\tau_F} + \frac{F_0(t, \mathbf{r}, \mathbf{v})}{\tau_0} \tag{5.11}$$

where F is the actual phase space distribution of the system and F_0 is a Maxwellian distribution[††] . This equation physically means that the non-equilibrium distribution function, F, loses particles exponentially on a time scale of τ_F and these particles are replaced by a Maxwellian distribution, F_0, on a time scale of τ_0. Assuming a uniform spatial distribution of particles, the spatial term, $\mathbf{r}$, is dropped for the remainder of this section, and the only concern is with the distribution of velocities. From here, any reference to "space" and "volume" only refers to regions of velocity space. The solution to the ordinary differential equation (Eq. 5.11) given an initial velocity distribution of F_{in} at $t = 0$ is

---

[**]Energy relaxation refers to the process by which the energy exchange during collisions causes the energy distribution to assume a Maxwellian. The energy relaxation time is generally defined as a characteristic time over which this process takes place.

[††]F is used rather than f to signify that this distribution is not normalized to 1, rather, it is normalized to n where $\int_\infty F d^3 v = n$.
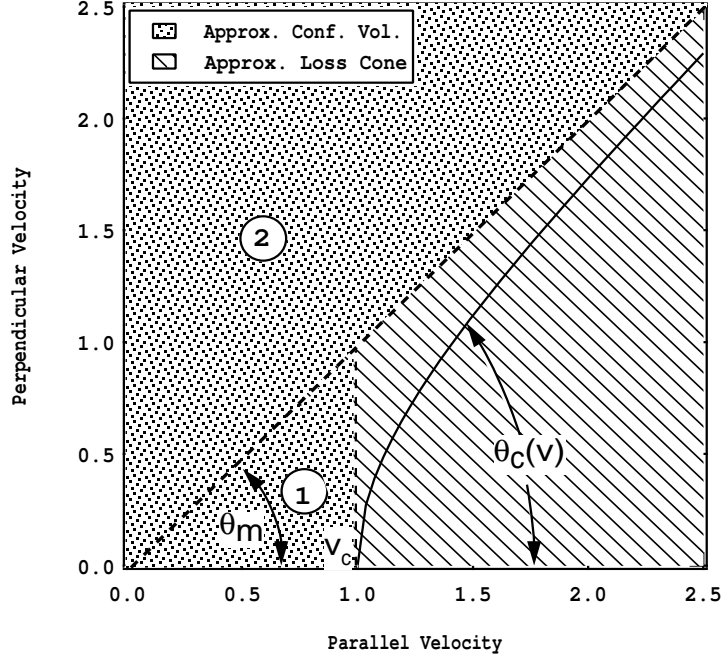
Figure 5.5: Approximated confinement and loss regions for confinement time analysis

$$F(t, \mathbf{v}) \;=\; F_0(\mathbf{v}) + [F_{in}(\mathbf{v}) - F_0(\mathbf{v})] \exp\left(-\frac{t}{\tau_0}\right) \tag{5.12}$$

assuming $\tau_F = \tau_0$. The initial velocity distribution function is given by

$$F_{in}(\mathbf{v}) \;=\; \left\{ \begin{array}{cc} 0 & \text{in the loss region} \\ \text{Maxwellian} & \text{in confinement region} \end{array} \right\} \tag{5.13}$$

The confinement volume and loss region are approximated as shown in Fig. 5.5 for geometric and mathematical simplification (without this simplification an analytical solution would not be possible). The actual loss region is smaller than this approximation so confinement time determined using this approximation would result in a conservative estimate.

In the confinement region the initial speed distribution[‡‡] for $\theta_m > \theta > \pi - \theta_m$

[‡‡]The speed distribution is illustrated here as the confinement depends on the absolute magnitude

128
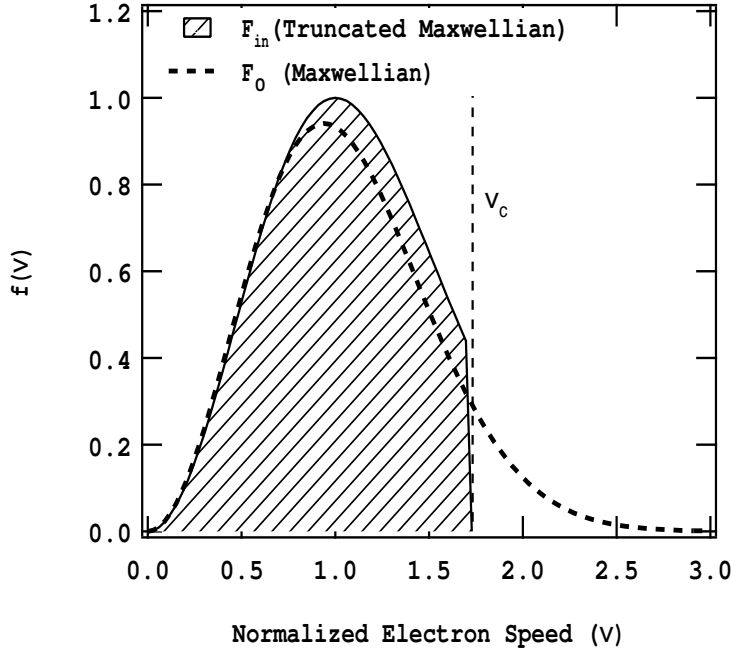
Figure 5.6: Initial (truncated Maxwellian) and final (Maxwellian) speed distributions for $\theta < \theta_m$.

(Region 2, in Fig. 5.5) is given by a Maxwellian (all speeds are confined for this range of pitch angle) and for $\theta < \theta_m$ (Region 1, in Fig. 5.5) the initial distribution is given by a truncated Maxwellian speed distribution, shown in Fig. 5.6 , where the function is Maxwellian for $v < v_c$ and zero for $v > v_c$.

In the velocity-space confinement region the velocity distribution is given by

$$F_{in}(\mathbf{v}) \;=\; An \left(\frac{\beta}{\pi}\right)^{3/2} \exp(-\beta v^2) \tag{5.14}$$

where $\beta = m_e/(2kT_e)$ and A is a normalization constant. To find the normalization constant it is recognized that particles only exist in the confinement region (the loss region is empty) so integrating over only the confinement region will normalize

---

of the velocity given a particular pitch angle, θ.

the function to n.

$$n = \iiint_\infty d^3v F_{in} = \iiint_{conf.vol.} d^3v F_{in} = \int_0^{2\pi} d\phi \int_0^{\theta_m} 2\sin\theta d\theta \int_0^{v_0} F_{in} v^2 dv$$
$$+ \int_0^{2\pi} d\phi \int_{\theta_m}^{\pi-\theta_m} \sin\theta d\theta \int_0^\infty F_{in} v^2 dv$$

$$(5.15)$$

In this integration, the first and second volume integrals are the integrals over regions 1 and 2 (Fig. 5.5), respectively and the upper bound $v_0 = v_c/cos\theta_c$. Evaluating the integrals gives a normalization constant of

$$A = \left\{ \left[\frac{-2v_c}{\sqrt{\pi}v_{||}} \exp\left(\frac{-v_c^2}{v_{||}^2}\right) + \mathrm{erf}\left(\frac{v_c}{v_{||}}\right) - 1 \right] (1 - \cos\theta_m) + 1 \right\}^{-1} \qquad (5.16)$$

where $v_{||}$ is the parallel thermal velocity of an electron. Thus, the total initial distribution is given by

$$F_{in}(\mathbf{v}) = \left\{ \begin{array}{ll} 0 & \text{in the loss region} \\ An\left(\frac{\beta}{\pi}\right)^{3/2} \exp(-\beta v^2) & \text{in the confinement region} \end{array} \right\} \qquad (5.17)$$

where the loss region is represented by $v > v_c$ and $(\theta < \theta_m$ or $\theta > \pi - \theta_m)$ and the confinement region is represented by $\theta_m < \theta < \pi - \theta_m$ or $v < v_c$.

The initial distribution relaxes to a Maxwellian distribution, F_0, as collisions scatter particles into the empty region of velocity space vacated by the loss cone, where

$$F_0(\mathbf{v}) = n\left(\frac{\beta}{\pi}\right)^{3/2} \exp(-\beta v^2) \qquad (5.18)$$

Substituting these into Eq. (5.12) gives the distribution function as it relaxes in

130

time:

$$
F(t, \mathbf{v}) \;=\; \left\{ \begin{array}{ll} n \left(\frac{\beta}{\pi}\right)^{3/2} \exp(-\beta v^2) \left(1 + (A-1)\exp(-\frac{t}{\tau_0})\right) & \text{loss region} \\[2mm] n \left(\frac{\beta}{\pi}\right)^{3/2} \exp(-\beta v^2) \left(1 - \exp(-\frac{t}{\tau_0})\right) & \text{confinement region} \end{array} \right\}
$$
(5.19)

Therefore, the Krook collision operator is given by

$$
\frac{\delta F(t, \mathbf{v})}{\delta t} \;=\; \left\{ \begin{array}{ll} n \left(\frac{\beta}{\pi}\right)^{3/2} \exp(-\beta v^2)\frac{1}{\tau_0}\exp(-\frac{t}{\tau_0}) & \text{loss region} \\[2mm] n \left(\frac{\beta}{\pi}\right)^{3/2} \exp(-\beta v^2)\frac{(A-1)}{\tau_0}\exp(-\frac{t}{\tau_0}) & \text{confinement region} \end{array} \right\}
$$
(5.20)

The time derivative of the distribution function at time $t = 0$ describes the change in the distribution at the time that the loss cone is empty. In the confinement volume considered in the Hall Electron Mobility Gage, all particles in the loss cone will immediately disappear from the trap, thus the loss cone is always empty and the time derivative of F at $t = 0$ corresponds to the steady-state change in the distribution function assuming that the distribution within the confinement region remains constant (replenished by the electron loading source) due to steady-state operation. Ultimately, the goal in this analysis is to quantify the flux of particles from the confinement region (Regions 1 and 2 in Fig. 5.5) to the loss cone. Flux in velocity space may be understood by an analogy to flux in configuration space. (This elegant math trick was provided by Ref. [132].) By density conservation in configuration space

$$
\frac{\partial n(\mathbf{x}, t)}{\partial t} \;=\; -\nabla \cdot \Gamma
$$
(5.21)

where Γ is particle flux. By analogy in velocity space where $\mathbf{J}_v$ is given to be the flux

$$
\frac{\partial F(\mathbf{v}, t)}{\partial t} \;=\; -\nabla_v \cdot \mathbf{J}_v
$$
(5.22)

where F may be thought of as the "velocity-space density." A volume integral in velocity space may be applied to make use of Gauss' theorem to convert the volume

integral of this divergence to a surface integral of the flux

$$\int\limits_{conf.vol.} d^3v \frac{\partial F(t, \mathbf{v})}{\partial t} = -\int\limits_{conf.vol.} d^3v \nabla_v \cdot \mathbf{J}_v = \int\limits_{loss\ region} d\mathbf{S}_v \cdot \mathbf{J}_v \qquad (5.23)$$

This results in the surface integral of a flux, which in this case represents the flux of particles in velocity space through the loss cone surface, or equivalently, the particle loss rate from the confinement volume. Thus, the flux of electrons from confined velocity space to the loss cone at $t = 0$ is found by evaluating the volume integral of the distribution function, F, over the confinement volume

$$\int\limits_{conf.vol.} d^3v \frac{\partial F(t, \mathbf{v})}{\partial t} = -\frac{n}{\tau_0} \frac{(A-1)}{A} \qquad (5.24)$$

This flux is negative representing flux out of the confinement volume. The average confinement time of a particle, then, is given as the density over the flux

$$\tau_p = \frac{\tau_0 A}{(A-1)} \qquad (5.25)$$

Various limits of the confinement time may be investigated by inspection of Eq. (5.25). Inspection of A reveals that particle confinement time is a function of the simple magnetic mirror loss cone angle, θ_m (since the loss region has been approximated), critical velocity to overcome the electrostatic potential, v_c, and the velocity parallel to the magnetic field, $v_{||}$. Here various limits become apparent. It may be seen that as θ_m approaches zero, $A = 1$, giving zero flux and an infinite particle confinement time. Physically, this limit means the loss region volume approaches zero and thus the entire velocity space is a Maxwellian in its initial state (i.e. no relaxation). Another interesting limit is when $v_c/v_{||} \ll 1$, $A = 1/\cos\theta_m$ which is equivalent to the solution of the BGK relaxation for a magnetic mirror confinement without electro-

static confinement (i.e. Region 1 in Fig. 5.5 is included in the loss region). Finally, when $v_c/v_{||} \gg 1$, A approaches unity, giving small flux and a particle confinement time that approaches infinity. This limit physically means that if the electrostatic confining potential is much greater than the thermal velocity of electrons, the losses are very small. The magnitude of the parameter, $v_c/v_{||}$, is critical when investigating particle confinement times in the Hall Electron Mobility Gage (i.e. a large $v_c/v_{||}$ results in long confinement times).

Particle confinement times in the Mobility Gage vary based on the mirror ratio, the depth of the electrostatic potential well, and the thermal velocity of electrons. Since the geometry of the apparatus is fixed, the magnetic mirror ratio (and thus loss cone angle, θ_m) is constant, but v_c and $v_{||}$ change with both anode-to-cathode voltage and with position within the trap. The normalization constant and confinement times versus $v_c/v_{||}$ are plotted in Fig. 5.7. Confinement time is given in terms of $\tau_p \nu_{en}$; this number physically represents the average number of scattering collisions an electron may undergo and still be confined by the trap. A minimum ratio, $v_c/v_{||}$, may be calculated to determine the minimum radial particle confinement time expected within the Hall Electron Mobility Gage. The velocity needed to overcome the potential difference between the local potential and the cathode electrode is also the maximum energy available to electrons starting at the cathode. If an electron gains all of the energy available from the field, the maximum parallel thermal energy of the electron is $e\phi_w/3$[§§], corresponding to a velocity of $\sqrt{2e\phi_w/3m_e}$; thus, the lower limit is $v_c/v_{||} = \sqrt{3}$. Therefore the minimum value of $A = 1.03$, which corresponds to $\tau_p \nu_{en} = 34.3$.

In the case of minimum $v_c/v_{||}$, radial losses are shown to be fairly insignificant as the confinement time is significantly greater than the scattering time (i.e. $\tau_p \nu_{en} > 1$). The radial losses are expected to be even more insignificant than depicted by the

---

[§§]The total energy is $e\phi_w$, which in a thermalized distribution corresponds to $3kT/2$. The energy parallel to the magnetic field is $kT/2$ because of equipartition of energy, which corresponds to an energy of $e\phi_w/3$.

minimum $v_c/v_{||}$. The radial confinement time is expected to be greater than the minimum confinement time for several reasons: 1.) Electrons are loaded into the trap potential well with very little energy at a location where the depth of the potential well is greater than the average electron energy (rather than electrons starting at the cathode where the potential well does not exist). This is described in more detail in Sections 4.5 and 6.3.5. 2.) Electrons are expected to have sufficient energy to suffer inelastic collisions, either excitation or ionizing, so electrons lose energy on the order of the excitation/ionization threshold in an inelastic collision thereby "cooling" the electron population. 3.) The volume approximation for confinement and loss regions was conservative where the approximation overestimated the loss region. The actual loss region is smaller than was approximated. 4.) In this analysis, the energy relaxation time (time to fill the Maxwellian tail of the distribution) was taken to occur on the same time scale as the directional scattering time. Electrons were found to suffer collisions with neutrals much more frequently than with other electrons so the time for significant energy transfer during collisions is 5 orders of magnitude less than the time for significant momentum transfer. This was presented in more detail in Section 5.2.3. Particles enter the loss region through direction *and* energy changes; if energy changes are much smaller and/or less frequent than estimated by the BGK approximation, the model has overestimated the radial particle flux. Based on these considerations, in the operation of the Hall Electron Mobility Gage the radial confinement time is expected to be long compared to the momentum transfer collision frequency (i.e. $\tau_p \nu_{en} \gg 1$). As an example, for data obtained (presented in Chapter 6) in the case of $\phi_w = 134$ V, an electron temperature of $T_e = 28$ eV was measured by a planar probe. In this example, $v_c/v_{||} = 3.09$ corresponding to $\tau_p \nu_{en} = 1.3 \times 10^4 \gg 1$, indicating that radial losses are negligible.

5.3.3 Characteristic Single Particle Motion

Based on the motion in magnetic and electric fields presented in Chapter 2 along with the confinement outlined above, the resulting characteristic motion within the Hall Electron Mobility Gage may be considered by four modes: a gyration perpendicular to the magnetic field, a radial bounce within the potential well, an azimuthal drift (the three of these shown in Fig. 5.3), and an axial mobility.

The highest frequency motion is the electron gyro-frequency, which is given by Eq. (2.2). In the Hall Electron Mobility Gage the electron gyro-frequency was found to vary from 5.3×10^8 to 3.2×10^9 s^{-1} (8×10^7 to 5×10^8 Hz) for magnetic fields varying from 0.003 to 0.018 Tesla. The Larmor radius was found to be in the range of 1 to 5 mm for an electron temperature of 20 eV. The second mode of electron motion is the thermal motion along the magnetic field, given by $u_{\parallel}$. Assuming electrons are radially confined in a potential well (described in Section 5.3.1 for confinement analysis) this corresponds to a "bouncing" motion resembling a simple harmonic oscillator between the inner and outer radii of the trap annulus. The "bounce" frequency was determined by assuming a simple harmonic oscillator. (This only serves as an order of magnitude estimate and does not take into account the exact geometry of the field conditions, most notably the "flat-ness" at the center of the trap where the confining electrostatic field force does not increase linearly with distance from centerline.) This frequency, ν_{bounce}, is on the order of 10^7 Hz. The third mode is the slow azimuthal drift of electrons due to the $\mathbf{E} \times \mathbf{B}$ drift, which is approximately E_z/B_r. This closed drift results in the "magnetron" motion of electrons orbiting the channel annulus. The "magnetron" frequency is given by $\nu_{mag} = 1/\tau_{mag}$, where the magnetron time, τ_{mag}, is the time for electrons to make one orbit around the channel annulus. The magnetron time is estimated as the circumference of the channel annulus, 1 m, (at channel center) divided by the $\mathbf{E} \times \mathbf{B}$ drift velocity. The magnetron frequency was found to be in the range of 10^5 to 5×10^6 Hz for the experimental parameters explored.

When these frequencies were compared to that of the electron-neutral collision frequency it was found that several "bounces" and "magnetron" orbits would be possible between classical (electron-neutral) collisions. If Bohm mobility were assumed, there would be several effective "collisions"[¶¶] per magnetron orbit and the collision frequency would be on the same order, or higher in some cases, than the bounce frequency. This characteristic motion is represented schematically in Fig. 5.3 and found to be similar to the electron motion in a Hall thruster[43, 133], which is described in more detail in Section 5.4. [***]

5.4   Comparison to Hall Thruster Electron Dynamics

Through the analysis of this chapter, it has been made apparent that the plasma environment in the Hall Electron Mobility Gage is vastly different from the plasma environment of a Hall thruster. Various plasma parameters for the Hall Electron Mobility Gage and a Hall thruster are presented in Table 5.1. A low plasma density combined with high-temperature particles results in a Debye length in the Hall Electron Mobility Gage that is much greater than any characteristic dimension in the Mobility Gage and also much greater than λ_D found in a Hall thruster. Assuming the plasma density may be controlled and limited to the range described in Section 5.2.2 ($10^{10} - 10^{11}$ m^{-3}), the plasma contribution to the applied field is negligible. Because of the relative length scales (that is $\lambda_D > L_{plasma}$) the electric field in the Mobility Gage may be controlled externally, as plasma Debye shielding of external fields is negligible. This is directly opposite of the field in a Hall Thruster, where the shape and strength of the electric field is controlled almost entirely by the plasma.

[¶¶]The effective Bohm collision frequency, used on occasion in computer models[34], is the collision frequency when substituted for ν_m in Eq. (2.52) that results in Bohm mobility. This is given by $\nu_{Bohm} = \omega_{ce}/16$.

[***]These three modes of particle motion (cyclotron, bounce, and magnetron) are found in several geometries (Penning trap, magnetron discharge, near-Earth space plasma, etc.) where the field configurations (e.g. swapping of the radial and axial fields) may differ but the same principles apply [134, 135, 136].

The long Debye length also renders the plasma in the Hall Electron Mobility Gage insusceptible to self-sustained plasma waves and oscillations, which are a prevalent characteristic of Hall thruster discharges[25].

Despite the differences in plasma parameters, the single particle dynamics are notably similar. The field conditions and resulting dynamical frequencies are provided in Table 5.1. Most of the Hall thruster parameters presented in Table 5.1 were obtained directly from Ref. [9] with the following exceptions. The wall collision frequency in a Hall thruster has historically been estimated to be at least on the order of the electron-neutral collision frequency, but also depends on the electron energy distribution function[23]. In Table 5.1 the electron-wall collision frequency was estimated to be $\sim \nu_{en}$. The turbulent collision frequency was obtained from Ref. [23], which is the turbulent collision frequency used in the PIC simulation in order to adjust the electron transport so that simulated plasma parameters agree with experiment. The electric field range $(2 - 40 \text{ V/mm})$ was obtained across several references (2-10 V/mm was cited in Ref. [71], ~ 5 V/mm in Ref. [23], 20 V/mm in Ref. [5], and up to 40 V/mm in Ref. [7, 9]). The bounce frequency for a Hall thruster was estimated as $\nu_{bounce} = 1/\tau_{bounce} = \bar{v}_e/(\text{channel width})$ with the parameters of $\bar{v}_e$ and channel width obtained from Ref. [9]. Because of the recreation of similar electric and magnetic field conditions in the Mobility Gage and the radial confinement of electrons, in absence of dielectric walls, the resulting electron dynamics exhibit scaling of dynamical frequencies— that is $\omega_{ce} > \nu_{bounce} > \nu_{mag} > \nu_{en}$— comparable to a Hall thruster.

This environment allows for isolation of single-particle effects and effects of static field geometry while eliminating the effects of collisions with dielectric walls and fluctuation-induced transport. Since the electric and magnetic fields are designed and aligned in the same way as a Hall thruster, mobility (classical and/or anomalous) based on effects of single particle motion in the field geometry would be present in this device, directly analogous to a Hall thruster. An enormous field of research

is devoted to the study of plasma instabilities, plasma waves and turbulence, and the coupled nature of transport with these phenomena, where much of the research effort of turbulent transport in Hall thrusters is devoted to the development of a self-consistent solution. The Hall Electron Mobility Gage is obviously limited in the ability to investigate such plasma dynamics, but consequently, transport observed in the Hall Electron Mobility Gage represents mobility occurring in the Hall thruster that is not correlated with fluctuations. It is of note that the vacuum electric fields may exhibit oscillations of their own due to noise in electrical circuitry, where these types of ambient oscillations may (or may not[137]) be damped by the self-field of the more dense Hall thruster plasma. Because of symmetry in the physical geometry of the Hall Electron Mobility Gage, these oscillations may only occur in the axial and radial direction and may not exist in the azimuthal direction (except in the case of slight asymmetries). Effects of these oscillations may be investigated in this device, where details of this investigation are presented in Chapter 7.

The absence of the dielectric walls in the Hall Electron Mobility Gage simplifies the environment in some ways, yet makes the correlation between the two geometries slightly more difficult to formulate. Quantifying the contribution of electron-wall collision frequency in a Hall thruster is a complex task due to the formulation of the sheath at the dielectric wall, the space charge saturation at the wall, and the effects of the secondary electron emission of the wall material. This is in addition to the complicating factors involved in the kinetic evolution of the electron distribution function, which also governs the electron flux to the walls. These effects are all incontrovertibly removed in the Hall Electron Mobility Gage. It is shown in Section 5.3.2 that collisions with the physical geometry of the pole material in the Hall Electron Mobility Gage are expected to be infrequent and pertain only to electrons with velocity much greater than the average velocity of the bulk plasma. The confining electrostatic potential well confines the bulk of plasma electrons serving to reflect electrons from the volume periphery to the center of the azimuthal channel. This

effect is much like the effect provided by the sheath at the dielectric wall in a Hall thruster discharge channel, which serves to repel the plasma electrons from the dielectric walls. The difference between the two lies in the fact that the electron losses in the direction parallel to the magnetic field are significantly reduced in the Hall Electron Mobility Gage, as the confining potential well is nominally greater than the energy available to electrons and the Maxwellian distribution is only depleted at very high energies. In contrast, the electron distribution in the Hall thruster has been shown to be highly anisotropic with a strongly depleted Maxwellian in the direction parallel to the magnetic field as the sheath voltage is only presumed to be on the order of the mean electron energy[23]. This was presumed to play a much lesser role in the Hall Electron Mobility Gage and the effects of collisions with the dielectric are removed and only the effects of the "reflection" off the sheath remain.

Obviously the entire problem of electron mobility in Hall thrusters cannot be solved using this apparatus, particularly the self-consistent problem of turbulent transport. However, a piece of the puzzle may be discovered in the absence of the complicating effects of fluctuations and wall effects, that has not been previously isolated in this geometry. For example, it was proposed[55] that the reflection off the sheath could contribute to the energy exchange between parallel and perpendicular energy components acting as a scattering mechanism for transport. It was also shown by Eggleston that resonant particle transport occurs on a single-particle level in the absence of collective effects in a Penning trap due to field asymmetries[114]. Effects such as these, if present in a Hall thruster, may be investigated using the Hall Electron Mobility Gage due to the similarities exhibited between the Mobility Gage and a Hall thruster.
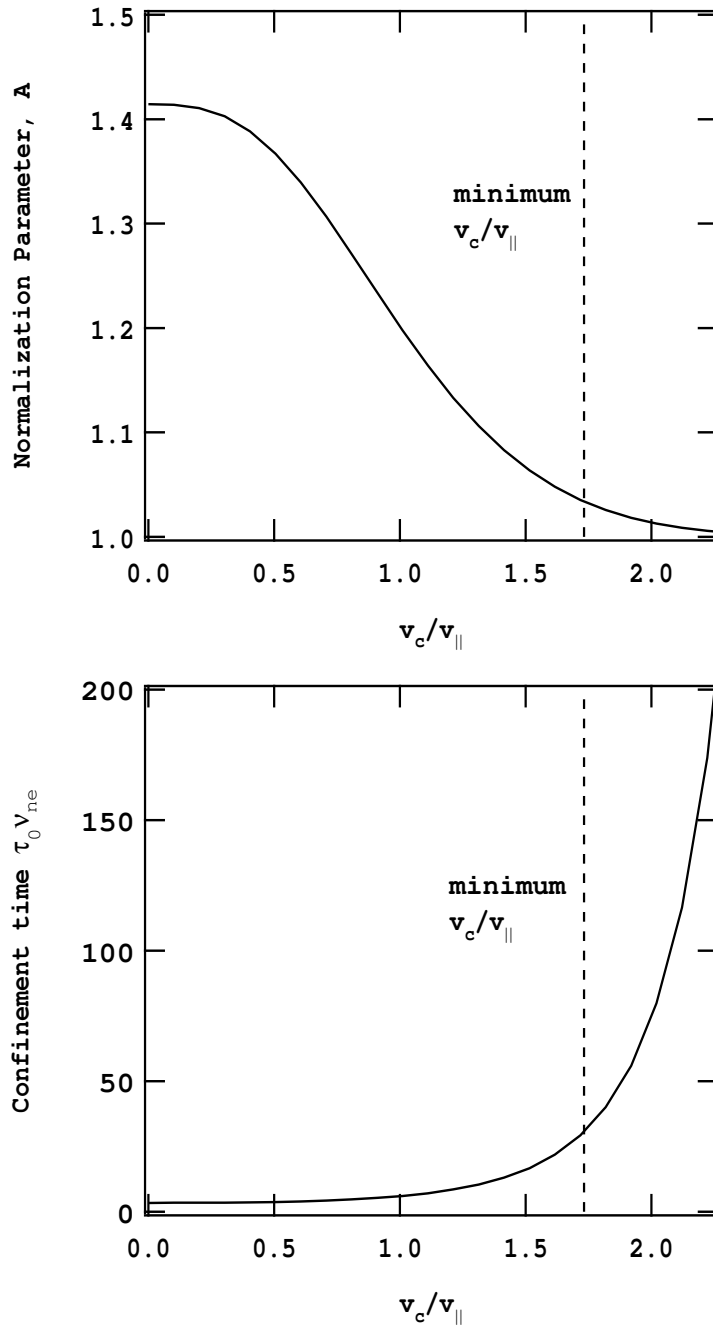
Figure 5.7: Normalization constant and particle confinement time versus $v_c/v_{||}$.

Chapter 6

Experimental Methods & Characterization

The purpose of this chapter is to present the details of the experimental setup of the Hall Electron Mobility Gage, including calibration procedures and experimental methods for verification of design criteria. First, an overview of the entire setup is presented in Section 6.1. The goal of the investigation presented in this dissertation is to examine mobility in Hall Electron Mobility Gage in response to magnetic and electric fields and pressure. The three of these parameters are presented in Section 6.2 with methods for control, measurement, and/or calibration. Section 6.3 then explores the plasma properties within the confinement volume, specifically electron density, electron temperature and ion density. Electron density is important in limiting the self-field of the electron plasma and in controlling the Debye length. Electron density is also needed to quantify mobility (described in Chapter 7). Therefore, it is crucial to maintain the ability to measure and control this quantity. Electron temperature is determined by the same diagnostics as electron density and is necessary in determining the classical cross-field mobility with which to compare the experimentally determined mobility. Furthermore, insight on the electron dynamics in the Hall Electron Mobility

Gage may be gained in the examination of electron temperature. Finally, ion density is important to determine the validity of the non-neutral (single-component) plasma diagnostics used to find T_e and n_e. The diagnostic methods for measuring these quantities are presented along with a characterization of the quantities in response to the control parameters of magnetic and electric field and pressure. The ultimate objective of this chapter is to thoroughly characterize the Mobility Gage including all controlled variables and resulting plasma parameters.

6.1   Experimental Setup (Overview)

The entire experimental setup is shown in Fig. 6.1 and a detailed view of the Hall Electron Mobility Gage with a circuit diagram is shown in Fig. 6.2. The Hall Electron Mobility Gage was operated in the Isp Lab Vacuum Test Facility #2, a 2-m-diameter, 4-m-long cylindrical vacuum chamber. Rough pumping was accomplished through a two-stage mechanical pump, capable of delivering 400 cfm. High vacuum was achieved through the use of three turbomolecular pumps with a combined throughput of 6,000 liters per second providing a base pressure below 10^{-6} Torr. All experiments presented herein were conducted within this facility.

An ion gage (shown in Figs. 6.1 and 6.2) was mounted directly to the Mobility Gage in order to obtain a local measure of pressure inside the Mobility Gage. Background gas (krypton, argon or helium) was introduced directly into the vacuum tank where gas flow was controlled through mass flow controllers (shown in Fig. 6.1) to vary the base pressure from 10^{-6} to 10^{-4} Torr. (Pressure measurements are described in more detail in Section 6.2.2.) The magnetic and electric fields (Fig. 6.2) were created through magnetic windings and parallel plates, respectively, where the electrical schematics for both are shown. The inner and outer magnetic coils were supplied by independently controlled Sorensen DLM60-10 power supplies operated in current-limited mode. The current directions for the inner and outer coils are shown in Fig.
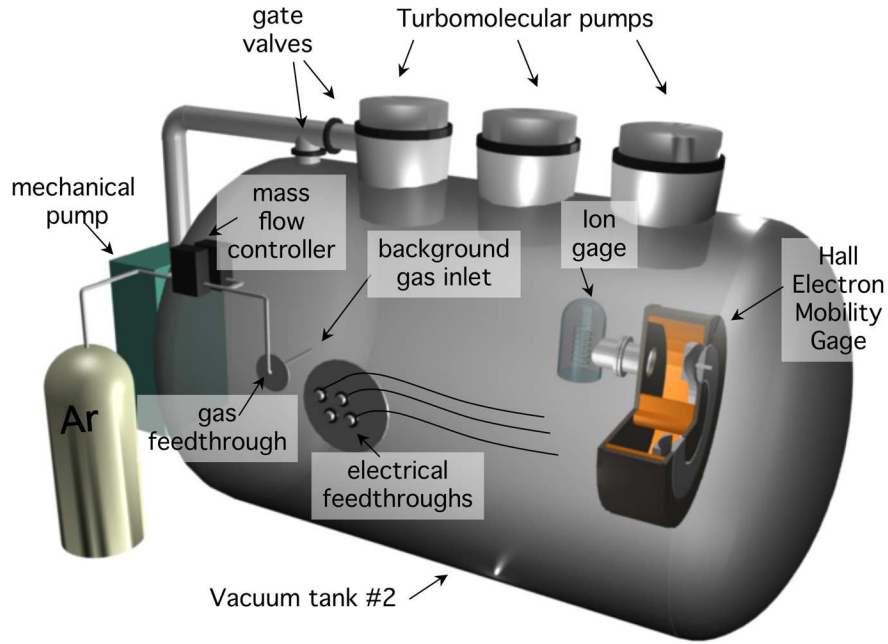
Figure 6.1: Experimental setup for the Hall Electron Mobility Gage.

6.2, as well. The electric field was created using a Sorensen DHP600 programmable power supply and 390 μF filtering capacitors were employed, as shown, to dampen oscillations in the power supply voltage. The detailed control, verification, and calibration procedures for the magnetic and electric fields are presented in Sections 6.2.1 and 6.2.3.

The thermionically emitting filament (introduced in Section 4.4) was used as an electron source, where the electron density within the confinement volume was controlled through control of the emission circuit. The filament heater supply (Sorensen 18-10) and bias circuit (voltage divider) are also shown where the control/measurment of heater current, I_h, and filament bias, V_f, are noted in the figure. The plasma parameters were measured using the electrostatic probe and various current measurements, which are indicated in Fig. 6.2. The electrostatic probe was used to measure
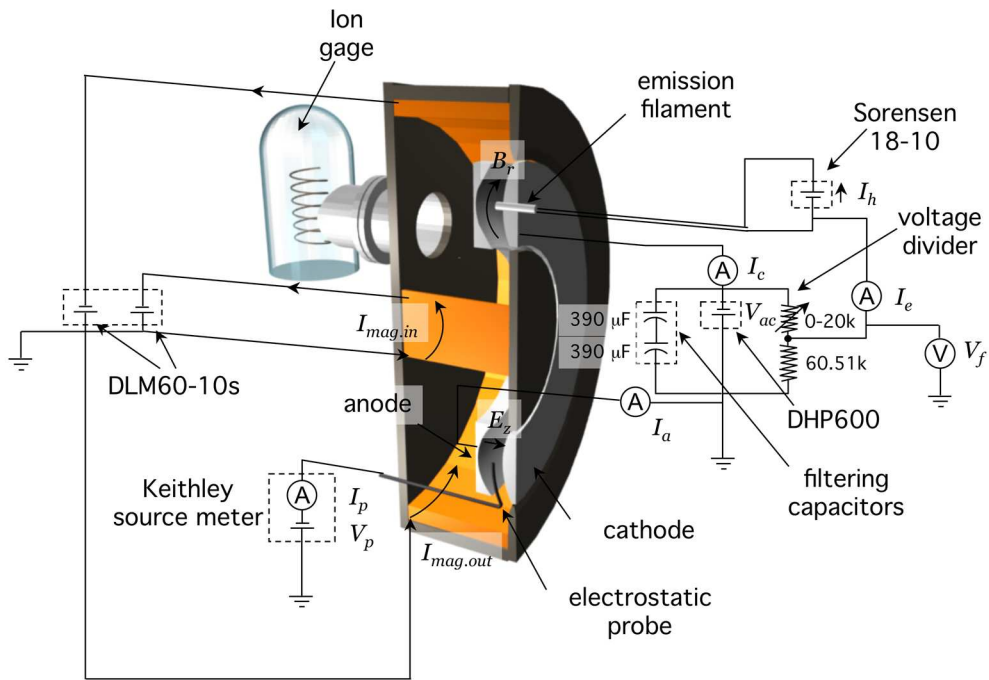
Figure 6.2: Experimental setup and electrical schematic for the Hall Electron Mobility Gage.

electron density and electron temperature through analysis of an I-V characteristic, where the source-meter circuit with current and voltage measurements (I_p and V_p) are shown in the figure. The cathode current, shown as I_c in Fig. 6.2, was measured using a Keithley 485 pico-ammeter, where the measurement was used to estimate the ion density. The anode current, I_a, was measured using a Femto DLPCA200 variable-gain, low-noise current amplifier. The anode current is imperative in measuring axial flux of electrons to determine mobility, where the details of this measurement are described in Chapter 7. Each of the aspects of the setup are described in more detail in the following sections.

6.2 Control Parameters

The electron mobility in the Hall Electron Mobility Gage was investigated in response to three main, independently-controlled parameters. The ability to independently control these parameters is advantageous for studying electron mobility in Hall thruster fields as trends of mobility may be examined in response to these parameters in order to gain insight into the mechanism driving the transport. It is impossible for these three parameters to be separated in an operating Hall thruster as the three are internally coupled by the creation and transport of the plasma. The control and/or measurement of these three parameters is described in the following sections.

6.2.1 Magnetic Field

The inner and outer magnetic coil currents were supplied using two independently-controlled Sorensen DLM60-10 power supplies operated in current-limited mode. The control of these power supplies could be achieved manually or through LabView control using an analog channel. The magnetic field was designed as described in Chapter 4 using Maxwell SV[121] axisymmetric field solver. In order to verify the Maxwell numerical solution the magnetic field was measured directly using a single-axis Gauss probe (Walker MG-7D) with an accuracy of 0.10 mT. Chronologically this magnetic field verification was done before the design and fabrication of the electrodes. A field map was taken for a single condition where 2 A were on the inner and outer magnet coils (1240 and 620 Amp-turns, respectively). The radial magnetic field was measured over a spatial grid of the entire confinement volume cross section (cross section size 100 mm(radial) x 50 mm(axial)) at one azimuthal location, with 2-mm grid spacing. An axial magnetic field measurement was not feasible in the area of the confining volume of the Hall Electron Mobility Gage due to the geometry of the probe and direction of the sensitive axis. That is, access was only possible in the axial

direction; the magnetic pole geometry did not allow radial access as the probe length ($\sim$ 6 inches) was larger than the spacing between the inner/outer magnetic coils and the confinement volume. The positioning of the probe was achieved by mounting the probe on a manual two-axis translation stage with 0.01 mm accuracy, where the (relative) position accuracy was much smaller than the size of the probe and so will not introduce additional experimental error in excess of the uncertainty of the sensor position within the Gauss probe. Since the translation stage only had a range of 28 mm $\times$ 28 mm, several setups were required to map the entire 100×50 mm cross section where positioning error may have changed between setups.

Figure 6.3 shows the simulated radial magnetic field (B_r) over the cross-section of the confining volume. [t] The inset for comparison is noted and the radial magnetic field measured by the Gauss probe and this inset are compared in Fig. 6.3*. The error between the simulated and measured magnetic fields, shown as a contour map in Figure 6.4, was found to be < 20 percent, where the error was in the range of 5-10 percent over the majority of the actual confinement volume cross section. The error was determined by

$$\text{Error} \;=\; \frac{B_{r,sim} - B_{r,exp}}{B_{r,sim}} \tag{6.1}$$

and is represented in Fig. 6.4 as fractional error. The simulated radial magnetic field was higher than the experimental data for all cases. A rotation of the probe in the r-z plane would produce this result, as the component of the field measured by the probe would not capture the entire radial component of the field. Furthermore, if the rotation caused the measurement axis to be sensitive to the axial field, the error would be greatest near the face of the magnetic pole where the field was strictly radial and the axial component was negligible. This was exhibited where the error was the greatest near the pole face and smallest at locations where the axial field was the

---

*This data was taken prior to the summer of 2006, where in July of 2006, a significant amount of this data was confiscated by an unknown thief in Sacramento, Calif. who walked off with the laptop on which this data was stored. Only a small inset of this data is shown in Fig. 6.3 as this was the only data recovered.
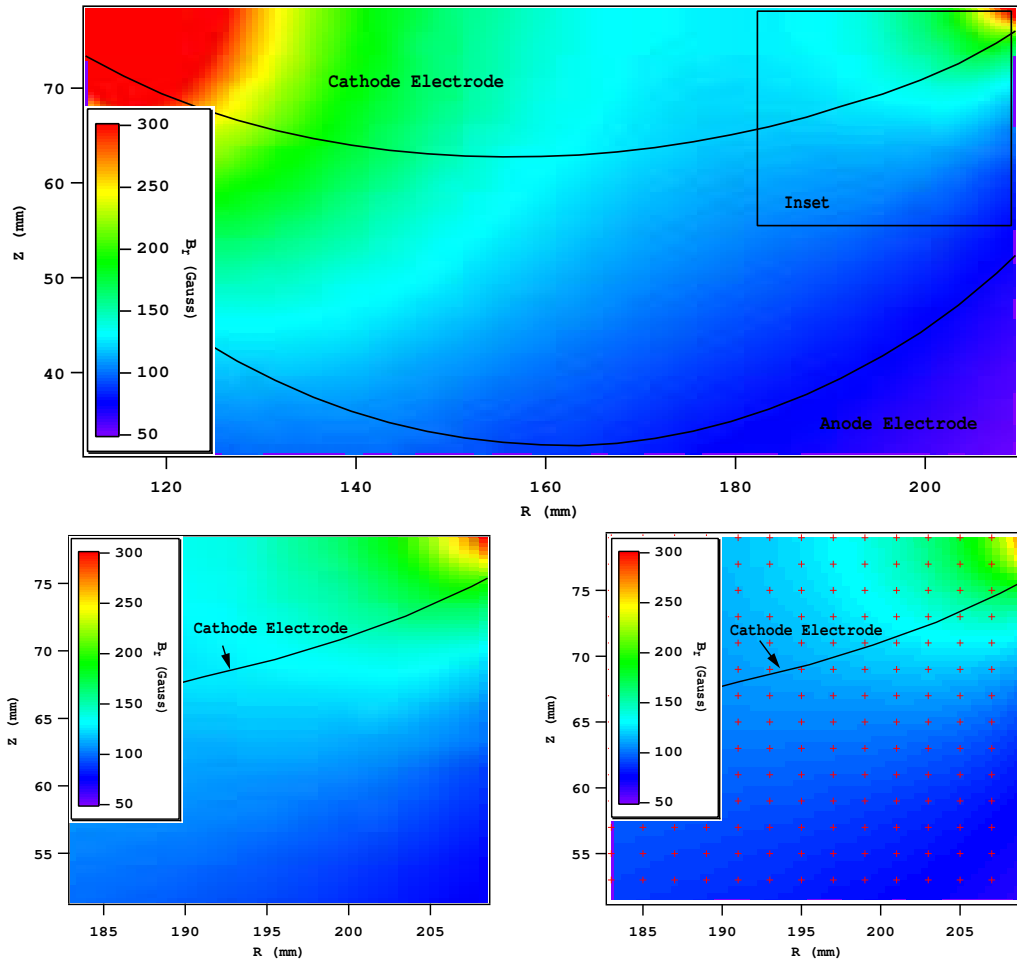
Figure 6.3: Simulated radial magnetic field (top) showing data inset, simulated radial magnetic field for inset (bottom left) and measured magnetic field (bottom right) where the grid resolution of the data acquisition is shown.

greatest. Therefore, a rotation of the probe was presumed to be the cause of error in these measurements. Because of the small discrepancy in the actual confinement volume, which could mostly be attributed to positioning error, the magnetic field simulations were assumed to be accurate, which was particularly important for the design of the contoured electrodes.

In the investigation of electron mobility it was necessary to vary the strength of the magnetic field over a wide range. As was described in Chapter 4 the core material of the magnetic poles achieved saturation when the interior magnetic field
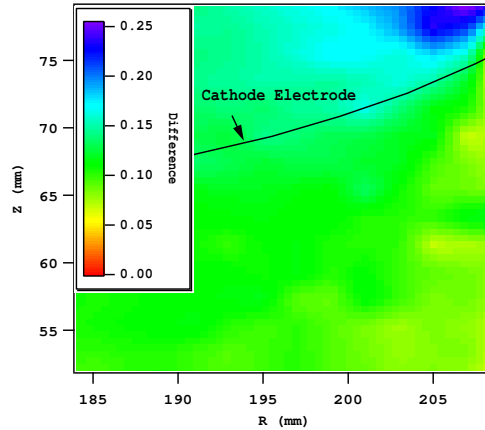
Figure 6.4: Error (shown as fractional error) between experimental and simulated magnetic field.

was greater than $\sim$ 1T (10,000 G). (The B-H curve was presented in Section 4.2, Fig. 4.5.) The inner pole achieved this interior magnetic field at a coil current of 3.25 Amps ($\sim$ 2000 Amp-turns), yet the outer pole had not saturated at the same current. If the Amp-turns on the inner coil and the outer coil were increased proportionally past this point, the field would no longer coincide with the electrode contours, but rather the field would become distorted as shown in Fig. 6.5 (shown with a coil current of 5 A corresponding to 3100 and 1550 Amp-turns on the inner and outer coils, respectively). Therefore the current on the inner pole must be increased at a greater rate with respect to the outer pole to compensate, as the material response to the applied field was in the non-linear region of the B-H curve when interior magnetic fields in the material exceed 1 T. Magnetic field models incorporating the B-H curve of the material were used to determine the "ideal" inner and outer magnetic coil Amp-turns to eliminate field distortion, as presented in Section 4.2. A magnetic field calibration procedure was employed to experimentally verify the model. Results of this analysis were previously reported in Ref. [118].

To experimentally verify the "ideal" currents on the inner and outer coils, found from the field models, it was assumed that electron confinement would be most "ef-
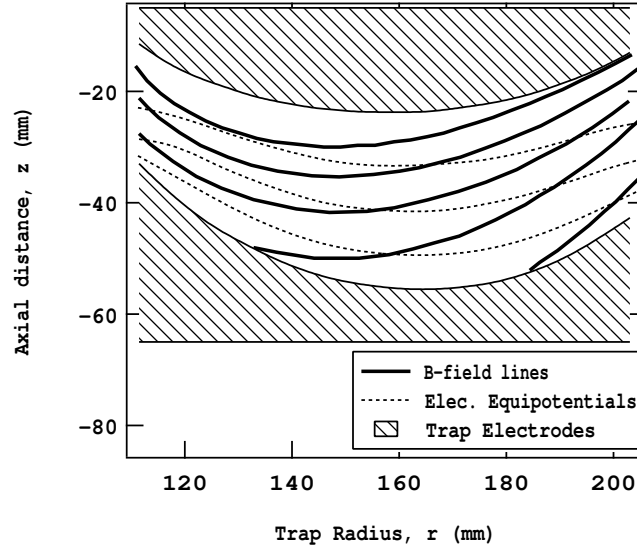
Figure 6.5: The distortion in the field lines caused by inner magnetic core material saturation showing magnetic field lines intersecting the electrodes.

fective" when magnetic field lines coincide with the electrostatic equipotential lines. This assumption comes from the fact that electrons are highly mobile along magnetic field lines and if magnetic field lines intersect the anode electrode, electrons have an "easy" path to reach the anode. Electrons would follow the principle of free mobility along field lines rather than cross-field mobility (explained in Chapter 2), which allows electrons to reach the anode much faster. The "effectiveness" of the confinement was assumed to be correlated with higher electron density (all other parameters held constant) and thus higher probe currents for the constant electric field and pressure. (For these experiments the electrostatic probe was biased to "local" potential.) For each value of inner coil current, the outer coil current was varied independently over a range of currents, where the test matrix is shown in Table 6.2.1. Using these assumptions, an "ideal" outer coil current was found for each inner coil current by finding the maximum of the probe current. For thoroughness, the procedure was employed for all values of coil currents, including cases where saturation in the center pole was not a concern. Given the assumptions noted, the most effective outer magnetic field would correlate with the peak in the recorded probe current over the parameters in-

Table 6.1: Test matrix for the optimized coil currents in the creation of the B-field

Inner Coil Current (A)	Outer Coil Current (A)
	(varied in increments of 0.05 A)
0.5	$0 - 2.5$
1.0	$0 - 2.5$
1.25	$0.5 - 4.0$
1.75	$0.5 - 4.0$
2.0	$1.5 - 4.25$
2.5	$1.5 - 4.25$
3.0	$1.5 - 4.25$
4.0	$1.5 - 4.25$
5.0	$2.0 - 4.5$
6.0	$2.0 - 4.5$
7.0	$2.0 - 4.5$
8.0	$2.0 - 4.5$
9.0	$2.0 - 4.5$

vestigated, so the ideal value of outer coil current was found by assessing the peak in the corresponding traces.[†]

Figure 6.6 shows a sample plot of probe current versus the outer magnetic current (in Amp-turns) for the case of 3 A (1860 Amp-turns) on the inner magnetic coils. Error bars are presented as the 95% confidence interval based on the standard deviation of the probe current (averaged over 100 measurements)— error bars in the plots of probe current do not take into account any other sources of experimental error. In this example, the maximum probe current, assumed to correlate with the maximum electron density in the trap, occurs at the ideal outer magnet current of 2.29 A (710 Amp-turns) for 3 A (1860 Amp-turns) on the inner coils. Similar probe investigations of trap performance were repeated over the range of inner coil currents

---

[†]For the "effectiveness" measurements the absolute measure of electron density was not necessary, as only the relative density was important. Thus, probe sweeps such as those described in Section 6.3.2 were not conducted at each variation of the outer magnetic field current. Rather the relative electron density was found from the relative probe current while the probe bias was held constant.
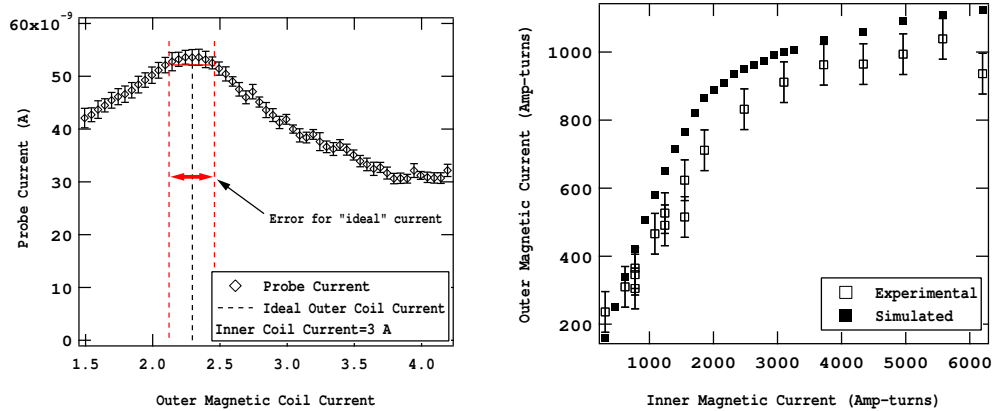
Figure 6.6: A sample plot of the ideal outer coil current for an inner coil current of 3 A determined through the *B*-field tuning procedure (left) and the experimentally and numerically determined ideal outer magnetic current in Amp-turns, for each inner magnet current (right).

considered in this work, where the ideal outer coil current was taken to be the value where the electron density (i.e. probe current) was at its maximum value. (Complete results are presented in Appendix B.) Figure 6.6 shows the ideal outer magnetic current values that correspond to each inner magnetic current for both the numerical simulations with Maxwell (described in Chapter 4) and experimental investigations using the probe technique. The method in determining error bars in the experimental data are schematically shown (red) in Fig. 6.6 (left). The range of the error bar was determined by extending the lower error bar (from the probe measurement) to the right and left until it intersects the experimental trace. The width of this box becomes the range for the error bars shown in Fig. 6.6 (right). The discrepancy between the simulated and experimental results may be a result of differences between the B-H curve used in simulations and the actual material properties of the magnetic poles, as machining, heat and or handling may change the magnetic properties of the material. Differences may also arise out of variations between the electrode design and the actual geometry of the electrodes, or positioning inaccuracies of the electrodes. Because these sources of error are systematic in nature, the experimental values for ideal inner and outer coil currents were used in all experiments, rather than

151

the simulated values, although the discrepancy between the two is relatively small. These experimental values were used in the mobility experiments in variations of the magnetic field. The effect of this calibration procedure on mobility measurements is presented in Appendix B.

6.2.2   Pressure

Various background species (usually argon, krypton or helium) were introduced directly into the vacuum facility by controlling the flow rate with two MKS mass flow controllers (Model#1179A22CS18V– 0-20 SCCM range, Model#1479A21CR18M– 0-200 SCCM range) as shown in Fig. 6.1. The B-A type ion gage was mounted directly to the Hall Electron Mobility gage as shown in Fig. 6.2. The ion gage was calibrated for nitrogen (N2) and a correction factor was used appropriate for the specific gas species present. Assuming ambient room temperature and neglecting density gradients within the confinement volume, neutral density was calculated by the ideal gas law, presented in Eq. 5.4

Pressure measurements were taken while all other testing equipment was grounded and turned off (i.e. no magnetic coil current, cathode and anode electrodes grounded, filament heater turned off and filament circuit grounded) in order to remove any effects on the pressure reading. The pressure was measured before and after any data collection so any temporal variation can be accounted for and incorporated in the experimental error. During any other data collection the mass flow rate was held constant and the ion gage was disabled as the ion gage emission filament was found to interfere with the Hall Electron Mobility Gage diagnostics.

To verify the control of pressure through the mass flow controllers a calibration was conducted for measured pressure versus flow rate. For this calibration the flow rate of argon was varied from 0.1 to 200 SCCM and resulting pressure measured with the ion gage, and the calibration curve is shown in Fig. 6.7. The error bars
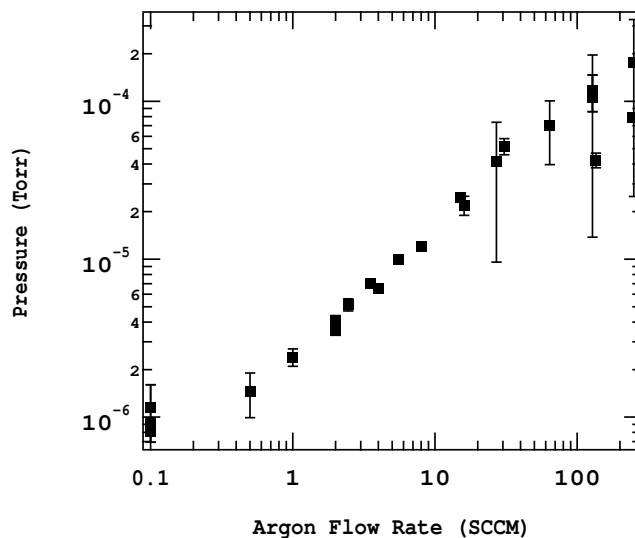
Figure 6.7: Calibration curve for pressure versus flow rate (Ar).

shown represent the variation in pressure measured at each flow rate. Since the number of measurements is small (2-4 measurements) at each flow rate this is not representative of the true scatter in pressure measurements. It was found that the background pressure could be varied from 10^{-6} to 10^{-4} Torr by varying the flow rate of the background gas. These results verify the ability to control pressure adequately over more than two orders of magnitude by varying the background gas flow rate.

Variations in this calibration curve will occur mainly due to outgassing of components within the vacuum facility. Outgassing rates depend on a number of uncontrollable parameters such as humidity (which determines the amount of moisture absorbed by components within the facility) and debris in the vacuum facility. Leak rates also affect the calibration data where any changes in fittings or feedthroughs (gas or electrical) may change the leak rate. Outgassing rates decreased with the amount of time the setup was held at high vacuum (better than 1×10^{-5} Torr). Temporal variation in the relation of pressure to flow rate was expected, and this calibration only serves as a qualitative verification of the ability to control pressure. Pressure was always measured directly using the ionization gage to maintain accuracy. Because of

this temporal dependency, efforts have been made to randomize the data acquisition to reduce time-dependent facility effects. The process of randomization is described in more detail in Section 7.3.

6.2.3 Electric Field

Because the plasma density was controlled to be sufficiently low and the Debye length sufficiently long (see Section 5.2), the electric field was assumed to be rigid and could be determined using Maxwell SV[121] electrostatic field solver. The "plasma potential" was never measured directly, as the self-field of the plasma was found based on electron density and calculation of resulting space charge potential (Section 5.2) to be negligible compared with the applied electric field. The electric field was controlled by applying a voltage bias between the anode and cathode electrodes (acting as parallel plates) using a Sorensen DHP series programmable power supply (shown in Fig. 6.2). The electric field and potential was estimated by the vacuum solution, which was solved spatially within the confinement volume. The term "local" potential, used frequently throughout this document, refers to the unperturbed vacuum potential found from this field solver, as described in Section 4.2.

In addition to the static electric field, however, it was suspected that the transient electric field conditions could affect particle dynamics as there would be no plasma shielding or dampening of externally applied fields. It was presumed, for example, that switching noise of the Sorensen DHP power supply may be transmitted to the cathode and/or anode electrodes and appear as oscillations in the applied electric field. To measure the oscillations introduced by the switching noise, a fast Fourier transform (FFT) was taken on the anode electrode using an Agilent 54621A Oscilloscope. Capacitors (450 WV, 390 μF, electrolytic) were incorporated in parallel (Fig. 6.2) to act as a filter for the switching noise and dampen the oscillations introduced by the cathode bias power supply. In order to quantify the effectiveness of the fil-

154
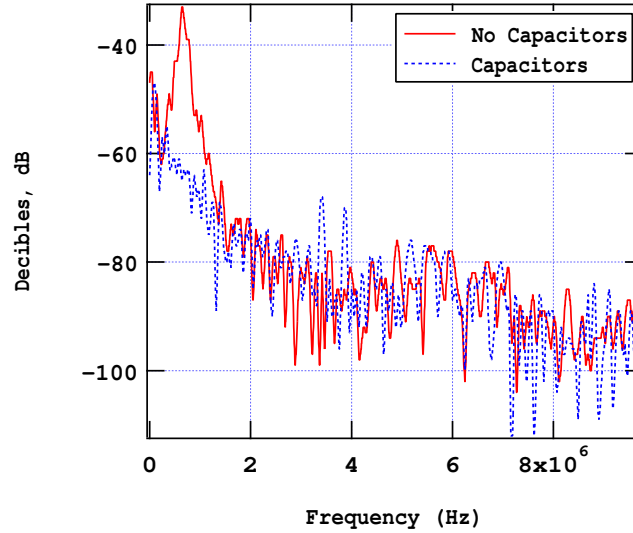
Figure 6.8: FFT taken at the anode electrode. The red (solid) trace represents the FFT without capacitors where the blue (dashed) trace was taken with capacitors in parallel with the cathode bias.

tering capacitors, a FFT was taken on the anode electrode with and without the capacitors incorporated. The red (solid) trace in Fig. 6.8 shows the FFT taken at the anode electrode where no filtering capacitors were employed. The FFT shows that oscillations were prominent in the 100-700 kHz range. Another FFT was taken upon inclusion of filtering capacitors and the resulting FFT is shown in Fig. 6.8 as a blue (dashed) trace, where it is apparent that the noise in the 100-700 kHz range was reduced significantly. Mobility measurements were obtained with and without the filtering capacitors, which is presented in Chapter 7. During the course of any other experimental data acquisition the filtering capacitors were incorporated.

6.3   Device Operation and Plasma Properties

This section serves as a characterization of the Hall Electron Mobility Gage, where the operation and resulting plasma properties are confirmed. First, it was necessary to measure and control electron density in order that the assumption of negligible

plasma self fields would remain valid. Second, it was desired to investigate electron temperature so that classical electron mobility may be calculated. Furthermore, the measurement of electron temperature was desired to gain insight into particle dynamics. Ion density was measured in order to determine both the bounds of the experimental diagnostics (single-component probe theory). Ion density measurements are also important to quantify the variation in axial electron flux due to ejected electrons from electron-impact ionization collisions. Finally, it was desired to experimentally confirm the assumption that collisions with the magnetic pole material could be regarded as negligible. This was done through an investigation of electron density as a function of emission filament bias, where when the emission filament bias was sufficiently negative (with respect to local potential) electrons would obtain sufficient energy to suffer collisions with the magnetic pole material. These considerations are presented in the following sections.

6.3.1   Probe Diagnostics

A planar Langmuir probe was used to determine electron temperature and electron density, where the probe theory presented in this section was first published in [118]. The probe (shown in Fig. 6.2) is a 2.36-mm-diameter tungsten rod encased in heat-shrink tubing to insulate all but the face of the probe. The probe was biased and current was measured using a Keithley 2410 sourcemeter, which was controlled manually or through GPIB (General Purpose Interface Bus) using NI Labview, in order to obtain an I-V characteristic. The temperature and density were extracted through a curve fit. For this in-situ measurement, the probe was positioned 180 degrees around the trap circumference from the emission filament (as shown in Fig. 6.2) so that the planar collection surface would be sensitive only to electrons that confined in the azimuthal confinement volume (rather than electrons directly emitted from the loading filament).

Because the electron plasma has a directed azimuthal flow from the $\mathbf{E} \times \mathbf{B}$ drift, considerations must be made that deviate from probe theory in plasmas with only thermal motion. Furthermore, in quasi-neutral plasmas, electron density is found from the ion saturation current of an I-V probe characteristic (since $n_e \sim n_i$); however, because the electron density is expected to be significantly higher than ion density, the I-V characteristic may not be interpreted in the traditional way. In this configuration the electron density and temperature may be found by examining the electron-retarding region of the I-V characteristic since ion current is expected to be negligible (i.e. $V_p < \phi_{local}$, where V_p and ϕ_{local} are probe and local unperturbed potential, respectively). The method presented here exhibits similarities to methods used by Kremer et al[138] and Himura et al[139].

A probe theory for the plasma conditions and geometry encountered in this work can be constructed by adapting the analyses of Gombosi for one-directional flux of a thermal gas on a surface moving relative to the gas[48]. In a flowing plasma the total velocity, $\mathbf{v}$, is characterized by a combination of the random thermal motion, $\mathbf{c}$, and the bulk motion of the plasma, or flow velocity, relative to the probe surface, $\mathbf{u}$, where $\mathbf{v} = \mathbf{u} + \mathbf{c}$. Assuming that the plasma is in thermal equilibrium, the Maxwell-Boltzmann distribution of the plasma is given by

$$f = n_\infty \left(\frac{\beta}{\pi}\right)^{3/2} \exp\left(-\beta(c_1^2 + c_2^2 + c_3^2)\right) \tag{6.2}$$

where n_∞ is the electron density in absence of a probe, $\beta = m_e/(2kT_e)$ and c_i is the i-th component of the thermal velocity. The current flux to the probe is then given by

$$J_p = e \int_{-\infty}^{\infty} dv_1 \int_{-\infty}^{\infty} dv_2 \int_{v_{3,min}}^{\infty} v_3 f(\mathbf{v}) dv_3 = e n_\infty \sqrt{\frac{\beta}{\pi}} \int_{v_{3,min}}^{\infty} v_3 \exp\left(-\beta c_3^2\right) dv_3 \tag{6.3}$$

where v_i is the i-th component of the total velocity and v_3 is the velocity component

perpendicular to the probe. the minimum velocity, $v_{3,min}$, an electrn can have and still be collected by the probe[‡] is given by

$$v_{3,min} = \left[\frac{-2e(V_p - \phi_{local})}{m_e}\right]^{1/2} \tag{6.4}$$

Substituting a change of variable in Eq. (6.3) ($v = c + u$) and evaluating the integral over c_3, the current flux to the probe in the retarding region is given by:

$$J_p = \frac{1}{4}en_\infty\bar{v}_e\left\{\exp\left(\sqrt{V_0} - s_3\right)^2 + \sqrt{\pi}s_3\left[1 - \text{erf}\left(\sqrt{V_0} - s_3\right)\right]\right\} \tag{6.5}$$

where $\bar{v}_e$ is the average electron velocity given by $\sqrt{8kT_e/\pi m_e}$, $V_0 = -e(V_p - \phi_{local})/kT_e$ and $s_3 = \sqrt{\beta}u_3 = v_f/v_{th}$. This result takes on a form similar to classical Langmuir probe theory[122] (this equation is usually used to determine electron temperature) with a correction factor added to account for the directed flow of electrons due to the $\mathbf{E} \times \mathbf{B}$ drift. This may be used as a curve fit in the retarding region of an I-V probe characteristic to determine electron density and electron temperature. This probe theory reduces to the simple thermal case as the flow velocity approaches zero. Therefore, when taking measurements with no directed flow (i.e. collection surface normal is parallel to the radial magnetic field) this same probe theory can be used with $v_f = 0$.

Based on the analysis in Section 5.3.2, the distribution function for electrons is expected to be Maxwellian except for the truncation of the high-energy tail at the energy corresponding to the trap depth, which depletes the electron distribution at energies higher than this. The distribution is expected to follow the Maxwellian distribution below this energy. Upon scattering of electrons, the truncated distribution may be scattered in three directions. The probe collection surface is sensitive to the electron velocity (energy) normal to the probe. It is only appropriate to expect the velocity (and energy) distribution in the direction normal to the probe to be Maxwellian

---

[‡]in the electron retarding region of the I-V characteristic

158
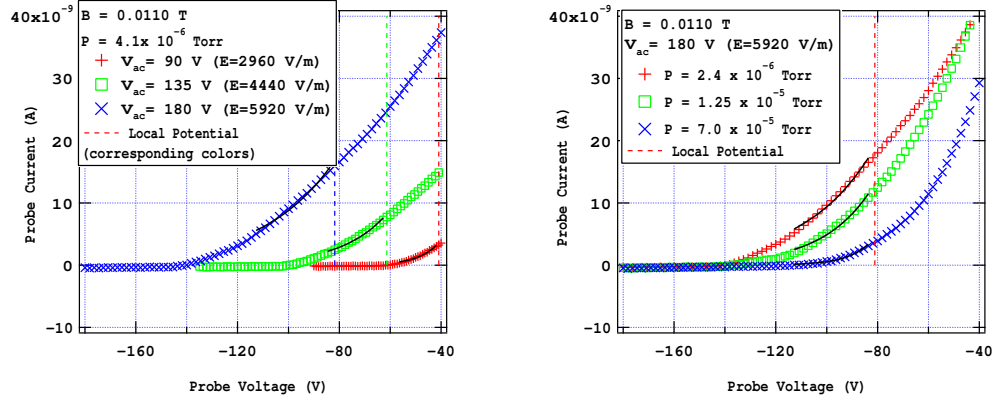
Figure 6.9: Current-voltage characteristics for an internal particle flux probe. Solid lines indicate best fits of the probe model given by Eq. (6.5). Traces for three electric field conditions are shown (left), for a constant magnetic field and pressure, and traces for three pressure conditions are shown (right), for a constant electric field and magnetic field.

below the energy of one-third the trap depth, due to equipartition of energy among the three dimensions. Above this energy, a Maxwellian may not be an appropriate approximation due to the depletion in the Maxwellian tail. This is described more thoroughly in Section 5.3.2. Therefore, the curve fit was conducted from the upper bound at local potential ($\phi_{local} - V_p = 0$) and the lower bound at one-third of the trap depth at the location of the probe.

Figure 6.9 presents characteristic probe traces for the conditions noted. Characteristic I-V probe traces for three electric fields with the magnetic field and pressure held constant are shown in Fig. 6.9 (left). The probe is positioned on channel centerline, collection surface normal to the radial direction, 10 mm from the anode, and the local unperturbed plasma potential at the probe is known from numerical electrostatic models of the vacuum field. Since the probe collection surface was aligned parallel to the flow direction, the $\mathbf{E} \times \mathbf{B}$ flow would not affect the probe collection. Using Eq. (6.5) for a curve fit, with $V_f = 0$, in the retarding region of the probe I-V characteristic electron temperature and electron density were found, where curve fits are shown as solid lines in Fig. 6.9. For the example cases shown, an electron temper-

ature of 8.0 eV with an electron density of 1.0×10^{10} m^{-3} was found for the electric field of 2.9×10^3 V/m (corresponding to an anode-to-cathode voltage of $V_{ac} = 90$ V), for 4.4×10^3 V/m ($V_{ac} = 135$ V) electron temperature was 17.8 eV and density was 1.5×10^{10} m^{-3}, and for 5.9×10^3 V/m ($V_{ac} = 180$ V), electron temperature was 28.0 eV and density 2.6×10^{10} m^{-3}. Figure 6.9 (right) shows characteristic probe traces for three pressure conditions with the magnetic and electric fields held constant. For the example cases shown, an electron temperature of 26.9 eV with an electron density of 2.9×10^{10} m^{-3} was found for the pressure condition of 2.4×10^{-6} Torr, for 1.25×10^{-5} Torr the electron temperature was found to be 19.2 eV and density was 2.3×10^{10} m^{-3}, and for 7.0×10^{-5} Torr the electron temperature was found to be 9.2 eV and density 1.0×10^{10} m^{-3}. These traces show adequate curve fits and plausible results confirming the ability to measure electron density and electron temperature. Only in certain cases where there is significant ion density (on the same order as the electron density) is the single-component plasma probe theory invalid, which are described in Appendix E.

6.3.2   Electron Density

The measurement and control of electron density achieves several purposes. First, electron density serves as a measure of the space charge, where to have confinement, the density must be limited according to the constraints presented in Section 5.2.2. Second, the measurement of electron density, combined with the axial current density, results in a direct measure of electron mobility (see Chapter 7). Third, since electron-electron collisions do not contribute to transport (see Section 2.2.3), the electron density is not expected to have any significant effect on mobility within the Hall Electron Mobility Gage; concurrent measurements of electron density and mobility may confirm this assumption (see Chapter 7). Finally, measurements of electron density may allow a direct measurement of radial losses to the magnetic pole geom-

etry. Therefore, it is important to have a method to accurately measure electron density and to effectively control electron density. Electron density was measured using a planar electrostatic probe, which was described in Section 6.3.1. A parametric characterization follows to assess the ability to control electron density.

It was desired to control the electron density within the confinement volume through control of the emission filament circuit for electron loading. The physical construction of the thermionically emitting filament was described in Section 4.5 and the electrical schematic is shown in Fig. 6.2. The controllable parameters of the trap loading circuit are the filament bias and the filament heater current. The filament heater current was used to control the temperature of the filament, T, in Eq. (4.6). Ideally, the control of the filament heater current would enable control of the electron density, where variations in filament heater current is the focus of this section. Variations in filament bias serve to accelerate the emitted electrons to higher energies, which is used to characterize the radial losses, described in Section 6.3.5. Several experiments were conducted to quantify the effects of the filament heater current on the resulting electron density.

First, it was desired to determine the basic characteristics of the electron *emission* due to changes in filament heater current. Since filament diameters may vary between filaments (filaments need to be replaced on a regular basis due to the combination of their delicacy and careless graduate students), and since filament characteristics temporally vary over the lifetime of a single filament, the trends may only be examined in relative terms when varying filament heater current.

Figure 6.10 shows emission current versus heater current on the bottom axis and emission current versus temperature using Eq. 4.6 on the top axis. It is shown in Fig. 6.10 that a very small increase in heater current (< 10 percent) can result in orders of magnitude differences in emission current (under these conditions of electric and magnetic field) showing the relative effectiveness of the filament heater current

161
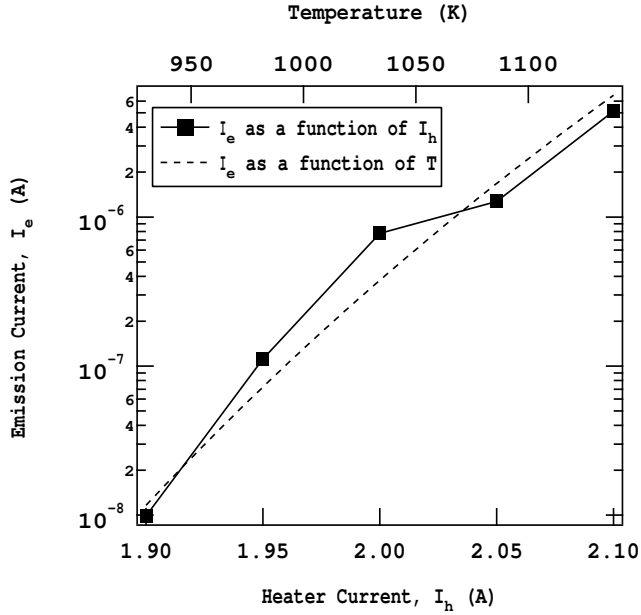
Figure 6.10: Emission current versus filament heater current (bottom axis) and emission current versus temperature (top axis) using Eq. (4.6).

as a control for electron emission, and consequently as a control of density as will be shown in the following paragraphs.

Preferably, the electron *density* could be controlled explicitly with the filament heater current. Therefore, a parametric study was conducted to determine the electron density as a function of filament heater current, for several conditions of electric field and magnetic field. For each magnetic and electric field combination the filament heater current was varied, the pressure and filament bias were held constant, and the resulting emission current and electron density were measured. Figure 6.11 shows the electron density as a function of emission current for three cases of magnetic field and four cases of electric field.

A series of dashed lines are shown representing a heater current of 2.34 A for the respective electric field conditions. For a constant heater current and constant electric field, the emission current was found to increase with decreasing magnetic field. Also, for a constant heater current and magnetic field, the emission current was found to

162
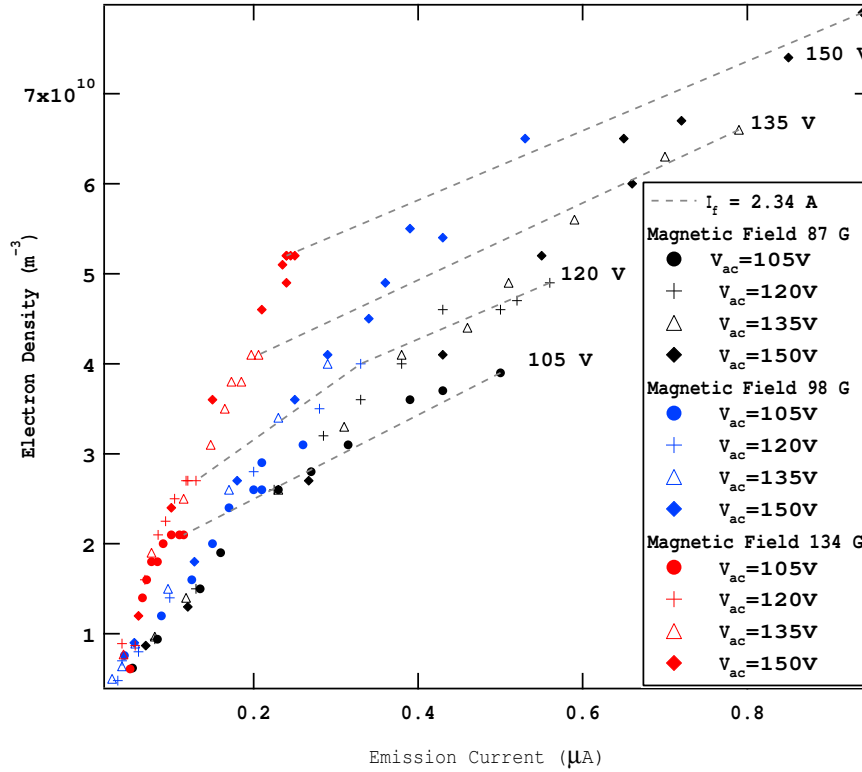
Figure 6.11: Electron density shown as a function of emission current where a constant heater current of 2.34 A is shown as dashed lines corresponding to the anode-to-cathode voltages indicated.

increase with increasing electric field. These characteristics are thought to be due to a space charge limitation due to the presence of electrons in the immediate vicinity of the filament where the space charge is affected oppositely by the magnetic field and electric field. That is, a higher magnetic field corresponds to lower axial electron velocity and thus a higher space charge field in the immediate vicinity of the filament. On the contrary, a higher electric field corresponds to a higher axial electron velocity and thus a lower space charge in the immediate vicinity of the filament.[§]

Figure 6.12 shows the electron density as a function of heater current for three

---

[§]This space charge field is only hypothesized to exist in the immediate vicinity of the filament where the electron temperature is relatively low (< 1 eV) and thus the Debye length is smaller than the confinement volume width (< 100 mm). Within a small distance from the filament, as electrons gain energy quickly from the electric field, the Debye length quickly becomes large compared with characteristic device dimensions.
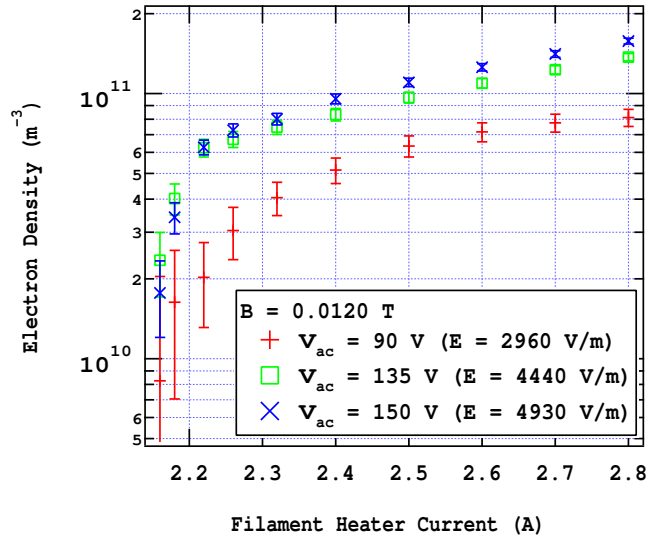
Figure 6.12: Electron density as a function of heater current for three electric field conditions and a constant magnetic field and pressure (conditions noted on figure).

electric field conditions and a constant magnetic field and pressure. The intrinsic variation of density with electric field may be seen; however, the total variation in electron density due to the filament current was greater than the small variations with the control parameters. During most mobility experiments, the filament heater current was held constant where, according to Fig. 6.11, variations in electron density should be expected. However, since electron-electron collisions do not contribute to mobility, these variations are not expected to affect mobility as long as the density is maintained according to the limits outlined in Section 5.2.2.¶ It was shown in Fig. 6.12 that electron density may be controlled adequately by varying the filament heater current, although electron density varies intrinsically with electric and magnetic field.

¶To verify, the electron mobility was examined as a function of electron density (described in Chapter 7) where the filament heater current was varied to control electron density and resulting mobility was measured.

6.3.3   Electron Temperature

The electron temperature was investigated as a function of electric field, magnetic field and pressure. Since the average electron velocity, coming from a measure of the electron temperature, determines the classical collision frequency, the electron temperature was needed for comparison of experimental mobility to classical, as explained in Section 7.2. The order of magnitude of electron temperature was not expected to vary so the order of magnitude of classical mobility will be the same regardless of the measured electron temperature. However, if electron temperature changes as a function of the parameters (of E, B and pressure), and if the resulting experimental mobility within the Hall Electron Mobility Gage depends on electron temperature (as classical mobility does), the trends of the experimental mobility with E, B and pressure may reflect this. For example, if the pressure was found to influence the electron temperature and if the mobility in the Hall Electron Mobility Gage were dependent on the classical electron-neutral-collision frequency (which is a function of temperature), the trend of experimental mobility with pressure would not be the expected 1:1 scaling when examining mobility as a direct function of pressure, due to the covariance between electron temperature and mobility. In short, the variation of temperature with all parameters was desired as a way to explain observed trends in electron mobility with the control parameters. Furthermore, an examination of temperature with the variable parameters would result in a more thorough understanding of the electron dynamics within the confining volume. For instance, the electron temperature was expected to increase with increasing electric field, as greater energy would be available to electrons. Observing this trend would confirm the understanding of these dynamics.

The measurement of electron temperature was achieved through the method described in Section 6.3.1. Electron temperature measurements were taken versus electric field, magnetic field and pressure for several combinations of the "other" two
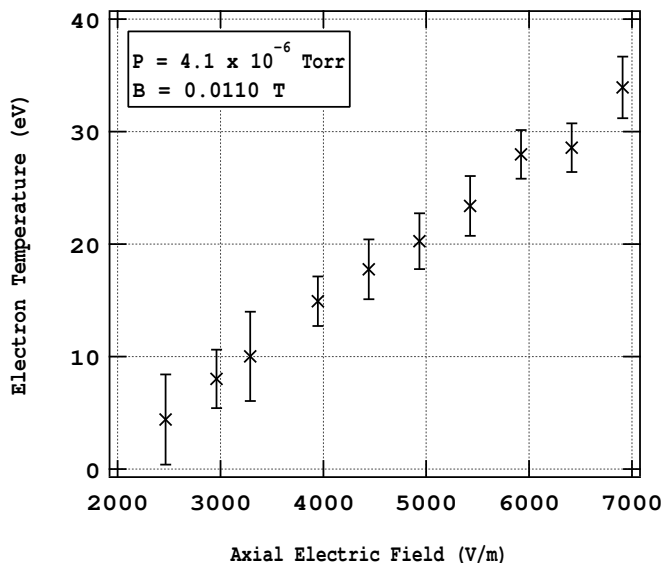
Figure 6.13: Electron temperature versus electric field for constant pressure and magnetic field.

variables. Two notable trends were observed in this investigation. First electron temperature was found to increase with electric field in all cases of magnetic field and pressure. The electron temperature versus electric field is shown in Fig. 6.13 for constant magnetic field and pressure. There is a statistically significant trend$^{\parallel}$ where increasing electric field corresponds to increasing electron temperature. This result was expected as a greater electric field corresponds to greater energy available to electrons. As electrons migrate through the confinement volume from cathode to anode, they gain energy from the electric field. Although some of this energy is lost through inelastic collisions, the electron temperature exhibits a roughly proportional increase with electric field where the electron temperature corresponds to a constant fraction of the total available energy.

The second trend was a decrease in electron temperature with increasing pressure; however, this trend was only statistically significant at cases of high electric field and magnetic field. Electron temperature versus pressure is shown in Fig. 6.14 for

---

$^{\parallel}$Error bars were calculated using the method described in Appendix D.
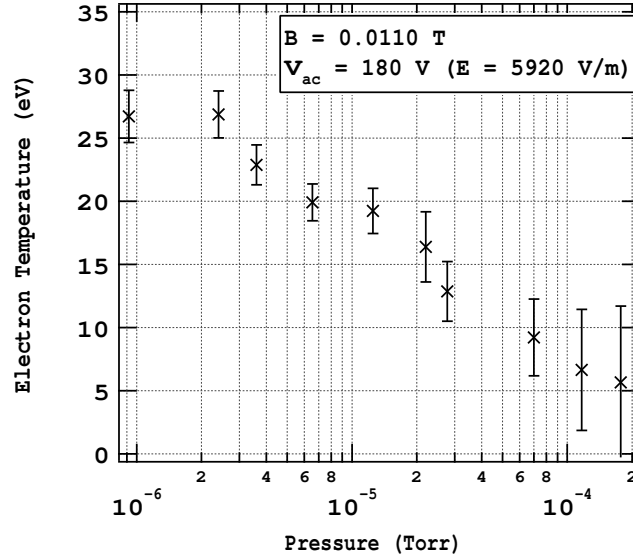
Figure 6.14: Electron temperature versus pressure for constant electric field and magnetic field.

a representative case (field conditions noted on plot). This decrease may at first appear logical as an increase in pressure corresponds to a greater probability of inelastic collisions, which cool electrons. However, this result is interesting in that it gives the first indication of non-classical mobility, which is discussed in Section 7.6. A short explanation of this rationale is provided as follows. Given purely classical mobility, the electron temperature should not change with pressure, as the same number of collisions is necessary to traverse the trap from cathode to anode for a constant electric and magnetic field regardless of the pressure. The pressure only determines the average axial velocity with which an electron may traverse from cathode to anode. The variation in electron temperature with pressure indicates that under higher pressure conditions, electrons suffer more collisions in their path from cathode to anode, which indicates that another mechanism is causing mobility in addition to collisions. This point is addressed fully in Section 7.6.

6.3.4 Ion Density

Within the Hall Electron Mobility Gage electrons may gain energy from the electric field sufficient to ionize background neutrals and in higher-pressure conditions the mean free path would become small enough where ionization of background neutrals would be significantly probable (described in Section 5.2.2). Characterization of ion density was desired for two key purposes: 1.) to determine if and when non-neutral plasma diagnostics are appropriate (i.e. in order to use non-neutral probe theory presented in Section 6.3.1, which neglects ion current) and 2.) to quantify the change in axial electron flux due to ionization, which affects mobility measurements. (See Section 7.1 for a description of mobility measurements and methods to account for ionization.)

The ion density within the Hall Electron Mobility Gage was found from a combination of axial ion current density and axial ion velocity, where the ion density is given by:

$$n_i = \frac{J_{iz}}{qu_{iz}} \tag{6.6}$$

The axial current density was obtained through a current measurement at the cathode, I_c, where the surface area, A_c, is known and $J_c = I_c/A_c$. The ion velocity obtained through acceleration due to an electric field (initial velocity is assumed to be zero; collisions are neglected) is given by:

$$u_{iz} = \sqrt{\frac{2q_i\phi}{m_i}} \tag{6.7}$$

where ϕ is the potential difference between the start and end positions of the ion. (Collisions for ions are neglected since the mean free path for ion-neutral collisions, even at the highest pressure conditions is ~ 0.5 m, using a collision cross section of $\sim 5 \times 10^{19}$ m^2[140, 141].) An upper bound of ion velocity may be calculated from the maximum velocity that ions were able to attain for the full acceleration of the

trapping volume, i.e. setting ϕ equal to the anode to cathode voltage. However, this corresponds to a lower bound for ion density (which is helpful for setting error bars, see Appendix D, but not entirely useful for assessing the bounds of applicability for non-neutral plasma diagnostics). As a more conservative approximation, the starting point for ions was taken to be half the distance between the anode and cathode so that the potential, ϕ, was estimated as $V_{ac}/2$. (If ions were created uniformly over the confinement volume, this would be a good approximation. It is suspected that more significant ionization occurs closer to the anode because electrons have gained greater energy from the field, and thus have a greater probability of ionizing collisions. If this is the case, this estimate will be conservative as a maximum ion density.) The resulting density was then approximated by:

$$n_i = \frac{J_c}{e}\sqrt{\frac{m_i}{eV_{ac}}} \qquad (6.8)$$

where e is substituted for q_i assuming single ionization (similar estimation used in [142]).

Ion density measurements were taken versus electric field, magnetic field and pressure for several combinations of the other two variables. Ion fraction (n_i/n_e) was also found by concurrently obtaining electron density measurements. The most notable trend was the increase in ion density and ion fraction with pressure. Figure 6.15 shows the ion density and the ion density fraction (n_i/n_e) versus pressure for three cases of electric field (all three shown on each plot). From the lowest pressures to the highest pressures investigated the ion density varied from less than one percent of the electron density to approximately equal to the electron density. The magnitude of ion density was greater for higher electric fields as can be seen in Fig. 6.15 (left). However, the ion density fraction (right) shows insignificant change with electric field, reflecting the concurrent change in electron density with electric field.

In the calculation for the ion density fraction for the conditions corresponding to
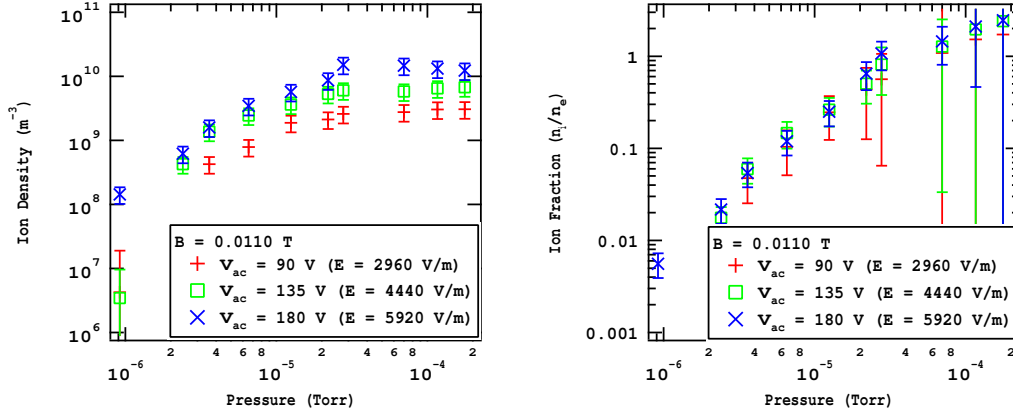
Figure 6.15: Ion density, n_i (left), and ion density fraction, n_i/n_e (right), versus pressure for a constant magnetic field and three conditions of electric field as noted.

the highest pressures, the error bars grow significantly large due to the inaccuracy in measuring the electron density. Since under these conditions the ion density is also found to be high, this calls into question the diagnostic techniques for determining electron density under these conditions, since the probe theory neglects ion current on the electrostatic probe. The bounds on the diagnostic techniques are visibly apparent in the pressure sweeps, where the plots showing ion fraction versus pressure exhibit increasing error bars as the ion fraction approaches one. This point is discussed in greater detail in Appendix E on the bounds of the diagnostic techniques.

The most obvious and consistent trend in ion density occurred with increases in pressure. An investigation of the trends of ionization with all of the control parameters may lead to further insight into electron dynamics in the Hall Electron Mobility Gage. As was presented in Section 2.2.1 the mean free path decreases with increasing pressure. At the lowest pressures investigated, the mean free path for electron-neutral collisions (for argon) is nearly 300 m and for electron-impact ionization is > 900 m. At the highest pressures investigated the mean free path for electron-neutral collisions is 3 m and for ionization is 11 m. It is apparent that the reduction in mean free path corresponds to a much higher chance of ionization. The dependence of ionization on

170

magnetic field and electric field is less straightforward. For the magnetic field, even though these results were not presented in graphical form, at the condition of zero magnetic field, for all conditions of electric field and pressure, there was no measurable ion current at the cathode. This is a result of the short path length of electrons within the confinement volume. At zero magnetic field, electrons travel on straight paths from the emission filament to the anode (~ 0.3 m), which is much shorter than the mean free path for ionization even in the highest-pressure condition. However, even a small increase in magnetic field (even at the lowest field conditions explored where the field ~ 25 G) there was a notable ion density at the highest-pressure conditions. With the application of a magnetic field the path length electrons take from filament to anode is significantly increased.

Besides the desire to quantify ionization for practical reasons (diagnostics, etc.), it is interesting to note that investigating ionization trends with electric field, magnetic field and pressure may give insight into the type of mobility exhibited. The probability of ionization increases when the path length for electrons within the confinement volume approaches the mean free path for electron-neutral collisions. The existence of ionization points to the obvious fact that collisions are taking place within the Hall Electron Mobility Gage, where the transport may not be described by a strictly collisionless mechanism (such as Bohm mobility). However, these results also suggest that at low pressures, there is another mechanism driving transport, as negligible ionization is observed even though electrons possess sufficient energy to ionize. Although a quantitative analysis has not been thoroughly explored, there also may be insight gained into the average path length for electrons based on a comparison of relative ion density and mean free path. This is presented in Section 7.6.

6.3.5 Collisions with Poles

The electron losses to the poles were hypothesized to be negligible based on the analysis of Section 5.3.2. In order to experimentally verify this claim, an investigation of collisions with the poles was conducted by examination of the electron density in response to the filament bias. At the condition investigated in Section 5.3.2, the electrons were assumed to be emitted from the filament with negligible energy (filament bias was assumed to be equal to unperturbed local potential), so that electrons would be confined within the potential well. However, if the filament were biased sufficiently negatively with respect to the unperturbed local potential, electrons would be able to gain enough energy to escape the potential well and collide with the magnetic pole material.

Electrons are emitted at a distance from the cathode (3 mm) where the depth of the potential well is equal to the difference between unperturbed local potential at the location of the filament and cathode potential (as shown in Section 4.5). The local potential at the location of the filament is given by

$$\phi_{local,f} = V_c + \frac{\Delta z_{c-f}}{\Delta z_{c-a}} V_{ac} \tag{6.9}$$

where V_c is the cathode voltage, Δz_{c-f} is the axial distance from the cathode to the filament, Δz_{c-a} is the axial distance from the cathode to the anode, and V_{ac} is the anode to cathode voltage given by $V_{ac} = V_a - V_c$. As electrons travel through the confinement volume they gain energy from the field and correspondingly, the depth of the trap increases at the same rate. (This is explained in greater detail in Section 5.3.2.) Therefore electrons emitted with very little energy at the surface of the emission filament would never have enough energy to escape the potential well (save for rare combinations of collisions that are responsible for filling the Maxwellian tail of the energy distribution). However, if electrons start with energy equal to the trap depth, they may easily escape the trap and collide with the poles. If an electron

suffers one collision with the pole and is re-emitted, it will likely reach the other pole (which is at the same potential) provided it is not scattered by a collision within the confinement volume and will suffer another collision. This may contribute to mobility in a way analogous to collisions with dielectric walls in a Hall thruster[47].

The filament heating circuit was biased using a voltage divider circuit between the anode and cathode electrodes. A variable resistor ($0 - 20$ kΩ) was employed between the cathode electrode and filament bias, in series with a 60.51 kΩ resistor between the filament bias and the anode electrode, so that the filament bias could be varied from cathode potential to ~ 25 percent of anode potential (resistance values indicated in Fig. 6.2). When the filament is biased at the local unperturbed potential of the vacuum field ($V_f = 10\%$ anode potential**), electrons only gain energy in the direction of the field where the trap depth matches the energy gain and only the highest energy electrons are able to escape the potential well. However, when the filament is biased negatively with respect to the local unperturbed potential of the vacuum field ($V_f < 10\%$ of anode potential) electrons are able to gain energy transverse to the axial electric field (as can be seen by the potential distribution in Fig. 4.12) which gives electrons higher energy relative to the depth of the trap. The more negatively the filament is biased, the greater the energy that can be attained by electrons, where if the filament bias is equal to the cathode voltage, the majority of electrons would have energy sufficient to escape the trap.

First, electron *emission* was investigated as a function of filament bias. For five heater currents, electron emission was measured for a range of filament voltages, where the anode-to-cathode voltage was held constant at 100 V, and the magnetic coil current was 0 A. The results are shown in Fig. 6.16. As the filament voltage approaches cathode voltage (0% of V_{ac}) the emission current remains constant. Conversely, for filament voltages above local unperturbed potential, where $V_f > 10\%$ of

---

** The filament voltage expressed as a percentage of anode-to-cathode voltage is given by $(V_f - V_c)/V_{ac} \times 100\%$ and local potential is $(\phi_{local} - V_c)/V_{ac} \times 100\% = 10\%$.
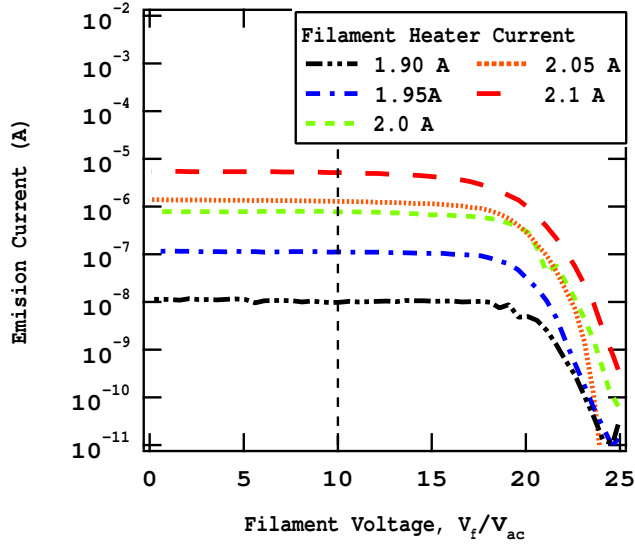
Figure 6.16: Emission current, I_e, versus filament voltage, V_f/V_{ac}, for several heater currents where the filament voltage is expressed as a percentage of anode-to-cathode voltage.

anode potential, the emission current remains relatively constant until the filament is significantly electron attracting at the point of $\sim 20 - 25\%$ above local unperturbed potential, and emission decreases significantly.

Electron *density* was measured for the same range of filament voltages where the filament voltage was varied from $0 - 25\%$ of anode-to-cathode voltage, for a constant electric field, magnetic field and pressure. Fig. 6.17 shows the electron density versus filament voltage. As the filament voltage approaches the cathode voltage the electron density shows a sharp decline. Since the emission current was found to be relatively constant over this range of filament bias voltage, the change in electron was thought to have been due to the electron dynamics within the confinement volume (rather than an artifact of the loading mechanism). This sharp decline in electron density was an indication that electrons were able to escape the confining potential well and were lost through recombination. This result has two implications. 1.) Electron collisions with poles result in decreased electron density, which suggest losses from the confinement volume rather than collisions that result in enhanced mobility. 2.) Electrons may

174
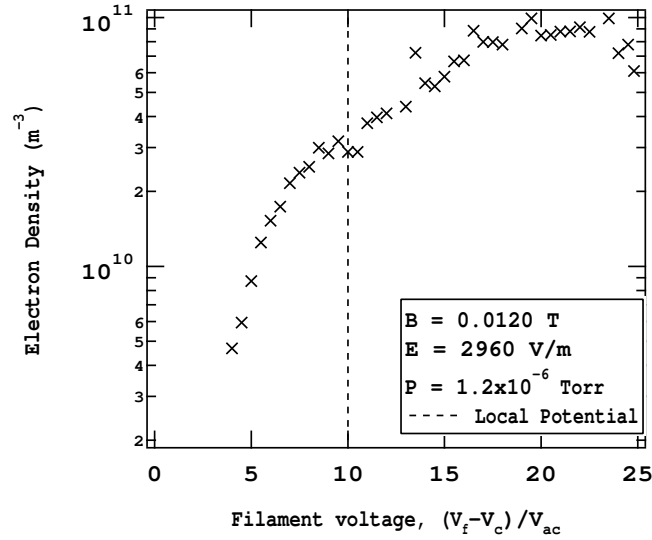
Figure 6.17: Electron density as a function of filament bias. Electric field, magnetic field and pressure are noted.

be "forced" out of the confinement volume, or by appropriately setting the filament bias (at local potential) losses may be minimized. Mobility measurements were also obtained versus filament bias and are presented in Chapter 7.

6.4   Summary

The characterization of the Hall Electron Mobility Gage resulted in a greater understanding of the trap operation. The most notable results of the characterization are as follows. First, the ability to control electron density by the filament heater current was confirmed, where electron density may be limited to the constraints presented in Section 5.2.2, and electron density may be varied over more than an order of magnitude with changes in the filament heater current. Electron temperature investigations showed that electron temperature increases with electric field, as expected. Electron temperature investigations also showed that under some conditions (namely, the highest electric and magnetic fields investigated) a decrease in temperature with

pressure was observed. These temperature measurements will be discussed in greater detail in Section 7.6, where electron temperature may be investigated as a means to characterize the transport exhibited. Ion density measurements showed an increase in ion density and ion density fraction with pressure, due to the increased probability of ionizing collisions as the mean free path for electron-neutral (and ionizing) collisions was reduced. This is also discussed in greater detail in Section 7.6, as the ionization may provide information on the path length of electrons within the confinement volume. Finally, collisions with poles was investigated by an measurement of electron density as a function of emission filament bias, where the emission filament bias controlled the initial energy of electrons upon electron loading into the confinement volume. When electrons were given sufficient energy to escape the confining potential well electron density decreased suggesting electron losses through recombination at the magnetic pole material. This suggested that the result of collisions with poles was recombination rather than a scattering mechanism to drive electron transport. This is explored in Section 7.5.2 in terms of mobility versus filament bias. Through this characterization the author has become more confident in the dynamics and inner workings of the Hall Electron Mobility Gage so that reliable mobility measurements may be obtained, as described in Chapter 7.

Chapter 7

Mobility

The purpose of this chapter is to present the experiments and results of mobility studies within the Hall Electron Mobility Gage. First, the methods for mobility measurement and the overall testing methods are presented along with the process used to calculate classical and Bohm mobility in Sections 7.1 through 7.3. The results of mobility versus the control parameters of magnetic field, pressure, and electric field are presented in Section 7.4. Non-classical mobility was exhibited in nearly all cases where the difference between the observed mobility and classical mobility was outside the realm of experimental error. The magnitude of the experimental mobility was also compared with Bohm mobility where the magnitude of mobility in the Hall Electron Mobility Gage was significantly lower than the Bohm description (using Bohm coefficient of 1/16). In order to further understand the electron mobility exhibited in the Mobility Gage additional studies were conducted investigating mobility in response to changes in electron density, wall collisions, the probe perturbation and electrostatic oscillations, which are presented in Section 7.5. These studies failed to provide an explanation for the enhanced mobility but provided confirmation of certain assumptions previously cited (e.g. that Coulomb collisions and collisions with the magnetic pole geometry were insignificant). Further analysis revealed supporting evidence for a collisionless mechanism contributing to transport within the Hall Electron Mobility

Gage, which is presented in Section 7.6. This evidence, combined with the dependence of mobility on pressure, led to the conclusion that mobility within the Hall Electron Mobility Gage may be driven by the combination of a collisional and a collisionless mechanism. The experiments, results, and analysis described here are presented in more detail in the following sections.

7.1 Mobility Measurement Strategy

The transverse mobility, μ_{ez}, is defined as the constant of proportionality between the cross-field velocity of electrons and the electric field orthogonal to the magnetic field. For the geometry of the Hall Electron Mobility Gage this corresponds to the axial (z) velocity, u_{ez}, and axial electric field, E_z, where the axial velocity is given by Eq. (1.1) and to reflect the geometry of the Hall Electron Mobility Gage is given by

$$u_{ez} = \mu_{ez}E_z \tag{7.1}$$

In the Hall Electron Mobility Gage the electric field is known from the numerical solution of the vacuum electrostatic configuration because the electron density is sufficiently low and Debye length sufficiently long that the field can be assumed rigid (Section 5.2). Therefore, only a measurement of the axial velocity was necessary to determine the mobility. A measurement of current at the anode (with known area, $A_a = 0.099$ m^2) gives the axial current density, $J_a = I_a/A_a$, which, given a measurement of electron density, provides the axial velocity, where

$$u_{ez} = \frac{J_a}{qn_e} \tag{7.2}$$

Electron density was derived using the probe theory of Section 6.3.1 to interpret the measured I-V probe characteristic. Thus, the cross-field mobility was evaluated experimentally by combining the result of the probe sweep with the axial (anode)

current so that

$$\mu_{ez} = \frac{J_a}{E_z q n_e} \tag{7.3}$$

The approximation of $J_{ez} \sim J_a$ assumes constant axial flux between the probe and the anode, as the measurement of density was taken at the axial location of the probe but the measurement of axial flux was taken at the anode. Any change in flux corresponds to error in this approximation. In particular, any ionization that takes place between the probe and the anode becomes a higher axial electron flux at the anode, corresponding to a measurement of mobility that is artificially inflated. This effect may be significant under some conditions, such as the high pressure condition where ionization is significant (described in Section 6.3.4). (Any radial electron losses through recombination at the magnetic core surfaces that take place between the probe and the anode correspond to a lower axial flux at the anode, but this effect was shown in Section 5.3 and Section 6.3.5 to be negligible.)

In order to account for the change in axial electron flux due to ionization, a correction to the axial current density was applied in order to refine the trends. The axial current density at the electron loading filament may be estimated by $J_{ez}(z_{filament}) = I_e/A_a$, and the electron density at the anode collection surface is given by $J_{ez}(z_{anode}) = I_a/A_a$. Under conditions where ion density is significant $(n_i > 0.10 n_e)$, $J_{ez}(z_{filament}) < J_{ez}(z_{anode})$.

As a first order approximation, the axial current density was assumed to increase linearly between the emission filament and the anode electrode. It is possible that the density may not increase linearly with axial distance, but rather exponentially due to cascading electrons ionizing or some other non-linear profile. However, this may be a function of all parameters of electric and magnetic field and pressure and without experimental data for spatial electron density variations, making any assumption of the electron density profile would be suspect. A linear profile would be a conservative estimate over an exponential profile, as the exponential profile would result in a

greater correction to mobility measurements. Spatial ionization data in the similar geometry of a planar magnetron discharge shows a roughly linear relation between relative ionization and distance from the cathode (target) for the lowest pressures examined[143]. Although the low-pressure condition in the planar magnetron was higher than the pressures in the Hall Electron Mobility Gage, similar principles may apply as the pressure is further decreased in the planar magnetron discharge. This justification is by no means exhaustive, but gives credence to the use of a linear approximation in lieu of a highly non-linear model (e.g. a model where the ionization exhibits an exponential increase or extremum at some spatial location, which has been shown to occur at higher pressures in the magnetron[144].) Further experiments are outlined in Chapter 8 that would serve to create a more accurate account of the ionization and effects on the diagnostics.

On the assumption that current density increases linearly from the loading source to the anode, the resulting equation for current density as a function of axial position may be given by

$$J_{ez}(z) \ = \ \frac{1}{A_a} \left[I_e + \frac{(I_a - I_e)\, z}{\Delta z_{f-a}} \right] \tag{7.4}$$

where Δz_{f-a} is the distance from the loading filament to the anode, and z is the position of interest where $z = 0$ at the filament and $z = \Delta z_{f-a}$ at the anode. Therefore a measurement of emission current is also required to determine the change in axial flux with axial distance within the confinement volume.*

The measurement of electron density was taken at the probe location where to determine the cross-field mobility, the axial flux must also be determined at the location of the probe. Therefore, the experimental electron mobility given in Eq.

---

*In some cases a measurement of emission current was not obtained, where a statistical analysis (presented in Appendix C) was employed in order to estimate the emission current based on known parameters of E, B, pressure and anode current.
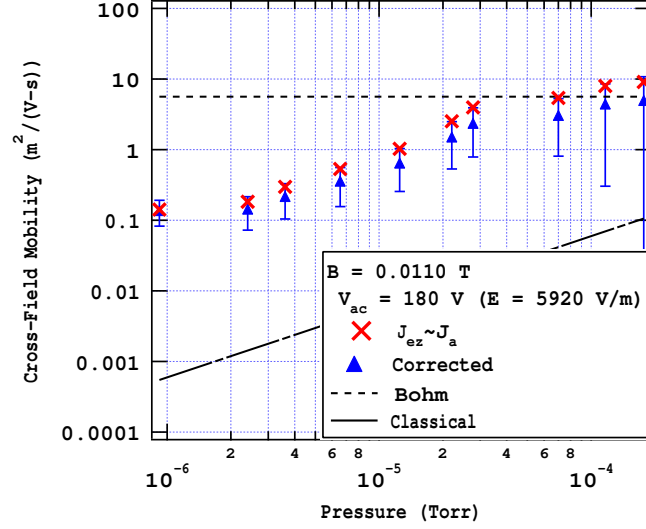
Figure 7.1: Mobility versus pressure assuming constant axial flux ($\times$) and with the correction for non-constant axial flux ($\triangle$).

(7.3) was modified and given by

$$\mu_{ez} = \frac{J_{ez}(z_{probe})}{E_z q n_e} = \frac{1}{A_a}\left[I_e + \frac{(I_a - I_e)\, z_{probe}}{\Delta z_{f-a}}\right]\frac{1}{E_z q n_e} \tag{7.5}$$

In the case of no ionization $I_e = I_a$ so Eq.7.5 reduces to Eq. 7.3 given $J_{ez} = I_a/A_a$. However, in the case of high ion density, such as in the case of high pressure, the correction may be significant, especially in exploring trends with pressure. An example is shown in Fig. 7.1 where the uncorrected mobility and the corrected mobility are shown. This correction does not change the order of magnitude of the measured mobility but may help to refine trends, especially with pressure where ion density also exhibits a strong trend with pressure (Section 6.3.4). Since the calculation of mobility combines several experimental parameters with varying experimental uncertainty, the error in the measurement of mobility is found through propagation of errors, which is presented in Appendix D.

181

7.2 Classical and Bohm Mobility

A calculation of classical mobility and Bohm mobility were needed for comparison of mobility results. In the investigations in the Hall Electron Mobility Gage the Hall parameter (given by Eq. (2.43)) was > 1000 for all cases of magnetic field and pressure. Classical (cross-field) mobility is given in Eq. (2.52) in the case of high Hall parameter. In terms of the geometry of the Hall Electron Mobility Gage the classical cross-field mobility is given by

$$\mu_{ez} = \frac{\nu_m}{\omega_{ce} B_r} \tag{7.6}$$

For the calculation of classical mobility an estimation of momentum-transfer collision frequency and the magnetic field were needed.

The magnetic field strength was determined from the Maxwell SV[121] numerical solutions where the verification of the numerical solution was presented in Section 6.2.1. For a particular case of coil current the magnetic field strength was taken to be the average magnetic field strength over the axial profile of the magnetic field, since the field varies 30% ($0.90 B_{max}$ to $0.60 B_{max}$, as described in Section 4.2) over the confinement volume cross section. The axial profile was taken at the minimum magnetic field indicated by profile #2 in Fig. 4.3.

The momentum transfer collision frequency was calculated based on the electron-neutral collision frequency, since Coulomb collisions were found to be negligible (Section 5.2.3). The electron-neutral collision frequency is given by Eq. (2.31) where n_0 is the neutral density, σ is the collision cross-section and $\bar{v}$ is the electron velocity. The neutral density was calculated using the ideal gas law given by Eq. (5.4), based on the pressure measured with the B-A type ion gage. The electron velocity was calculated from the measured temperature (described in Section 6.3.3) and given as the average velocity of a Maxwellian distribution, $\bar{v}_e = \sqrt{8kT_e/\pi m_e}$. The electron-neutral collision cross section was estimated from the cross-section data provided in the Siglo

database[3], which for argon is shown in Fig. 2.4. The cross section was found based on the electron energy given by $3kT_e/2$, where the electron temperature was given by the experimentally measured value. Bohm mobility was calculated using the same magnetic field as in the case for classical mobility and is given by Eq. 2.65. In each plot presented in Section 7.4 these values of classical and Bohm mobility are given to reflect the range of parameters explored as indicated in each respective section.

7.3 Testing Methods

In order to investigate mobility the diagnostic method for measuring mobility, described in Section 7.1, was used while employing the following test methods. This section describes the randomizing test methods executed to measure mobility, in order to minimize systematic error arising out of temporal facility effects. The testing matrix used to examine the mobility trends with electric and magnetic fields and pressure (neutral density) was randomized to reduce the error introduced by temporal and/or unknown facility effects. Methods were employed to completely randomize the electric and magnetic field parameters (since these can be automated with reliable repeatability) within randomized pressure "blocks." Temporal effects are expected as a result of outgassing, among other unknown and unmeasurable quantities such as emission filament variation or ambient temperature changes. Pressure was varied by allowing a constant mass flow of the background gas into the vacuum chamber as described in Section 6.2.2. Because of outgassing effects, a constant mass flow does not necessarily correspond to the same pressure or the same partial pressure of argon (or other background gas). To reduce variability of outgassing effects on the trends observed in magnetic and electric fields, the pressure was varied within a randomized complete block design[145]. A randomized complete block design was chosen for two reasons. First, varying and measuring the pressure (described in Section 6.2.2) needs to be done manually while the rest of the system is disabled, and randomiz-

ing this into the entire test matrix is unfeasible due to time constraints. Moreover, if the pressure were completely randomized (rather than "blocking"), differences in outgassing may be introduced to contribute to the variability observed in the electric and magnetic field data, where the error introduced may overwhelm the trends with electric and magnetic field. Conversely, if the pressure were held constant for each sweep of electric and magnetic fields, the variation in mobility due to electric and magnetic field would arise out of the "true" differences in the fields, rather than out of the differences in outgassing rates or any other variation, leading to the inability to achieve the same pressure condition in each instance.

The method for all data acquisition for mobility measurements is presented in Fig. 7.2. Variation in electric and magnetic fields was achieved through automated means so complete randomization of these parameters was possible. For each "block" of pressure, a matrix was constructed through a computational random number generator, which randomized the order of each combination of electric and magnetic field. This was done for each parameter "sweep." A "sweep" of 10 magnetic field conditions was taken for three pressure conditions and three electric field conditions. The randomizing program created an output indicating the order for the experimenter to execute the three pressure conditions (manually) and created a random order for the execution of the 30 combinations of electric and magnetic field which were executed within the LabView data acquisition program, within each pressure block. A new matrix for the execution order of electric and magnetic field was computed within each pressure block. Similarly, a "sweep" of 10 electric field conditions was taken for three pressure conditions and three magnetic field conditions. The program directed the experimenter to execute the pressure conditions in a specified order and the 30 conditions of electric and magnetic field were randomized in order of execution and were automated by the data acquisition program in LabView. For the execution of the pressure sweeps, the program indicated the order of execution for the 10 pressure conditions and randomized the order of execution for the three parameters of electric
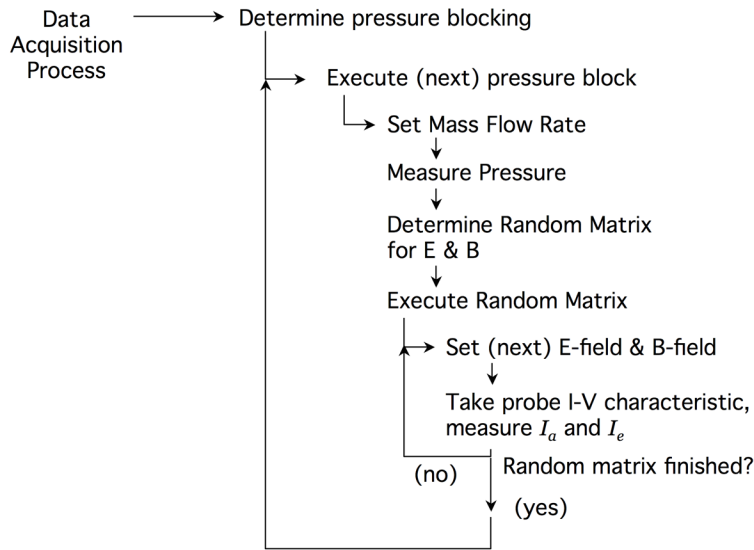
Figure 7.2: Data acquisition method for measuring mobility in the Hall Electron Mobility Gage.

and magnetic field (9 combinations total) within each pressure condition, where a new execution order was determined for each pressure "block."

At each of the testing conditions anode current and emission current were recorded, along with a probe sweep to find electron temperature and density for each combination of parameters. This test matrix was executed to investigate trends of mobility with electric field, magnetic field and pressure and also for investigation of other factors suspected to cause mobility (described in Section 7.5).

7.4   Mobility vs. Control Parameters

Mobility was examined in response to the parameters of magnetic field, electric field and pressure according to the test method in Section 7.3. According to classical mo-

bility, the cross-field mobility should scale as B^{-2}, should scale 1:1 with pressure, and should remain constant with E (as it is the *constant* of proportionality between axial velocity and E). The trends of mobility with E, B and pressure may be investigated independently, which would not be possible in an operating Hall thruster (as described in Chapter 3). The results of these investigations are presented along with classical and Bohm mobility for comparison in the following sections. Error bars are presented as calculated using the error analysis presented in Appendix D.

7.4.1 μ_{ez} vs. Magnetic Field

Mobility was examined in response to magnetic field where sweeps of magnetic field (10 conditions) were taken for several combinations of electric field and pressure. Test methods described in Section 7.3 were used for randomization of the data acquisition, and the diagnostics described in Section 7.1 were used to measure mobility. Results of mobility versus magnetic field are displayed in Fig. 7.3 for two electric fields and three pressure conditions (as noted). Error bars shown were calculated using the error analysis presented in Appendix D.

Traces for classical and Bohm mobility are shown as thick solid and dashed lines, respectively. The classical and Bohm mobility values are determined as a function of magnetic field for the pressure conditions noted. These plots show that mobility lies between classical and Bohm mobility. There was a general decrease in mobility with increasing magnetic field where in most cases the change in mobility over the range of magnetic field was statistically significant. However, within the bounds of experimental error it is not possible to determine whether the experimental mobility exhibits a B^{-2} or B^{-1} trend. Curve fits are shown in Fig. 7.3 for B^{-2} and B^{-1} scaling, as solid and dotted lines, respectively, with the equation for the curve fit displayed on each respective plot. It appears that the B^{-2} curve fit for the low pressure conditions provides a better fit, where the B^{-1} curve fit for the high pressure conditions provides
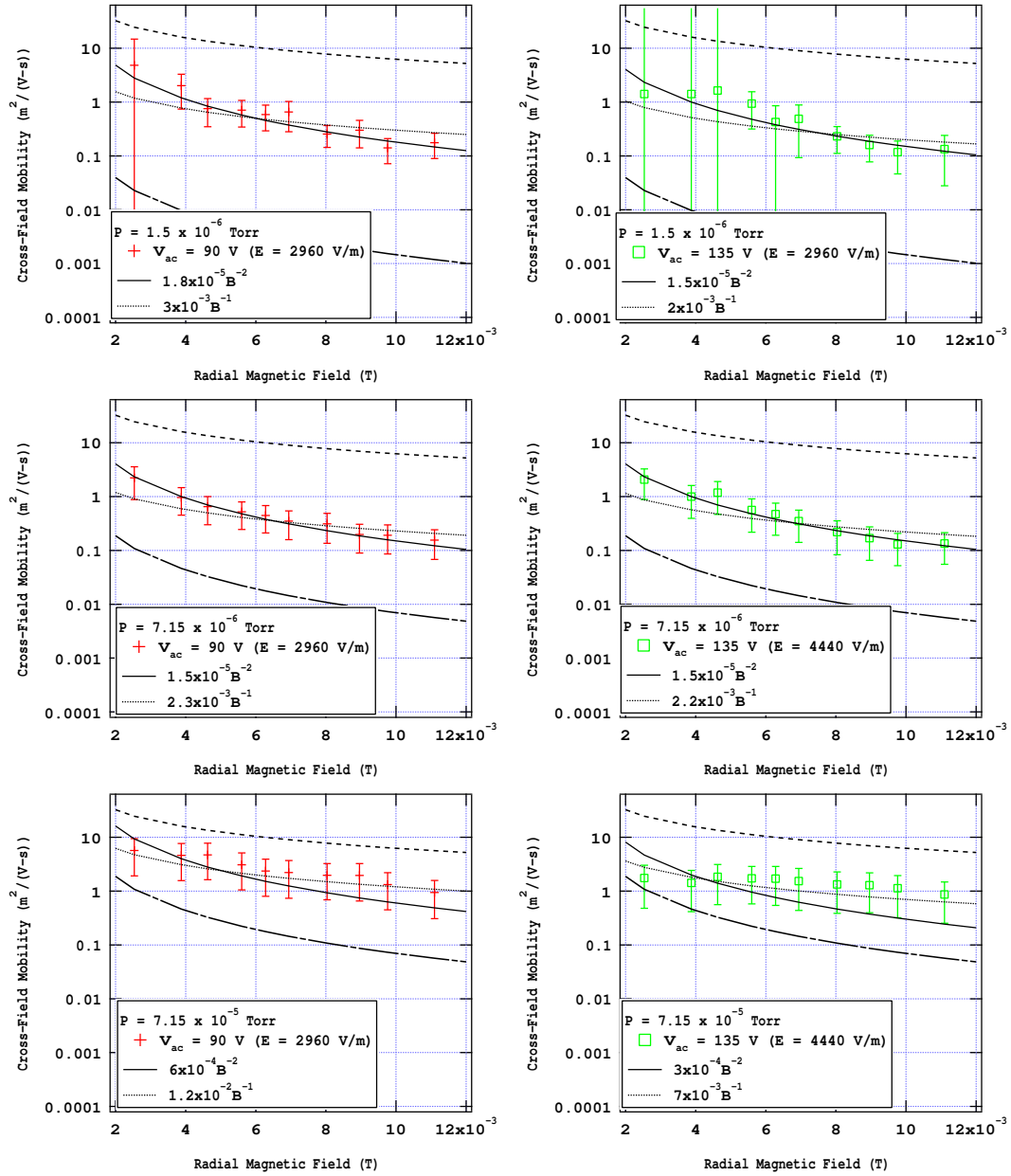
Figure 7.3: Experimental mobility versus magnetic field for an electric field of 2.9×10^3 V/m (left) and 4.4×10^3 V/m (right) and a pressure of 1.5×10^{-6} Torr (top), 7.15×10^{-6} Torr (center) and 7.15×10^{-5} Torr (bottom). Classical and Bohm mobility are shown as long dashed and short dashed lines, respectively.

a better fit. However, this is purely speculative as both curve fits lie within the realm of experimental error for almost all conditions.

7.4.2 μ_{ez} vs. Pressure

Mobility was examined in response to pressure (which may be equivalently expressed as neutral density by Eq. (5.4)). The mobility investigation was conducted according to the methods described in Section 7.3, and mobility was measured using the diagnostics described in Section 7.1. Mobility versus pressure was investigated for several combinations of magnetic field and electric field, where results are shown in Fig. 7.4. Again, the magnitude of the experimental mobility was found to be between the classical and Bohm values. There is a general increase in mobility with pressure where in most cases, the change in mobility is statistically significant. A curve fit is shown in Fig. 7.4 in the form $\mu_{ez} = C_1 P^{1.0}$ which is the classical scaling of mobility with pressure. For the second curve fit the mobility was allowed to have a "collisionless" component so the form of the curve fit was

$$\mu_{ez} = C_1 P^{1.0} + C_2 \tag{7.7}$$

where C_1 is the coefficient of the pressure dependent component (collision dominated) and C_2 is the "collisionless" component of mobility. The coefficients are shown on respective plots. This curve fit seemed to match the data better than the purely classical scaling; however, the difference is so slight that this trend cannot be confirmed without extending the range of pressure significantly lower.

7.4.3 μ_{ez} vs. Electric Field

Mobility was examined in response to electric field for several combinations of magnetic field and pressure, according to the methods of Section 7.1 and 7.3. Results
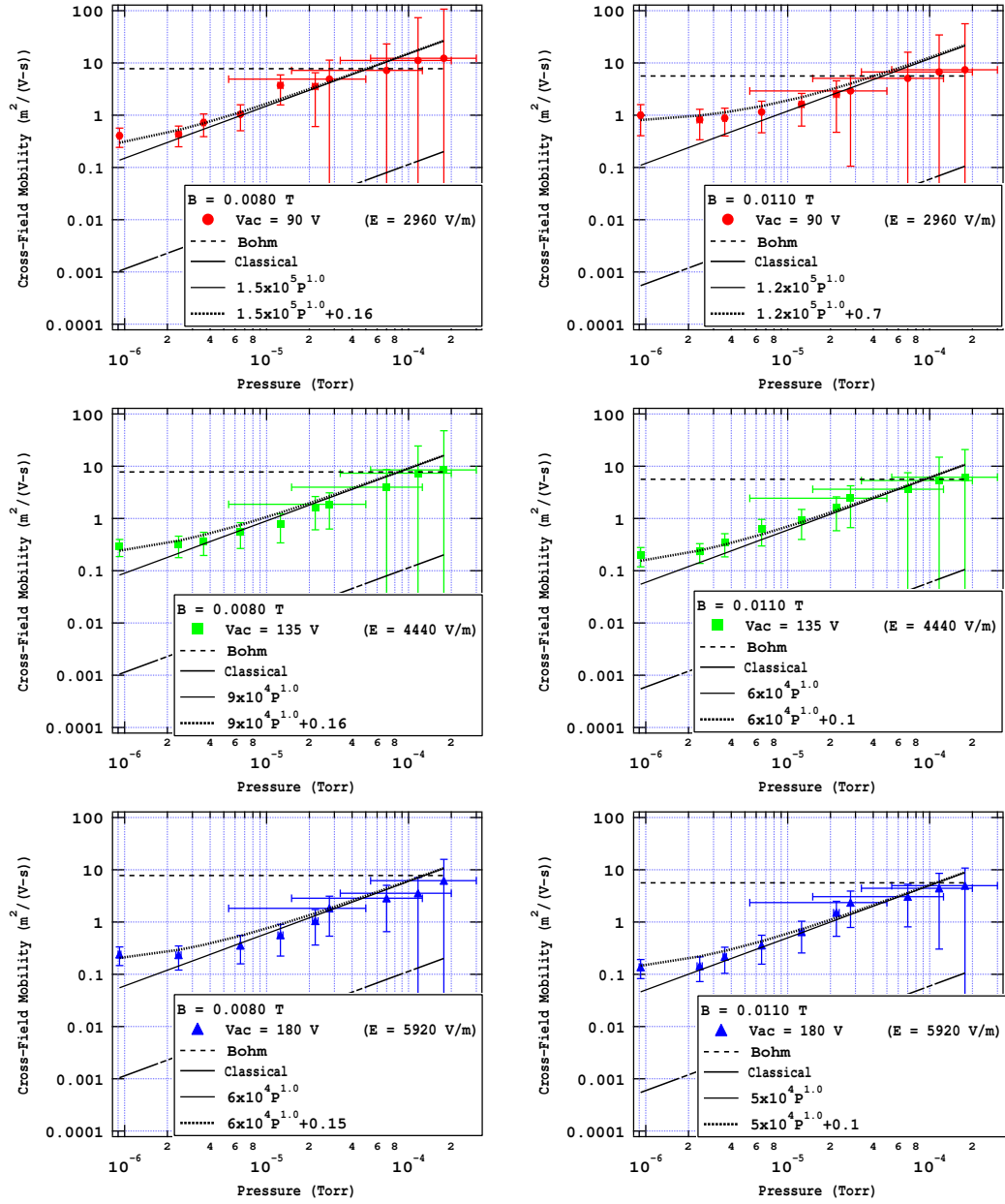
Figure 7.4: Mobility versus pressure for a magnetic field of 0.080 T (left) and 0.0110 T (right) for an electric field of 2.9×10^3 V/m (top), 4.4×10^3 V/m (center) and 5.9×10^3 V/m.

are shown in Fig. 7.5. The values of classical and Bohm mobility are shown as long-dashed and short-dashed lines, respectively. The magnitude of experimental mobility is above the classical value by more than an order of magnitude and is also below
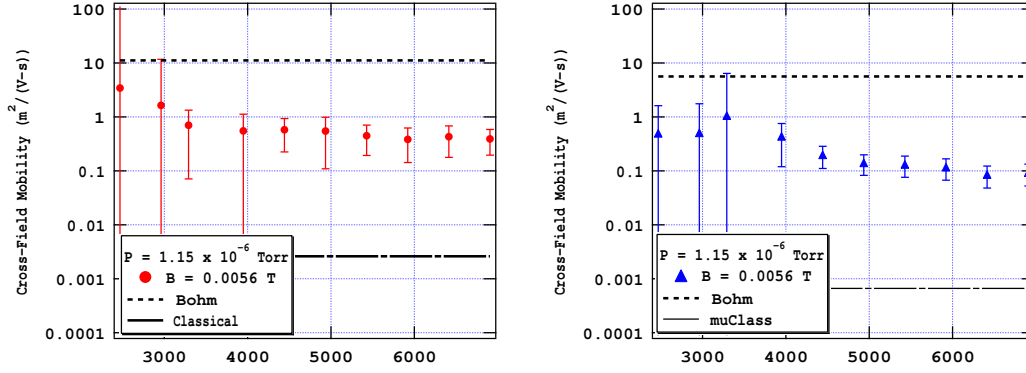
Figure 7.5: Mobility versus electric field for a magnetic field of 0.080 T (left) and 0.0110 T (right) for a pressure of 1.2×10^{-6} Torr

Bohm mobility. These results show that the experimental mobility follows neither classical or Bohm mobility, where the difference is statistically significant. Within the experimental error any trends of mobility with electric field cannot be resolved. This only indicates that the axial velocity varies proportionally with E with μ representing the constant of proportionality. This was not unexpected as both classical and Bohm mobility (and for that matter, any form of mobility, whether free, cross-field, fluctuation-induced, etc.) do not vary with E. At low electric fields the mobility appears to increase as electric field is decreased. However, the small change in mobility is not statistically significant and can not be resolved within the experimental error. Representative cases are shown in Fig. 7.5, but this trend (constant μ with E) was exhibited for all cases of pressure and magnetic field.

7.5 Other Mobility Investigations

7.5.1 μ_{ez} vs. Electron Density

Mobility was not expected to vary with electron density as electron-electron collisions do not result in net transport for electrons (p. 177 of Ref. [38]). Furthermore, if the
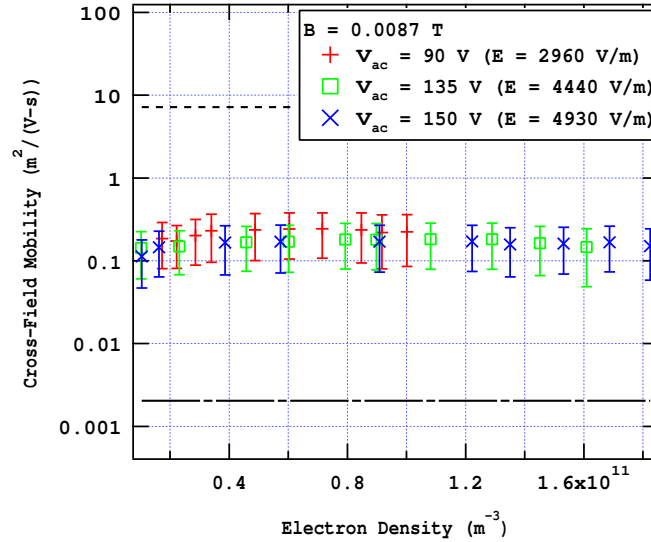
Figure 7.6: Mobility versus electron density for three electric fields, as indicated.

self-field of the plasma is in fact negligible, there would be no discernible variation in electron dynamics with changes in electron density. To confirm these assumptions the filament heater current was varied to vary the electron density over an order of magnitude as described in Section 6.3.2, and mobility measurements were obtained. Figure 7.6 shows the mobility as a function of electron density, n_e. If electron-electron collisions were responsible for transport, where the Coulomb collision frequency is directly proportional to the electron density, a change in mobility would be evident upon an order of magnitude change in electron density. The electron density had no statistically significant effect on the electron mobility indicating that electron-electron interactions were negligible over the range of electric field, magnetic field and pressure investigated.

7.5.2   "Wall" Collisions

It was hypothesized that electron collisions with the magnetic pole geometry at the confinement volume periphery could contribute to mobility by an effect analogous

to electron-wall collisions in a Hall thruster. (Wall effects in Hall thrusters were described in detail in Section 3.3.2.) The electron collision at the pole could result in a specular reflection of electrons, which would in effect be analogous to an electron-neutral collision acting on the time scale of the "bounce" collision frequency (described in Section 5.3.3) rather than the electron-neutral collision frequency.

Collisions with the magnetic pole geometry were investigated in Chapter 6 where an investigation of electron density versus loading filament bias (which was used to vary electron energy with respect to the potential well depth) was conducted. This was presented in Section 6.3.5. It was deduced from the investigation presented in Section 6.3.5 that collisions with poles resulted in electron recombination at the poles rather than a specular reflection and thus, enhanced mobility. However, a reduced electron density could be observed in the case of a much higher electron velocity, as well. Therefore, to confirm the initial supposition, the investigation was extended to include mobility measurements in response to filament bias. The anode current and the resulting mobility are presented in Fig. 7.7 where local unperturbed potential is shown as a vertical dashed line. The anode current profile shows the same general shape as the electron density profile (shown in Fig. 6.17) and thus the mobility (which is roughly the ratio of I_a to n_e) remains constant with filament bias voltage. This indicates that even under the condition where electrons were "forced" out of the confinement volume (by biasing the loading filament sufficiently) the only result is electron recombination at the poles rather than enhanced mobility. Therefore, the electron losses to the poles were regarded as an insignificant contribution to mobility.

7.5.3   Probe Configuration

The original mounting of the probe was axial through a slot in the anode, as shown in Fig. 7.8 rather than radial, as is shown in Fig. 6.2 It was suspected that physical obstruction of the probe within the confining volume could lead to substantial increases
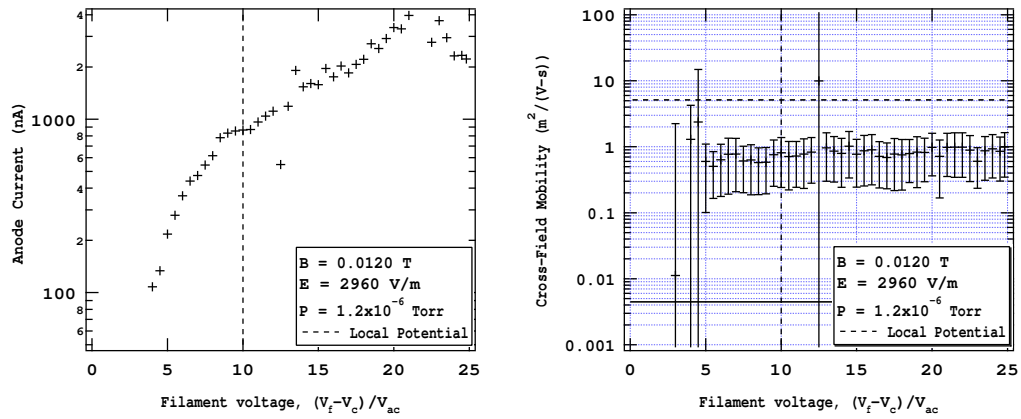
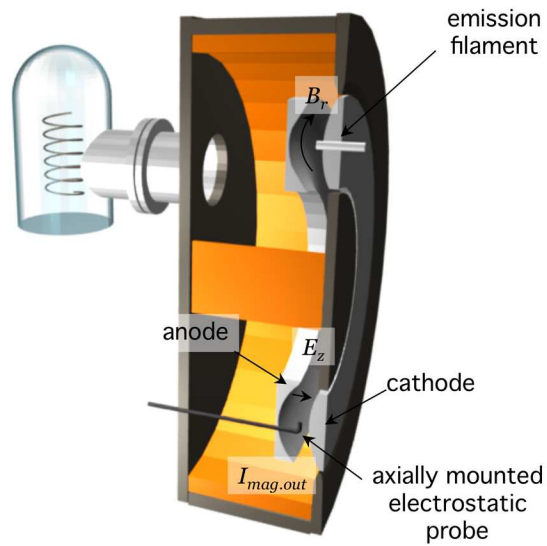**Figure 7.7:** Mobility versus filament bias.

Figure 7.8: Cross section of the Hall Electron Mobility Gage showing the original mounting configuration of the probe (axial probe mount).

in electron mobility by collisions of the electrons with the probe geometry. Electrons encounter this obstruction on the order of the magnetron orbit frequency which is greater than the electron-neutral collision frequency (see Table 5.1), up to three orders of magnitude under some conditions. In addition, during each magnetron orbit, electrons may have several "encounters" with the probe, since the bounce frequency is greater than the magnetron orbit and may pass the geometry of the probe several times. Furthermore, this obstruction was extended over the axial distance from the probe to the anode (where the axial flux measurement was taken). The mobility measurement represents an average mobility over the distance from the probe to the anode. Therefore, in the distance from the probe to the anode, electrons have several opportunities for encounters with the physical geometry of the probe. A collision with the physical geometry of the probe would have a scattering effect analogous to an electron-neutral collision frequency. Since the probe is insulated with heat shrink tubing (rather than an exposed metal surface) electrons are not expected to be "lost" upon collisions with the probe geometry, as with collisions with the magnetic pole material (described in Sections 6.3.5 and 7.5.2).

It was also suspected that the probe, which is a conductor and thus a constant equipotential surface, could perturb the vacuum field structure to cause an asymmetrical effect that could lead to enhanced mobility. Since the probe is a conductor, it provides an equipotential surface that extends perpendicular to the unperturbed vacuum equipotential surfaces created by the parallel anode and cathode electrodes. The perturbation in the potential structure creates an electric field radially outward from the probe surface which, in some cases is azimuthal. An azimuthal electric field (as described in Section 2.3) with a radial magnetic field creates an $\mathbf{E} \times \mathbf{B}$ drift in the axial direction allowing electrons to axially cross magnetic field lines without collisions. The perturbation of the probe extends a distance radially and azimuthally over an axial cross section and the electron trajectories may encounter this perturbation differently each "pass" depending on the bounce motion and the magnetron orbit.

Since the encounter with the probe structure is not always at the same radial location, the $\mathbf{E} \times \mathbf{B}$ displacement would be random. The net first-order effect is zero net transport, since the $\mathbf{E} \times \mathbf{B}$ drifts would average to zero (much like that described by Ref. [78]). However, Yoshikawa and Rose[78] show that randomized $\mathbf{E} \times \mathbf{B}$ drifts may produce a second order effect that leads to net transport that is proportional to the fluctuation amplitude or equivalently the variance of the displacement of $\mathbf{E} \times \mathbf{B}$ drifts (Eq. (2.71) and (2.72)). Perez-Luna *et al.*[133] show the effect of an electrostatic wave on a single particle trajectory. An effect similar to this (due to a randomized azimuthal electric field perturbation) is hypothesized to exist in the Hall Electron Mobility Gage.

In the radial configuration an attempt was made to minimize the perturbation by extending the probe into the confinement volume radially along an electric equipotential contour (which is also a magnetic field contour), as shown in Fig. 6.2. The radial probe configuration minimizes both the electric equipotential perturbation and the physical obstruction between the probe and the anode.

Mobility data were taken for sweeps of each parameter of electric field, magnetic field and pressure at nine combinations of the other two parameters, and data were taken according to the randomized complete block design presented in Section 7.3. The results are presented in Fig. 7.11.

The magnitude of the measured mobility for both cases lies between the classical and Bohm values. In all cases the radial probe configuration resulted in lower mobility; however, the results were not statistically significant for all conditions due to scatter in the data and measurement uncertainty. The probe configuration had the most significant effect for the conditions of high magnetic field and low pressure. It is unclear whether the reduction in mobility was due to the electrostatic perturbation or the physical obstruction, which cannot be determined from this test. Future tests incorporating electrostatic asymmetries *without* the physical obstruction (only field

Figure 7.9: A comparison of axial and radially probe mounting configurations showing mobility versus pressure (left) for constant electric field and magnetic field and versus magnetic field (right) for constant electric field and pressure.
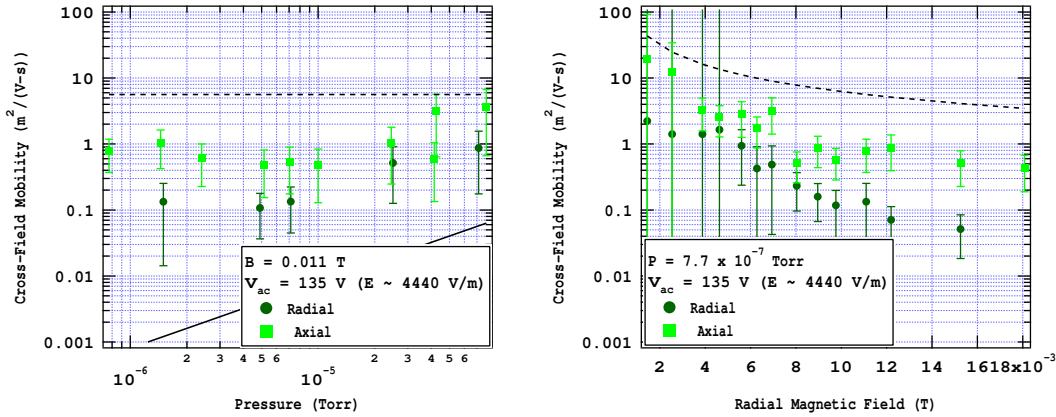
Figure 7.10: A comparison of axial and radially probe mounting configurations showing mobility versus pressure (left) for constant electric field and magnetic field and versus magnetic field (right) for constant electric field and pressure.

perturbations) may be able to confirm the cause of the enhanced mobility. Nonetheless, for all other tests presented in this dissertation the radial probe configuration was used.
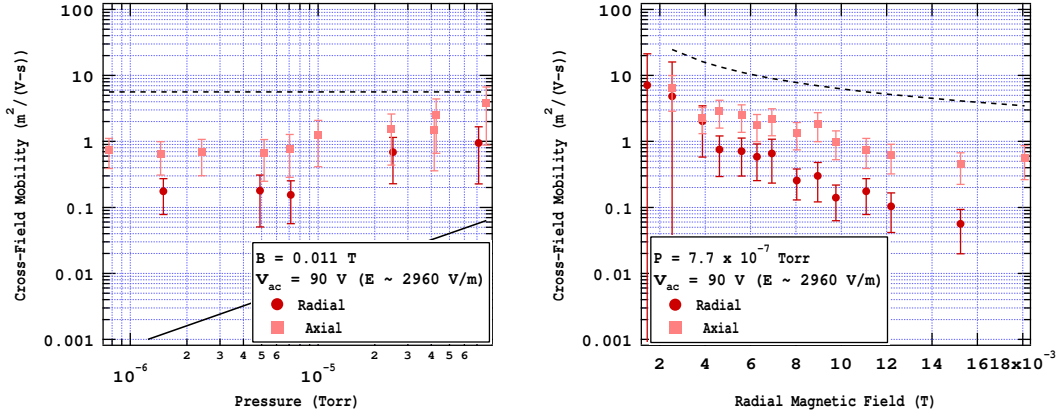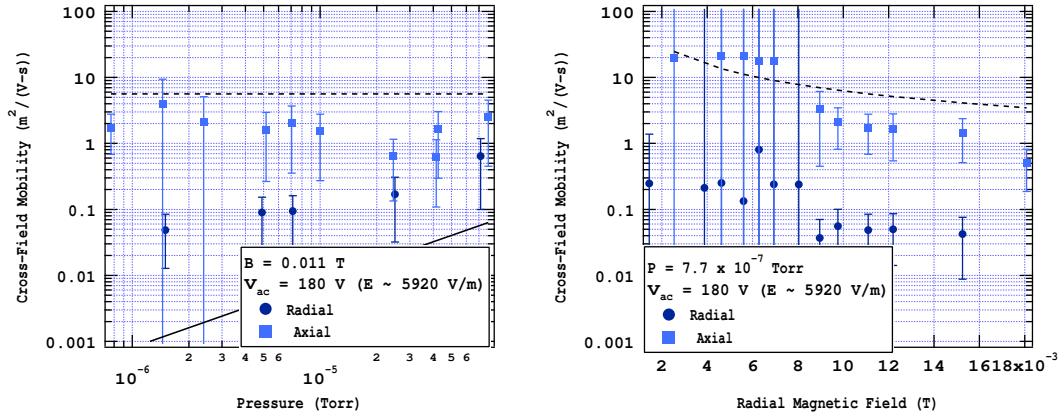
Figure 7.11: A comparison of axial and radially probe mounting configurations showing mobility versus pressure (left) for constant electric field and magnetic field and versus magnetic field (right) for constant electric field and pressure.

7.5.4 Electric Field Oscillations

Axial electric field oscillations were hypothesized to exist due to the transmission of switching noise to the anode and cathode electrodes. It was shown in Section 6.2.3 that filtering capacitors placed in parallel with the cathode electrode (shown in Fig. 6.2) were effective in reducing the fluctuations especially in the 100-700 kHz range. This frequency is on the same order as the magnetron frequency (see Table 5.1). It was thought that external oscillations that correlate with a dynamical frequency of the electron plasma may contribute to the electron mobility (especially since collective plasma effects are not able to shield the noise due to the long Debye length). Therefore, mobility was examined in response to random oscillations in the 100-700 kHz range by conducting mobility measurements with and without the capacitors incorporated. The results of these experiments are shown in Fig. 7.12.

While electrostatic oscillations on the anode/cathode potential were significantly reduced (shown in Section 6.2.3), the incorporation of filtering capacitors had no significant effect on the measured mobility within the measurement uncertainty represented by the error bars.

197

Figure 7.12: Mobility versus magnetic field for an electric field of 3.3×10^3 V/m (top), 4.4×10^3 V/m (center) and 5.9×10^3 V/m (bottom) for measurements taken with and without filtering capacitors incorporated at the cathode electrode.

198

7.6 Supporting Evidence of Non-classical Mobility

Corroborating evidence of non-classical mobility in the Hall Electron Mobility Gage exists in addition to the absolute magnitude of the electron mobility measurem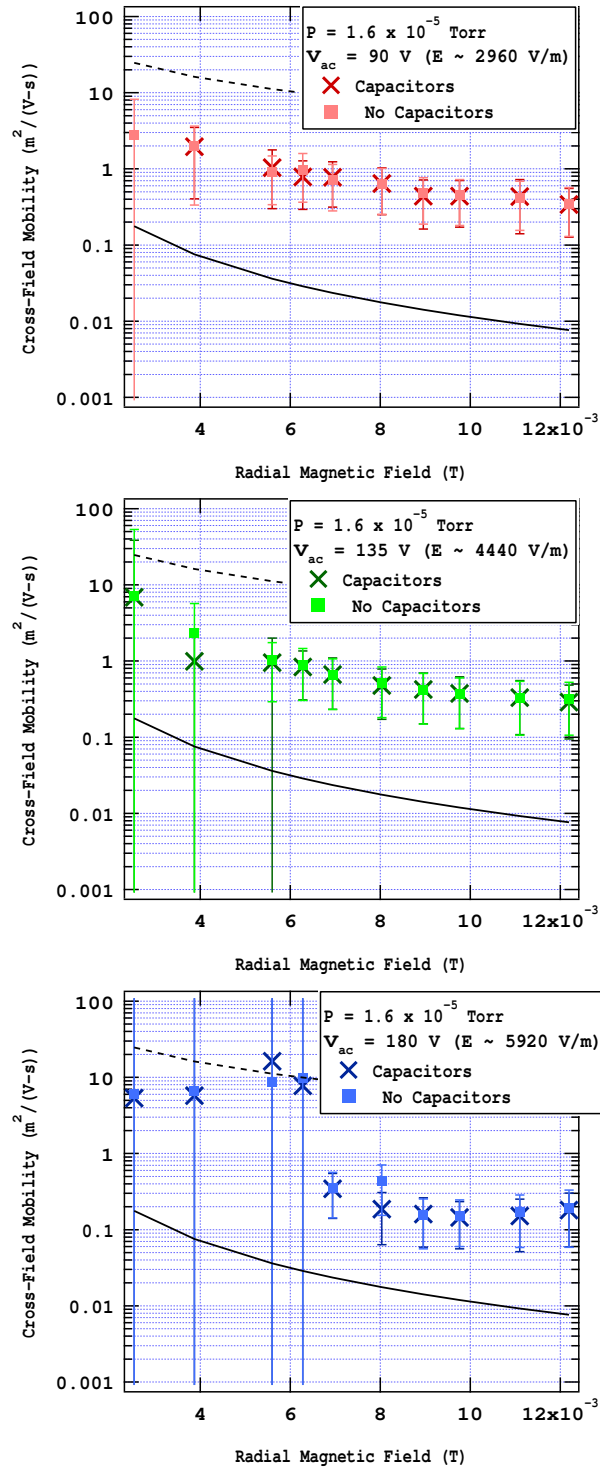ent. First, the electron temperature was found to exhibit non-classical trends, particularly with pressure, where a decrease in electron temperature with pressure was observed (Section 6.3.3). An analysis of electron temperature is presented in Section 7.6.1 where trends of electron temperature with pressure and electric field are explored for Bohm mobility, classical Mobility and a combination of an unknown collision-less mobility mechanism with classical mobility. This analysis was adapted from Ref. [8], which predicts electron temperature due to various transport mechanisms. More evidence supporting collisionless mobility comes from an analysis of the ionization within the confinement volume. It was found that in inspecting the mean-free-path for electron-neutral collisions and a peak in the ion density as it varies with electric field, the path length and axial velocity of electrons within the Hall Electron mobility Gage may be inferred, which agree with the measured mobility and thus axial velocity of electrons. This analysis is presented in Section 7.6.2. These lend support for the existence of a non-classical, collisionless mobility within the Hall Electron Mobility Gage.

7.6.1 Electron Temperature Analysis

Results for electron temperature with variation of the controlled parameters of electric field and pressure were presented in Section 6.3.3. Some general trends of electron temperature were shown to be statistically significant where the variation in electron temperature over the range of the parameters investigated was greater than the experimental error. The trends observed include the decrease in electron temperature with increasing pressure, particularly at high electric and magnetic fields and the in-

crease in electron temperature with increasing electric field. On closer inspection it is suggested that these trends indicate a collisionless transport mechanism. The reasoning for this interpretation is presented below. (The response of electron temperature to neutral density was first presented in Ref. [118].)

An argument may be made that, given purely classical mobility, the axial profile of electron energy should be unchanging with neutral density (pressure); conversely, if electron temperature (at a particular axial location) were found to vary with neutral density, a non-classical transport mechanism was present that was not dependent on electron-neutral collisions. Assuming electrons are magnetized (large Hall parameter), the number of total collisions required to traverse a given distance across the magnetic field is fixed by the field conditions, regardless of how often collisions take place. This may be realized by inspection of Eq. (2.55) which gives the axial step length of magnetized electrons, which only depends on E and B. At constant electric field, the total energy available to electrons is fixed as well. Electrons lose a certain amount of energy through inelastic collisions with neutrals, which is dependent on incident electron energy, where incident energy is governed by the energy gained from the electric field and thus energy losses are also fixed by the field conditions. Therefore, the net energy change for electrons as they traverse the confinement volume axially is independent of collision frequency, since both the total number of collisions and the energy gain and loss for an electron moving through the confinement volume are fixed by the field conditions. In other words, the collision frequency would only affect the total residence time of electrons in the trap (or equivalently axial velocity, u_{ez}), but collision frequency would not affect the total energy gain and collisional cooling effects as an electron traverses from the loading filament to the anode. (In the limit of complete vacuum where collision frequency is zero, an electron will not move through the confinement volume and will remain indefinitely in an azimuthal $\mathbf{E} \times \mathbf{B}$ orbit.) Therefore, if collisions are solely responsible for cross-field mobility, the axial profile of electron temperature (or electron temperature at a given axial location) will be

constant with collision frequency and hence neutral density.

In the case of collisionless or anomalous mobility, electron temperature could be dependent on electron-neutral collision frequency. To illustrate this, consider a mechanism for cross-field electron mobility that allows electrons to move across the field in complete absence of neutrals (vacuum condition). The time-of-flight required to travel from cathode-to-anode would be finite regardless of collision frequency (in contrast to collisional mobility where time-of-flight would be infinite in the absence of collisions). The presence of neutrals would, however, affect the temperature of the electrons because of collisional cooling; the degree to which electrons are cooled depends on the number of collisions an electron encounters while moving through the trap. In the limit of absolute vacuum an electron experiences no collisions and gains the maximum amount of energy from the field, displaying a high electron temperature. In the case of low neutral density, electrons are cooled as they suffer collisions during their journey; as neutral density increases the amount of "cooling" would increase, showing a decrease in T_e as n_0 is increased. It follows then that the observed variation of electron temperature with neutral density is consistent with a mobility mechanism that does not require electron-neutral collisions.

The second "non-classical" temperature trend is observed in the investigation of electron temperature with electric field. Electron temperatures have been found to increase proportionally with electric field, with the constant of proportionality defined as a fraction of the total available energy, as shown in Fig. 6.13, but sometimes to values that correspond to energy that is significantly higher than the excitation or ionization energies for argon (where electron energy is given as $E_e = 3kT_e/2$). The electron temperatures are realistic given the amount of total energy available to electrons from the applied field. However, energy is lost in excitation and ionization collisions, as described by the analysis given below. At the highest electric fields the electron temperature corresponds to an energy that is in some cases much higher than the excitation and ionization energies of argon (11.5 eV and 15.8 eV, respectively).

The values of measured electron temperature are not expected by classical theory as the cross-section for excitation and ionization collisions increases rapidly at energies above the ionization/excitation threshold and inelastic collisions become much more probable. Inelastic collisions would serve to "quench" the electron temperature. Therefore, if only collisions were responsible for cross-field mobility, electrons would gain energy until the electron energy was sufficient for excitation or ionization where any energy gain in excess of the excitation/ionization energy would be lost in the next collision. Electron energy for classical mobility, then, would be expected to approach the excitation/ionization energy but then would remain constant, regardless of V_{ac} or axial distance traveled within the confinement volume. The measured electron temperatures correspond to electron energy which is sometimes significantly higher than the excitation or ionization energies, even within the realm of experimental error.

This type of electron temperature investigation (i.e. determining the type of mobility based on analysis of electron temperature) is illustrated eloquently by Levchenko[8] in the derivation of an electron energy equation for classical and Bohm mobility. This equation accounts for energy gain from the electric field and energy losses due to ionizing collisions. Here the equations are adapted from Levchenko to reflect both the nomenclature used throughout and the geometry of the Hall Electron Mobility Gage (axial E, radial B). The change in electron thermal energy (of an electron population) is given by

$$\frac{\partial \epsilon_e}{\partial z} \; = \; E_z - \psi_e \bar{\epsilon}_i \tag{7.8}$$

where E_z is the axial rate of energy gain due to the electric field, $\psi_e \bar{\epsilon}_i$ is the energy loss per distance traveled and ϵ_i is the energy change (loss) per collision (in Levchenko[8] this energy loss accounts for both the ionization energy loss from the incident electron and the addition of the "born" electron in the electron energy distribution with energy equivalent to the neutral density, i.e. very low energy). The energy loss per distance

traveled ($\psi_e \bar{\epsilon}_i$) may be expressed as

$$\psi_e \bar{\epsilon}_i = \frac{\nu_i \bar{\epsilon}_i}{u_{ez}} \tag{7.9}$$

where ν_i is the ionization collision frequency given by

$$\nu_i = n_0 \langle \sigma_{ion} v_e \rangle = n_0 \int\limits_0^\infty \sigma_i(v_e) v_e f(v_e) dv_e \tag{7.10}$$

and u_{ez} may be found using the mobility coefficient and electric field (Eq. (1.1)). Substituting the classical mobility coefficient and the Bohm mobility coefficient (Eq. (2.52) and (2.65), respectively) results in equations (7.11) and (7.12):

$$\frac{\partial \epsilon_e}{\partial z} = E_z - \frac{e}{m_e} \frac{\sigma_i}{\sigma_m} \frac{B_r^2}{E_z} \bar{\epsilon}_i \tag{7.11}$$

$$\frac{\partial \epsilon_e}{\partial z} = E_z - n_0 \sigma_i \bar{v}_e \frac{16 B_r}{E_z} \bar{\epsilon}_i \tag{7.12}$$

(the constant cross-section approximation has been made in these equations, which does not have any consequence on the main point of presenting these equations—it only removes an integral so it is more convenient to write)

Within these equations it is apparent that the energy in the classical solution is not dependent on neutral density; however, the energy in the equation solved using the Bohm mobility coefficient retains a dependence on neutral density. Equation 7.12 would retain the dependence on neutral density for any collisionless mobility mechanism, where in the general case the energy equation is given by

$$\frac{\partial \epsilon_e}{\partial z} = E_z - \frac{n_0 \sigma_i \bar{v}_e}{\mu_{ez} E_z} \bar{\epsilon}_i \tag{7.13}$$

A numerical model was employed to determine the classical and Bohm electron energy (and thus electron temperature where $E_e = 3kT_e/2$) for the Hall Electron Mobility

Figure 7.13: Electron temperature versus E_z (top) and versus P (bottom) showing measured electron temperature and numerically derived electron temperature (solid lines, corresponding colors) for classical (left) and Bohm (right) models based on the analysis of Ref. [8]

Gage, based on the energy analysis by Levchenko. Here, the step in distance was fixed and the energy change was variable per step. In this analysis, electrons born out of ionizing collisions were given an energy of 0.1 eV[146] and the total energy was recalculated incorporating the "born" electrons into the distribution. The constant cross-section approximation was used where the average energy per step was used to determine the corresponding momentum-transfer and ionization cross sections. The results to the classical and Bohm models for electron temperature with pressure and electric field are shown in Fig. 7.13.

The electron temperatures calculated using the Bohm mobility model were much

higher than measured values. However, given the order of magnitude of the experimental mobility, which was always less than the Bohm mobility, it was suspected that the Bohm model overestimated the axial velocity (and thus energy gain) so the disagreement was not unexpected. Adapting the analysis shown above (Eq. (7.13)), a third model was applied presenting an anomalous mobility constant in addition to the classical mobility, which varies with neither B nor pressure and is given as a constant of $\mu_{AN} = 0.005^{\dagger}$. The energy equation in this case is given by

$$\frac{\partial \epsilon_e}{\partial z} = E_z - \frac{n_0 \sigma_i \bar{v}_e}{(\mu_c + \mu_{AN}) E_z} \bar{\epsilon}_i \qquad (7.14)$$

This analysis (of μ_{AN}) is in no way meant to be exhaustive, but is presented only to qualitatively examine the effects of a constant "axial leakage current" that allows electrons to traverse from anode to cathode in absence of collisions, which could dominate at low pressures. The results of this analysis are presented in Fig. 7.14.

The "axial leakage current" model captures both of the "anomalous" trends noted above. The "quenching" of the electron temperature with electric field is exhibited in Fig. 7.13 (top left), where the "axial leakage current" model (Fig. 7.14, (top)) shows the increase in electron temperature with electric field well beyond the ionization and excitation thresholds, similar to what was observed. The variation of electron temperature with pressure is exhibited in Fig. 7.14 (bottom). showing at least qualitative agreement with observations, especially at high electric and magnetic fields.

The trends captured by the "axial leakage current" model at least qualitatively agree with what is observed, particularly concerning the variation of electron temperature with pressure. The trends of electron temperature represented by the "axial leakage current" model also qualitatively agree with the trends of temperature with electric field, where in the classical model the electron temperature is "quenched" at

---

†The choice of the value of $\mu_{AN} = 0.005$ was largely arbitrary. The only justification for using this value is that under higher pressure conditions, the classical mobility dominates ($\mu_{class} > 0.005$) and under the lowest pressure conditions, the anomalous mobility dominates ($\mu_{class} < 0.005$).
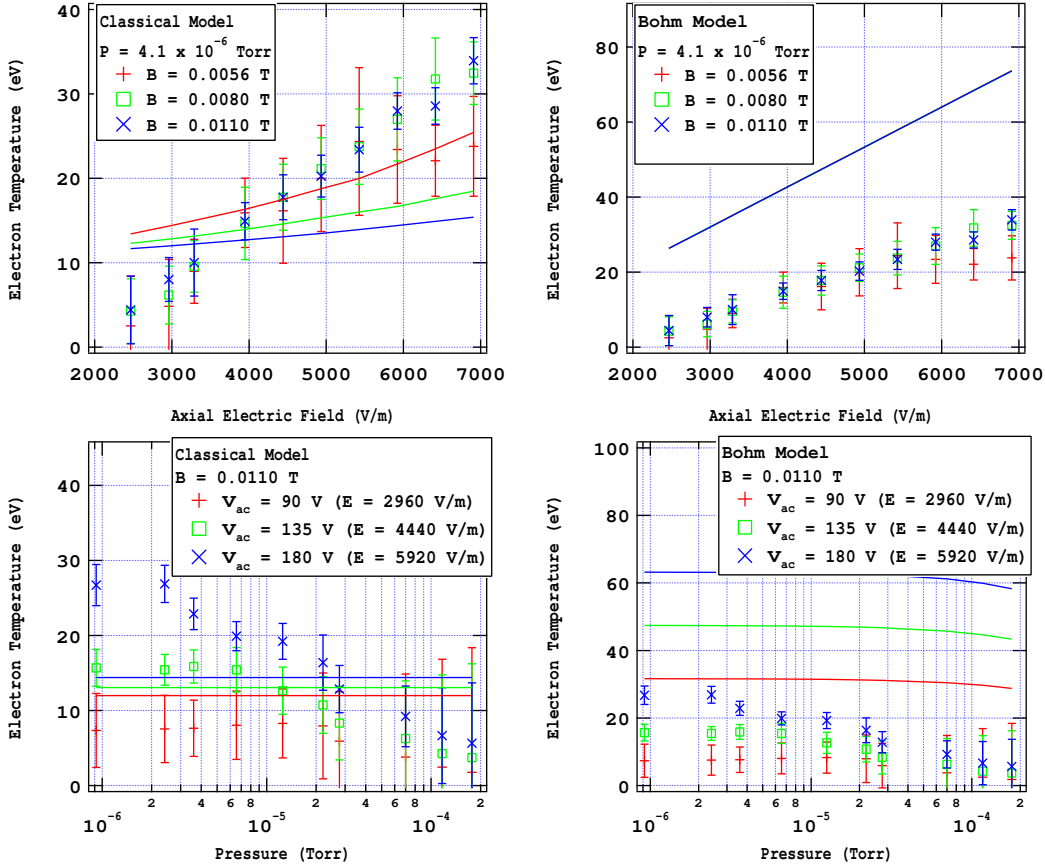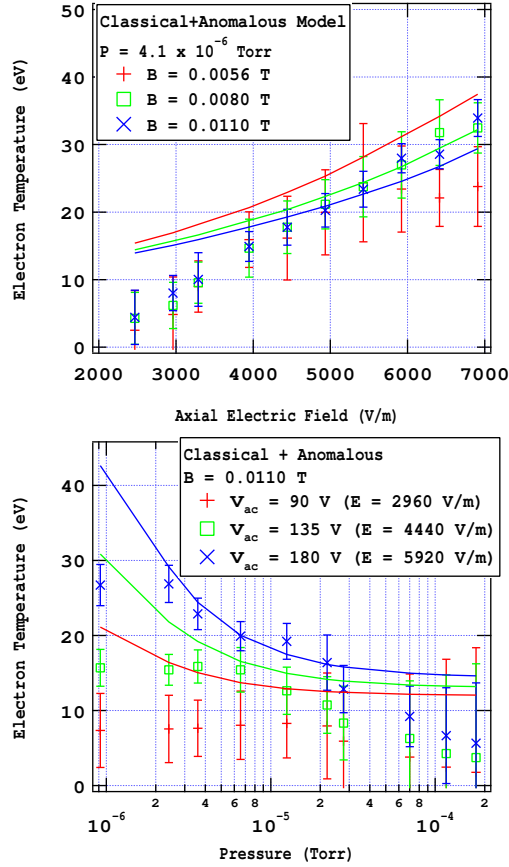
Figure 7.14: Electron temperature versus E_z (top) and versus P (bottom) showing measured electron temperature and numerically derived electron temperature (solid lines, corresponding colors) for classical mobility with the addition of a small anomalous component, based on the analysis of Ref. [8]

a lower value but the "axial leakage current" model results in an electron temperature increasing more prominently with electric field. Although the classical model for electron temperature is not far outside the realm of experimental error, the trends are more fully captured with the "axial leakage current" model. This provides corroborating evidence for a collisionless mobility mechanism in light of the mobility measurements obtained. These results are encouraging and give credence to the existence of a collisionless mechanism contributing to the overall mobility in the Hall Electron Mobility Gage.
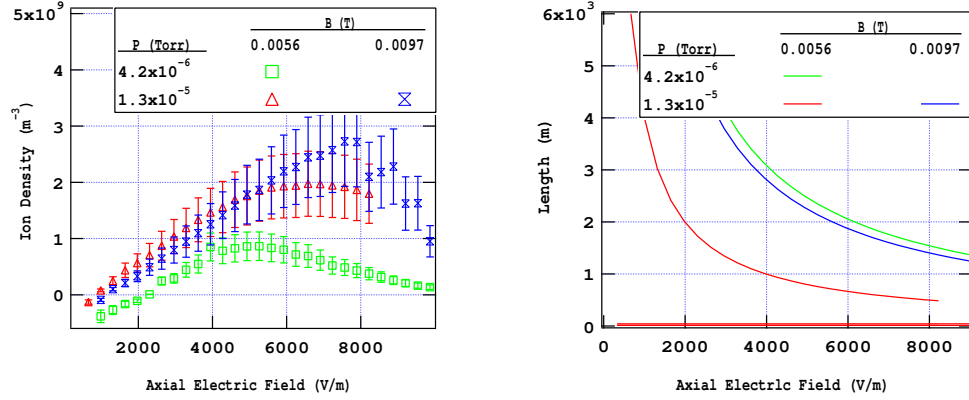
Figure 7.15: The ion density versus electric field for two conditions of pressure at a constant magnetic field (red and green) and two magnetic field conditions at a constant pressure (red and blue) (left) and the classical path length given by Eq. (7.18) for the conditions noted.

7.6.2 Path Length Analysis

Besides the desire to quantify ionization for practical reasons (diagnostics, etc.), it was found that ionization trends may give insight into mobility. The existence of ionization points to the obvious fact that collisions are taking place within the Hall Electron Mobility Gage, where the transport cannot be described by a strictly collisionless mechanism (such as Bohm mobility). However, the ion density results also suggest that at low pressures, there is another mechanism driving transport as negligible ionization is observed, even when electrons have sufficient energy to ionize background neutrals. In investigations where the electric field was extended beyond the field conditions typically employed in the Hall Electron Mobility Gage experiments, the ion density reached a peak value, where increasing the field beyond this point resulted in decreased ionization (for constant pressure and magnetic field). Figure 7.15 shows the ion density versus electric field for representative traces. In these plots there is a discernible peak in ion density as the electric field was increased, where the peak was shifted depending on the parameters of magnetic field and pressure. The blue and red traces ($\times$ and $\triangle$) show two different magnetic field conditions at the

same pressure. The green (○) and red (△) traces show the same magnetic field conditions for two different pressures. The peak occurs at a higher electric field for a higher pressure (peak∼pressure) and occurs at a higher electric field for a higher magnetic field (peak∼magnetic field). This peak is thought to exist due to the tradeoff between increasing energy (greater chance of ionization) and decreasing path length for electrons within the confining volume. It is hypothesized that the drop off occurs at the point where the path length for electrons becomes shorter than the mean free path for ionization. Taking this one step further, this peak may be used to infer a path length for electrons. The residence time for an electron within the confinement volume (time required for an electron to travel from filament to anode) is given by

$$\tau_{res} = \frac{\Delta z_{f-a}}{u_{ez}} \tag{7.15}$$

where Δz_{f-a} is the axial distance between the filament and the anode and u_{ez} is the axial velocity. The average path length is given by

$$\ell = \bar{v}_e \tau_{res} \tag{7.16}$$

where $\bar{v}_e$ is the average thermal velocity. Substituting for the residence time, and using the mobility equation for u_{ez} results in a path length of

$$\ell = \frac{\bar{v}_e \Delta z}{\mu_{ez} E_z} \tag{7.17}$$

Classically the path length is given by

$$\ell = \frac{\bar{v}_e e B^2 \Delta z}{\nu_{en} m_e E_z} \tag{7.18}$$

The classically determined path lengths (corresponding colors) are shown in Fig. 7.15 (right) for each of the conditions presented in Fig. 7.15 (left). It would be logical to deduce that the peak in Fig. 7.15 (left) occurs where the path length equals the

mean free path for electrons. However, the path lengths found from the classical equation are 2-3 orders of magnitude higher than the mean free path for each of these conditions. It is likely (especially due to the non-classical mobility observed) that the path length is much shorter than that which was classically determined.

The general equation (Eq. (7.17)) was used in reverse to determine the mobility suggested by the peak in ionization. This method is illustrated as follows: if the path length were set equal to the mean free path at the electric field, magnetic field and pressure conditions of the peak, the mobility at which the equality would be satisfied may be calculated as.

$$\mu_{ez} = \frac{\bar{v}_e \Delta z}{\lambda_m E_{z,peak}} \tag{7.19}$$

For the green trace the mean free path is 40 m (electron temperature was approximated as 15 eV). Setting this equal to the path length, using the electric field of 4.9×10^3 V/m corresponding to the peak ion density, and using $\bar{v}_e$ corresponding with 15 eV electrons results in a mobility of 0.40 m^2/(V-s), which is shockingly close to that which was found experimentally (Fig. 7.5). (Δz in this case is 0.027 m.) For the red trace, with the peak at $E = 6.6 \times 10^3$ V/m and a mean free path of 13 m, the mobility was found to be 0.90 m^2/(V-s) which also agrees well with the data (Fig. 7.4). For the blue trace, with the peak at 7.5×10^3 V/m and mean free path of 13 m, the mobility was found to be 0.80 m^2/(V-s). Unfortunately there was no experimental data for comparison at this electric field condition, however, qualitatively this is lower than the previous (red) trace, which given the higher magnetic field, is plausible. These values of mobility are in striking agreement with the experimental results and even exhibit the right trends (lower mobility for lower pressure and higher magnetic field). Although, the limited data makes this analysis suspect and far from conclusive, it surprisingly exhibits remarkable agreement with the experimental results.

7.7 Summary

The order of magnitude of mobility observed is 20 to 100 times the classical value and only approaches the classical value (where classical mobility lies within the bounds of experimental error) at the highest pressures investigated. It was observed that the mobility tends to decrease with magnetic field where the decrease is statistically significant. However, within the bounds of experimental error it was not possible to determine whether the experimental mobility exhibits a B^{-2} or B^{-1} trend. A curve fit was applied to the experimental data, where the trend of mobility with B showed less than B^{-2} scaling under some conditions where the B^{-1} scaling agreed better with the experimental data; however, a curve fit of B^{-2} still falls within the error bars representative of the experimental uncertainty in those conditions. In general, the experimental mobility increased with pressure, but yet again, it is not possible to discern whether the experimental mobility exhibits classical (1:1) scaling with pressure within the experimental error. It appears that the mobility exhibits more classical scaling at higher pressures and at lower pressures another mechanism dominates where the mobility fails to continue to decrease with decreasing pressure, although this is merely speculative. (Future work includes construction of a high vacuum facility to extend the pressures 2-3 orders of magnitude lower to examine this trend.) The mobility does not exhibit any decisive trend with electric field, which confirms the definition that mobility as a constant of proportionality between the axial velocity and electric field.

Although trends could not be resolved within the experimental error, classical trends appear to be at least qualitatively represented where mobility increases with pressure, decreases with magnetic field and remains constant with electric field. Therefore, the mobility mechanism is thought to either exhibit similar trends to classical or it is possible that the mobility mechanism in the Hall Electron Mobility Gage exhibits a combination of classical mobility with an anomalous component. The latter

is speculated to be likely due to the apparent "flattening" of mobility with further decreases in pressure, pointing to a constant mobility at low pressures. These statements are purely speculative since they cannot be resolved within the experimental error.

The experimental mobility was higher than the classical mobility, where this difference was statistically significant within the experimental error, and lower than Bohm mobility, also statistically significant within the experimental error. It is undeniable that non-classical mobility was observed in the Hall Electron Mobility Gage. The following measurements and trends confirm the existence of collisionless and/or enhanced mobility in the Hall Electron Mobility Gage:

1. The magnitude of the directly measured mobility is 20-100 times the classical value of mobility

2. The trends of electron temperature, especially the variation of temperature with pressure, support the existence of a collisionless mobility mechanism.

3. The peak in ion density with electric field suggests a path length much shorter than the classical path length for electrons within the confinement volume. The mobility suggested by this analysis does not agree with the classical value but shows remarkable agreement with experimentally measured mobility.

Other mobility experiments conducted failed to provide the source of the enhanced mobility, where the mechanism responsible for mobility in the Hall Electron Mobility Gage remains elusive. However, the experiments presented herein provide insight into what is *not* causing the enhanced mobility. These are as follows:

1. The investigation of the trap loading effects (particularly in the variation of the filament bias) indicate that collisions with pole geometry were an unlikely cause of enhanced mobility. This, with the absence of dielectric walls, rules out any analogy to near wall conductivity.

2. Coulomb collisions due to electron-electron interactions were ruled out by the measurements of electron density.

3. The indiscernible change in mobility upon the dampening of noise on the electrodes (responsible for axial electric field oscillations) suggested that mobility was not caused by external circuit noise introduced at the anode and cathode electrodes in the range of 100-700 kHz.[‡]

4. Bohm mobility was disregarded due to the absence of oscillations, the mobility magnitude, and the electron temperature analysis

The mobility was affected by both the magnetic field misalignment and the probe configuration. The magnetic field distortion due to the saturation of the inner magnetic core material produced enhanced mobility at high magnetic field conditions, shown in Appendix B. The correction of the distortion was presented in Section 6.2.1 but failed to produce classical mobility. The probe configuration also did have a statistically significant effect under some conditions where the axial probe configuration produced higher mobility, and although the radial probe configuration served to reduce the mobility, the new configuration also failed to bring the experimental mobility to the level of classical mobility. Both of these effects were "corrected" and yet classical mobility was not observed. Measurements of mobility have yet to be taken in complete absence of the probe where the path length analysis provides a possible means for investigating the contribution of the probe to the overall mobility.

Several mechanisms that are hypothesized to be responsible for electron mobility in Hall thrusters were absent in the Hall Electron Trap. Collective plasma oscillations are negligible compared to the thermal motion of the electrons (given as a consequence of the long Debye length) so that instabilities will not lead to the growth and propagation of plasma waves within the plasma. External oscillations are also

---

[‡]A similar effect was postulated by Eggleston in Penning trap experiments with the same indiscernable result[112].

tentatively precluded by investigation of axial oscillations in the 100-700 kHz range; however, higher frequency oscillations have yet to be explored. Near wall conductivity is the other leading theory for the mechanism of enhanced mobility in Hall thrusters. The dielectric walls were physically absent in the Hall Electron Mobility Gage and collisions with magnetic poles were found to be negligible based on both the theoretical analysis presented in Section 5.3 and the experimental analysis presented in Sections 6.3.5 and 7.5.2. The experimental mobility found in the Hall Electron Mobility Gage was on the whole, lower than the mobility in Hall thruster plasmas, so the possibility of these mechanisms (wall effects and oscillations) contributing to mobility still exists. However, the notable result of these experiments is that without these effects, mobility remains non-classical.

Chapter 8

Conclusions & Future Work

8.1   Contributions of This Work

The achievement of this work has been to recreate anomalous mobility in an $\mathbf{E} \times \mathbf{B}$ drift device, the Hall Electron Mobility Gage, that provides insight into mechanisms that could cause mobility in Hall thrusters and other similar configurations. There is little doubt that non-classical and non-Bohm mobility was exhibited in the Hall Electron Mobility Gage. Besides the order of magnitude mobility observed, there were several observations that provided corroborating evidence of a collisionless transport mechanism which resulted in electron cross-field mobility in excess of the classical value. The source of the enhanced mobility remains unknown, but the two most cited contributors to mobility in Hall thrusters, wall effects and oscillation-induced or Bohm mobility, were shown to be absent. The mobility observed in this device was lower than what has been typically observed in Hall thrusters, so the findings presented in this document do not negate the possibility of one or both of these effects contributing to Hall thruster mobility. However, this work has identified the existence of another mobility mechanism, inherent in these devices, which is higher than classical mobility and has not been previously identified.

In the design of the Hall Electron Mobility Gage, the electric and magnetic field geometry of a Hall thruster was replicated, both in magnitude and shape. The resulting dynamics of charged particles within the fields exhibit comparable behavior. Ions are unmagnetized, the electron gyro-motion is the highest frequency micromotion, followed by a bounce frequency where free streaming electrons oscillate radially within a potential well, and a magnetron frequency where the $\mathbf{E} \times \mathbf{B}$ drift causes an annular orbit. Electrons are also influenced by an axial electric field which drives axial transport. These field conditions and dynamics are analogous between the Hall Electron Mobility Gage and the Hall thruster. The Hall Electron Mobility Gage exhibits two distinct and significant deviations from the environment of a Hall thruster. These are the absence of collective plasma oscillations and the absence of dielectric walls, both being cited as the dominant contributors to cross-field electron mobility. These two contributors were absent in the Hall Electron Mobility Gage, where this claim was confirmed both analytically and experimentally.

First, the Hall Electron Mobility Gage does not support collective plasma oscillations. This statement was initially validated (presented in Section 2.1.3) by the analytical model presented by Pines and Bohm[57] where on length scales small compared to the Debye length, collective plasma effects become insignificant and the motion is dominated by thermal motion, that must be described on a single-particle level. The Debye length of the plasma in the Hall Electron Mobility Gage was controlled to be much larger than the confinement volume dimensions by maintaining a low-density and high temperature plasma. These conditions were confirmed experimentally through measurements of electron temperature and density and based on the measurements combined with the derivation of Pines and Bohm, it was anticipated that collective plasma oscillations would not be sustained in the Hall Electron Mobility Gage.

Very obviously the physical absence of dielectric walls removes the near-wall conductivity, proposed to exist in Hall thrusters. However, it was presumed that

collisions between electrons and the physical geometry of the magnetic pole material in the Hall Electron Mobility Gage may contribute to mobility in a similar way to wall effects in Hall thrusters. Through a velocity space analysis (presented in Section 5.3) it was found that due to the depth of the confining potential well, the energy of the trapped electrons and the slow energy diffusion (which would serve to "fill" the Maxwellian tail of the energy distribution) collisions with magnetic pole geometry were expected to be infrequent under the condition of a "deep" potential well relative to the electron energy. "Wall" collisions were investigated experimentally where collisions with poles were "forced" by varying the emission filament bias to be strongly electron repelling. Significantly reduced electron density in this case was observed presumably due to electron losses at the magnetic poles. However, even under the condition of reduced electron density mobility remained unchanged, where the electron collisions with the poles produced electron losses due to recombination rather than an enhanced mobility. Upon increasing the emitting filament bias (to the local potential at the location of the filament) a stable electron density was maintained with few electron losses. The analytical and experimental results suggested that collisions with the geometry of the magnetic poles were insignificant.

Three independent sources were all in support of the fact that a collisionless mobility mechanism was present in the Hall Electron Mobility Gage. First, the order of magnitude of measured mobility was 20 to 100 times the classical value. Second, the trends of mobility with electron temperature, particularly the variation in temperature with pressure, suggested a non-classical mobility mechanism. Furthermore, the strong increase in temperature with electric field well beyond the excitation and ionization potentials, which would serve to "cool" electrons, suggested that collisions were not the only mechanism of transport. The final effect supporting non-classical mobility was the analysis of the path length of electrons, where a peak in ion density was observed with variations in electric field. On the premise that the peak in the ionization equates with the point where the path length was equal to the mean free

path, mobility was inferred by the equation for path length presented in Section 7.6.2. The mobility deduced by the path length analysis exhibited striking agreement with experimental measurements of mobility under the same conditions. Furthermore, the path length suggested by the classical model was much too long for this phenomenon (the peak in ion density) to exist. In this analysis, the number of data points were few, but the agreement warrants further investigation into this method of experimentally measured mobility. The order of magnitude, combined with the temperature and ionization trends with variations in control parameters, provided convincing evidence that non-classical mobility was in fact present.

Other investigations were conducted in order to assess possible mechanisms for non-classical mobility. The probe configuration was investigated for both electrostatic and physical perturbations. Also the magnetic field-electrode alignment was investigated for all field conditions explored. Both of these did have an effect on mobility. However, upon "correction" of these effects, the observed mobility still did not behave classically. The investigation of mobility with variation in electron density also ruled out the effect of electron-electron Coulomb collisions, where the Coulomb collision frequency is a direct function of electron density. Finally, external electrostatic field oscillations were investigated resulting in no discernable effects. These investigations provided great evidence to what the non-classical mobility mechanism is *not*, yet the mechanism driving the anomalous mobility has yet to be identified.

The trends of the measured mobility with controlled parameters exhibit some evidence of collisional classical mobility including an increase in mobility with pressure, decrease in mobility with magnetic field and no statistically significant change in mobility with electric field. Although inferring the functional relationship of the mobility trends with magnetic field and pressure is purely speculative within the realm of experimental error, it was noted that the relation of mobility with pressure exhibited less than 1:1 (especially at low pressures) and the relation with magnetic field may scale with B^{-1}, where neither trend would be expected of classical. If the apparently

non-classical trends are found to be statistically significant upon further investigation it would be likely that the total mobility is a combination of collisional mobility and an anomalous component. (These trends may be refined upon obtaining additional experimental data and refining diagnostics techniques.)

A remaining possibility for a mechanism driving enhanced mobility is a mechanism that is inherent in the geometry of the $\mathbf{E} \times \mathbf{B}$ drift device. $\mathbf{E} \times \mathbf{B}$ drift devices, used mostly for plasma propulsion or material processing, have been plagued by anomalous mobility since their inception. The applications where these devices are used require a relatively dense plasma (relative to the plasma in the Hall Electron Mobility Gage among other non-neutral plasma devices). The experiments performed on these devices have typically been plagued by the confounding factors of a turbulent plasma combined with complicated plasma self-field structures (wall-sheath effects, etc.). Because of the requirements of these applications, the reduction of plasma density in order to reduce the plasma environment to quiescent, non-oscillating, and uncoupled has never been attempted. While classical (or near classical) transport has been observed in the geometry of a Penning trap, classical transport has never been observed in an $\mathbf{E} \times \mathbf{B}$ drift device. The results of these experiments lead one to believe that an $\mathbf{E} \times \mathbf{B}$ device may not be capable of exhibiting classical mobility (because gosh darnit, we tried) due to the inherent geometry of the device. The existence of a transport mechanism introduced at the reflection at the radial periphery due to the confining potential has been proposed by Thomas[55], which is based on single particle effects and would be present in the Hall Electron Mobility Gage. The mobility in the Hall Electron Mobility Gage remained 20-100 times the classical value, where identifying and/or eliminating the anomalous mechanism for mobility in the Hall Electron Mobility Gage may provide gains for several types of $\mathbf{E} \times \mathbf{B}$ drift devices.

8.2   Future Work

As is always the case, this experimental investigation led to just as many (probably more) questions as conclusions. Several goals and proposed methods are presented in this section for the future of this project to confirm, validate, and/or test new hypotheses.

8.2.1   Refinement of Diagnostic Techniques

It was identified in Section 6.3.4 that in certain cases ionization is significant so that the non-neutral probe theory may no longer be valid. Appendix E explores the possibility of applying an adapted form of neutral probe theory in these cases. Refining the diagnostics in this way may lead to more accurate measurements of density, temperature and ultimately mobility. Upon application of this theory, trends in experimental mobility may be more adequately resolved, especially at high pressures where ionization was found to be significant. However, an analytical analysis is needed to account for the ion flow velocity which deviates from neutral probe theory in an ambient plasma.

It was also identified in Sections 7.1 that the existence of ionization between the probe and cathode provide a non-constant axial electron flux, which affects the measurement of mobility. In the data presented in Chapter 7 a correction was applied to the mobility (described in Section 7.1) in attempts to rectify the error introduced by this effect. However, the correction factor assumed a purely linear axial variation in electron density due to ejected electrons from ionization. This was a rough analysis where improvement would be possible and necessary to refine the experimental trends of mobility with control parameters. In order to account for this apparent error, a local measurement of axial flux may be obtained so that the change in axial flux would be inconsequential (since density and axial flux would be measured at the

same axial location). The local axial flux measurement would be difficult in that presently, the current measured on the anode ($A_a \sim 1$ m) is on the order of ~ 1 μA. A probe to measure axial flux, with collection area of $\sim 5 \times 10^{-6}$, would mean measuring currents on the order of pA. While this is well above the fundamental limit for current measurements, noise and other errors may overwhelm the measurement. If instrumentation limits this measurement (due to noise and/or low axial current) a better axial profile of electron density may be employed to produce a more accurate correction to the difference in axial flux between the probe and anode.

8.2.2   Path Length Analysis

The striking agreement in the mobility obtained through the "peak ionization" method with independent experimental measurements of mobility, presented in Section 7.6.2, warrants further investigation. It was assumed *a priori* that the peak in ion density with changes in magnetic field would occur at the point where the path length of electrons in the confinement volume (ℓ_{f-a}) begins to fall below the mean free path for electron-neutral collisions (λ_m). This statement must be analytically verified. On the assumption that the peak in the ionization does equate with the point where $\lambda_m = \ell_{f-a}$, this may present another method of determining mobility within the Hall Electron Mobility Gage. The mobility deduced by the path length analysis has strong agreement with experimental measurements of mobility under the same conditions. However, the number of data points where this analysis was carried out was few so these results need confirmation. This method may provide a way to assess the influence of the electrostatic probe. Although the measurements presented in Section 7.6.2 were taken with the probe physically in place (floating), the diagnostics in the path-length analysis do not require the electrostatic probe. Thus, this method allows for mobility measurements in absence of the probe so that a comparison may be made.

8.2.3 Low pressure operation

It was speculated that the trends with pressure tend to "flatten" at low pressure where further decreases in pressure do not correspond to any decrease in mobility. Rather the mobility maintains a constant value hypothesized to be collisionless and thus not affected by background pressure. However, over the range of pressures explored, the mobility trend with pressure cannot be confirmed. Therefore it is proposed that a new experimental setup be created that may allow for pressures lower by 1-3 orders of magnitude. While in this experimental setup, this trend only begins to be apparent, extending the pressures lower will either confirm or deny the existence of this trend. Low-pressure investigations have been conducted in Penning trap and other non-neutral plasma experiments which have resulted in successfully identifying additional transport mechanisms such as asymmetry-induced transport[147], the theory of like-particle collisions [35], and resonant particle transport[112].

8.2.4 Investigation of "Bounce" Mobility

There is no known effect that would contribute to mobility in the Hall Electron Mobility Gage that would not also be present in a Hall thruster (save for the presence of the electrostatic probe, but it is thought to be highly unlikely that the probe entirely accounts for the enhanced mobility). A remaining possibility is an effect inherent in the geometry of the Hall configuration. Enhanced mobility was also observed in magnetron discharges (both planar and classic), which have slight variations in geometry but also exhibit the Hall type "confinement" mechanism for electrons. In all of these devices electrons freely stream on magnetic field lines making many radial (or axial in the case of the classic magnetron) bounces, where the "bounce" frequency is only superceded by the electron gyro-frequency, and is much higher than the magnetron frequency and classical collision frequency (for both electron-neutral and Coulomb collisions). The bounce frequency was determined in the Hall electron mobility gage

to be on the order of 1×10^7 Hz (based on a harmonic potential well with the approximate geometry and field conditions of the confinement volume). If this frequency were used in addition to the electron-neutral collision frequency in the classical equation the mobility would fall on the same order of magnitude as the observed mobility (Fig. 8.1). The following equation was used for "Bounce" mobility in Fig. 8.1:

$$\mu_{ez} = \frac{\nu_m + \nu_{bounce}}{\omega_{ce}B} \tag{8.1}$$

Furthermore, at the "turning point", where electrons are reflected back toward the center of the confinement area, a drastic change in electric field is experienced on a similar time/length scale as a gyro-orbit, where the electric field is aligned perpendicular to the magnetic field at the center and nearly parallel to the magnetic field at the turning point. A similar change in electric field is exhibited in all of these devices: at the "target" cathode in magnetron discharges, at the pole geometry of the Hall Electron Mobility Gage, and at the dielectric sheath in a Hall thruster. The change in field conditions over a gyro-orbit calls into question the guiding center theory typically used to describe electron dynamics in these field conditions. This presents compelling evidence for geometrical effects.

Experimental, computational, and analytical techniques may be employed in order to investigate the effects of the "bounce" on the micromotion of electrons. The thought that the phase of the electron upon reflection from the sheath (or in the Hall Electron Mobility Gage, the confining potential well) may affect the motion of the particle has been previously suggested. This notion was investigated analytically by Thomas[55] and Keidar[84], where efforts are ongoing. This may be investigated experimentally by creating a modified Hall Electron Mobility Gage where the "bounce" frequency may be varied and effects explored.
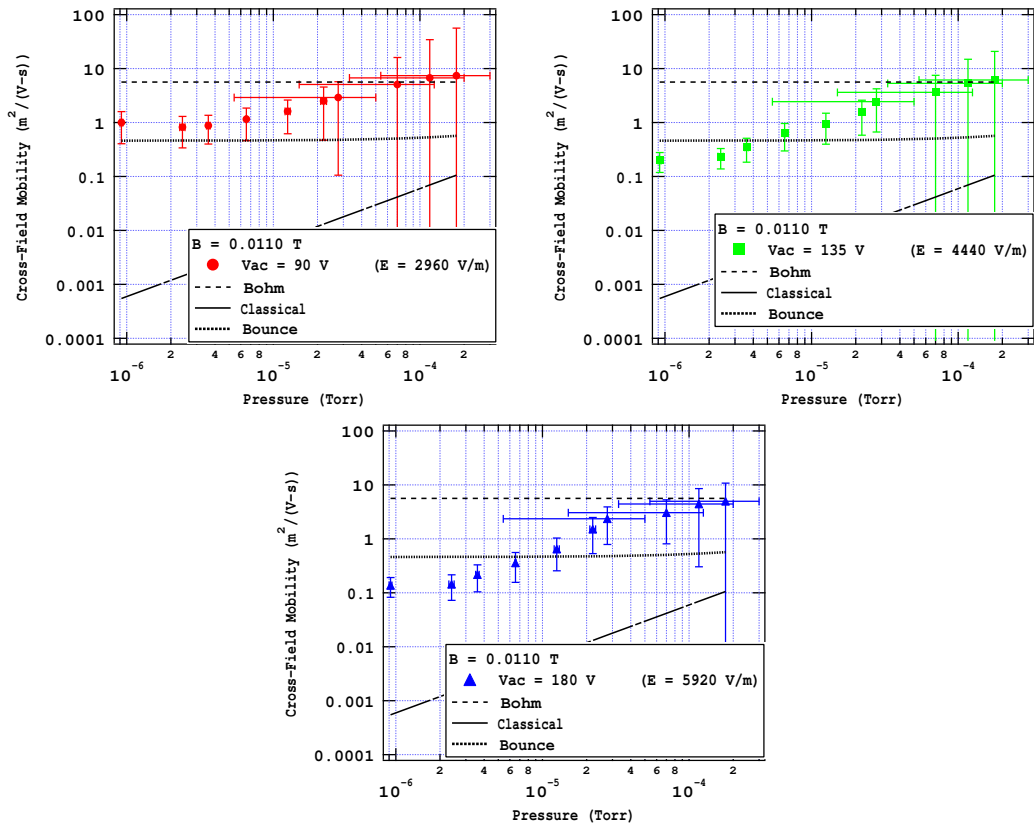
Figure 8.1: "Bounce" mobility using Eq. (8.1) showing mobility on the same order of magnitude as experimental observations.

Appendix A

Machine Drawings of Mobility Gage

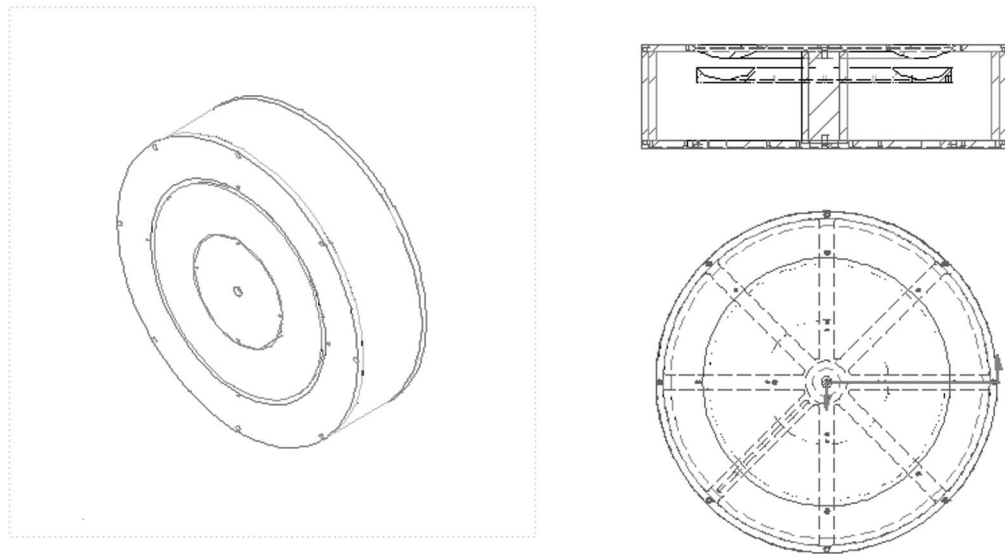**Figure A.1:** Assembled Hall Electron Mobility Gage

Figure A.2: Anode Electrode
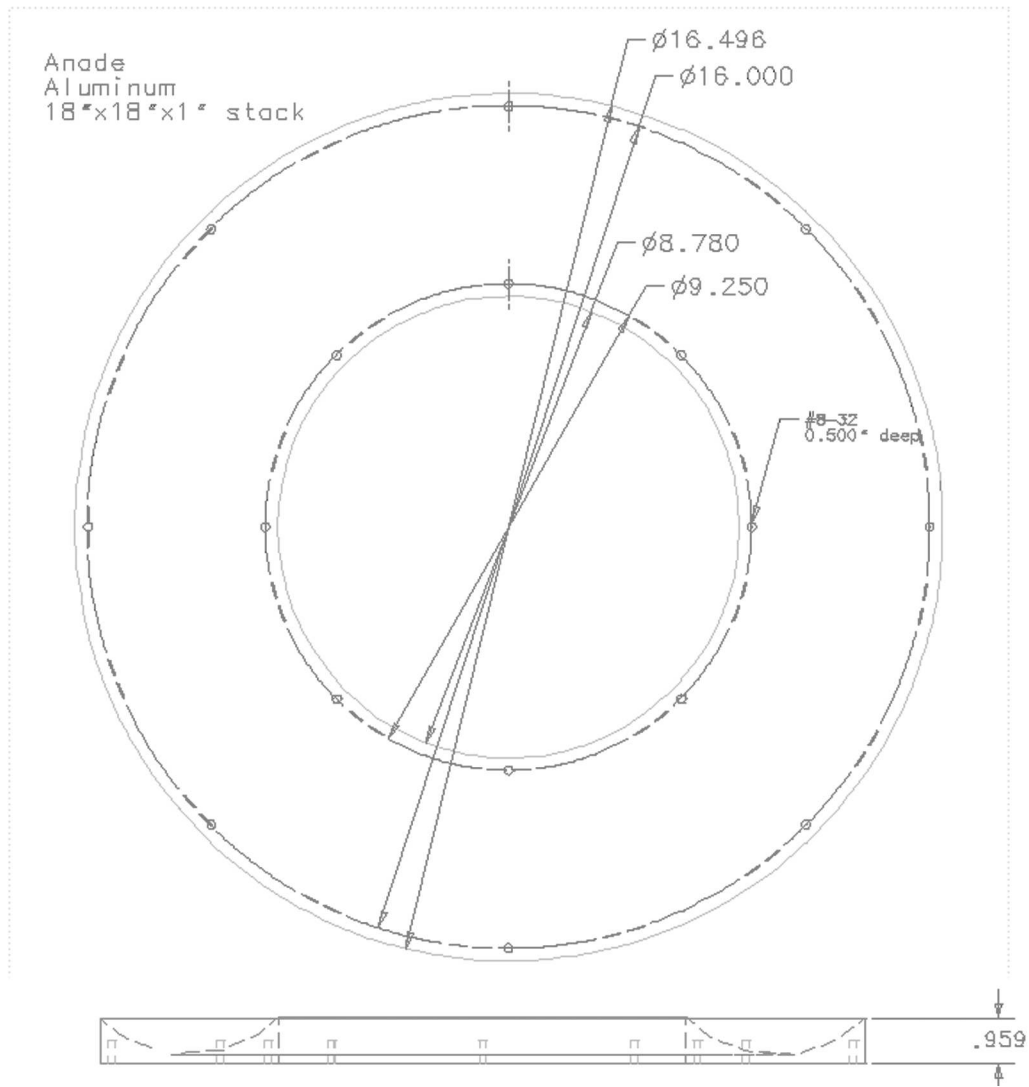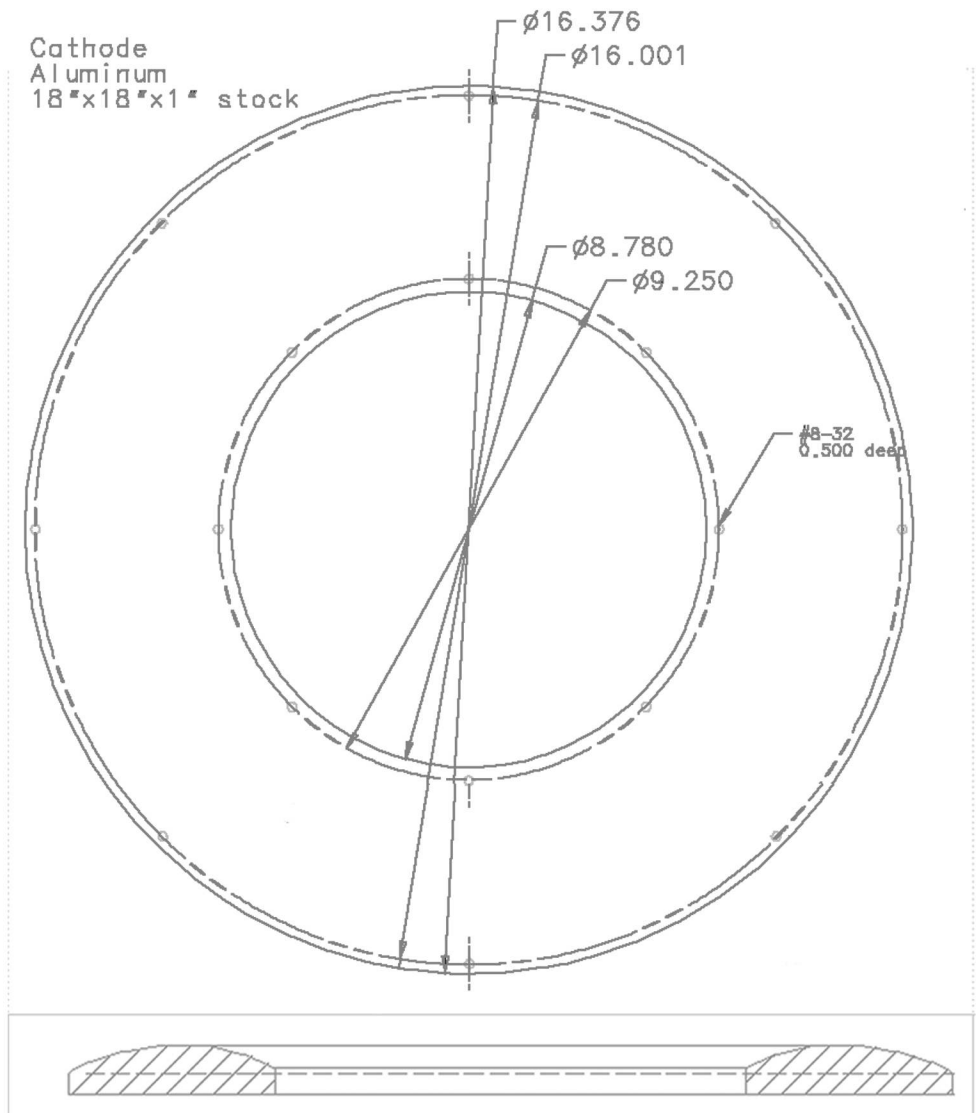
226

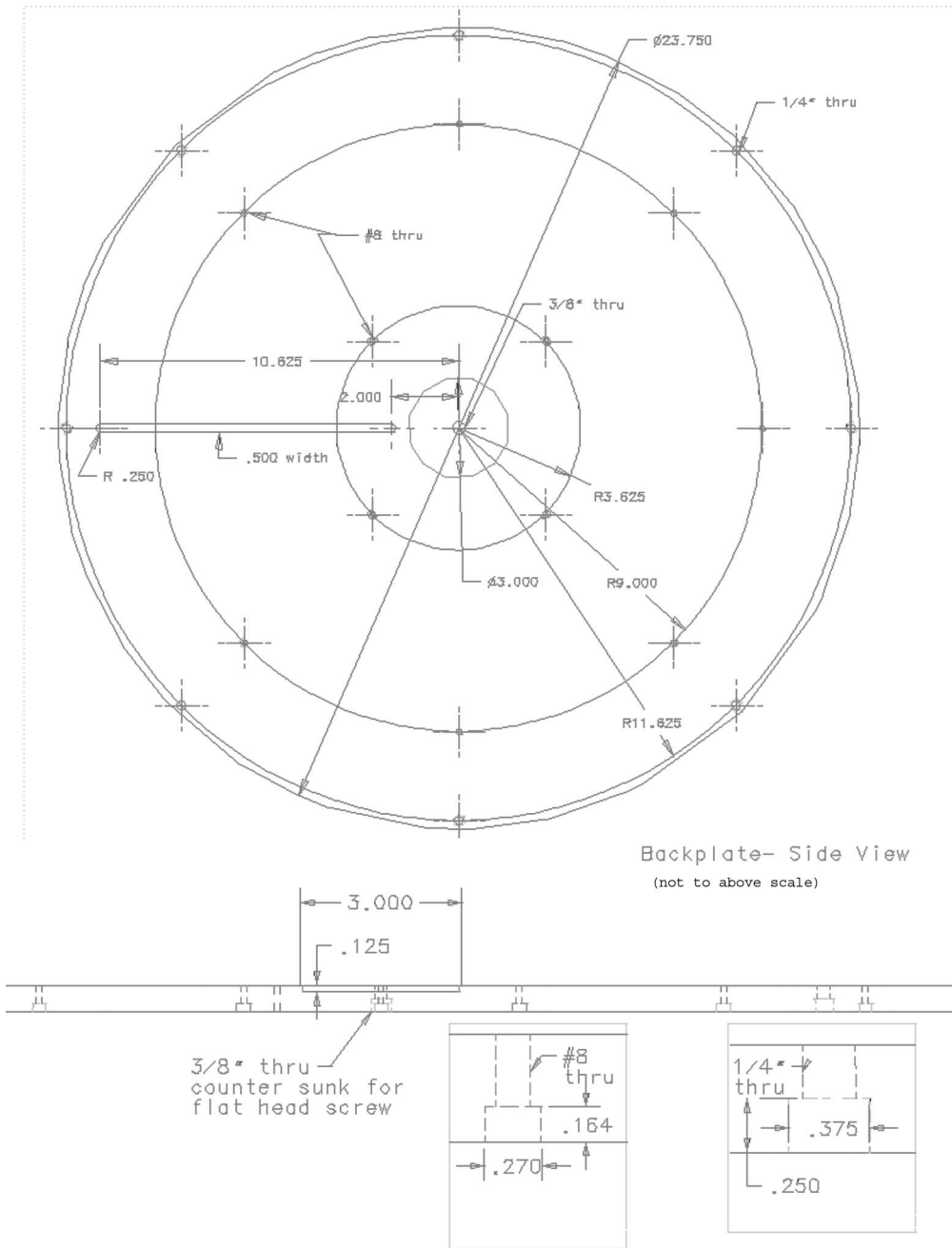**Figure A.3:** Cathode Electrode

Figure A.4: Backplate, geometry and bolt pattern
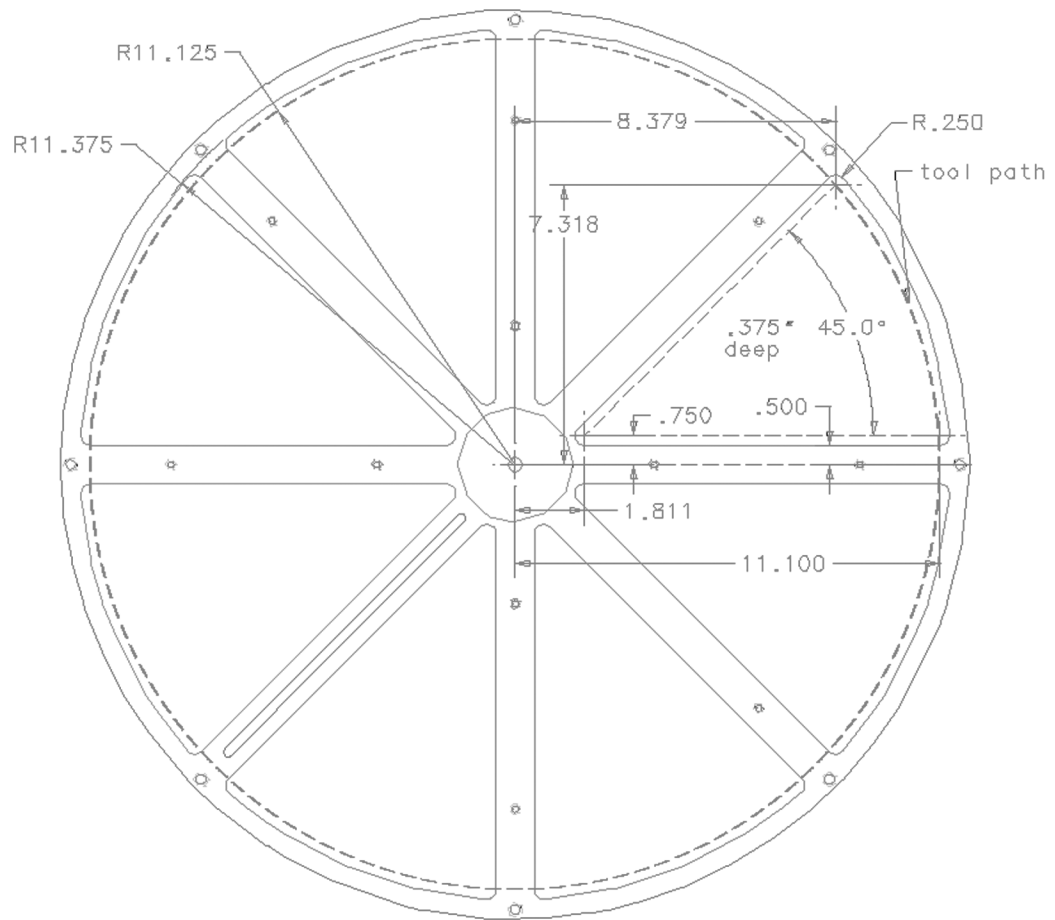
228

Figure A.5: Backplate, cutouts
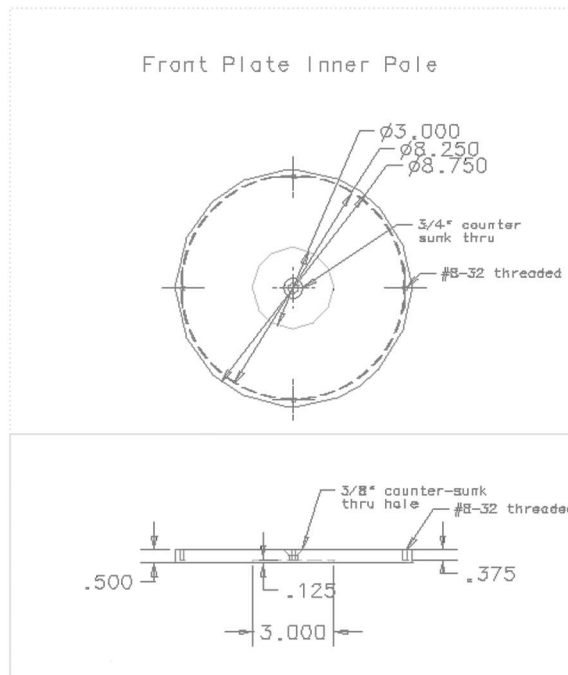
Figure A.6: Front plate, center
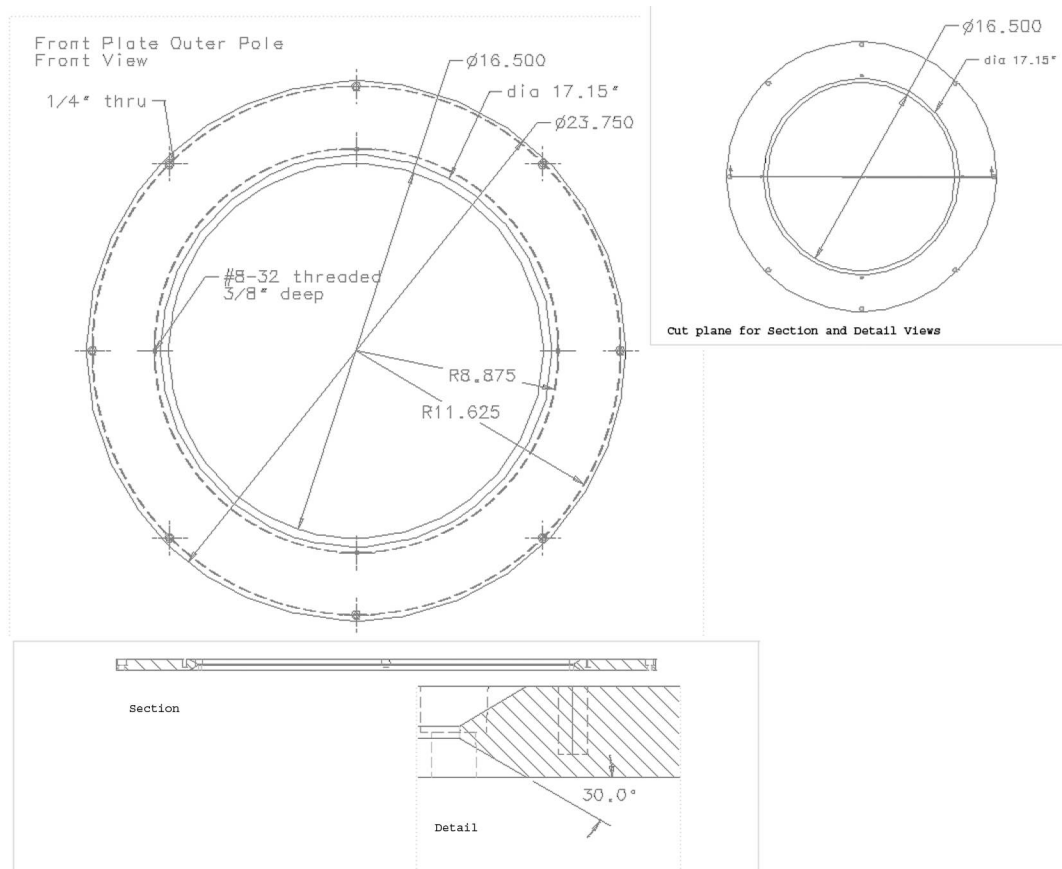
Figure A.7: Front plate, outer

Figure A.8: Center Pole

TOP

Outer Pole

⌀22.750

⌀23.750

Qty 8 bolt pattern
1/4-20, .5"deep
centered
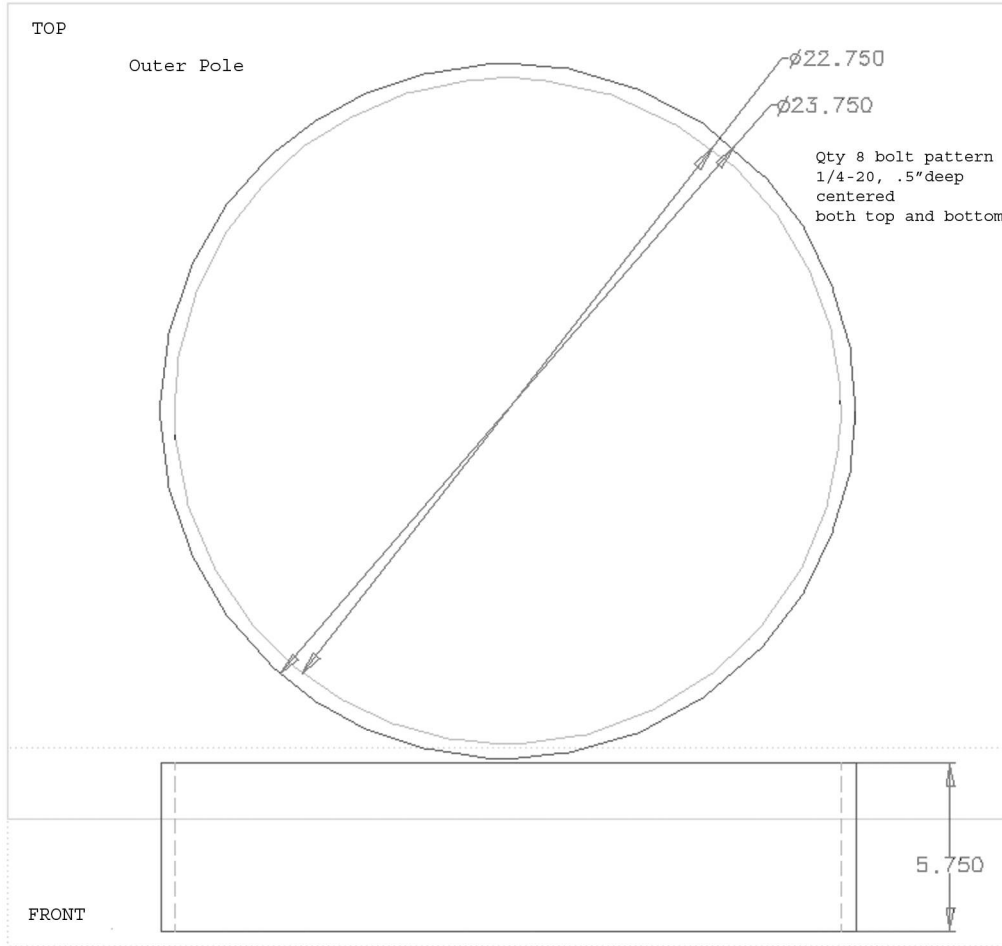both top and bottom

5.750

FRONT

Figure A.9: Outer cylinder

Appendix B

Magnetic Field Tuning

The saturation of the inner magnetic core material of the Hall Electron Mobility Gage resulted in a distortion of the magnetic field, where if the coil currents on the inner and outer magnetic coil were increased proportionally, the magnetic field lines no longer coincided with the electric equipotential lines and the anode and cathode electrodes. This is described in more detail in Chapter 4 and Chapter 6. Maxwell SV[121] was used to numerically model the magnetic field using the B-H curve for the material. Using the magnetic field models an "ideal" outer coil current was determined for each inner magnetic coil current so that the shape of the magnetic field was maintained upon increases in magnetic field magnitude. The procedure for the experimental verification of the "ideal" coil currents was described in Section 6.2.1. The complete set of data used to find the "ideal" coil currents is presented in Fig. B.2.

Mobility versus magnetic field was taken prior to the incorporation of the magnetic field tuning procedure and is shown in Fig. B.3. Figure B.3 presents mobility measurements taken in response to magnetic field for a constant electric field and pressure. (Data for determining the experimental error were unavailable for the "No B-field Tuning" case.) The effects of the magnetic field tuning are significant as shown by the "tuned" case in Fig. B.3 where ideal coil currents (presented in Section 6.2.1)
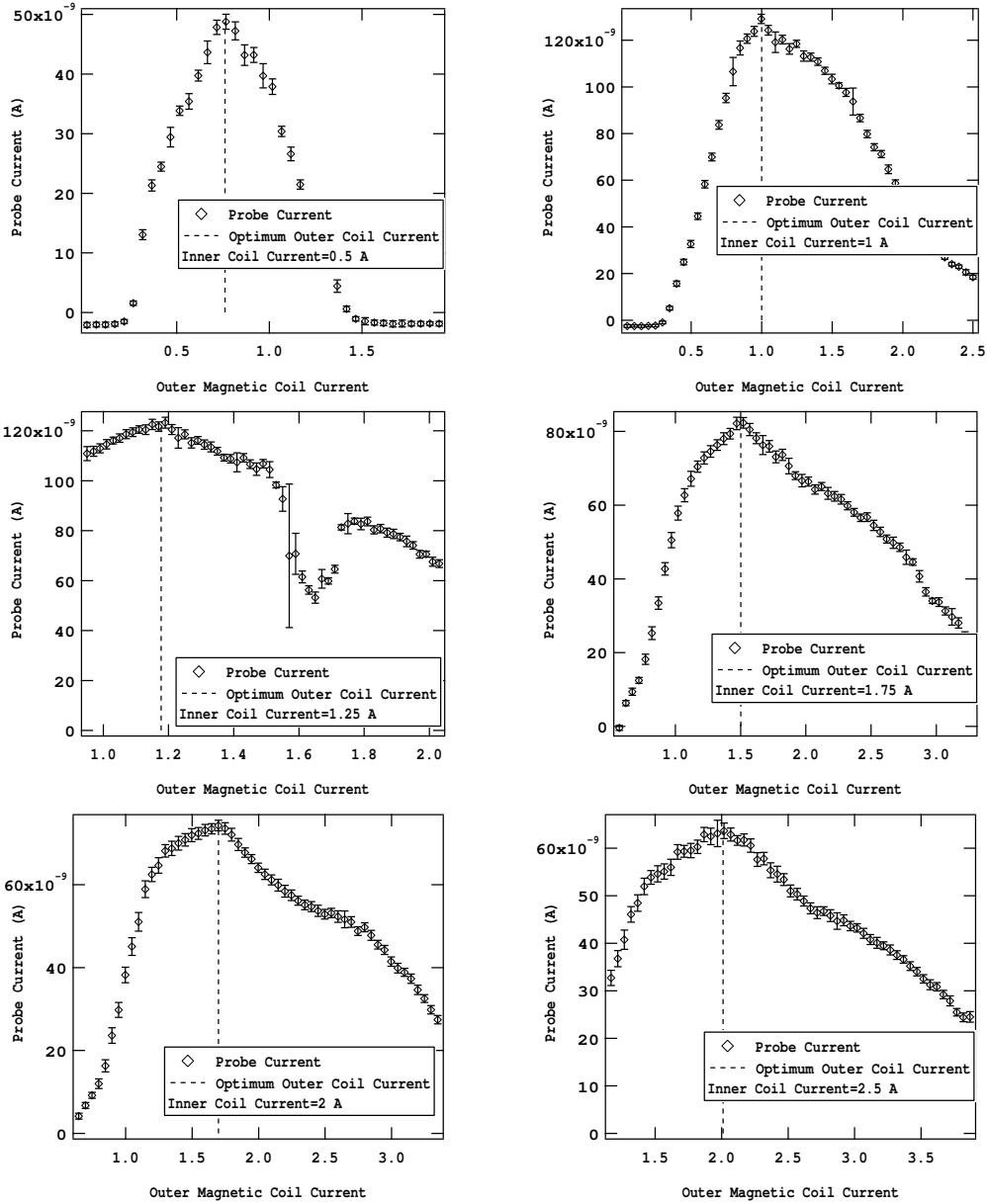
Figure B.1: Data for the magnetic field tuning procedure outlined in Section 6.2.1

were employed in the magnetic field variation. This is one representative case, where similar results were found for different electric fields and pressures. For all other mobility data presented within this document the magnetic field variation was achieved by using the ideal magnetic coil currents based on the data presented in Section 6.2.1.
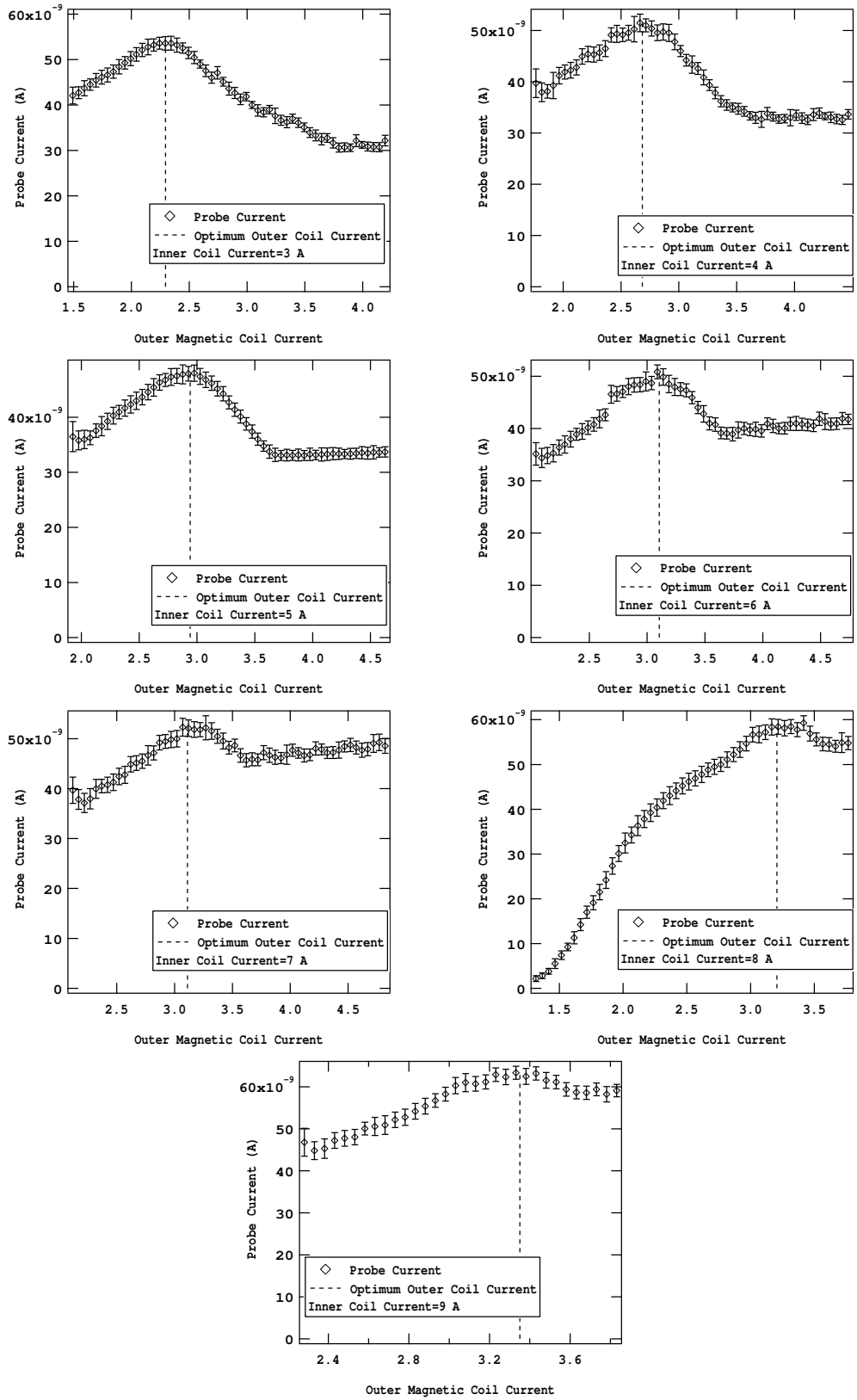
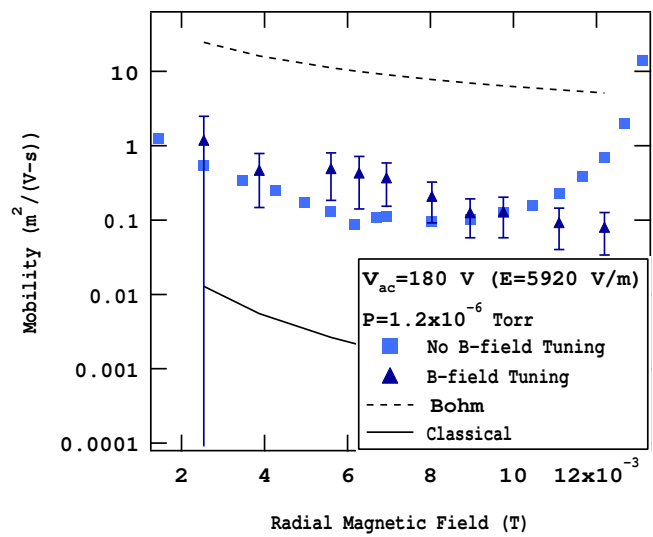**Figure B.2:** Data for the magnetic field tuning procedure outlined in Section 6.2.1

235

Figure B.3: Mobility versus magnetic field for a constant electric field and pressure, showing the effect of the magnetic field tuning on the resulting mobility at high magnetic fields.

236

Appendix C

Emission Current Estimation

Ionization that occurs between the probe and the anode causes the axial electron flux to vary spatially within the confinement volume. More specifically the ionization causes the axial electron flux to increase with axial distance from the loading filament to the anode collection area. In the determination of mobility, the combination of a density measurement with a measurement of axial flux gives a measure of axial velocity (from which electron mobility is directly determined as electric field is prescribed and known). The axial flux was measured at the anode with the approximation of $J_a \sim J_{ez}(z_{probe})$. However, in cases where the ionization is high this approximation would not be valid (as described in Chapter 7). In order to account for the variation in axial electron flux, the electron flux was postulated to increase linearly from the location of the loading filament to the anode electrode according to Eq. (7.4). This requires a measurement of emission current, I_e, which was not obtained for all experiments. Rather than repeating all past mobility experiments, a statistical analysis was explored for a possible method to estimate I_e in the cases where data for I_e was not available. This required one test where I_e and I_a were recorded for a large parameter space, rather than repeating all other tests for mobility. It was found that I_e was highly predictable with very little error if conditions of electric field, E, magnetic field, B, pressure, P and anode current, I_a were known. These parameters

were recorded and/or measured for all mobility experiments. Therefore the statistical model was employed to estimate the emission current in the cases where I_e was not measured directly. The statistical model was based on experimental data of I_e and I_a taken over a parameter space of E (V_{ac}), B and pressure, where the development of the statistical model is described as follows.

The anode current was measured in all experimental investigations of mobility. The difference between the emission current and the anode current comes from the ionization that occurs under certain conditions. An increase in pressure was primarily responsible for increases in ion density (shown in Section 6.3.4), where although to a lesser extent, electric field and magnetic field also had an effect on ion density. Since ionization varies with all of these parameters it is important to have an estimation of emission current that is a function of E (V_{ac}), B and pressure. Data for filament emission current and anode current were taken for a parameter space of electric field, magnetic field, and pressure, and the following model was developed to estimate the emission current for the cases where the data for I_e was not obtained. (Prior data sets were obtained where the importance of I_e in the measurement of mobility was not yet known.)

The filament emission current has been found to vary temporally and between different filaments. (i.e. For a given filament heater current, the emission current has been found to vary throughout a test and between tests.) These effects cannot be controlled, nor can they be measured easily or accurately. Therefore, an investigation has been done to establish whether changes in the filament heater current affect the *ratio* of emission current to anode current (since the relative difference is what is important). For a constant pressure, filament heater current was varied for all combinations of three conditions of magnetic field and four conditions of electric field (12 total combinations) and measurements were taken of emission current and anode current versus filament heater current. A small backflow of argon kept pressure constant at 5×10^{-6} Torr. Here, a ratio of anode current to emission current is

Table C.1: ANOVA table for $\ln(I_e/I_a)$ using I_h as a predictor.

Regression Equation	$\ln(I_e/I_a) = 0.192 + 0.177I_h$				
Predictor	Coef	SE Coef	T	P	
Constant	0.1922	0.6068	0.32	0.752	
Ih	0.1768	0.2705	0.65	0.515	
$S = 0.179773$	$R^2 = 0.4\%$	$R^2(adj.) = 0.0\%$			

Analysis of variance

Source	DF	SS	MS	F	P
Regression	1	0.01381	0.01381	0.43	0.515
Residual Error	114	3.68431	**0.03232(MSE)**		
Total	115	3.69812			

measured as the dependent variable to model as a function of filament heater current, electric field and magnetic field. The data obtained for $\ln(I_a/I_e)$ versus filament heater current are shown in Figs. C.1 through C.4.* A simple linear regression predicting $\ln(I_a/I_e)$ verses filament heater current was performed with the results presented in the ANOVA table, Table C. All of the statistical results indicate that the heater current, I_h, is not a strong predictor of $\ln(I_e/I_a)$. The R^2 for this simple regression is less than 1% where the R^2 represents the percent of the variance in the values of $\ln(Ia/Ie)$ that can be explained by knowing the value of I_h. The resulting R^2 shows that (almost) none of the variance in $\ln(I_a/I_e)$ is explained by I_h. This was a desired result as data for I_h was absent in the same cases where data was missing for I_e.

Next, a multiple regression was performed, including E (V_{ac}) and B as predictors, where the results show that E (V_{ac}) and B were much more influential in $\ln(I_a/Ie)$ than the filament heater current. The results of the regression are shown in Table C. These results indicate that $\ln(I_a/I_e)$ was much more heavily influenced by the electric and magnetic fields and there was very little influence due to the filament

---

*The natural log is generally used in the case of ratio quantities in order that the error follows a normal distribution.

Table C.2: ANOVA table for $\ln(I_e/I_a)$ using I_h, V_{ac}, and B as predictors.

Regression Equation	$\ln(I_e/I_a) = -0.837 - 0.009I_h + 0.000251V_{ac} + 36.8B$			
Predictor	**Coef**	**SE Coef**	**T**	**P**
Constant	-0.8372	0.3395	-2.47	0.015
Ih	-0.0092	0.1492	-0.06	0.951
Vac	0.00025070	0.00001773	14.14	0.000
B	36.842	4.486	8.21	0.000
$S = 0.0988402$	$R^2 = 70.4\%$	$R^2(adj.) = 69.6\%$		

Analysis of variance

Source	DF	SS	MS	F	P
Regression	3	2.60395	0.86798	8.85	0.000
Residual Error	112	1.09417	**0.00977(MSE)**		
Total	115	3.69812			

heater current. Attempts have been made to keep the filament current constant during other tests so the temporal variations (which will be less than the imposed variations during this test) are expected to contribute very little to the variation in $\ln(I_a/I_e)$. (The exception to this is the data obtained in Sections 6.3.2 and 7.5.1. However, the emission current was directly measured in these experiments so the prediction if I_e using this model was unnecessary.) Therefore, the heater current is neglected in predicting $\ln(I_a/I_e)$.

The results of the multiple regression shown above indicate that E (V_{ac}) and B are strong predictors of $\ln(I_a/I_e)$, and it was shown (Section 6.3.4) that pressure strongly influences ionization. Therefore, to refine the model, data were taken for a parameter space of E (V_{ac}), B, and pressure. For this parameter space, each parameter is swept through 8 to 10 values for 9 combinations of the other two parameters (all combinations for three values of each). Emission current and anode current were recorded and the results are shown in Figs. C.1 through C.4 (Each of these figures represents the same data plotted against a different parameter in order to show the relation between $\ln(I_e/I_a)$ and the control parameters).
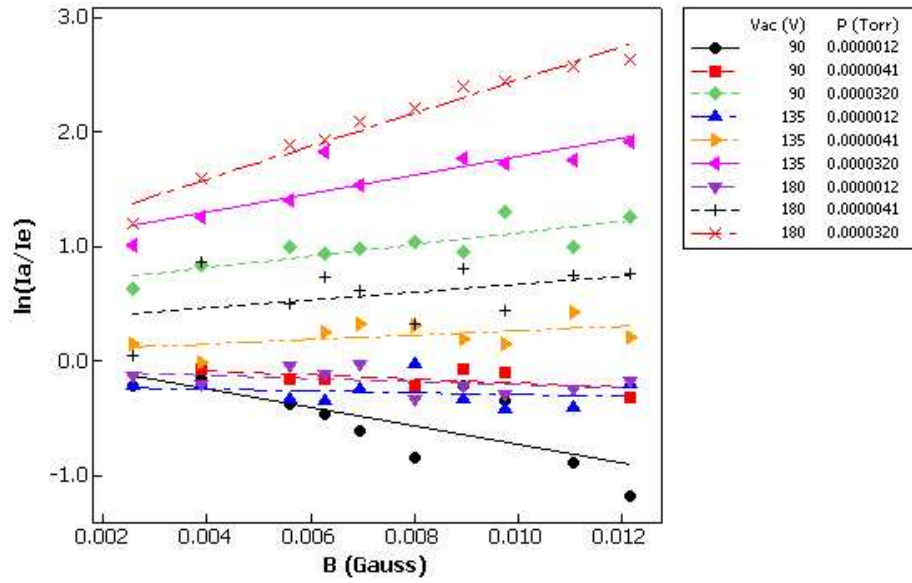
Figure C.1: Results of the parameterization data where $\ln(I_e/I_a)$ is shown as a function of magnetic field (B).

Figure C.2: Results of the parameterization data where $\ln(I_e/I_a)$ is shown as a function of anode-to-cathode voltage, V_{ac}.

Figure C.3: Results of the parameterization data where $\ln(I_e/I_a)$ is shown as a function of the natural log of pressure, $\ln(P)$.
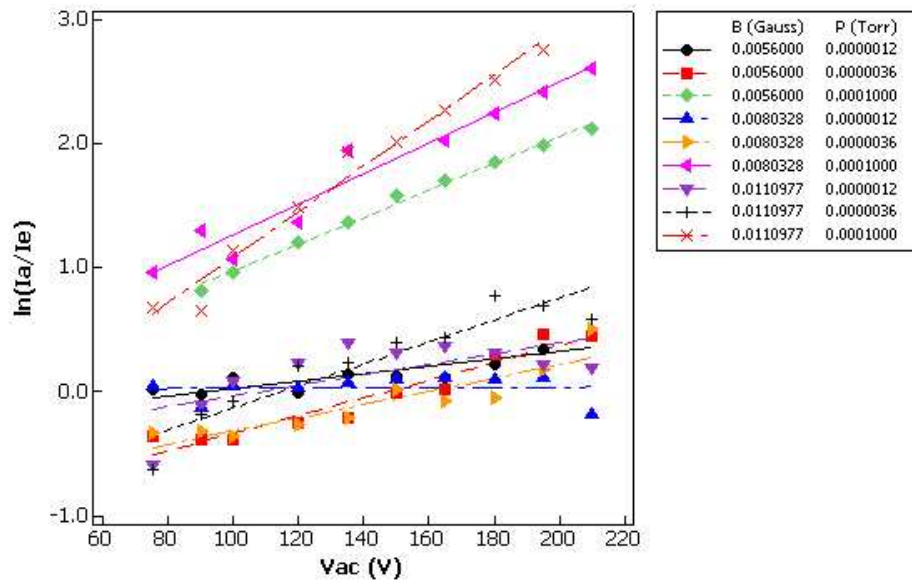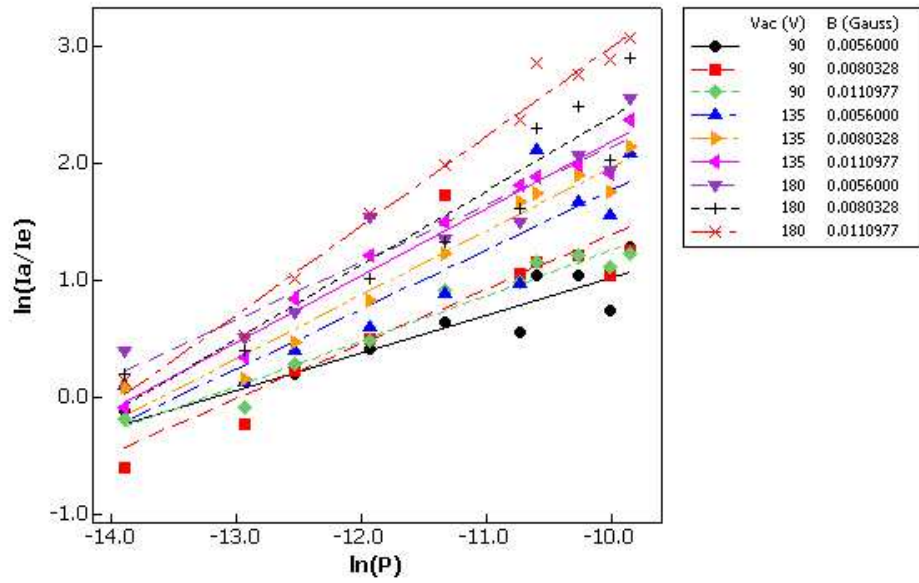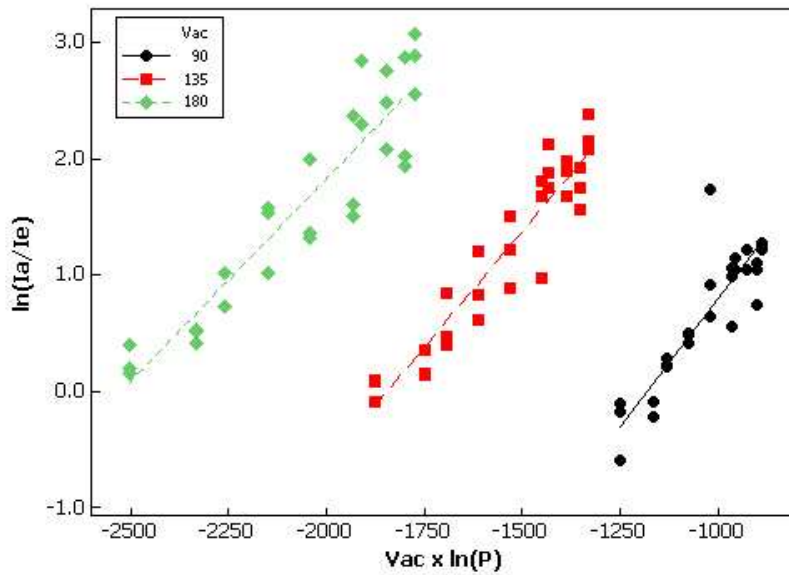

Figure C.4: Results of the parameterization data where $\ln(I_e/I_a)$ is shown as a function of $E\ln(P)$.
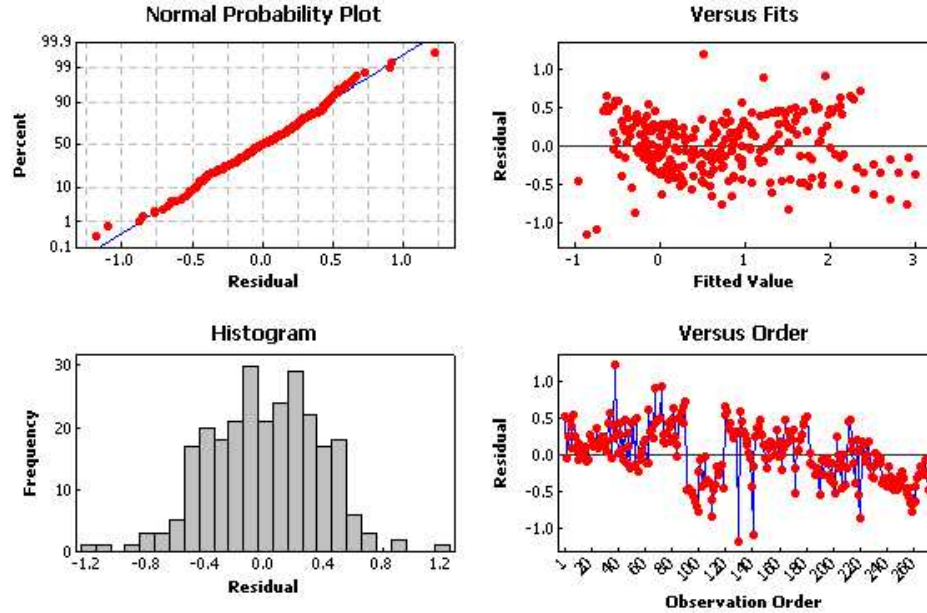
Figure C.5: Residual plots showing normal scatter for the model presented in Table C

Variable selection for the multiple regression analysis was accomplished by inspection of the scatter plots. From these plots it was apparent that the ionization depends on all three factors of E (V_{ac}), B and pressure. However, it was also apparent that there were two-factor interactions, particularly between electric field and pressure, where the linear dependence of $\ln(I_a/I_e)$ on pressure varies with different values of E (V_{ac}) and vice-versa. This indicates that a factor containing both E (V_{ac}) and P is present for a linear regression model. Figure C.4 shows the same data as shown in Fig. C.3, except the x-axis is the parameter $V_{ac} \times \ln(P)$ (the three magnetic field conditions were combined in this plot, as the dependence was weak compared to the dependence on E (V_{ac})). The linear (constant slope for all E (V_{ac}) and B) dependence of $\ln(I_a/I_e)$ on $V_{ac} \times \ln(P)$ is shown. A multiple regression model for the parameters of V_{ac}, B, $\ln(P)$ and $V_{ac} \times \ln(P)$ was conducted and the results are shown in Table C. The residuals of this model are shown in Fig. C.5.

These results give credence to the linear model to predict $\ln(I_a/I_e)$ and ultimately

243

Table C.3: ANOVA table for $\ln(I_e/I_a)$ using $\ln(P) \times V_{ac}$, $ln(P)$, V_{ac}, and B as predictors.

Regression Equation

$\ln(I_e/I_a) = 2.26 + 0.00168V_{ac} \times \ln(P) + 0.260\ln(P) + 0.0289V_{ac} + 38.9B$

Predictor	Coef	SE Coef	T	P
Constant	1.1567	0.6109	3.69	0.000
Vac x ln(P)	0.0016808	0.0003495	4.81	0.000
ln(P)	0.00025070	0.00001773	14.14	0.000
Vac	0.028899	0.004235	6.82	0.000
B	38.870	9.177	4.24	0.000

$S = 0.373767$ $R^2 = 84.7\%$ $R^2(adj.) = 84.5\%$

Analysis of variance

Source	DF	SS	MS	F	P
Regression	4	199.906	49.976	357.74	0.000
Residual Error	258	36.043	**0.140(MSE)**		
Total	262	235.948			

I_e (since I_a was measured for all conditions). As a general rule the null hypothesis (the hypothesis that the predictor parameters could have come up with the same results "by chance") may be rejected if the p-value, given in Table C, is less than a significance level of $\alpha = 0.05$. A significance level of 0.05 is commonly used, which corresponds to a confidence interval of 95% that the hypothesis can be rejected if the p-value is below $\alpha = 0.05$, for various tests (F-test, T-test, etc.).[†] The T-test p-values for the coefficients and the F-test p-value for the entire model are each less than 0.0005. (Explanations of the T-test and F-test may be found in Ref. [148]. The important aspect to note is that the p-values were significantly low for all tests which indicates a good fit for the regression.) These, combined with inspection of the normal probability plot showing normalized scatter in the data (Fig. C.5), indicate that the regression equation presented in Table C provided a good fit to the experimental data

[†]These general guidelines may be found in [145, 148] and [149] among other statistical analysis textbooks. Other significance levels may be used but the author would rather not break tradition.

over the range of operating parameters explored and that the error was normally distributed. Therefore, the estimation of $\ln(I_e/I_a)$ was predicted by the parameters of V_{ac}, B, $V_{ac} \times \ln(P)$, and $\ln(P)$ given by equation

$$\hat{Y} = \langle \ln(I_e/I_a) \rangle = 2.26 + 0.00168 V_{ac} \times \ln(P) + 0.260 \ln(P) + 0.0289 V_{ac} + 38.9B \quad \text{(C.1)}$$

The error of this model propagates into the determination of the measured mobility (Appendix D). Since it was desired to predict a value for I_a/I_e this prediction must take on a range based on the error in the model (using a prediction interval). The prediction interval is estimated by[148]

$$\left\{ \begin{array}{c} L \\ U \end{array} \right\} = \hat{Y} \mp s_{\hat{Y}} t_{n-2,1-\alpha/2} \quad \text{(C.2)}$$

where L and U are the lower and upper bound, respectively, $\hat{Y}$ is the estimate of the expected value of Y and $s_{\hat{Y}}$ is given by

$$s_{\hat{Y}}^2 = \left[1 + \frac{1}{n} + \frac{(X - \bar{X})^2}{\sum_i (X_i - \bar{X})^2} \right] \hat{\sigma}^2 \quad \text{(C.3)}$$

The range of Eq. (C.2) is determined through inspection of the mean squared error (MSE) given in Table C and a 95% confidence interval is desired. The variance of the sample, $s_{\hat{Y}}^2$, may be estimated by the mean square error of the linear model (because of the large number of samples[148]) and the t-value ($t_{n-2,1-\alpha/2}$) for the 95% confidence interval is given as 2.26 for $n = 164$ (where n is the number of degrees of freedom– i.e. the number of data points used to predict $\hat{Y}$). Thus, the interval is approximated as ± 0.846 for the prediction of $\ln(I_a/I_e)$.

Since the anode current was recorded for all mobility data obtained, the model developed may be used to solve for the emission current as a function of anode current

(in the cases where emission current was not recorded), where I_e is given by

$$I_e = I_a \exp\left[-\left(\hat{Y} \pm s_{\hat{Y}} t_{n-2,1-\alpha/2}\right)\right] \tag{C.4}$$

This estimation of emission current was used in cases where the emission current was not obtained in mobility data.

This may be incorporated into the computation of mobility by replacing Eq. (7.4) with

$$J_{ez}(z) = \frac{I_a}{A_a}\left(\exp(-\hat{Y}) + \frac{(1 - \exp(-\hat{Y}))z}{\Delta z_{f-a}}\right) \tag{C.5}$$

so that experimental mobility is given by

$$\mu_{ez} = \frac{J_a(CF)}{E_z q n_e} \tag{C.6}$$

where CF is given by

$$CF = \exp(-\hat{Y}) + \frac{(1 - \exp(-\hat{Y}))z}{\Delta z_{f-a}} \tag{C.7}$$

The variance of CF is then given by

$$\sigma_{CF}^2 = \left(\frac{\partial(CF)}{\partial\hat{Y}}\right)^2 \sigma_{\hat{Y}}^2 \tag{C.8}$$

and $s_{\hat{Y}} \approx \sigma_{\hat{Y}}^2 \approx MSE$(from Table C). The variance introduced using this prediction (σ_{CF}^2) was then incorporated within the error analysis (Appendix D) for the cases where this estimation was used.

Appendix D

Error Analysis

The following sources of error occur and can be quantified in the determination of the mobility and other parameters:

1. Anode current measurment

2. Curve fit for T_e and n_e

3. Estimation of emission current, $I_e{}^*$

4. Pressure measurement

5. Ion density estimation

where each of these are described in more detail below.

Anode Current Measurement: For the anode current measurement 100 measurements of anode current I_a were obtained ($n = 100$) when the probe was biased to local potential (prior to I-V probe sweep). The average of these measurements is used in the computation of the mobility and the standard deviation of the sample was calculated. To find the standard deviation of the mean (often called the standard

---

*where applicable, see Appendix C.

error) the sample standard deviation was divided by $\sqrt{n}$ and the variance (σ^2/n) was used in the propagation of error for the error in the experimental mobility described below (Eq. (D.3)).

Curve Fit for T_e & n_e: The curve fit to find T_e and n_e uses the Levenberg–Marquardt algorithm to fit a non-linear function (Eq. (6.5)) using the least squares method. With this curve fit a residual was calculated as a measure of the deviation of the data from the curve fit, where the residual was the weighted mean error and given by:

$$\frac{1}{N} \sum_{i=0}^{N-1} w_i (f_i - y_i)^2 \tag{D.1}$$

where N is the length of the array of dependent values, w_i is the i-th element of the array of weights for the observations, f_i is the i-th element of the array of y-values of the fitted model, and y_i is the i-th element of the array of dependent values. In the curve fit used for T_e and n_e the weights are set to 1, as the relative uncertainty in the measured value (I_p) is not known as a function of any other parameter. The curve fit also generates a covariance matrix, where the covariance, C, is given by the following equation:

$$C = \frac{1}{2} D^{-1} \tag{D.2}$$

where D is the Hessian[150] of the function with respect to its parameters. The diagonal elements of the covariance matrix for the curve fit[148] give the variance of the corresponding fit parameters, n_e and T_e.

Estimation of emission current, I_e: A variance is associated with the prediction of the emission current where the variance, $s_{\hat{Y}}$ was given by Eq. C.3, This is the variance for the predicted value $\hat{Y} = \langle \ln(I_e/I_a) \rangle$. Since the Eq. (C.1) was used to estimate I_e, the error associated with $\hat{Y}$ propagates into the estimation of I_e. The prediction of I_e is incorporated into the calculation for experimental mobility (Eq. (C.6)) by a correction factor, CF, given by Eq. (C.7) with variance given by Eq.

(C.8).

Pressure Measurement: The error due to the pressure measurement corresponds to horizontal error bars when mobility is inspected as a function of pressure. Pressure measurements were taken before and after each matrix of E and B (for all pressure blocks) where E and B are randomized to prevent any temporal effects in pressure from coupling to trends with electric and magnetic field. (Randomization is discussed in more detail in Section 7.3) The two pressure measurements were averaged and the error bar for pressure is found using Eq. (D.6) with a 95% confidence interval for $n = 2$.

Ion Density Estimation: The ion density was determined according to the methods presented in Section 6.3.4. To assess the error in this estimate, error bars were employed based on the minimum ion density, which was found by employing the maximum theoretically possible velocity of ions. The maximum velocity is the velocity obtained from acceleration through the entire field from anode to cathode, evaluating Eq. (6.7) at $\phi = V_{ac}$. The difference between the density found at maximum velocity and the density found using $V_{ac}/2$ was used as an estimate for the standard deviation. A 95% confidence interval was applied according to Eq. (D.6).

When a combination of parameters (each with respective errors) was used, for example in the calculation of mobility, the variance of each element was combined through the propagation of errors which is given by the general equation

$$\sigma_{total}^2 = \sum_{j=0}^{p-1} \left(\frac{\partial Y}{\partial \beta_j} \right)^2 \sigma_{\beta_j}^2 \tag{D.3}$$

For example, within the calculation of mobility, the total variance of the mobility is estimated by

$$\sigma_{total}^2 = \sum_{j=0}^{p-1} \left(\frac{\partial \mu_{ez}}{\partial \beta_j} \right)^2 \sigma_{\beta_j}^2 = \left(\frac{\partial \mu_{ez}}{\partial I_a} \right)^2 \sigma_{I_a}^2 + \left(\frac{\partial \mu_{ez}}{\partial (CF)} \right)^2 \sigma_{CF}^2 + \left(\frac{\partial \mu_{ez}}{\partial n_e} \right)^2 \sigma_{n_e}^2 \tag{D.4}$$

For the calculation of mobility, taking the first partial derivatives, the variance is given by

$$\sigma_{total}^2 = \left(\frac{CF}{A_a e n_e E_z}\right)^2 \sigma_{I_a}^2 + \left(\frac{I_a}{A_a e n_e E_z}\right)^2 \sigma_{CF}^2 + \left(\frac{-I_a(CF)}{A_a e n_e^2 E_z}\right)^2 \sigma_{n_e}^2 \qquad (D.5)$$

assuming statistical independence of the variables I_a, CF and n_e. The justification for the approximation of independence is that the three independent variables control the three dependent variables where the total number of degrees of freedom in the system is preserved. The 95% confidence interval is used so error bars are defined by

$$\left\{\begin{array}{c} L \\ U \end{array}\right\} = Y \mp t_{m,1-\alpha/2}\sigma_{total} \qquad (D.6)$$

where alpha is 0.05 and Y is the parameter of interest (such as mobility).

Propagation of error was used in any instance where combinations of measurements were needed. As another example, in the determination of the ion fraction the error in ion density and electron density were both taken into account. To assess the error in the ion density fraction, Eq. (D.3) was used to account for the combination of error due to both $\beta_1 = n_i$ and $\beta_2 = n_e$.

Since the standard deviation of the sample (given by σ_{total}) is only an estimate of the true scatter of the data, a better estimate of the standard deviation of any quantity may be obtained by combining several individual measurements. This employs the method of pooling where the more accurate estimate of the true standard deviation is given by

$$\sigma = \frac{(\sigma_1 n_1 + \sigma_2 n_2 + ... + \sigma_p n_p)}{(n_1 + n_2 + + n_p - p)} \qquad (D.7)$$

Since each measurement of the variance for mobility contains the same number of degrees of freedom ($n_1 = n_2$) the standard deviation of the pooled samples of mobility

is given by

$$\sigma = \frac{(\sigma_1 + \sigma_2 + ... + \sigma_p)}{p} \tag{D.8}$$

Averaging several measurements also allows for greater confidence due to the repetition of measurements, where the standard deviation of the means is given by $\sigma_{mean} = \sigma/n$. This method was employed whenever possible in reducing the uncertainty in measurements. Error bars given in experimental results reflect this error analysis.

Appendix E

Adaptation of Neutral Probe Diagnostics

The main source of error in the determination of mobility was the curve fit used to determine T_e and n_e. Under certain conditions the error due to the measurement of n_e and T_e overwhelms the magnitude of the respective measurements. The error in measurement was particularly high under two types of conditions: 1.) low electric field and 2.) high pressure. In the first case, the source of the error was an extremely low probe current (< 0.5 nA) due to the low density within the confinement volume approaching the limits of instrumentation where the noise in the circuitry overwhelms the signal. In the second case the error was due to the presence of ion current, where the single-component assumption (and neglect of ion current) which is key to interpretation of the probe I-V characteristic no longer was valid. Figure E.1 shows a trace exhibiting these conditions where ion current was obvious at sufficiently negative probe voltages. This appendix suggests alternatives for achieving more reliable data in the conditions where the single-component plasma assumption was not valid. This analysis was not used in the processing of the data presented in Chapters 6 and 7, as the model is still in preliminary stages, but a method is suggested as follows, that
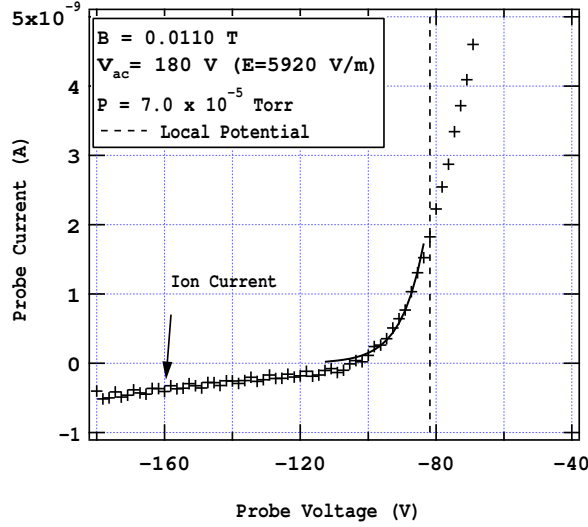
Figure E.1: Probe trace exhibiting ion current where non-neutral probe theory is no longer valid

may be used to refine the probe theory for future experiments.

In the case of high pressure, the error in the curve fit was due to significant ionization within the confinement volume where the neglect of ion current in the single-component probe theory becomes invalid. This point is made obvious by examination of Fig. 6.15, which shows ion density fraction versus pressure. As the pressure is increased, the ion density fraction approaches unity, but at the same time the experimental error grows (as seen by the error bars) due to the error in n_e. The error bars become large when the ion fraction is $\sim 50\%$. The I-V characteristics under these conditions were extremely repeatable where the curve fit resulted in highly repeatable values of electron temperature and electron density. However, the precision should not be misinterpreted as accuracy, as the curve fit was equally inaccurate in all cases, leading only to a high precision. Under the conditions of high ion density it was apparent that single-component probe theory no longer was valid. An adaption of neutral probe theory is presented below, which may be employed in future experiments, in order to refine the measurements under the condition of high relative ion density.
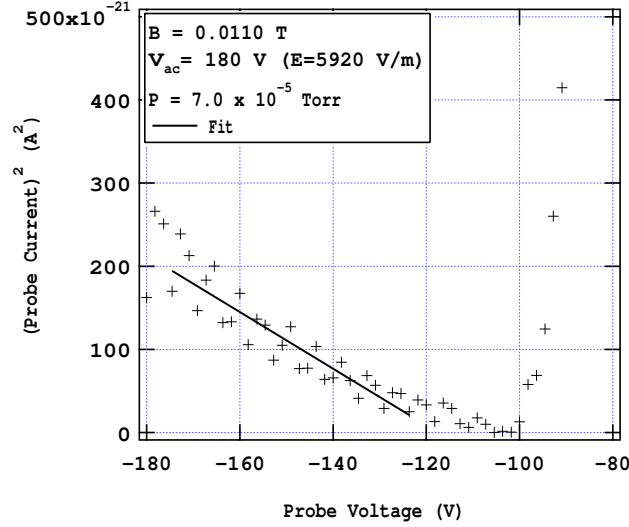
Figure E.2: Square of probe current in ion collection region of I-V characteristic given in Fig. E.1. The trendline was used to find ion density and also used in the determination of electron current in the probe I-V characteristic shown in Fig. E.3

and the slope of the plot was used to find ion density, where the ion density is given by the equation

It is suggested that the adaptation of neutral probe theory be employed in the case of $n_i/n_e > 50\%$ to achieve more reliable results. Figure E.1 shows a probe trace for an electric field of 180 V, magnetic field of 0.0110 T and pressure of 7×10^{-5} Torr, where ion current is clearly seen. Applying neutral probe theory[122] to the trace in Fig. E.1 the ion density was found using the ion collection region of the I-V characteristic. Here the square of the ion current was plotted versus probe voltage (Fig. E.2)

$$n_i = \frac{1.42 \times 10^{15} \left(m_i(\text{amu})\right)^{1/2} \left(-\text{slope}\right)^{1/2}}{A_p(\text{m}^2)} \tag{E.1}$$

The equation of the fit was given by

$$I^2 = -3.2 \times 10^{-21} \tag{E.2}$$

and equation (E.2) resulted in an ion density of 1.2×10^{11} m^{-3} for the case presented
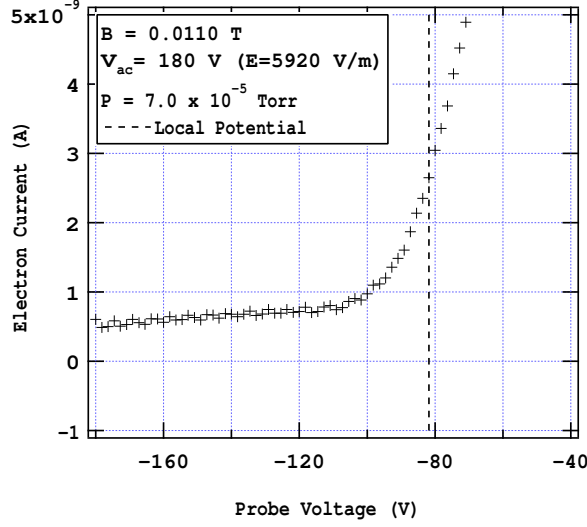
Figure E.3: Electron current from probe I-V characteristic determined using Eq. (E.3).

in Fig. E.1.

The pure electron current (Fig. E.3) was found by subtracting the ion current from the total probe current where the electron current was estimated by

$$I_e = I_p + \sqrt{-3.2 \times 10^{-21}V_p - 4 \times 10^{-19}} \tag{E.3}$$

This analysis deviates from standard neutral probe theory, as there was no electron saturation due to the long Debye length. However, the electron saturation current is generally used to infer plasma potential, which was already known from the vacuum solution. Using the slope of the line in the plot of $\ln(I_e)$ versus V_p (Fig. E.4), electron temperature was found to be $T_e = 38$ eV and the electron density was found from Eq. (E.4) given by

$$n_e = \frac{4I_e\left(V_p = \phi_p\right)}{eA_p\sqrt{\frac{8kT_e}{\pi m_e}}} \tag{E.4}$$

This is the exact solution as was presented in Section 6.3.1, except a correction to the probe current was made (previous step) to account for the ion current. The electron
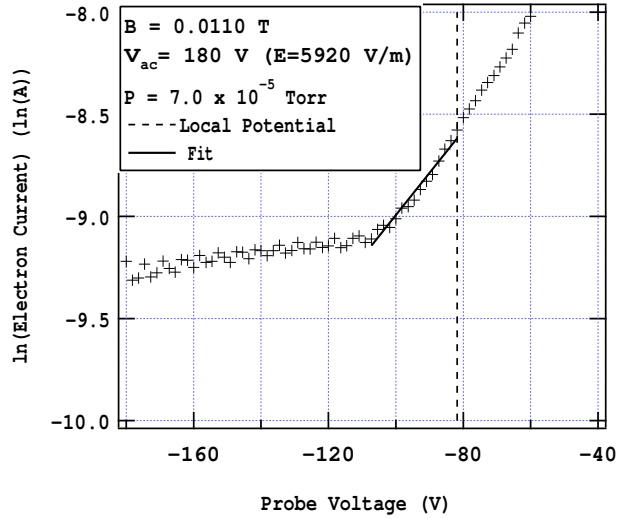
256

Figure E.4: The natural log of the electron current from Fig. E.3, where the curve fit is used to estimate electron temperature.

density in this case was found to be $n_e = 5.4 \times 10^9$ m^{-3}. (If the correction due to ion current was not employed the electron density from this equation would be $n_e = 3.7 \times 10^9$ m^{-3}.)

These results are, at the very least, in a range that is plausible. It was suspected that ion density was approximately equal to electron density where here they differ by a factor of ~ 20. However, these results may also have significant error due to the ion flow, which comes as a result of ion acceleration due to the electric field. The probe theory presented here may over or under estimate the ion density and also may misrepresent the total ion contribution to the probe current, which affects the interpretation of the curve for electron temperature and electron density. Furthermore, the concept of ion saturation is also not entirely relevant under these conditions where Debye shielding is absent.

This method may eventually lead to plausible results; however, certain considerations are yet needed to account for the ion flow (as ions are accelerated axially by the field). Furthermore accounting for the ion flow must be coupled with the position

and orientation of the probe and must also account for the lack of ion saturation. For example, when the probe is in certain locations/orientations the ion flow may be accelerated by the field in the direction of the probe surface so ion density would be overestimated; the converse may also be true where the ion current may be accelerated away from the probe surface to the ion density is underestimated. These two cases are highly likely to occur as the curved magnetic field acts as an ion lens[?]. Even though the probe was oriented with the collection surface parallel to z, the ions may have a radial component to their trajectories due to the "lens." The electron temperature and density found using this method are highly dependent on the adjustment of the probe current for the ion contribution, where Eq. (E.1) may need to be modified in the case of flowing ions. This method is not yet complete and is also discussed in Section 8.2.1. To complete this analysis, an accurate model of the ion current due to the above factors is necessary. For the purposes of the results presented in Chapters 6 and 7 it was determined that in cases where the ion density is greater than 50% of the electron density the results are considered unreliable, where the unreliable results are represented by large error bars. This condition appears to consistently at pressures above 3×10^{-5} Torr. Using an adapted neutral probe theory in these cases is a viable option when this method is fully developed to fully account for the directed ion current.

Appendix F

Permission to Use Material

The following letters grant the author permission to reproduce the cited copyrighted images for use in this dissertation:

Emily C. Fossum
Michigan Tech University
1018 R.L. Smith Bldg
1400 Townsend Dr.
Houghton, MI 49930
(906)487-1734
ecfossum@mtu.edu

June 16, 2009

Richard Hofer, Ph.D.
Jet Propulsion Laboratory
4800 Oak Grove Dr., MS 125-109
Pasadena, CA   91109
Richard.R.Hofer@jpl.nasa.gov

Dear Dr. Richard Hofer,

This letter will confirm our recent e-mail correspondence. I am completing a doctoral dissertation at Michigan Tech University entitled "Electron Transport in ExB Devices." I would like your permission to reprint in my dissertation excerpts from the following:

Hofer, R. R., "Development and Characterization of High-Efficiency, High-Specific Impulse Xenon Hall Thrusters," Ph.D. Dissertation, University of Michigan, 2004.

The excerpts to be reproduced are: Figures 5.4 and 5.5, the axial and radial magnetic field profiles of the NASA-173Mv1.

The requested permission extends to any future revisions and editions of my dissertation, including non-exclusive world rights in all languages, and to the prospective publication of my dissertation by UMI. These rights will in no way restrict republication of the material in any other form by you or by others authorized by you. Your signing of this letter will also confirm that you own the copyright to the above-described material.

If these arrangements meet with your approval, please sign this letter where indicated below and return it to me. Thank you very much.

Sincerely,

Emily C. Fossum

PERMISSION GRANTED FOR THE
USE REQUESTED ABOVE:

_____

Richard R. Hofer

Date: _____

Figure F.1: Letter granting the author permission to reproduce copyrighted images for use in Fig. 4.4.

Emily C. Fossum
Michigan Tech University
1018 R.L. Smith Bldg
1400 Townsend Dr.
Houghton, MI 49930
(906)487-1734
ecfossum@mtu.edu

June 16, 2009

James Haas, Ph.D.
Air Force Research Laboratory
Edwards Air Force Base
james.haas@edwards.af.mil

Dear Dr. James Haas,

This letter will confirm our recent e-mail correspondence. I am completing a doctoral dissertation at Michigan Tech University entitled "Electron Transport in ExB Devices." I would like your permission to reprint in my dissertation excerpts from the following:

Haas, J. M.,"Low-perturbation Interrogation of the Internal and Near-field Plasma Structure of a Hall Thruster Using a High-Speed Probe Positioning System," Ph.D. Dissertation, University of Michigan, 2001.

The excerpts to be reproduced are: Figure 5.81.a. (Plasma potential and electric field data for the P-5 Hall thruster, 1.6 kW)

The requested permission extends to any future revisions and editions of my dissertation, including non-exclusive world rights in all languages, and to the prospective publication of my dissertation by UMI. These rights will in no way restrict republication of the material in any other form by you or by others authorized by you. Your signing of this letter will also confirm that you own the copyright to the above-described material.

If these arrangements meet with your approval, please sign this letter where indicated below and return it to me. Thank you very much.

Emily C. Fossum

PERMISSION GRANTED FOR THE
USE REQUESTED ABOVE:

James Haas

Date: _16JUN09_

Figure F.2: Letter granting the author permission to reproduce copyrighted images for use in Fig. 4.9.

References

[1] Blender 3d design course, http://www.gryllus.net/blender/3d.html. Hirsig, N.

[2] Feynman, R. P. *Perfectly Reasonable Deviations from the Beaten Track: The Letters of Richard P. Feynman;* Basic Books, 2005.

[3] The Siglo Database, http://www.siglo-kinema.com. CPAT and Kinema Software. 1 June 2009.

[4] Courtesy of Michigan Technological University Office of Marketing and Communication. *Houghton, MI,* **May 2007**.

[5] Hofer, R. R. *Development and Characterization of High-Efficiency, High-Specific Impulse Xenon Hall Thrusters* PhD thesis, University of Michigan, Ann Arbor, Mich., **2004**.

[6] Courtesy of Magna-Tech PM Laboratories. *Cinnaminson, NJ,* **April 2006**.

[7] Haas, J. M. *Low-perturbation interrogation of the internal and near-field plasma structure of a Hall thruster using a high-speed probe positioning system* PhD thesis, University of Michigan, Ann Arbor, Michigan, **2001**.

[8] Levchenko, I.; Keidar, M.; Ostrikov, K. *Phys. Lett. A* **2009**, *373*, 1140–1143.

[9] Bouchoule, A.; Boeuf, J.-P.; Heron, A.; Duchemin, O. *Plasma Phys. Control. Fusion* **2004**, *46*, B407–B421.

[10] Kerslake, W. R.; Ignaczak, L. R. In *28th Joint Propulsion Conference and Exhibit*, pages AIAA–92–3516, Huntsville, AL, 6-8 July, 1992.

[11] Zhurin, V. V.; Kaufman, H. R.; Robinson, R. S. *Plasma Sources Sci. Technol.* **1999**, *8*, R1.

[12] Kim, V. *J. Propul. Power* **1998**, *14*(5), 736–743.

[13] Gulczinski, F. S. I.; Spores, R. A. In *32nd AIAA/ASME/SAE/ASEE Joint Propulsion Conferene*, pages AIAA–1996–2973, Lake Buena Vista, Fla., 1996.

[14] Space technology experiment satellite completes mission (http://www.nro.gov/PressReleases/prs_rel31.html). NRO Press Release. 18 June 1999.

[15] Estublier, D.; Saccoccia, G.; Gonzalez del Amo, J. *ESA Bulletin* **15 Feb 2007**, pages 40–46.

[16] International Space Technologies, Inc. debuts its stationary plasma thrusters on Loral-built MBSat satellite (http://ssloral.com/html/pressreleases/pr20040628.html). Space Systems Loral Press Release. 28 June 2004.

[17] The first US Hall thruster is operational in space (http://www.space-travel.com/ reports/ The_First_US_Hall_Thruster_Is_Operational_In _space _999.html). *Space Travel: Exploration and Tourism,* Staff Writers. 6 March 2007.

[18] de Grys, K. H.; Welender, B.; Dimicco, J.; Wenzel, S.; Kay, B.; Khayms, V.; Paisley, J. In *41st Joint Propulsion Conference & Exhibit*, pages AIAA 2005–3682, Tucson, Ariz., 10-13 July, 2005.

[19] Hofer, R. R.; Randolph, T. M.; Oh, D. Y.; Snyder, J. S.; de Grys, K. H. In *42nd Joint Propulsion Conference & Exhibit*, pages AIAA–2006–4469, Sacramento, Calif., 9-12 July, 2006.

[20] Choueiri, E. Y. *J. Propul. Power* **2004**, *20*(2), 193–203.

[21] Janes, G. S.; Lowder, R. S. *Phys. Fluids* **1966**, *9*(6), 1115–1123.

[22] Pote, B.; Tedrake, R. In *27th International Electric Propulsion Conference*, pages IEPC–2001–35, Pasadena, Calif., 15-19 October, 2001.

[23] Kaganovich, I. D.; Raitses, Y.; Sydorenko, D.; Smolyakov, A. *Phys. Plasmas* **2007**, *14*, 057104.

[24] Koo, J. W.; Boyd, I. D. *Phys. Plasmas* **2006**, *13*, 033501.

[25] Choueiri, E. Y. *Phys. Plasmas* **2001**, *8*(4), 1411.

[26] Knoll, A.; Thomas, C. A.; Gascon, N.; Cappelli, M. A. In *42nd AIAA/ASME/SAE/ASEE Joint Propulsion Conferene*, Sacramento, California, 2006.

[27] Taccogna, F.; Schneider, R.; Longo, S.; Capitelli, M. In *43rd AIAA/ASME/SAE/ASEE Joint Propulsion Conference & Exhibit*, pages AIAA–2007–5211, Cincinnati, Ohio, 8-11 July, 2007.

[28] Goebel, D. M.; Katz, I. In *Fundamentals of Electric Propulsion: Ion and Hall Thrusters*; Yuen, J. H., Ed.; John Wiley & Sons, 2008.

[29] Komurasaki, K.; Arakawa, Y. *J. Propul. Power* **1995**, *11*(6), 1317–1323.

[30] Fife, J. M. *Hybrid-PIC Modeling and Electrostatic Probe Survey of Hall Thrusters* PhD thesis, Massachusetts Institute of Technology, Cambridge, Mass., **1998**.

[31] Garrigues, L.; Boyd, I. D.; Boeuf, J. P. *J. Propul. Power* **2001**, *17*(4), 772–779.

[32] Hagelaar, G. J. M.; Bareilles, J.; Garrigues, L.; Boeuf, J. P. *J. Appl. Phys.* **2003**, *93*(1), 67–75.

[33] Fernandez, E.; Scharfe, M. K.; Thomas, C. A.; Gascon, N.; Cappelli, M. A. *Phys. Plasmas* **2008**, *15*(1), 012102.

[34] Hofer, R. R.; Katz, I.; Mikellides, I. G.; Goebel, D. M.; Jameson, K. K.; Sullivan, R. M.; Johnson, L. K. In *44th Joint Proupulsion Conference & Exhibit*, pages AIAA–2008–4924, Hartford, Conn., 21-23 July, 2008.

[35] O'Neil, T. M. *Phys. Rev. Lett.* **1985**, *55*(9), 943.

[36] Dubin, D. H. E.; O'Neil, T. M. *Phys. Plasmas* **1998**, *5*(5), 1305.

[37] Keidar, M.; Boyd, I. D. *App. Phys. Lett.* **19 Sept. 2005**, *87*(12), 121501.

[38] Chen, F. F. *Introduction to Plasma Physics and Controlled Fusion, 2nd Edition;* Plenum Press, 1984.

[39] Spitzer, L. J. *Astrophys. J.* **1952**, *116*, 299.

[40] Northrop, T. G.; Teller, E. *Phys. Rev.* **1960**, *117*(1), 215.

[41] Goldston, R. J.; Rutherford, P. H. *Introduction to Plasma Physics;* Taylor & Francis Group, LLC, 1995.

[42] Tanenbaum, B. S. *Plasma Physics;* McGraw-Hill, 1967.

[43] King, L. B. In *International Electric Propulsion Conference*, page 258, Princeton, NJ, 31 Oct-4 Nov, 2005.

[44] Baldwin, D. E. *Rev. Mod. Phys.* **1977**, *49*(2), 317.

[45] Catto, P. J.; Bernstein, I. B. *Phys. Fluids* **1981**, *24*(10), 1900.

[46] Shokri, B.; Niknam, A. R. *Phys. Plasmas* **2005**, *12*, 072107.

[47] Kaganovich, I. D.; Raitses, Y.; Sydorenko, D. In *43rd AIAA/AS-ME/SAE/ASEE Joint Propulsion Conference & Exhibit*, pages AIAA–2007–5206, Cincinnati, Ohio, 8-11 July, 2007.

[48] Gombosi, T. I. *Gaskinetic Theory;* Cambridge University Press, 1994.

[49] Villani, C. In *Handbook of Mathematicaal Fluid Dynamics, Vol. 1*; Friedlander, S., Serre, D., Eds.; Elsevier Science: Amsterdam, Netherlands, Jul 2002.

[50] Bhatnagar, P. L.; Gross, E. P.; Krook, M. *Phys. Rev.* **1954**, *94*, 511–525.

[51] Rosenbluth, M. N.; MacDonald, W. M.; Judd, D. L. *Phys. Rev.* **1957**, *107*(1), 1–6.

[52] Chandrasekhar, S. *Rev. Mod. Phys.* **Jan 1943**, *15*(1), 1–89.

[53] Callen, J. D. *Fundamentals of Plasma Physics, http://homepages.cae.wisc.edu/ callen/book.html, Draft Jan 21. 2003;* 2003.

[54] Choueiri, E. Y. *Phys. Plasmas* **1999**, *6*(5), 2290.

[55] Thomas, C. A. *Anomalous Electron Transport in the Hall-Effect Thruster* PhD thesis, Stanford University, **2006**.

[56] Cook, I. In *Plasma Physics and Nuclear Fusion Research*; Gill, R. D., Ed.; Academic Press Inc.: London, 1981; pages 293–304.

[57] Pines, D.; Bohm, D. *Phys. Rev.* **1952**, *85*(2), 338.

[58] Davidson, R. C. *Physics of Nonneutral Plasmas;* Imperial College Press and World Scientific Publishing Co. Pte. Ltd., 2001.

[59] Berg, H. C. *Random Walks in Biology;* Princeton University Press, 1983.

[60] Einstein, A. *Annalen der Physik* **1905**, *17*, 549–560.

[61] Brown, S. C. *Introduction to electrical discharges in gases;* John Wiley & Sons, Inc, 1966.

[62] Spitzer, L. J. *Physics of fully ionized gases;* Interscience Publishers (John Wiley & Sons), 1962.

[63] Helander, P.; Sigmar, D. J. *Collisional Transport in Magnetized Plasmas;* Cambridge University Press, 2002.

[64] Dubin, D. H. E.; O'Neil, T. M. *Phys. Rev. Lett.* **1988**, *60*(13), 1286.

[65] Bohm, D. In *Characteristics of Electrical Discharges in Magnetic Fields;* Chapter 2; Guthrie, A., Wakerling, R. K., Eds.; McGraw-Hill: New York, 1949; pages 13–76.

[66] Kadomtsev, B. B.; Pogutse, O. P. *Nucl. Fusion* **1971**, *11*, 67.

[67] Wagner, F.; *et al. Phys. Rev. Lett.* **1982**, *49*(19), 1408.

[68] Stacey, W. M. *Fusion Plasma Physics;* Wiley-VCH Verlag GmbH &Co KGaA, 2005.

[69] Lundin, D.; Helmersson, U.; Kirkpatrick, S.; Rohde, S.; Brenning, N. *Plasma Sources Sci. Technol.* **2008**, *17*, 025007.

[70] Sheridan, T. E.; Goekner, M. J.; Goree, J. *J. Vac. Sci. Technol. A* **1990**, *8*(1), 30.

[71] Meezan, N. B.; Hargus, W. A.; Cappelli, M. A. *Phys. Rev. E* **2001**, *63*, 026410.

[72] Bohm, D.; Gross, E. P. *Phys. Rev.* **1949**, *75*(12), 1851–1864.

[73] Bohm, D.; Gross, E. P. *Phys. Rev.* **1949**, *75*(12), 1864–1876.

[74] Looney, D. H.; Brown, S. C. *Phys. Rev.* **1954**, *93*(5), 965.

[75] Sturrock, P. A. *Phys. Rev.* **1960**, *117*(6), 1426–1429.

[76] Bohm, D. In *The Characteristics of Electrical Discharges in Magnetic Fields;* Chapter 1; Guthrie, A., Wakerling, R. K., Eds.; McGraw-Hill: New York, 1949; pages 1–12.

[77] Cohen, A. J. *NASA Technical Note* **1968**, *NASA TN D-4758*.

[78] Yoshikawa, S.; Rose, D. J. *Phys. Fluids* **1962**, *5*(3), 334–340.

[79] Morozov, A. I. In *39rd International Electric Proupulsion Conference*, pages IEPC–93–101, Seattle, Washington, 1993.

[80] Morozov, A. I. In *39rd International Electric Proupulsion Conference*, pages IEPC–95–05, Moscow, Russia, 1995.

[81] Lashinsky, H. *Phys. Rev. Lett.* **1964**, *12*(5), 121–123.

[82] Gorshkov, O. A.; Shagaida, A. A. *High Temperature Apparatuses and Structures* **2008**, *46*(4), 529–534.

[83] Spektor, R. In *30th International Electric Propulsion Conference*, pages IEPC–2007–70, Florence, Italy, 17-20 Septemver, 2007.

[84] Keidar, M.; Brieda, L. In *44th AIAA/ASME/SAE/ASEE Joint Propulsion Conference & Exhibit*, pages AIAA–2008–5186, Hartford, CT, 21-23 July, 2008.

[85] Black, D. C.; Mayo, R. M.; Caress, R. W. *Phys. Plasmas* **1997**, *4*(10), 3581.

[86] Raitses, Y.; Staack, D.; Keidar, M.; Fisch, N. J. *Phys. Plasmas* **2005**, *12*, 057104.

[87] Meezan, N. B.; Cappelli, M. A. *Phys. Rev. E* **2002**, *66*, 036401.

[88] Lazurenko, A.; Albarede, L.; Bouchoule, A. *Phys. Plasmas* **2006**, *13*(8), 083503.

[89] Lazurenko, A.; Dudok De Wit, T.; Cavoit, C.; Krasnoselskikh, V.; Bouchoule, A.; Dudeck, M. *Phys. Plasmas* **2007**, *14*, 033504.

[90] Krall, N. A.; Rosenbluth, M. N. *Phys. Fluids* **1963**, *6*(2), 254–265.

[91] Davidson, R. C.; Krall, N. A. *Phys. Fluids* **1970**, *13*(6), 1543.

[92] Rosenberg, M.; Krall, N. A.; McBride, J. B. *Phys. Fluids* **1985**, *28*(2), 538–543.

[93] Kennel, C. F.; Engelmann, F. *Phys. Fluids* **1966**, *9*(12), 2377.

[94] Hall, D. E.; Sturrock, P. A. *Phys. Fluids* **1967**, *10*(12), 2620.

[95] Lerche, I. *Phys. Fluids* **1968**, *11*(8), 1720.

[96] Davidson, R. C. *Methods in Nonlinear Plasma Theory;* Academic Press, 1972.

[97] Stringer, T. E. In *Plasma Physics and Nuclear Fusion Research*; Gill, R. D., Ed.; Academic Press Inc.: London, 1981; pages 305–318.

[98] Bernstein, I. B.; Engelmann, F. *Phys. Fluids* **1966**, *9*(5), 937.

[99] Cook, I. In *Plasma Physics*; Keen, B. E., Ed.; Institute of Physics: London, 1974.

[100] Scharfe, M. K.; Thomas, C. A.; Scharfe, D. B.; Gascon, N.; Cappelli, M. A.; Fernandez, E. In *43rd AIAA/ASME/SAE/ASEE Joint Propulsion Conference & Exhibit*, pages AIAA–2007–5208, Cincinnati, Ohio, 8-11 July, 2007.

[101] Lomas, P. J. *J. Phys. D: Appl. Phys.* **1976**, *9*, 1705–1713.

[102] Bradley, J. W. *Plasma Sources Sci. Technol.* **1998**, *7*, 572–580.

[103] Kolev, I.; Bogaerts, A. *Contributions to Plasma Physics* **2004**, *44*(7-8), 582–588.

[104] Davidson, R. C.; Chao, E. H. *Phys. Plasmas* **1996**, *3*(7), 2615.

[105] deGrassie, J. S.; Malmberg, J. H. *Phys. Rev. Lett.* **1977**, *39*(17), 1077–1080.

[106] deGrassie, J. S.; Malmberg, J. H. *Phys. Fluids* **1980**, *23*(63).

[107] Chao, E. H.; Davidson, R. C.; Paul, S. F.; Morrison, K. A. *Phys. Plasmas* **2000**, *7*(3), 831–838.

[108] Eggleston, D. L.; O'Neil, T. M.; Malmberg, J. H. *Phys. Rev. Lett.* **1984**, *53*(10), 982.

[109] Espejo, J.; Quraishi, J.; Robertson, S. *Phys. Rev. Lett.* **2000**, *84*(24), 5520–5523.

[110] Robertson, S.; Espejo, J.; Kline, J.; Quraishi, Q.; Triplett, M.; Walch, B. *Phys. Plasmas* **2001**, *8*(5), 1863–1869.

[111] Dubin, D. H. E. *Phys. Plasmas* **1998**, *5*(5), 1688–1694.

[112] Eggleston, D. L. *Phys. Plasmas* **1997**, *4*(5), 1196.

[113] Cappelli, M. A.; Hargus, W. A.; Meezan, N. B. *IEEE Trans. Plasma Sci.* **1999**, *27*(1), 96–97.

[114] Eggleston, D. L.; O'Neil, T. M. *Phys. Plasmas* **1999**, *6*(7), 2699.

[115] Linnell, J. A.; Gallimore, A. D. *Phys. Plasmas* **2006**, *13*, 093502.

[116] Fossum, E. C.; King, L. B. *IEEE Trans. Plasma Sci.* **2008**, *36*(1), 2088.

[117] Fossum, E. C.; King, L. B. In *44th AIAA/ASME/SAE/ASEE Joint Propulsion Conference & Exhibit*, page 5190, Hartford, Conn.2008, 2009.

[118] Fossum, E. C.; King, L. B. In *43rd AIAA/ASME/SAE/ASEE Joint Propulsion Conferene*, page 5207, Cincinnati, Ohio, 2007.

[119] Fossum, E. C.; King, L. B. In *30th International Electric Propulsion Conference*, page 153, Florence, Italy, 2007.

[120] Fossum, E. C.; King, L. B.; Makela, J. M. In *42nd AIAA/ASME/SAE/ASEE Joint Propulsion Conference & Exhibit*, page 5173, Sacramento, Calif, 2006.

[121] http://www.ansoft.com/maxwellsv/.

[122] Hutchinson, I. H. *Principles of Plasma Diagnostics, 2nd Edition;* Cambridge University Press, 2002.

[123] Hutson, A. R. *Phys. Rev.* **1955**, *98*(4), 889.

[124] Robertson, S.; Walch, B. *Phys. Plasmas* **2000**, *7*(6), 2340–2347.

[125] Quraishi, Q.; Robertson, S.; Walch, B. *Phys. Plasmas* **2002**, *9*(8), 3264.

[126] Nunes, Y.; Wemans, A.; Gordo, P. R.; Ribau Tiexiera, M.; Maneira, M. J. P. *Vacuum* **2007**, *81*(11-12), 1511–1514.

[127] Oks, E. M.; Vizir, A. V.; Yushkov, G. Y. *Rev. Sci. Instr.* **1998**, *69*(2), 853–855.

[128] Morrison, K. A.; Davidson, R. C.; Paul, S. F.; Belli, E. A.; Chao, E. H. *Phys. Plasmas* **2001**, *8*(7), 3506.

[129] Haas, J. M.; Galimore, A. D. *IEEE Transactions on Plasma Science* **2002**, *30*(2).

[130] McHarg, B. B.; Oakes, M. E. *Phys. Fluids* **1975**, *18*(8), 1059.

[131] Catto, P. J.; Xing, Z. L. *Phys. Fluids* **1985**, *28*(1), 352.

[132] Callen, J. D. In *Fundamentals of Plasma Physics, Online Book;* 2006.

[133] Perez-Luna, J.; Dubuit, N.; Garrigues, L.; Hagelaar, J. M.; Boeuf, J.-P. *IEEE Transactions on Plasma Science* **2008**, *36*(4), 1212.

[134] Kretzschmar, M. *Physica Scripta.* **1992**, *46*, 544–554.

[135] Bradley, J. W.; Thompson, S.; Gonzalvo, Y. A. *Plasma Sources Sci. Technol.* **2001**, *10*, 490–501.

[136] Schekochihin, A. A.; Cowley, S. C.; Dorland, W.; Hammett, G. W.; Howes, G. G.; Quataert, E.; Tatsuno, T. *The Astrophysical Journal Supplement Series* **2008**, *2*, 0704.0044.

[137] Barral, S. In *30th International Electric Propulsion Conference*, page 261, Florence, Italy, 17-20 September, 2007.

[138] Kremer, J. P.; Sunn Pedersen, T.; Marksteiner, Q.; Lefrancois, R. G.; Hahn, M. *Rev. Sci. Instr.* **2007**, *78*, 013503.

[139] Himura, H.; Nakashima, C.; Saito, H.; Yoshida, Z. *Phys. Plasmas* **2001**, *8*(10), 4651–4658.

[140] Budtz, C. V.; Bottiger, J.; Kringhoj, P. *Vacuum* **2000**, *56*(1), 9–13.

[141] Frignani, M.; Grasso, G. *Technical Report; Nuclear Engineering Laboratory Montecuccolino; University of Bologna* **2006**, pages LIN–R01.2006.

[142] Pekker, L. *Plasma Sources Sci. Technol.* **1995**, *4*, 31–35.

[143] Christou, C.; Barber, Z. H. *Plasma Sources Sci. Technol.* **2002**, *11*, 37–46.

[144] Barber, Z. H.; Christou, C.; Chiu, K. F.; Garg, A. *Vacuum* **2002**, *69*(1-3), 53–62.

[145] Montgomery, D. C. *Design and Analysis of Experiments;* John Wiley & Sons, Inc., 2005.

[146] Grissom, J. T.; Compton, R. N.; Garrett, W. R. *Phys. Rev. A* **1972**, *6*(3), 977.

[147] Kriesel, J. M.; Driscoll, C. F. *Phys. Rev. Lett.* **2000**, *85*(12), 2510.

[148] Bethea, R. M.; Duran, B. S.; Boullion, T. L. *Statistical Methods for Engineers and Scientists;* Marcel Dekker, Inc., 1995.

[149] Hocking, R. R. *Biometrics* **1976**, *32*, 1–49.

[150] Schabenberger, O.; Gotway, C. A. *Statistical methods for spatial data analysis;* Chapman & Hall/CRC Press, 2005.